Karlsruhe Institute of Technology

NEUTRAL HIGGS BOSON SEARCHES IN THE $\mathrm{H} \to \tau\tau \to \mu\mu$ DECAY CHANNEL

Zur Erlangung des akademischen Grades eines
DOKTORS DER NATURWISSENSCHAFTEN
von der Fakultät für Physik des
Karlsruhe Institut für Technologie (KIT) genehmigte

DISSERTATION

von

Dipl. Phys. Agni Bethani
aus Athen, Griechenland

Referent: Prof. Dr. Thomas Müller
Institut für experimentelle Kernphysik

Korefferent: Prof. Dr. Günter Quast
Institut für experimentelle Kernphysik

Tag der mündlichen Prüfung: 5. Juli 2013

Erklärung der Selbständigen Anfertigung meiner Dissertationsschrift

Hiermit erkläre ich, dass ich die Dissertationsschrift mit dem Titel

Neutral Higgs boson searches in the $\mathrm{H} \rightarrow \tau\tau \rightarrow \mu\mu$ **decay channel**

selbständig und unter ausschliesslicher Verwendung der angegebenen Hilfsmittel angefertigt habe.

Agni Bethani

Karlsruhe, 19 Juni 2013

Abstract

This dissertation describes the search for Higgs bosons decaying to a pair of τ leptons both decaying to muons. The analysis was performed using events recorded by the CMS detector at the LHC in 2011 and 2012, at centre-of-mass energy 7 TeV and 8 TeV respectively. The dataset corresponds to total integrated luminosity of 17 fb^{-1}, 4.9 fb^{-1} taken at 7 TeV centre-of-mass energy and 12.1 fb^{-1} at 8 TeV. The results were interpreted in the context of both the Standard Model and the Minimal Supersymmetric Standard Model. Upper limits were set to the Higgs production cross section in the former case and on the $(\tan\beta,\ m_A)$ plane in the latter. The update of this analysis with more data, combined with other $\tau\tau$ final states, lead to the first evidence of the Higgs coupling to τ leptons.

Included in this document is also the study of the Z boson production followed by $\mathrm{Z} \rightarrow \tau\tau$ decay with two muons in the final state. This analysis was performed with 36 pb^{-1} of data collected in 2010, at centre-of-mass energy 7 TeV, by the CMS experiment. The result of this study was the measurement of the Z production cross section in proton-proton collisions. The analysis procedures developed for the Z boson decay to τ leptons were used to commission the Higgs boson searches in the same decay channel.

Acknowledgements

First, I would like to express my gratitude to Alexei Raspereza, my research advisor and supervisor who guided and encouraged me and taught me everything I know. I would like to thank Professor Thomas Müller for giving me the opportunity to join the University of Karlsruhe and his advice through the years. I would also like to thank everyone in the KIT/DESY Higgs group, especially to Professor Günter Quast for sharing his invaluable experience and for his support from the very beginning to the very end.

Last but not least, I thank my mum and Chris, for their love and moral support.

Contents

Chapter 1

Introduction

On the 4th of July 2012, a new boson was discovered at the Large Hadron Collider (LHC) in Geneva. This new particle according to the latest measurements is compatible with the Higgs boson, the last missing piece of the Standard Model. The news of the discovery caused a lot of excitement in the physics community and it was also covered by popular press.

The Standard Model (SM) is the theory that describes a wide range of phenomena in particle physics. In the context of the SM, the electroweak symmetry breaking (EWSB), a mechanism which generates the masses of the vector bosons Z and $W^{\pm}$, is achieved by introducing a complex scalar doublet leading to the prediction of the Higgs boson. The theory of the SM was developed during the 60's and 70's. Since then all other theoretically predicted particles have been observed experimentally, apart from the Higgs boson. Until last year.

Physicist have been searching for the Higgs boson in many collider experiments, such as LEP, HERA and Tevatron, with no success. The LHC has opened a new era in particle physics. The energy and the luminosity feasible at the LHC, exceed by far those of previous colliders. The LHC is a proton-proton collider build inside an already existing ring with 26.7 km circumference, previously hosting the LEP collider, at CERN in Geneva. By design the LHC is able to accelerate and collide protons at centre of mass energy 14 TeV. However during the first LHC period 2010-2012 the maximum centre of mass energy was 8 TeV.

The main Higgs production mechanism at the LHC is gluon fusion but there is also contribution from vector boson fusion and associated production with a vector boson. There are many Higgs decays that can be used as signatures to search for the Higgs boson, such as $\mathrm{H} \to \gamma\gamma$, $\mathrm{H} \to ZZ$ and $\mathrm{H} \to \tau\tau$. Precision electroweak measurements constrain the SM Higgs mass $m_H < 158$ GeV. In this mass region, the $\mathrm{H} \to \tau\tau$ decay channel has the second largest branching fraction, after the decay channel to a pair of b quarks which however suffers from large QCD background. According to the SM, the Yukawa coupling of the Higgs boson to fermions, generates the fermion masses. This aspect of the theory is tested directly in the search of the Higgs boson decaying to τ pairs.

However the SM isn't perfect. There are many arguments that suggest that new physics is necessary to describe the universe as we know it. Evidence for dark matter, the neutrino oscillation and the gravity are not predicted by the SM. There are many theories attempting to extent the SM to new territories. One of the most popular ideas is Supersymmetry. The minimal supersymmetric scenario is the Minimal Supersymmetric Standard Model (MSSM). In the context of the MSSM, the Higgs decay into τ pairs may be enhanced. Therefore the $\tau\tau$ final state is sensitive to new physics.

The current thesis describes the search of the Higgs decay to a pair of τ leptons both decaying to muons. This search, combined with other τ decay final states, led to the first evidence of Higgs couplings to leptons. This analysis was performed with data collected in 2011 and 2012 at the LHC, corresponding to total integrated luminosity of 17 fb^{-1}. The $\mathrm{H} \to \tau\tau \to \mu\mu$

is a particularly demanding channel. The main challenges are the large dimuon background $Z\gamma* \rightarrow \mu\mu$, and the small topological branching fraction of the $\tau\tau \rightarrow \mu\mu$ decay, which is approximately 3%. Despite the challenges, this channel is worth exploring. When combined with the other decay channels the improvement of the result, in terms of exclusion limits, is in the order of 10%.

Another study included in this document is the analysis of the $Z \rightarrow \tau\tau \rightarrow \mu\mu$ events. The result of this study was the measurement of the Z production cross-section in proton-proton collisions. The measurement was combined with other CMS searches in different final states, and contributed to the official Z cross-section measurement. This analysis was performed with 36 pb^{-1} of data collected in 2010. The measurement of $Z \rightarrow \tau\tau$ events is important as these constitute a major source of irreducible background to the search for neutral Higgs Bosons decaying to τ leptons. Establishing signal in the $Z \rightarrow \tau\tau \rightarrow \mu\mu$ channel is a necessary step before attempting to search for Higgs signal in the same final state. The $Z \rightarrow \tau\tau \rightarrow \mu\mu$ analysis served for commissioning the $H \rightarrow \tau\tau \rightarrow \mu\mu$ searches.

Both searches use data collected with the CMS (Compact Muon Solenoid) detector. CMS is one of the two largest experiments along the LHC ring. The central feature of the CMS detector, as the name gives away, is a superconducting solenoid 13 m long and with internal diameter 6 m. The solenoid can generate a uniform magnetic field along the beam direction, up to 3.8 T. Inside the coil there is a tracking system fully based on silicon technology, a lead tungstate crystal electromagnetic calorimeter and a hadronic calorimeter made of layers of brass and scintillator. Outside the solenoid, integrated into the steel magnetic flux return yokes, there is the muon detecting system, which consists of gas ionisation chambers.

This document is divided in eight chapters:

- First is a summary to the SM theory with emphasis to the EWSB and the Higgs mechanism. In the same chapter, we introduce the idea of SUSY and the Higgs sector in the context of the MSSM.
- The third chapter is a description of the CMS detector and the data-acquisition system.
- The fourth chapter describes the muon trigger system, and gives in detail the High Level Trigger paths and their efficiencies, used in both analyses described in this thesis.
- In the fifth chapter the physics objects definitions and reconstruction methods are presented. In addition we describe analysis tools and algorithms common in both the Z cross section measurement and the Higgs searches.
- In the sixth chapter the study of the $H \rightarrow \tau\tau \rightarrow \mu\mu$ channel is described. The final measurement of the Z boson production cross section in combination with the other $\tau\tau$ final states is presented.
- The seventh chapter is a detailed report on the searches for neutral Higgs bosons in the $H \rightarrow \tau\tau \rightarrow \mu\mu$ channel. The analysis procedures and the results are presented here, along with the combination with the other $\tau\tau$ final states. The results were interpreted in the context of both the SM and the MSSM scenario. In the same chapter, a historical reference to the discovery of the Higgs boson on the 4^{th} of July last year, together with the latest measurements of its mass and spin. Finally the latest CMS results on the $H \rightarrow \tau\tau$ channel and the first evidence of the Higgs coupling to leptons are presented.

Chapter 2

The Standard Model and the Higgs boson

The Standard Model (SM) [1–5] of particle physics provides the modern understanding of all the interactions of subatomic particles, except those due to gravity. It was developed in the 1960s and 1970s and has stood for 30 years as the theory of particle physics, passing numerous stringent tests. In fact while it is believed that the standard model is not a perfect description of particle physics, it is expected to be incomplete rather than wrong. The latest triumph of the standard model was the discovery of a new boson with mass close to 126 GeV in July 2012, compatible with the predicted Higgs boson. The discovery of the Higgs-like particle is discussed in section 7.8.

2.1 Elementary particles

The building blocks of matter are elementary spin 1/2 particles, fermions, of two kinds: quarks and leptons. There are six types of quarks, also referred to as flavours: up, down, charm, strange, top and bottom quarks (u,d,c,s,t, and b respectively), each quark appearing in three so-called colours. Three charged particles the electron e, the muon μ, the tau τ and the corresponding neutrinos ν_e, ν_μ, ν_τ comprise the leptons. The quarks and the leptons are classified in three families of increasing mass.

In addition there are spin 1 particles, bosons, that are mediators of the three fundamental forces: electromagnetic, weak and strong. Electromagnetic radiation is emitted and absorbed in the form of photons γ. The $\mathrm{W}^\pm$ and Z^0 mediate the weak interactions and eight gluons (g) are the quanta of the colour force field. The SM particles and their properties are summarised in figure 2.1. Normal atomic matter is composed of up and down quarks (u and d) and electrons.

Only electrically charged particles interact with the photon. Weak interactions mediated by the Z and $\mathrm{W}^\pm$ bosons, involve both charged fermions and the electrically neutral neutrinos. While the electrons participate in electromagnetic and weak interactions the neutrinos interact only weakly. Unlike the leptons, each quark flavor undergoes colour altering interactions mediated by gluons in addition to electromagnetic and weak interactions. Colour interactions are much stronger than electromagnetic or weak interactions and they dominate the physics of quarks.

Experiments suggest that quarks don't exist as free particles. Strong forces bind them into two types of hadrons: baryons and mesons. The baryons are colour singlets formed by three quarks:

$$B = \sum_{ijk} \epsilon^{ijk} q_i q_j q_k, \tag{2.1.1}$$

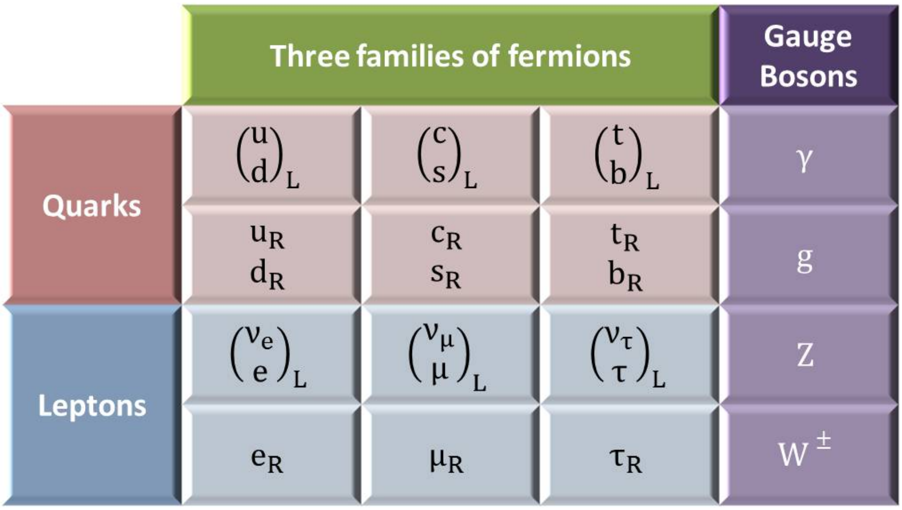

Figure 2.1: The particles of the Standard model.

Familiar examples of baryons are the protons and neutrons, p_{uud} and n_{udd} respectively, constitutes of the atomic nucleus. The mesons are also colour singlets but formed by a quark and an anti-quark pair:

$$M = \sum_i \bar{q}^{-i} q_i. \tag{2.1.2}$$

Mesons are, for example, the $\pi^{\pm}_{u\bar{d},d\bar{u}}$, $\pi^{0}_{\frac{u\bar{u}+d\bar{d}}{\sqrt{2}}}$, $K^{\pm}_{u\bar{s},s\bar{u}}$ and $K^{0}_{s\bar{d}}$. All indices i,j and k run over the three colour states of quarks and ϵ^{ijk} is the completely antisymmetric Levi-Civita tensor.

A heavy particle will decay spontaneously to lighter particles through standard model interactions when such a decay is kinetically allowed. These decays correspond to transitions of heavier fermions to lighter ones, mediated by γ, Z and $W^{\pm}$. This is the reason why matter in the universe today is composed only of members of the lightest family, u-quarks, d-quarks and electrons, immersed in a bath of weakly interacting “invisible” neutrinos.

2.2 The Standard Model

Quantum field theories are a special kind of quantum mechanical theories which describe the behaviour of particles. A gauge theory is a type of field theory in which the Lagrangian is invariant under a group of local transformations. The term gauge refers to redundant degrees of freedom in the Lagrangian. The transformations between possible gauges, called gauge transformations, form a Lie group which is referred to as the symmetry group or the gauge group of the theory. Gauge fields are vector fields that have to be included in the Lagrangian in order to ensure its invariance under the local group transformations. This is the so called gauge invariance. When such a theory is quantised, the quanta of the gauge fields are called gauge bosons.

The standard model is a quantum field theory and also a gauge theory with the symmetry group $SU_c(3) \times SU_L(2) \times U_Y(1)$[1]. According to Noether's theorem for every symmetry there is a quantity, quantum number, which is conserved. Therefore in the SM there must be three quantum numbers, each associated with one of the three symmetries $SU_c(3)$, $SU_L(2)$ and $U_Y(1)$.

Why the SM is based on the gauge group $SU_c(3) \times SU_L(2) \times U_Y(1)$ is something we don't know yet. We have no deep understanding of why there are three symmetries or if there will be

---

[1] The SM theory is presented as described in [6] and [7].

more revealed in the future. This is the weakest point in our understanding of the SM. However it is a remarkable discovery that so far this group describes the experimental data accurately.

The specific gauge bosons associated with the generators of the algebra of the $SU_c(3) \times SU_L(2) \times U_Y(1)$ group are :

$$\begin{array}{lll} SU_c(3) & SU_L(2) & U_Y(1) \\ \downarrow & \downarrow & \downarrow \\ 8G^\alpha_\mu & 3W^\alpha_\mu & B_\mu \\ \alpha = 1, ..., 8 & \alpha = 1, 2, 3 & \end{array}$$

The eight spin 1 particles, $\mathrm{G}^\alpha_\mu(\mathrm{x})$, associated with the factor $\mathrm{SU}_c(3)$ are the gluons and the associated subscript “c” denotes “colour”. Any particle that transforms with respect to this factor of the gauge group, and couples to gluons is said to be coloured or carry colour. This type of interaction is called strong interaction and the particles which couple to gluons are said to be “strongly interacting”. Three spin 1 particles, $\mathrm{W}^\alpha_\mu(\mathrm{x})$, are associated with the factor $\mathrm{SU}_L(2)$, and one, $\mathrm{B}_\mu(\mathrm{x})$, with the factor $\mathrm{U}_Y(1)$. The quantum numbers related to the $\mathrm{SU}_L(2)$ and the $\mathrm{B}_\mu(\mathrm{x})$ are the isospin $\vec{T}$ and the hypercharge Y respectively. The electromagnetic charge is related to the hypercharge and the third component of the isospin T_3 by:

$$Q = Y + T_3 \tag{2.2.1}$$

The four spin 1 bosons associated with the factors $SU_L(2) \times U_Y(1)$ are related to the physical bosons that mediate the weak interactions, $\mathrm{W}^\pm$ and Z, and the photon, in a way that will be discussed later on.

The character of the interactions of fermions can be compactly summarised by their transformation properties with respect to the gauge group $SU_c(3) \times SU_L(2) \times U_Y(1)$. Each fermion family is made of five different representations:

$$Q^m_L(2,3)_{+\frac{1}{6}}, \qquad L^m_L(2,1)_{-\frac{1}{2}}, \qquad U^m_R(1,3)_{+\frac{2}{3}}, \qquad D^m_R(1,3)_{-\frac{1}{3}}, \qquad E^m_R(1,1)_{-1} \tag{2.2.2}$$

L(or R) refers to the left (or right) chiral projections:

$$\psi_{L(R)} \equiv \frac{1}{2}(1 \mp \gamma_5)\psi \tag{2.2.3}$$

The superscript m runs over the three families of fermions. The notation means that, for example, the left-handed up and down quarks of the m^{th} family, Q^m_L, form a doublet (2) of the $SU(2)_L$ group, carry hypercharge $+\frac{1}{6}$ and are in a triplet (3) under the $SU(3)_c$ group of strong interactions. The symbol L^m_L stands for the isospin doublet composed of the left-handed charged lepton l^m_L and the neutrino ν^m_L. The left handed fermions transform as a $SU(2)$ doublets, carry weak isospin and therefore are the ones that take part in the weak interactions. This is what the subscript “L” in the $SU(2)_L$ stands for. The symbols U^m_R, D^m_R, E^m_R stand for the right-handed up and down type quarks and the right handed leptons. The right handed fermions carry 0 isospin and are singlets under SU(2).

The SM Lagrangian must be invariant under the symmetry $SU_c(3) \times SU_L(2) \times U_Y(1)$. The most general form of a Lagrangian involving these fields is:

$$\begin{aligned} \mathcal{L}_{fg} = &- \frac{1}{4}G^\alpha_{\mu\nu}G^{\alpha\mu\nu} - \frac{1}{4}W^{\alpha\mu\nu}G^\alpha_{\mu\nu} - \frac{1}{4}B_{\mu\nu}B^{\mu\nu} \\ &- \frac{1}{2}\bar{L}_m\gamma^\mu D_\mu L_m - \frac{1}{2}\bar{E}_m\gamma^\mu D_\mu E_m - \frac{1}{2}\bar{Q}_m\gamma^\mu D_\mu Q_m - \frac{1}{2}\bar{D}_m\gamma^\mu D_\mu D_m - \frac{1}{2}\bar{U}_m\gamma^\mu D_\mu U_m \end{aligned} \tag{2.2.4}$$

where the covariant derivative is:

$$D_\mu = \partial_\mu - ig_1 Y B_\mu - ig_2 \frac{\tau^\alpha}{2} W_\mu^\alpha - ig_3 \frac{\lambda_b}{2} G^b \mu \tag{2.2.5}$$

The $g_{1,2,3}$ are the coupling strengths of the electromagnetic, weak and strong force respectively.

This Lagrangian describes well the interactions of matter and radiation, however it doesn't include any mass terms of the form $m_f \psi \bar{\psi}$, $m_B^2 B_\mu B^\mu$, $m_W^2 W_\mu W^\mu$ and $m_g^2 G_\mu G^\mu$. The presence of mass terms would break the $SU_c(3) \times SU_L(2) \times U_Y(1)$ symmetry and would violate the gauge invariance of the Lagrangian. According to experimental observation the gluons are massless, so the $SU_c(3)$ gauge invariance of the strong interactions is unbroken. However the Z and $\mathrm{W}^\pm$ bosons are massive. Therefore the $SU_L(2) \times U_Y(1)$ which describes the unified electroweak interactions must be broken. In other words, the electroweak symmetry breaking or EWSB for short, will give masses to the Z and $\mathrm{W}^\pm$ bosons. The same mechanism gives rise to the masses of quarks and charged leptons. In the SM the EWSB is achieved via the Higgs mechanism.

2.3 The Higgs mechanism

"...it was shown that the Goldstone theorem, that Lorenz covariant field theories in which spontaneous breakdown of symmetry under an internal Lie group occurs contain zero-mass particles fails if and only if the conserved currents associated with the internal group are coupled to gauge fields. ... as a consequence of this coupling, the spin-one quanta of some of the gauge fields acquire mass;..." Peter W. Higgs (1964). "Broken Symmetries and the Masses of Gauge Bosons". Physical Review Letters 13 (16): 508509.

The term spontaneous means that the symmetry is not broken explicitly by the interactions but rather by the asymmetry of the state of lowest energy, referred to as the vacuum quantum field theory. According to the Goldstone theorem the spontaneous symmetry breaking creates massless bosons, so called Goldstone bosons. If the broken symmetry also corresponds to a gauge symmetry, then the associated Goldstone boson and the massless gauge boson combine to form a massive gauge boson. This is the famous Higgs mechanism [8–11]. The Higgs mechanism preserves the number of states. A massless vector field, gauge boson, carries two degrees of freedom. By acquiring mass it picks up a third degree of freedom with longitudinal polarisation. The extra degree of freedom came from the Goldstone boson which is not longer in the theory.

The simplest way to implement the Higgs mechanism is to add a weakly coupled spin-0 particle to the theory with a potential that is minimised at a non-zero field value (figure 2.2). The field of such a particle spontaneously breaks the electroweak $SU_L(2) \times U_Y(1)$ symmetry. Hence, the EWSB is a result of the Higgs mechanism. The coupling of this field with the $\mathrm{W}_\mu^\alpha(\mathrm{x})$ and $\mathrm{B}_\mu(\mathrm{x})$ gauge bosons gives them mass.

Since the scalar field is supposed to produce a mass for the fermions as well, it must have Yukawa coupling with the fermions. Since all the fermions are either singlets or doublets under $SU_L(2)$ the new scalar field must itself be either a doublet or a triplet if it is to combine with two fermions into a gauge invariant Yukawa interaction. It turns out that a scalar triplet cannot by itself couple in a way that can generate masses for all the known massive fermions, but a scalar doublet can. The simplest choice is therefore to add a single complex scalar doublet called the Higgs field:

$$\phi = \begin{pmatrix} \phi^+ \\ \phi^0 \end{pmatrix} \tag{2.3.1}$$

The Lagrangian can be written as:

$$\begin{aligned}\mathcal{L}_{Higgs} =& (D_\mu\phi)^\dagger(D^\mu\phi) - V(\phi^\dagger\phi) \\ &+ \left(f_{mn}\bar{L}_m E_n \phi + h_{mn}\bar{Q}_m D_n \phi + g_{mn}\bar{Q}_m U_n \tilde{\phi} + h.c\right)\end{aligned} \tag{2.3.2}$$

and the potential is:

$$V(\phi^+\phi) = \lambda\left[\phi^+\phi - \frac{\mu^2}{2\lambda}\right]^2 \tag{2.3.3}$$

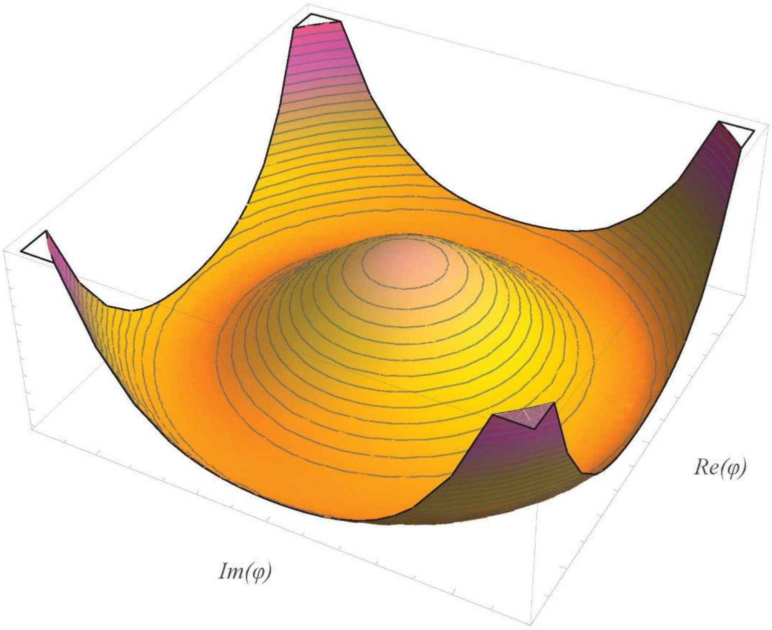

Figure 2.2: The illustration of the Higgs potential explains the spontaneous symmetry breaking. The Higgs potential is symmetric with a local maximum in the centre. The energy state in the centre is symmetric, however it is an excited state and therefore unstable. Because of the form of the potential, the stable final state at the minimum, the vacuum state, is not symmetric anymore. This is called spontaneous symmetry breaking.

Unitarity requires that the constants λ and μ^2 be real and stability demands that λ be positive. In order to ensure that the ground state not be $SU_L(2) \times U_Y(1)$ invariant we further require that μ^2 be positive. The covariant derivative must be:

$$D_\mu = \partial_\mu\phi - \frac{i}{2}g_2 W_\mu^\alpha \tau_\alpha \phi - \frac{i}{2}g_1 B_\mu \phi \tag{2.3.4}$$

Finally the complete standard model Lagrangian becomes:

$$\mathcal{L}_{SM} = \mathcal{L}_{fg} + \mathcal{L}_{Higgs} \tag{2.3.5}$$

Expanding around the minimum of its potential and applying a convenient gauge transformation, the scalar doublet can be written in the form:

$$\phi = \begin{pmatrix} 0 \\ (\upsilon + H(x))\frac{1}{\sqrt{2}} \end{pmatrix} \tag{2.3.6}$$

where the parameter v is the minimum, so called vacuum expectation value of ϕ and H(x) is a real scalar field called the standard model Higgs boson field representing the radial component of deviations from the vacuum expectation value. By minimising the potential 2.3.3 we find that the vacuum expectation value to be:

$$v^2 = \frac{\mu^2}{\lambda} \tag{2.3.7}$$

In order to determine the particle masses we must identify the mass terms in the complete Lagrangian. The expansion of $\mathcal{L}_{fg}$ only contributes to kinetic terms of the fermions and the spin 1 bosons. Everything else comes from the expansion of $\mathcal{L}_{Higgs}$. Using equations 2.3.4 and 2.3.6 we can write the covariant derivative as:

$$D_\mu = \frac{1}{\sqrt{2}} \begin{pmatrix} 0 \\ \partial_\mu H \end{pmatrix} - \frac{i}{2\sqrt{2}} \begin{pmatrix} g_2 W_\mu^3 + g_1 B_\mu & g_2 W_\mu^1 - i g_2 W_\mu^2 \\ g_2 W_\mu^1 + i g_2 W_\mu^2 & -g_2 W_\mu^3 + g_1 B_\mu \end{pmatrix} \begin{pmatrix} 0 \\ v + H \end{pmatrix} \tag{2.3.8}$$

The scalar potential term , using again 2.3.6, becomes:

$$V = \frac{\lambda}{4} \left[(v+H)^2 - \frac{\mu^2}{\lambda} \right]^2 \tag{2.3.9}$$

The Yukawa couplings may be expanded in an identical way:

$$\begin{aligned} \bar{L}_m E_n \phi &= \frac{1}{\sqrt{2}} \begin{pmatrix} \bar{\nu}_m \\ \bar{\mathcal{E}}_m \end{pmatrix}^T E_n \begin{pmatrix} 0 \\ v + H \end{pmatrix} \\ &= \frac{1}{\sqrt{2}} (v + H) \bar{\mathcal{E}}_m E_n \end{aligned} \tag{2.3.10}$$

and similarly for Q,U and D:

$$\begin{aligned} \bar{Q}_m U_n \bar{\phi} &= \frac{1}{\sqrt{2}} \begin{pmatrix} \bar{\mathcal{U}}_m \\ \bar{\mathcal{D}}_m \end{pmatrix} U_n \begin{pmatrix} v + H \\ 0 \end{pmatrix} \\ &= \frac{1}{\sqrt{2}} (v + H) \bar{\mathcal{U}}_m U_n \end{aligned} \tag{2.3.11}$$

Combining the above results, the Higgs Lagrangian is:

$$\begin{aligned} \mathcal{L}_{Higgs} = &- \frac{1}{2} \partial_\mu H \partial^\mu H - \lambda v^2 H^2 - \lambda v H^3 \\ &- \frac{\lambda}{4} H^4 - \frac{1}{8} g_2^2 (v+H)^2 |W_\mu^1 - i W_\mu^2|^2 \\ &- \frac{1}{8} (v+H)^2 (-g_2 W_\mu^3 + g_1 B_\mu)^2 \\ &- \frac{1}{\sqrt{2}} (v+H) [f_{mn} \bar{\mathcal{E}} E_n + h.c.] \\ &- \frac{1}{\sqrt{2}} (v+H) [g_{mn} \bar{\mathcal{U}} U_n + h.c.] \\ &- \frac{1}{\sqrt{2}} (v+H) [f_{mn} \bar{\mathcal{D}} D_n + h.c.] \end{aligned} \tag{2.3.12}$$

2.4 Boson masses

To determine the mass of the Higgs boson we have to compare the H^2 term of $\mathcal{L}_{Higgs}$ with the standard form $-\frac{1}{2}m_{\mathrm{H}}H^2$,which gives:

$$m_{\mathrm{H}}^2 = 2\lambda\upsilon^2 = 2\mu^2 \tag{2.4.1}$$

In the case of the vector bosons the relevant terms are:

$$-\frac{1}{8}g_2^2\upsilon^2|W_\mu^1 - iW_\mu^2|^2 - \frac{1}{8}\upsilon^2(-g_2W_\mu^3 + g_1B_\mu)^2 \tag{2.4.2}$$

W_1 and W_2 can be represented as the real and imaginary parts of a complex, charged field:

$$W_\mu^\pm = \frac{1}{\sqrt{2}}(W_\mu^1 \mp iW_\mu^2) \tag{2.4.3}$$

with mass:

$$M_{\mathrm{W}} = M_1 = M_2 = \frac{g_2\upsilon}{2} \tag{2.4.4}$$

The remaining vector fields that appear in the mass term are W_μ^3 and B_μ. The combination $g_1B_\mu - g_2W_\mu^3$ can be renormalised to define the mass eigenstate:

$$Z_\mu = \frac{-g_1B_\mu + g_2W_\mu^3}{\sqrt{g_1^2 + g_2^2}} \tag{2.4.5}$$

which is the last gauge boson Z, with mass:

$$M_{\mathrm{Z}}^2 = \frac{1}{4}(g_1^2 + g_2^2)\upsilon^2 \tag{2.4.6}$$

The final mass eigenstate is the combination of W_μ^3 and B_μ that is orthogonal to Z_μ:

$$A_\mu = \frac{g_1W_\mu^3 + g_2B_\mu}{\sqrt{g_1^2 + g_2^2}} \tag{2.4.7}$$

This is the field of the usual photon and remains massless.

2.5 Fermion masses

The mass terms, quadratic in the fermion fields come from the Yukawa couplings after the shifting of the scalar field by υ. The relevant terms are:

$$\mathcal{L} = -\frac{\upsilon}{\sqrt{2}}(f_{mn}\bar{\mathcal{E}}_mE_n + g_{mn}\bar{\mathcal{U}}_mU_n + h_{mn}\bar{\mathcal{D}}_mD_n + h.c.) \tag{2.5.1}$$

The mass terms induced by the Yukawa couplings of fermions to the Higgs vacuum expectation value are in general not diagonal in the family indices, m and n. They may be diagonalised following the procedure. The fermion fields can be redefined:

$$\begin{aligned} \mathcal{E}_m &= U_{mn}^e\mathcal{E}_n' & \qquad E_m &= V_{mn}^eE_n' \\ \mathcal{U}_m &= U_{mn}^u\mathcal{U}_n' & \qquad U_m &= V_{mn}^uU_n' \\ \mathcal{D}_m &= U_{mn}^d\mathcal{D}_n' & \qquad D_m &= V_{mn}^dD_n' \end{aligned} \tag{2.5.2}$$

where the matrices $U^{e,u,d}$ and $V^{e,u,d}$ act on the family indices and must be unitary in order to preserve the canonical form of the kinetic terms. It is always possible to choose $U^{e,u,d} = V^{e,u,d}*$ to ensure that the new mass matrices are diagonal:

$$U^{e\dagger} f V^e = V^{eT} f V^e = diag(f_e, f_\mu, f_\tau) \tag{2.5.3}$$

where f_e, f_μ, f_τ are real and non-negative. The same can be done for $V^{uT} g V^u$ and $V^{d^T} h V^d$. The mass terms then become:

$$\mathcal{L} = -\frac{\upsilon}{\sqrt{2}}(f_m \bar{\mathcal{E}}_m E_m + g_m \bar{\mathcal{U}}_m U_m + h_m \bar{\mathcal{D}}_m D_m + h.c.) \tag{2.5.4}$$

This equation can be written more simply using the Dirac spinors e_m, d_m and u_m defined as:

$$\begin{aligned} e_m &\equiv \mathcal{E}_m + E_m \\ d_m &\equiv \mathcal{D}_m + D_m \\ u_m &\equiv \mathcal{U}_m + U_m \end{aligned} \tag{2.5.5}$$

The final form of the mass terms is:

$$\mathcal{L} = -\frac{\upsilon}{\sqrt{2}}(f_m \bar{e}_m e_m + g_m \bar{u}_m u_m + h_m \bar{d}_m d_m + h.c.) \tag{2.5.6}$$

which compared to the standard form of mass terms $-m\bar{\psi}\psi$, gives the fermion masses:

$$m_n^e = \frac{\upsilon}{\sqrt{2}} f_n \upsilon, \; m_n^u = \frac{\upsilon}{\sqrt{2}} g_n \upsilon, \; m_n^d = \frac{\upsilon}{\sqrt{2}} h_n \upsilon \tag{2.5.7}$$

It is worth noticing that there is one independent Yukawa coupling parameter, f_n, for every mass, m_n. From the equation 2.3.12 and the discussion in this section, the interaction terms of the fermions with the Higgs boson take the form:

$$\mathcal{L} = -\frac{H}{\sqrt{2}}(f_m \bar{e}_m e_m + g_m \bar{u}_m u_m + h_m \bar{d}_m d_m + h.c.) \tag{2.5.8}$$

The conclusion is that the heavier a particle is, the stronger it couples to the Higgs boson. Therefore the Higgs decays more often into more massive particles provided that such a decay is kinetically allowed.

2.6 Theoretical and experimental constraints on Higgs

In the SM, the Higgs boson mass is given by

$$m_{\mathrm{H}} = \sqrt{\frac{\lambda}{2}}\upsilon, \tag{2.6.1}$$

where λ is the Higgs self-coupling parameter and υ is the vacuum expectation value of the Higgs field. The Fermi coupling $G_F = \frac{\sqrt{2}}{2\upsilon^2}$ is determined with precision of 0.6 ppm from muon decay measurements and fixes the value of υ =246 GeV. Since λ is presently unknown, the value of the SM Higgs boson mass m_{H} cannot be predicted.

The first theoretical constraint to the Higgs boson mass comes from the requirements of partial-wave unitarity of the longitudinal gauge boson scattering at tree-level [12]. A simple way to see this is to consider the $\mathrm{W}_L^+ W_L^- \to W_L^+ W_L^-$ case. The s-partial wave of the scattering amplitude in this case can be written like this:

$$\alpha_0(W_L^+ W_L^- \to W_L^+ W_L^-) = \frac{-G_F m_{\mathrm{H}}^2}{8\pi\sqrt{2}}\left[2 + \frac{m_{\mathrm{H}}^2}{s - m_{\mathrm{H}}^2} - \frac{m_{\mathrm{H}}^2}{s}\ln\left(1 + \frac{s}{m_{\mathrm{H}}^2})\right)\right] \tag{2.6.2}$$

where $\sqrt{s}$ is the centre of mass energy. The unitary condition for the reaction $W_L^+W_L^- \rightarrow W_L^+W_L^-$ reads:

$$| \alpha_0(W_L^+W_L^- \rightarrow W_L^+W_L^-) | \leq 1 \tag{2.6.3}$$

At the high energy limit where $s \gg m_\mathrm{H}^2$ the α_0 amplitude approaches the constant:

$$\alpha_0(W_L^+W_L^- \rightarrow W_L^+W_L^-) \longrightarrow -\frac{G_F m_\mathrm{H}^2}{4\pi\sqrt{2}} \tag{2.6.4}$$

Consequently, in order for the tree approximation to respect the unitarity bound at high energies the Higgs boson mass must satisfy:

$$m_\mathrm{H}^2 \leq \frac{4\pi\sqrt{2}}{G_F} \tag{2.6.5}$$

If we consider the requirements of partial wave unitarity on the system of four scattering channels $\mathrm{W}_L^+\mathrm{W}_L^-$, $\mathrm{Z}_L\mathrm{Z}_L$, HH and HZ_L, then a 4×4 matrix t_0 is formed:

$$t_0 \longrightarrow -\frac{G_F m_\mathrm{H}^2}{4\pi\sqrt{2}} \begin{bmatrix} 1 & \frac{1}{\sqrt{8}} & \frac{1}{\sqrt{8}} & 0 \\ \frac{1}{\sqrt{8}} & \frac{3}{4} & \frac{1}{4} & 0 \\ \frac{1}{\sqrt{8}} & \frac{1}{4} & \frac{3}{4} & 0 \\ 0 & 0 & 0 & \frac{1}{2} \end{bmatrix} \tag{2.6.6}$$

The most stringent unitary bound is derived from the requirement that the magnitude of the largest eigenvalue has to be less than one. The Higgs mass in this case has too satisfy:

$$m_\mathrm{H}^2 \leq \frac{8\pi\sqrt{2}}{3G_F} \simeq (1\,\mathrm{TeV}/c^2)^2 \tag{2.6.7}$$

Besides the upper bound on the Higgs boson mass from unitarity constraints , additional theoretical arguments place approximate upper and lower bounds on m_H [13, 14]. There is an upper bound based on the perturbativity of the theory up to the scale Λ at which the SM breaks down, and a lower bound derived from the stability of the Higgs potential.

The masses of all fermions are a consequence of EWSB, since the SM Higgs doublet is postulated to couple to the fermions through Yukawa interactions. However, the validity of the SM as an effective theory describing physics up to the Planck scale is questionable, because of the following “naturalness” argument. All fermion masses and dimensionless couplings are logarithmically sensitive to the scale Λ at which new physics becomes relevant. On the other hand scalar squared masses are quadratically sensitive to Λ. The observable SM Higgs mass has the following form:

$$m_\mathrm{H}^2 = m_{\mathrm{H}_0}^2 + \frac{kg^2\Lambda^2}{16\pi^2} \tag{2.6.8}$$

where m_{H_0} is a fundamental parameter of the theory. The second term is a one-loop correction in which g is an electroweak coupling and k is a constant, that is calculable within the low-energy effective theory. The two contributions arise from independent sources and one would not expect the observable Higgs boson mass to be significantly smaller than either of the two terms. Hence, if the scale of new physics Λ is much larger than the electroweak scale, unnatural cancellations must occur to remove the quadratic dependence of the Higgs boson mass on this large energy scale. If the Higgs boson mass m_H is below 180 GeV, all fields remain weakly interacting up to the Planck scale.

In addition, if m_H is too large, then according to the equation 2.6.1 the Higgs selfcoupling, λ, diverges at some scale Λ below the Planck scale. A Higgs boson mass of order of the electroweak scale is required from unitarity constraints and preferred by precision measurements of electroweak observables.

On the other hand, if m_{H} is too small, then the Higgs potential develops a second (global) minimum at a large value of the magnitude of the scalar field of order Λ. New physics must enter at a scale Λ or below, so that the global minimum of the theory corresponds to the observed $SU(2)_L \times U(1)_Y$ broken vacuum with $v = 246$ GeV.

Given a value of Λ, one can compute the minimum and maximum allowed Higgs boson masses. Conversely, the value of m_{H} itself can provide an important constraint on the scale up to which the SM remains successful as an effective theory. In particular, a Higgs boson with mass in the range 130 GeV $\lesssim m_{\mathrm{H}} \lesssim$ 180 GeV would be consistent with an effective SM description that survives all the way to the Planck scale. For smaller Higgs mass values, the stability of our universe prefers new physics at a lower scale. The lower bound on m_{H} can be reduced to about 115 GeV if one allows for the electroweak vacuum to be metastable [15], with a lifetime greater than the age of the universe. The main uncertainties in the stability and perturbativity bounds come from the uncertainties in the value of α_s and the top quark mass. Taking these uncertainties into account, a Higgs boson mass of about 125 GeV is close to the boundary of a SM that is consistent up to the Planck scale, and a SM that is unstable with a slow tunnelling rate.

Indirect experimental bounds for the SM Higgs boson mass are obtained from fits to precision measurements of electroweak observables. The Higgs boson contributes to the W and Z vacuum polarisation through loop effects, leading to a logarithmic sensitivity of the ratio of the W and Z gauge boson masses on the Higgs boson mass. A global fit to the precision electroweak data accumulated in the last two decades at LEP, SLC, the Tevatron, and elsewhere, gives at 95% C.L. $m_{\mathrm{H}} = 94^{+29}_{-24}$ GeV, or $m_{\mathrm{H}} < 152$ GeV. The top quark contributes to the $\mathrm{W}^{\pm}$ boson vacuum polarisation through loop effects that depend quadratically on the top mass, which plays an important role in the global fit. A top quark mass of 173.2 ± 0.9 GeV and a W boson mass of 80.385±0.015 GeV were used.

Thus, the SM is expected to be embedded in a more fundamental theory which will stabilise the hierarchy between the electroweak scale and the Planck scale in a natural way. A theory of that type would usually predict the onset of new physics at scales of the order of, or just above, the electroweak scale. Theorists strive to construct models of new physics that keep the successful features of the SM while curing its shortcomings, such as the absence of a dark matter candidate or a detailed explanation of the observed baryon asymmetry of the universe. In the weakly-coupled approach to electroweak symmetry breaking, supersymmetric (SUSY) extensions of the SM provide a possible explanation for the stability of the electroweak energy scale in the presence of quantum corrections.

2.7 Supersymmetry

Supersymmetry (SUSY) [16–18] refers to a symmetry relating fermions and bosons. Supergauge transformations transform scalar fields into spinors and boson fields into fermion fields. In a supersymmetric extension of the SM each of the known fundamental particles must have a superpartner with spin differing by $\frac{1}{2}$ unit.

SUSY can provide a solution to the “hierarchy” problem and explain the smallness of the breaking scale compared with the Planck scale. Within supersymmetric extensions of the SM, the supersymmetry-breaking effects, whose origins may lie at energy scales much larger than 1 TeV, can induce a radiative breaking of the electroweak symmetry due to the effects of the large Higgs-top quark Yukawa coupling. In this way, the electroweak symmetry breaking scale is intimately tied to the scale of supersymmetry breaking masses. Moreover, low-energy supersymmetry with a supersymmetry breaking scale in the order of 1 TeV allows the grand unification of the electromagnetic, weak and strong gauge interactions in a consistent way, strongly supported by the prediction of the electroweak mixing angle at low energy scales, with an accuracy at the percent level. Supersymmetry provides an explanation for the stability of the hierarchy of scales, provided that the supersymmetry-breaking masses, in particular those related to the stop sector, are at most in the TeV range.

A fundamental theory of supersymmetry breaking is unknown at this time. Nevertheless, one can parameterise the low-energy theory in terms of the most general set of soft supersymmetry-breaking normalisable operators. The Minimal Supersymmetric extension of the Standard Model (MSSM) [17] associates a supersymmetric partner to each gauge boson and chiral fermion of the SM, and provides a realistic model of physics at the weak scale. The particles of the MSSM are summarised in figure 2.3. This minimal model employs the minimal particle spectrum and soft-supersymmetry-breaking terms in order to parameterise the unknown fundamental mechanism of supersymmetry breaking. However more than 100 new parameters are introduced. Fortunately, only a subset of these parameters impact the Higgs phenomenology through tree-level and quantum effects.

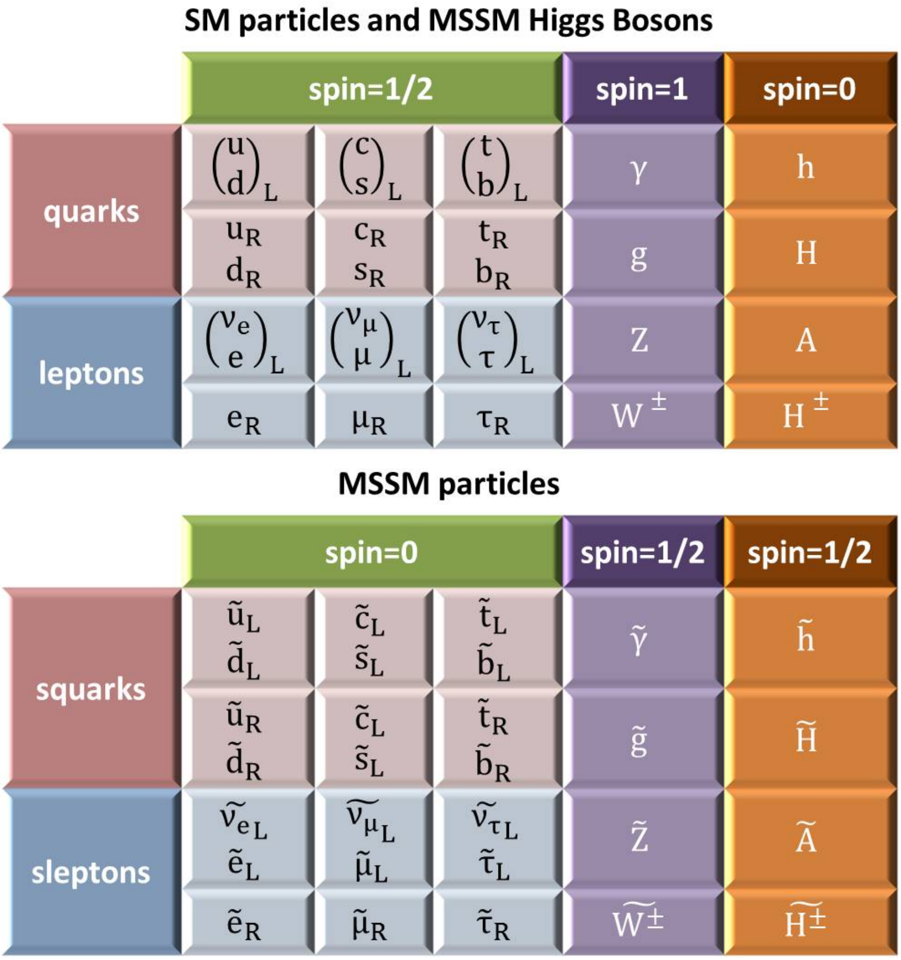

SM particles and MSSM Higgs Bosons

	spin=1/2			spin=1	spin=0
quarks	$\binom{u}{d}_L$	$\binom{c}{s}_L$	$\binom{t}{b}_L$	γ	h
	u_R d_R	c_R s_R	t_R b_R	g	H
leptons	$\binom{\nu_e}{e}_L$	$\binom{\nu_\mu}{\mu}_L$	$\binom{\nu_\tau}{\tau}_L$	Z	A
	e_R	μ_R	τ_R	$W^\pm$	$H^\pm$

MSSM particles

	spin=0			spin=1/2	spin=1/2
squarks	$\tilde{u}_L$ $\tilde{d}_L$	$\tilde{c}_L$ $\tilde{s}_L$	$\tilde{t}_L$ $\tilde{b}_L$	$\tilde{\gamma}$	$\tilde{h}$
	$\tilde{u}_R$ $\tilde{d}_R$	$\tilde{c}_L$ $\tilde{s}_L$	$\tilde{t}_R$ $\tilde{b}_R$	$\tilde{g}$	$\tilde{H}$
sleptons	$\tilde{\nu}_{eL}$ $\tilde{e}_L$	$\widetilde{\nu_\mu}_L$ $\tilde{\mu}_L$	$\tilde{\nu}_{\tau L}$ $\tilde{\tau}_L$	$\tilde{Z}$	$\tilde{A}$
	$\tilde{e}_R$	$\tilde{\mu}_R$	$\tilde{\tau}_R$	$\widetilde{W^\pm}$	$\widetilde{H^\pm}$

Figure 2.3: The particles of the Minimal Supersymmetric Standard Model

In constructing the MSSM, both hypercharge Y=-1 and Y=+1 complex Higgs doublets are required in order to obtain a supersymmetric extension of the Standard Model free of anomalies. Thus, the MSSM contains the particle spectrum of an extension of the Standard Model with two Higgs doublets and the corresponding supersymmetric partners. The two-doublet Higgs sector contains eight scalar degrees of freedom: one complex Y=-1 doublet, $\phi_d = (\phi_d^0, \phi_d^-)$ and one complex Y = +1 doublet, $\phi_u = (\phi_u, \phi_u^0)$. The notation reflects the way the MSSM Higgs sector couples to fermions. ϕ_d^0 couples exclusively to down-type fermion pairs while ϕ_u^0 to up-type.

When the Higgs potential is minimised, the neutral Higgs fields acquire vacuum expectation values:

$$\phi_d = \frac{1}{\sqrt{2}} \begin{pmatrix} \upsilon_d \\ 0 \end{pmatrix}, \; \phi_u = \frac{1}{\sqrt{2}} \begin{pmatrix} 0 \\ \upsilon_u \end{pmatrix} \tag{2.7.1}$$

where $\tan\beta \equiv \frac{\upsilon_u}{\upsilon_d}$ and the normalisation has been chosen such that $\upsilon^2 \equiv \upsilon_d^2 + \upsilon_u^2 = (246\,\mathrm{GeV})^2$. Spontaneous electroweak symmetry breaking results in three Goldstone bosons, which are absorbed and become the longitudinal components of the $\mathrm{W}^{\pm}$ and Z. The remaining five physical Higgs particles consist of a charged Higgs pair, $\mathrm{H}^{\pm}$, one CP-odd scalar, A and two CP-even scalars h and H. The CP even Higgs squared mass matrix is the following:

$$\mathcal{M}^2_{\mathrm{H,h}} = \begin{pmatrix} m_{\mathrm{A}}^2 \sin^2\beta + m_{\mathrm{Z}}^2 \cos^2\beta & -(m_{\mathrm{A}}^2 + m_{\mathrm{Z}}^2)\sin\beta\cos\beta \\ -(m_{\mathrm{A}}^2 + m_{\mathrm{Z}}^2)\sin\beta\cos\beta & m_{\mathrm{A}}^2 \sin^2\beta + m_{\mathrm{Z}}^2 \cos^2\beta \end{pmatrix} \tag{2.7.2}$$

The masses at tree level are:

$$m^2_{\mathrm{H,h}} = \frac{1}{2}\left(m_{\mathrm{A}}^2 + m_{\mathrm{Z}}^2 \mp \sqrt{(m_{\mathrm{A}}^2 + m_{\mathrm{Z}}^2)^2 - 4 m_{\mathrm{Z}}^2 m_{\mathrm{A}}^2 \cos^2 2\beta} \right) \tag{2.7.3}$$

The angle α arises when the matrix $\mathcal{M}^2_{\mathrm{H,h}}$ is diagonalised to obtain the physical CP-even Higgs states. From the above results one obtains:

$$\cos^2(\beta - \alpha) = \frac{m_{\mathrm{h}}^2 (m_z^2 - m_{\mathrm{h}}^2)}{m_{\mathrm{A}}^2 (m_{\mathrm{H}}^2 - m_{\mathrm{h}}^2)} 0 \leq \beta \leq \pi\ 2,\ -\pi\ 2 \leq \alpha \leq 0 \tag{2.7.4}$$

The two Higgs fields can be written as expansions in mass eigenstates:

$$\begin{aligned} \phi_u = & \frac{1}{\sqrt{2}} \begin{pmatrix} \sqrt{2}(H^- \sin\beta - G^- \cos\beta) \\ \upsilon_u + (H\cos\alpha - h\sin\alpha) + i(A\sin\beta + G\cos\beta) \end{pmatrix} \\ \phi_d = & \frac{1}{\sqrt{2}} \begin{pmatrix} \upsilon_d + (H\sin\alpha + h\cos\alpha) + i(A\cos\beta - G\sin\beta) \\ \sqrt{2}(H^+ \cos\beta + G^+ \sin\beta) \end{pmatrix} \end{aligned} \tag{2.7.5}$$

The supersymmetric structure of the theory imposes constraints on the Higgs sector. The Higgs self-interactions are not independent parameters but they can be expressed in terms of the electroweak gauge coupling constants. As a result, all Higgs sector parameters at tree-level are determined by two free parameters, which may be taken to be $\tan\beta$ and m_{A}. One significant consequence of these results is that there is a tree-level upper bound to the mass of the light CP-even Higgs boson, h. From the equation 2.7.3 we can derive:

$$m_{\mathrm{h}} \leq m_{\mathrm{Z}}^2 \cos^2 2\beta \tag{2.7.6}$$

This is an important difference between the MSSM and the SM, in which the value of the Higgs mass at tree-level is not constrained. In the Standard Model, $m^2_{HSM} = \frac{1}{2}\lambda\upsilon^2$ is proportional to the Higgs self-coupling λ, which is a free parameter. On the other hand, all Higgs self-coupling parameters of the MSSM are related to the squares of the electroweak gauge couplings.

The phenomenology of the Higgs sector depends in detail on the various couplings of the Higgs bosons to gauge bosons, Higgs bosons and fermions. The couplings of the Higgs bosons to W and Z pairs typically are either proportional to $\cos(\beta - \alpha)$ or $\sin(\beta - \alpha)$ or independent of the angles. All the vertices that contain at least one vector boson and exactly one non-minimal Higgs boson state $(\mathrm{H}, \mathrm{A}$ or $\mathrm{H}^{\pm})$ are proportional to $\cos(\beta - \alpha)$. The couplings are summarised in table 2.1. Note that there are no tree level couplings of A, $\mathrm{H}^{\pm}$ to the vector bosons W and Z.

$\cos(\beta-\alpha)$	$\sin(\beta-\alpha)$
HW^+W^-	HW^+W^-
HZZ	HZZ
ZAH	ZAH
$W^\pm H^\mp H$	$W^\pm H^\mp H$
$ZW^\pm H^\mp H$	$ZW^\pm H^\mp H$
$\gamma W^\pm H^\mp H$	$\gamma W^\pm H^\mp H$

Table 2.1: Summary of the Higgs coupling to Gauge boson in the MSSM.

2.8 Production and decays of the Higgs at the LHC

At the LHC, the main production processes are in order of importance: gluon fusion ($gg \to$ H), vector boson fusion (qqH or $q\bar{q}$H) and Higgs boson production in association with a vector boson ($W^\pm$H or ZH) or with a top-quark pair ($t\bar{t}$H). The Feynmann diagrams for these processes are shown in figure 2.4. The high center-of-mass energy of 7 TeV and 8 TeV in 2010-2011 and 2012 respectively, and the fact that both beams consist of protons has a strong impact on the parton luminosities. The LHC experiments are sensitive to Higgs bosons with much higher masses than in previous experiments. The gg luminosity is also enhanced at the LHC by the beam energy due to the large gluon PDF at lower parton momentum fraction x compared to that at higher x.

A variety of search channels are pursued by the LHC collaborations, ATLAS and CMS. A light Higgs (mass < 150 GeV/c^2) can be searched in the $\gamma\gamma$, $\tau\tau$, $b\bar{b}$ and two vector bosons WW* or ZZ* decay channels. The corresponding branching fractions are show in figure 2.6. The Higgs decays into two photons are rare, the branching fraction is quite small, however they have a very clean signature in the hadronic environment of the LHC. The channel $H \to ZZ \to 4l$ has also a distinct signature and very high mass resolution in the leptonic final state. The higgs decay to τ leptons has a high branching faction and can be accessible by all production mechanisms. The $H \to b\bar{b}$ despite having the highest branching fraction suffers from large multi-jet background and the rather low mass resolution of the b-quark system. In the case of a heavier Higgs, the WW^*/WW and ZZ^*/ZZ final states are the most sensitive. A light Higgs boson, as favoured by theoretical constraints and electroweak measurements, has a relatively large branching ratio into τ leptons, making the $H \to \tau\tau$ decay mode channel very promising. In addition the measurement of the $H \to \tau\tau$ decay rate provides a test of the SM prediction for the top Yukawa coupling.

When searching for neutral MSSM Higgs bosons the productions mechanisms under study are gluon fusion $gg \to \phi$ (ϕ = h,H,A) and associated production with a $b\bar{b}$ pair ($b\bar{b}\,\mathrm{h,H,A}$) (figure 2.7). The production of neutral MSSM Higgs bosons is dominated by the gluon fusion, however, for large values of $\tan\beta$ the Higgs associated production with a pair of $b\bar{b}$ becomes also significant. Over a wide range of m_{A}, neutral Higgs Bosons decay into a pair of τ leptons with a branching fraction about 10%. This is one of the reasons the $\tau\tau$ final state is worth exploring.

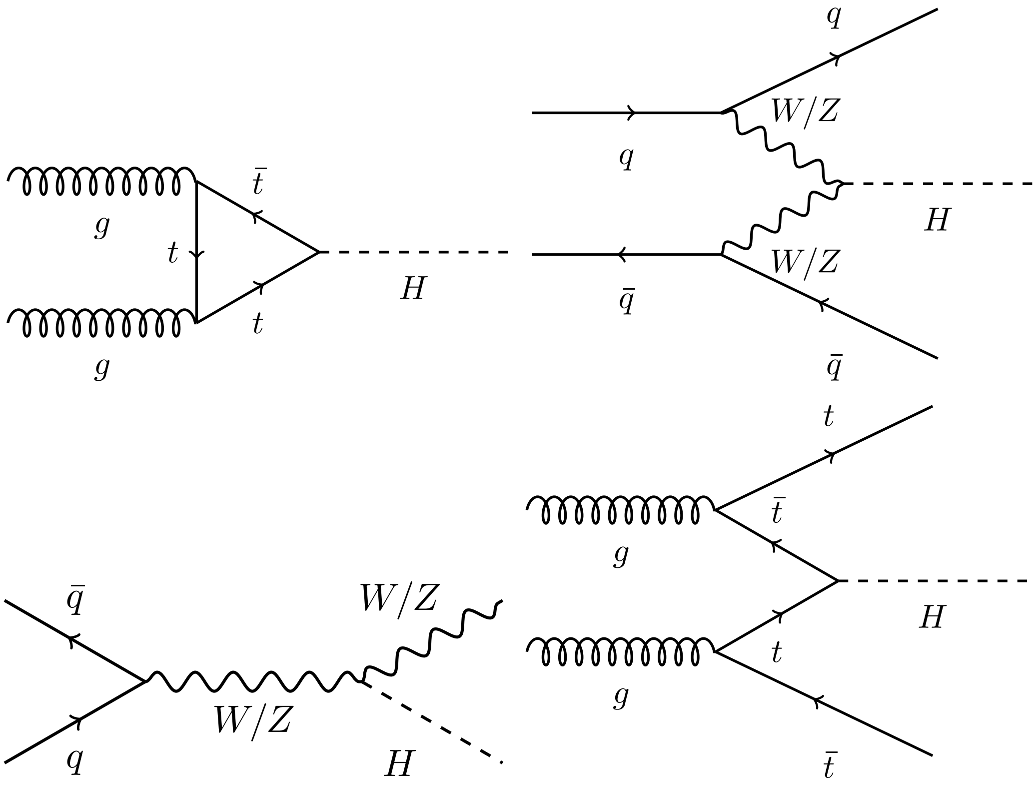

Figure 2.4: The main production processes are in order of importance: gluon fusion ($gg \to$ H), vector boson fusion (qqH or $q\bar{q}$H), Higgs boson production in association with a vector boson (W$^{\pm}$H or ZH) and last production in association with top-quark pair (t$\bar{\text{t}}$H).

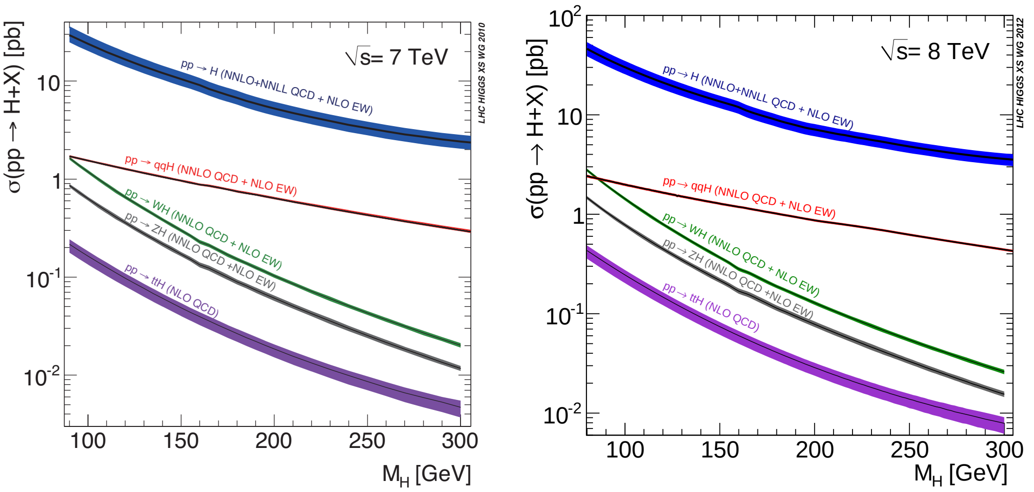

Figure 2.5: Standard Model Higgs boson production cross sections at centre of mass energy 7 TeV and 8 TeV. Source: [19]

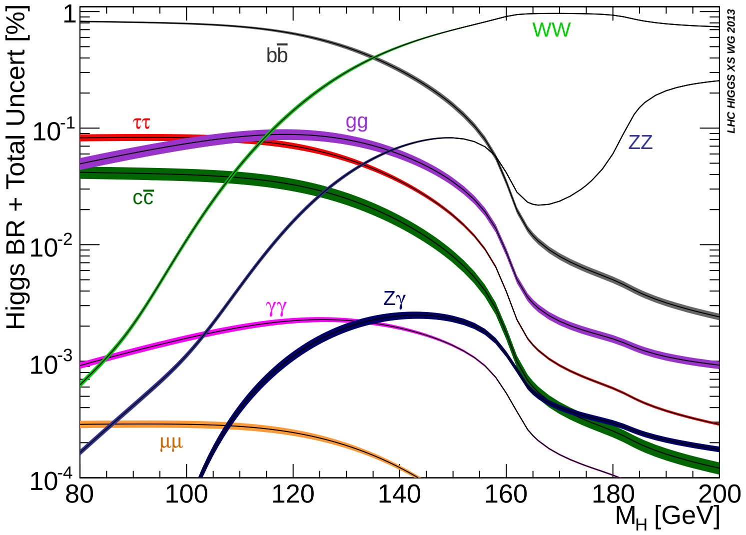

Figure 2.6: Standard Model Higgs boson decay branching ratios and total width. Source: [19]

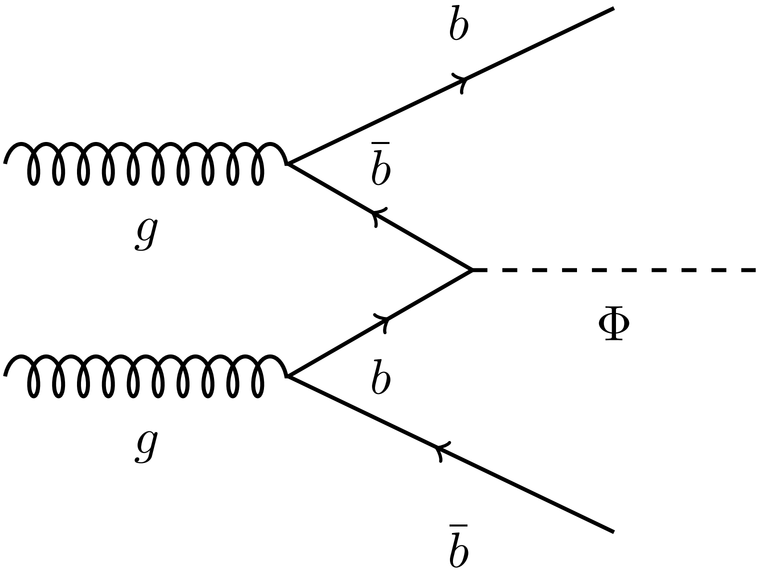

Figure 2.7: Higgs production in association with a b$\bar{\text{b}}$ pair. This process might be enhanced in SUSY models.

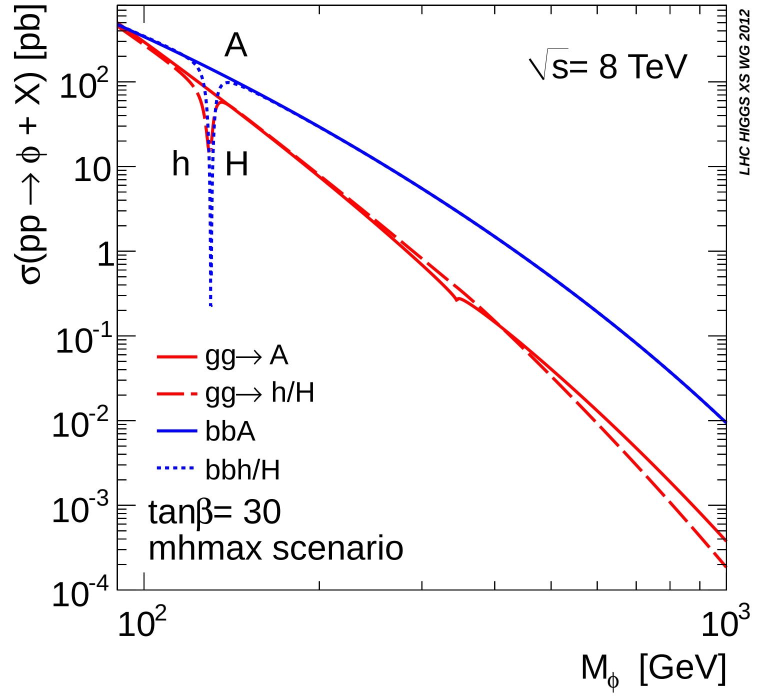

Figure 2.8: MSSM Cross Section summary for the mhmax scenario for $\tan\beta = 30$. Source: [19]

Chapter 3

The CMS detector

3.1 The Large Hadron Collider

The Large Hadron Collider (LHC) [20] is a superconducting hadron accelerator and collider installed in the 26.7 km tunnel that previously hosted the LEP machine. It is located at CERN, on the boarder between France and Switzerland, close to Geneva and about 100 m underground. There are two transfer tunnels each approximately 2.5 km in length, linking the LHC to the CERN accelerator complex which acts as beam injector. The LHC is designed to collide two counter rotating beams of protons or heavy ions. Since collisions occur between particles of the same charge, two separate acceleration cavities with two different magnetic field configurations are required. The LHC is not a perfect circle. It consists of eight 2.45 km long arcs, and eight 545 m long straight sections, the so called insertions. The arcs contain the “bending” superconducting dipole magnets, with 154 in each arc, 1232 in total. The exact layout of the straight section depends on the specific use of the insertion (experiment, injection, beam dumping e.t.c). The 1232 dipole magnets, whose design field reaches 8.33 T, are maintained at a fixed temperature via superfluid Helium at 1.9 K.

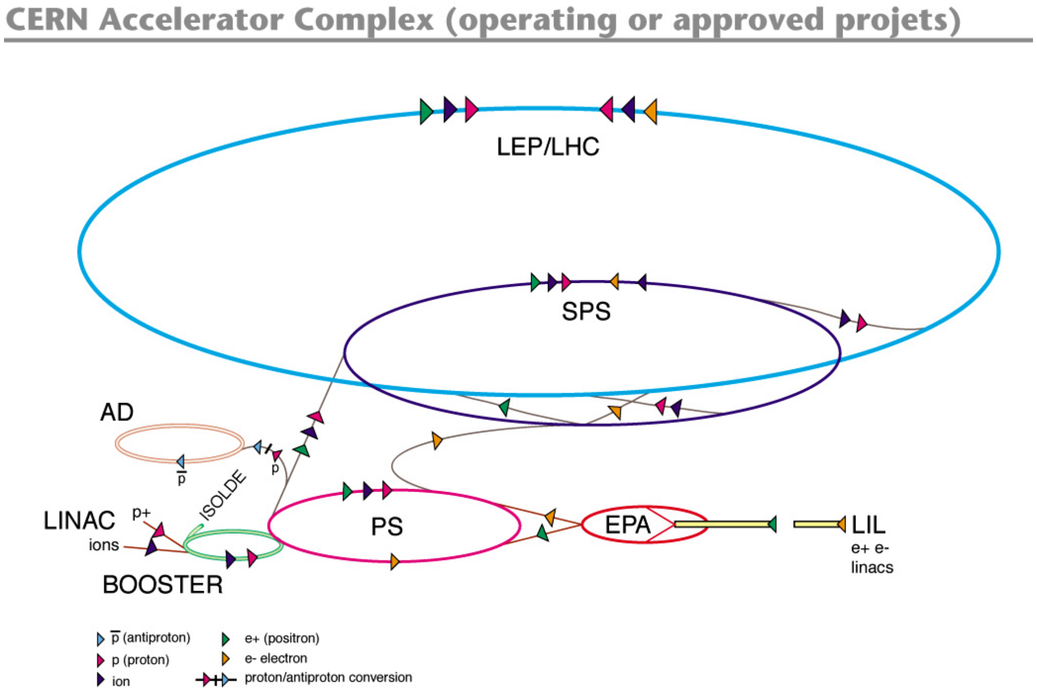

CENR AC _HF205_ V2/2/1998

Figure 3.1: CERN accelerator complex [21]

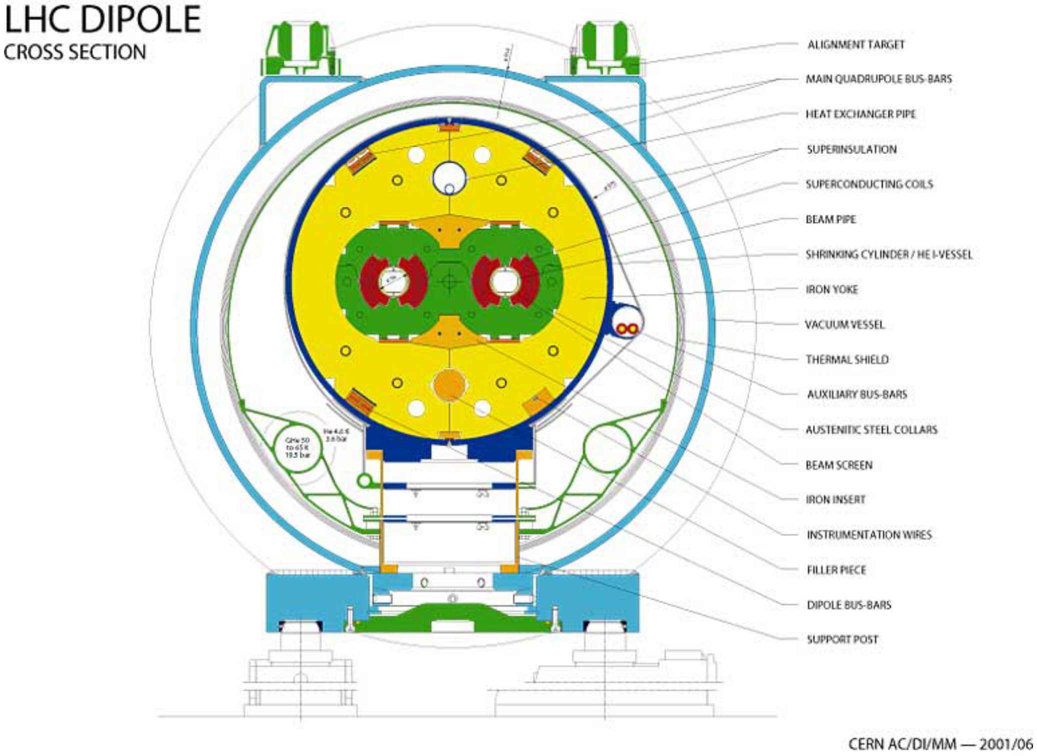

Figure 3.2: Cross section of the superconducting dipole magnet, one of the most important components of the LHC [22].

The protons or ions are first injected to Linac2, a linear accelerator and then transfered to the Proton Synchrotron Booster at an energy of 50 MeV. Here they are accelerated to 1.4 GeV/c. They are then transfered to the Proton Synchrotron (PS) ring where they are arranged into bunches with the correct time spacing and accelerated to 25 GeV/c. The proton (ion) beams are then passed on to the Super Proton Synchrotron (SPS), where they are accelerated to 450 GeV/c and finally injected to the LHC. Eight radio frequency (RF) resonating cavities are responsible for accelerating the proton beams to their final energy by 16 MeV per turn.

Six experiments are installed in the LHC: two large and multipurpose experiments, ATLAS (A Toroidal LHC ApparatuS) and CMS (Compact Muon Solenoid); two smaller and dedicated experiments, LHCb for b-physics and the study of the CP violation and ALICE (A Large Ion Collider Experiment) for heavy ion physics and the study of the quark gluon plasma; two more experiments designed to study collisions where the protons experience only very small deflections, LHCf (Large Hadron Collider forward) installed in the ATLAS forward region and TOTEM (TOTal Elastic and diffractive cross section Measurement) located in the forward region of CMS.

The aim of the LHC is to discover physics beyond the Standard Model with high centre of mass energy collisions. The rate of events generated in the LHC collisions is given by

$$N_{\text{event}} = L\sigma_{\text{event}} \tag{3.1.1}$$

where σ_{event} is the cross section of the processes under study and L the machine instantaneous luminosity. The machine luminosity depends only on the beam parameters and is given by

$$L = \frac{N_p^2 n_b f_{\text{rev}} \gamma_r}{4\pi\epsilon_n\beta^*} F \tag{3.1.2}$$

where N_p is the number of protons per bunch, n_b is the number of bunches per beam, f_{rev} is the revolution frequency, γ_r is the relativistic gamma factor, ϵ_n is the normalised transverse

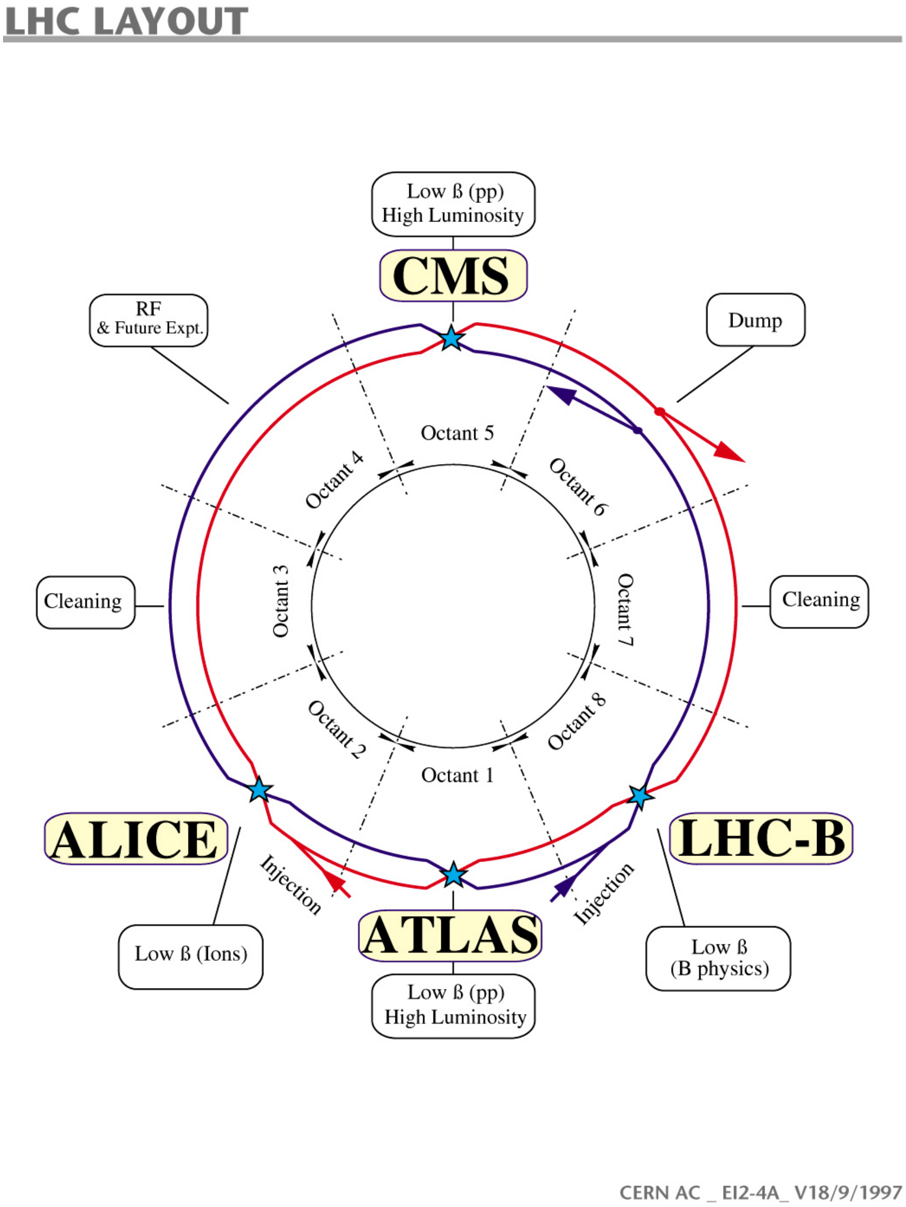

Figure 3.3: LHC layout [23].

beam emittance, β^* is the value of the beta function at the collision point which relates to the transverse size of the beams at the interaction point and F is the geometric factor due to the crossing angle of the two beams. The beams are approximately Gaussian in profile with a nominal width of about 16 μm and are made to collide where the four main experiments are located. Nominal instantaneous luminosity of $10^{34}\text{cm}^{-2}\text{s}^{-1}$ was expected, in CMS and ATLAS, to be reached with beams consisting of 2808 bunches with 1.15×10^{11} protons per bunch. In 2012 there were 1368 bunches per beam and the intensity was 1.6 to 1.7×10^{11} protons per bunch, which is 150% on the nominal value. During the first three years of running the LHC the bunch spacing was reduced gradually from 150 ns in 2010 to 50 ns in 2012. In the last week of proton-proton collisions a few physics runs took place with the nominal bunch spacing of 25 ns. As a result the LHC luminosity for the year 2012 reached a maximum of $7.73 \times 10^{33}\text{cm}^{-2}\text{s}^{-1}$, which is 77% of the nominal luminosity. During the first two years of operation. 2010 and 2011, the centre of mass energy was 7 TeV and was increased to 8 TeV in 2012. The nominal centre of mass energy of 14 TeV is going to be achieved after the Long Shutdown 1 (LS1).

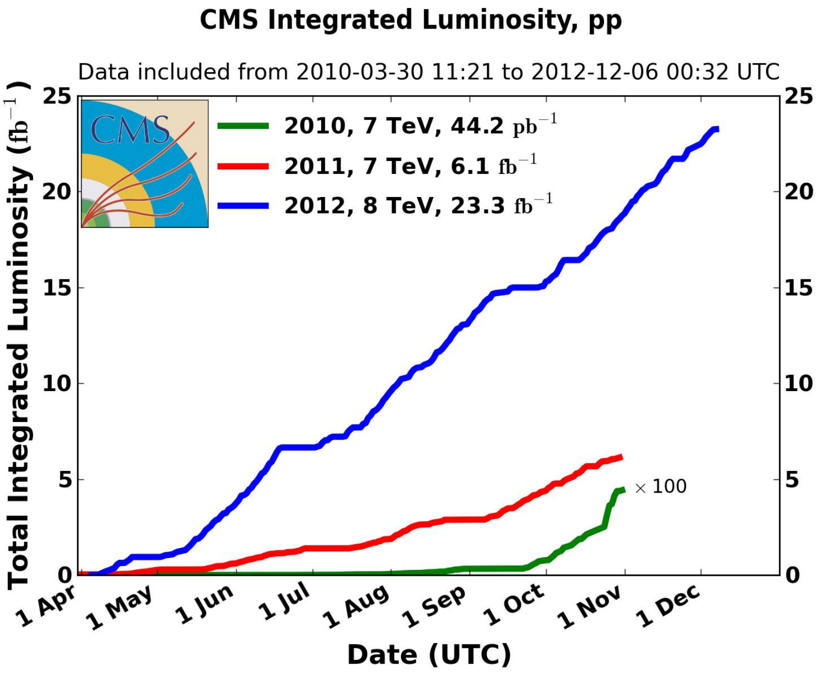

Figure 3.4: The integrated luminosity measured in CMS in 2012,2011 an 2010, as presented in the CMS week in December 2012, the last before LS1 from January 2013 until 2015. Source: [24]

3.2 The Compact Muon Solenoid

The Compact Muon Solenoid [25–27] is one of two general-purpose LHC experiments, ATLAS is the other. The CMS design, as the name itself gives away, is based on the idea of having the strongest magnet possible. A stronger magnetic field bends paths of charged particles more and when combined with high-precision position measurements in the tracker and muon detectors it allows precise momentum measurement, even for particles with very high energy.

3.2.1 The detector and the magnet

The main volume of the CMS detector is a multi-layered cylinder, 21 m long and 16 m in diameter, weighing more than 13000 tons. The innermost layer is a silicon-based particle tracker, surrounded by a scintillating crystal electromagnetic calorimeter which is itself surrounded with a sampling calorimeter for hadrons measuring particle energies. They fit inside a central superconducting solenoid magnet [28] 13 m long and 6 m in diameter. Outside the magnet are the large muon detectors, which are inside the return yoke of the magnet. The solenoid produces an axial field 3.8 T, while the yoke, a 12 sided iron structure, contains and guides the field. It also serves as a filter preventing all particles, apart from muons and neutrinos, from reaching the muon detectors. In addition it provides most of the detectors structural support.

3.2.2 The system of coordinates

The geometric position at which the main interaction point is expected to occur is designated as the origin of the CMS coordinate system. The x coordinate axis is defined along the LHC radius with direction towards the centre of the ring. The y coordinate axis is perpendicular to the x axis and points upwards. The z coordinate axis is tangential to the beam, and the direction is the one consistent with a right handed coordinate system. This Cartesian coordinate system is transformed into a cylindrical coordinate system defined by the radial distance r, the azimuthal angle ϕ, and the z coordinate, or a spherical coordinate system defined by the radial distance ρ, an azimuthal angle ϕ and a polar angle θ which begins in the positive direction of the z axis and proceeds counterclockwise. The plane transverse to the beam line is also referred to as the $r - \phi$ plane. We define the pseudorapidity η as an alternative to the polar angle by:

$$\eta = -\log\left(\tan\left(\frac{\theta}{2}\right)\right) \tag{3.2.1}$$

which is the massless limit of the rapidity y_r of a particle, defined by:

$$y_r = \log\left(\tan\left(\frac{E + p_z}{E - p_z}\right)\right) \tag{3.2.2}$$

where E and p_z are the energy and z component of the momentum of the particle. The pseudorapidity is preferred over the polar angle as the rate of particle production at hadron colliders is approximately constant as a function of η due to the Lorentz invariance of rapidity differences.

3.3 The CMS tracking system

The tracker [25, 29] is the innermost CMS subsystem. It is specifically designed to provide precise and efficient measurement of the tracks of charged particles as well as acurate reconstruction of secondary vertices. The tracking information is also used for triggering. The demand for high granularity and fast response result in an increase to the on detector electronics and hence to the cooling system required. Because of the intense particle flux and the radiation damage this causes, the required lifetime of approximately ten years is a challenge. In order to meet all the above requirements, the CMS tracking system is entirely based on silicon detector technology. CMS is the first experiment to use silicon detectors in the outer tracker region. With 200 m^2 of active silicon area is the largest silicon tracker ever built.

The silicon tracker is built according to an occupancy driven design. As particle flux increases towards the interaction point, so does the required detector granularity. The CMS silicon tracker consists of two main parts. The pixel tracker and the silicon strip tracker.

3.3.1 The pixel tracker

The pixel system is the part of the tracking system that is closest to the interaction region. Three cylindrical layers, 53 cm long with radius 4.4, 7.3 and 10.2 cm, of hybrid pixel detector modules (BPix) surround the interaction point. They are complemented by two disks of pixel modules (FPix) on each side at $|z| = 34.5$ and $|z| = 46.5$ cm with radius 6 and 15 cm. The overall pseudorapidity coverage is $|\eta| < 2.5$. The BPix contain 48 million pixels covering a total area of 0.78 m^2, while the FPix contain 18 million pixels summing up to 0.28 m^2. The pixel detector delivers three high precision space points on each charged particle trajectory. With a pixel size 100×150 µm^2, a spacial resolution of about 10 µm in the $r - \phi$ plane and 15 µm along the z axis can be achieved in the barrel and about 15 µm and 20 µm respectively in the endcaps.

3.3.2 The silicon strip tracker

The radial region between 20 cm and 116 cm is occupied by the silicon strip tracker. It is composed of three different subsystems. The Tracker Inner Barrel and Disks (TIB/TID) extend 55 cm in radius and are composed of 4 barrel layers, supplemented by 3 disks at each end. The

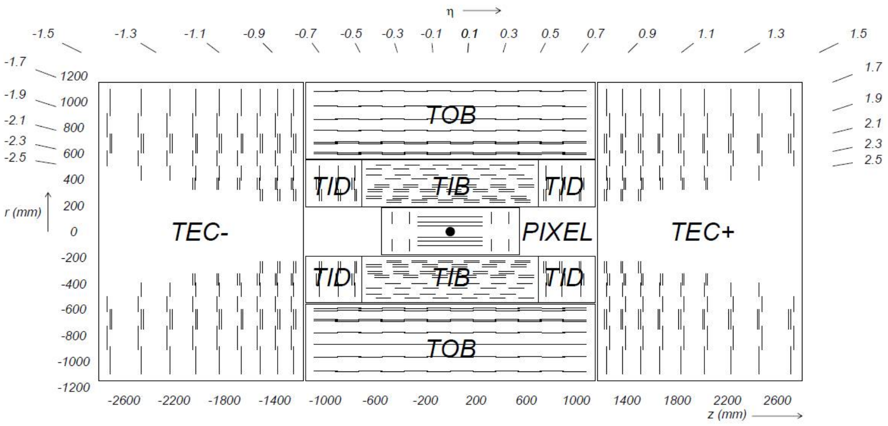

Figure 3.5: Schematic longitudinal view of the CMS tracking system. Source: [25].

TIB/TID use 320 µm thick silicon micro-strip sensors, with strips parallel to the beam axis in the barrel and radial on the disks. The strip pitch is 80 mm to 120 mm in the TIB, leading to a single point resolution of 23 µm to 35 µm. In the TID the mean pitch varies between 100 µm and 141 mm. The TIB/TID is surrounded by the Tracker Outer Barrel (TOB). It has an outer radius of 116 cm and consists of 6 barrel layers of 500 µm thick micro-strip sensors with strip pitches of 183 µm to 122 µm leading to single point resolution of 53 µm to 35 µm. The TOB extends in z between ±118 cm. Beyond this z range the Tracker EndCaps (TEC+ and TEC-, where the sign indicates the location along the z axis) cover the region $124\,\mathrm{cm} < |z| < 282\,\mathrm{cm}$ and $22.5\,\mathrm{cm} < |r| < 113.5\,\mathrm{cm}$. Each TEC is composed of 9 disks, carrying up to 7 rings of silicon micro-strip detectors, 320 µm thick on the inner 4 ringsand 500 µm thick on rings 5 to 7, with radial strips of 97 µm to 184 µm average pitch. The first two layers in both the TIB, TOB, TID and rings 1,2 and 5 of the TEC are realised with stereo modules, tilted one from the other by about 100 mrad, thus allowing for a more precise measurement of the z coordinate. The strip tracker is designed to provide a spacial resolution of about 40 to 60 µm in the $r - \phi$ plane and 500 µm along z. The momentum resolution for a 10 GeV charged particle track is 0.5%.

3.4 The Electromagnetic calorimeter

The electromagnetic calorimeter (ECAL) [25, 30] is a hermetic homogeneous calorimeter made of 61200 lead tungstate (PbWO^4) crystals mounted in the central barrel part, closed by 7324 crystals in each of the two endcaps. A preshower detector is placed in front of the endcap crystals. The use of high density crystals has allowed the design of a calorimeter which is fast, has fine granularity and is radiation resistant, all important characteristics in the LHC environment.

3.4.1 PbWO^4 crystals

The characteristics of the PbWO^4 crystals make them an appropriate choice for operation at LHC. The high density (8.28 g/cm^3), short radiation length (X$_0$=0.89 cm) and small Molière radius (2.2 cm) result in a compact calorimeter with fine granularity. The PbWO^4 produces scintillation light in fast, small, well-defined photon showers. The scintillation decay time of these crystals is of the same order of magnitude as the LHC bunch crossing time. About 80% of the light is emitted in 25 ns. The light output varies with temperature therefore, in order to maintain the energy resolution, a cooling system is installed to keep the crystal temperature stable at 18 ± 0.05 $°C$. Ionising radiation forms colour centres due to oxygen vacancies and impurities in the lattice. As a consequence there is loss of light transmission depended on the wavelength without changes to the scintillation mechanism. This kind of damage can be tracked and corrected for by monitoring the optical transparency with injected laser light. The emitted blue-green scintillation light, $\lambda = 420 - 430$ mm, is captured by photodetectors, that need to be radiation hard and operate within a strong magnetic field. The photodetectors chosen were avalanche photodiodes (APDs) for the barrel and vacuum phototriodes (VPTs) for the endcaps.

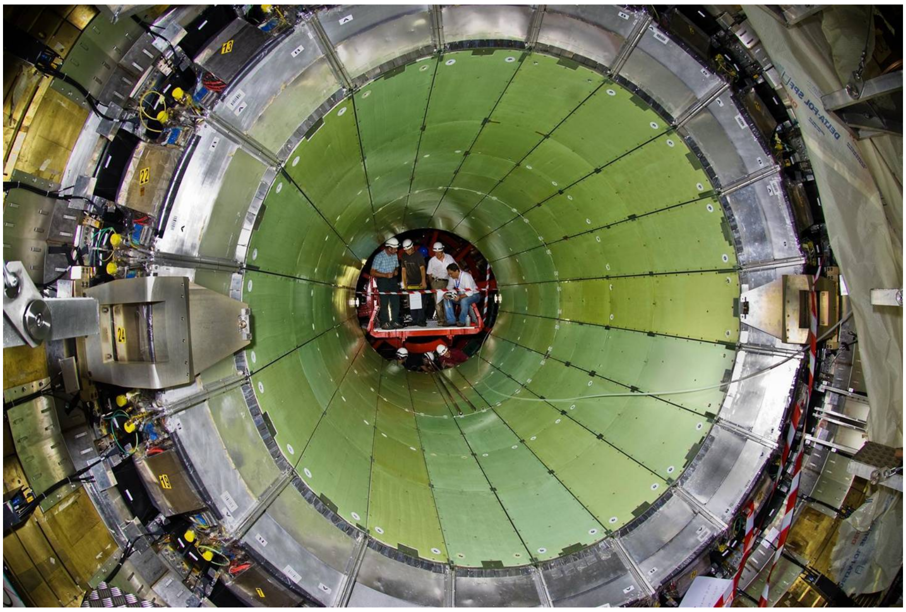

Figure 3.6: The ECAL barrel inside the hadronic calorimeter. Source: [25]

3.4.2 ECAL Barrel

The barrel part of the ECAL (EB) covers the pseudorapidity range $|\eta| < 1.479$. The barrel consists of 360 sections in ϕ and 2×85 in η, resulting in a total of 61200 crystals. The crystals have a tapered shape, slightly varying with position in η. In order to avoid cracks aligned with particle trajectories, they are mounted so that their axes form a small angle of 3° with respect to the vector from the nominal interaction vertex, in both the ϕ and η projections. The crystal cross section corresponds to approximately 0.0174×0.0174 in (η, ϕ) or 22×22 mm^2 at the front face of crystal, and 26×26 mm^2 at the rear face. The crystal length is 230 mm and corresponds to 25.8 X_0. The barrel crystal volume is 8.14 m^3 and weights 67.4 tons.

3.4.3 ECAL Endcaps

The endcaps (EE) cover the rapidity range $1.479 < |\eta| < 3.0$. The longitudinal distance between the interaction point and the endcap envelope is 315.4 cm, taking account the estimated shift toward the interaction point by 1.6 cm when the 3.8 T magnetic field is switched on. The endcaps are divided into two halves, “Dees”, each holding 3662 crystals. The crystals are arranged in a rectangular $x - y$ grid, with the crystals pointing at a focus 1300 mm beyond the interaction point, giving off-pointing angles ranging from 2 to 8 degrees. The crystal cross section is 30×30 mm^2 on the rear side, 28.62×28.62 mm^2 on the front side and their lenght is 220 mm, which corresponds to 24.7 X_0. The crystal volume at the endcaps is 2.90 m^3 and weights 24.0 tons.

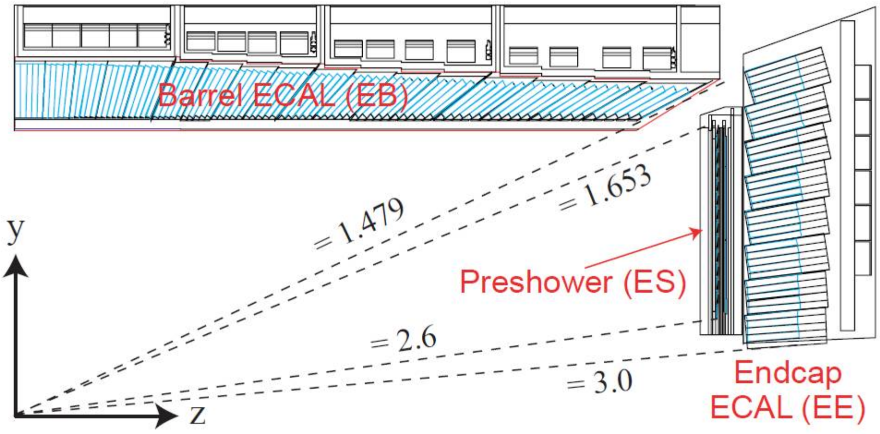

Figure 3.7: Transverse section of the ECAL, showing the configuration in rapidity. Source: [26]

3.4.4 Preshower

The principal aim of the CMS Preshower detector is to identify neutral pions in the endcaps within a fiducial region $1.653 < |\eta| < 2.6$. It also helps the identification of electrons against minimum ionising particles and improves the position determination of electrons and photons with high granularity. The Preshower is a sampling calorimeter with two types of layers, lead radiators and silicon strip sensors. The lead radiators initiate electromagnetic showers from incoming photons or electrons whilst silicon strip sensors, placed after each radiator, measure the deposited energy and the transverse shower profiles. The total thickness of the Preshower is 20 cm. The material thickness of the Preshower before reaching the first sensor plane is 2 X_0, followed by a further 1 X_0 before reaching the second plane. Thus about 95% of single incident photons start showering before the second sensor plane. The orientation of the strips in the two planes is orthogonal. The design is such that all lead is covered by silicon sensors, to account for effects such as shower spread and primary vertex spread. The lead planes are arranged in two Dees, one on each side of the beam pipe, with the same orientation as the crystal Dees.

The energy resolution of the ECAL is 1% for an electron or photon with energy 30 GeV.

3.5 The Hadronic calorimeter

The hadron calorimeters (HCAL) [25, 31] together with the ECAL subdetectors form a complete calorimetry system for the measurement of jets and missing transverse energy. The central barrel and endcap HCAL subdetectors completely surround the ECAL and are located inside the solenoid. The barrel (HB) and endcap (HE) are joined hermetically and partly overlapping they cover the rapidity range up to $|\eta| = 3.0$. The central shower containment in the region $|\eta| < 1.26$ is improved with an array of scintillators located outside the magnet in the outer barrel hadronic calorimeter (HO). Located at a distance of 11.2 m from the interaction point are the forward calorimeters (HF) and extend the pseudorapidity coverage down to $|\eta| = 5$.

3.5.1 Barrel and endcaps

The HB and HE are sampling calorimeters. The active region consists of plastic scintillator tiles, interlayed with 5cm thick copper absorber plates, parallel to the beam axis. The innermost and outermost plates are 7 cm thick and are made of stainless steel for structural strength. Since the HB and HE are immersed in the 3.8 T magnetic field of the solenoid, the materials are

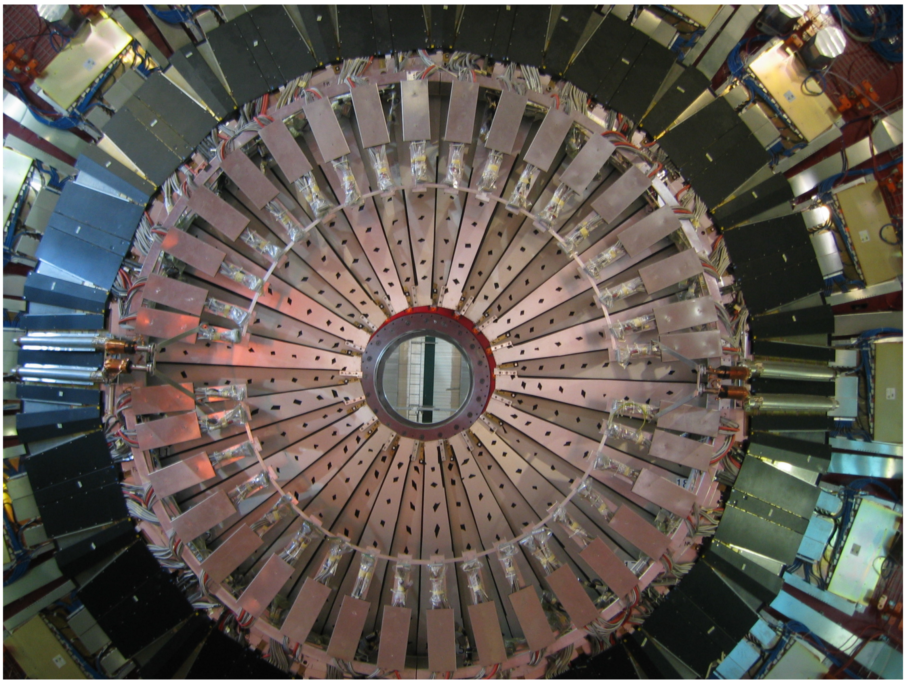

Figure 3.8: Hcal endcap [32].

chosen to be non-magnetic, copper alloy and stainless steel. The exact proportion of active material and absorber for each layer is:

- (Layer 0) 9 mm Scintillator/61 mm Stainless Steel
- (Layers 1-8) 3.7 mm Scintillator/50.5 mm Brass
- (Layers 9-14) 3.7 mm Scintillator/56.5 mm Brass
- (Layers 15+16) 3.7 mm Scintillator/75 mm Stainless Steel/9 mm Scintillator

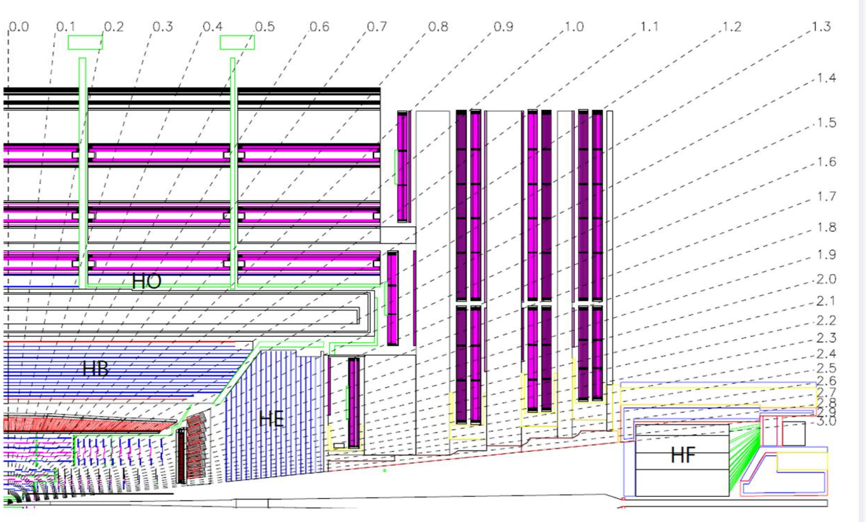

Figure 3.9: Longitudinal view of the CMS detector showing the locations of the hadron barrel (HB), endcap (HE), outer (HO) and forward (HF) calorimeters. Source: [25].

The first active layer is situated directly behind the ECAL. In the r, ϕ plane the barrel stretches from an inner radius of 1.77 m to an outer radius of 2.87 m. The rapidity range covered by the

HB is $|\eta| \leq 1.4$. The design of the absorber for the HE is driven by the need to minimise the cracks between HB and HE. Only brass absorber plates are used in the HE. The thickness of the brass plates is 78 mm while the scintillator thickness is 3.7 mm. There are 19 active plastic scintillator layers. The rapidity range of the HE is $1.3 < |\eta| < 3.0$. The individual tiles of scintillator in the HCAL are grouped into towers with a segmentation of $\eta \times \phi = 0.087 \times 0.087$ at central rapidity $|\eta| < 1.74$ and 0.09×0.174 to 0.5×0.174 at forward rapidity $1.74 < |\eta| < 3.0$. The light from individual Scintillator tiles is collected by wavelength-shifting fibres and then added optically for every tower to be finally read out with hybrid photodiodes (HPDs) mounted at the ends of the barrel mechanical structure.

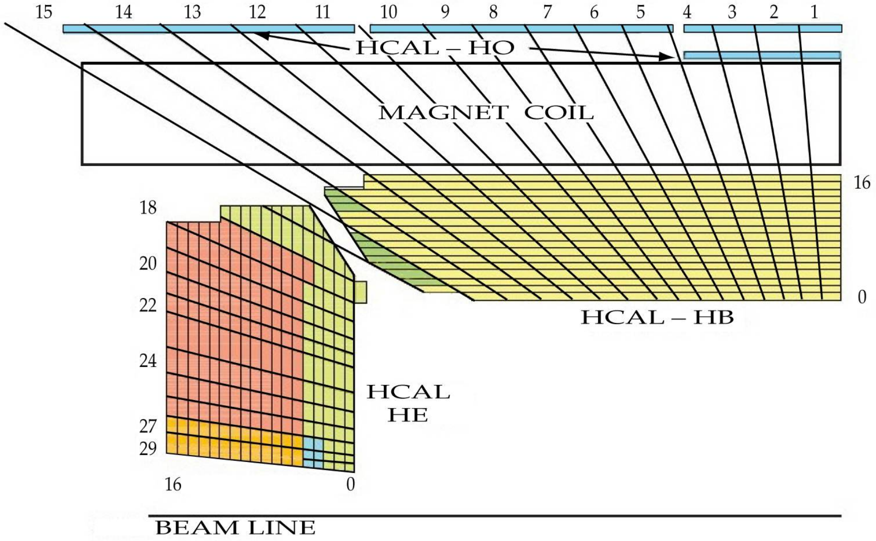

Figure 3.10: Longitudinal view of the CMS detector showing the locations of the hadron barrel (HB), endcap (HE) and outer (HO) calorimeters. The conventional numbering of the read out towers is indicated. Source: [25].

3.5.2 Outer hadron calorimeter

An additional layer of scintillators, the outer hadron calorimeter (HO), is placed outside of the solenoid. Since these are located within the return yoke along with the barrel muon detector, the segmentation of these detectors closely follows that of the barrel muon system. The entire assembly consists of 5 rings, 2.54 m wide along the z axis, each divided in 12 sectors. The 12 sectors are separated by 75 mm thick stainless steel beams which hold successive layers of iron of the return yoke as well as the muon system. The central ring, ring 0, has two layers of 10 mm thick scintillators on either side of the "tail catcher" iron, 18 cm thick, at radial distances 3.850 m and 4.097 m, respectively. All other rings have a single layer at a radial distance of 4.097 m. The panels in the 12 sectors are identical except those in rings ±1, where a single row of scintillator tiles is removed. The HO covers $|\phi| < 1.26$, with the exception of the space between successive muon rings in the ϕ direction.

3.5.3 Forward hadron calorimeter

To extend the hermeticity of the central hadron calorimeter system to pseudorapidity $|\eta| < 5$, as required for a good missing transverse energy measurement, CMS employs a separate set of forward calorimeters (HF) located 11.2 m from the interaction point, along the z axis. The calorimeters consist of iron absorbers and embedded radiation-hard quartz fibres, providing a fast collection of Cherenkov light. The thickness of the absorber plates is 78 mm while the scintillator thickness is 3.7 mm. There are 19 active plastic scintillator layers. The collected scintillation light is detected using radiation-hard photomultiplier tubes (PMT). The HF calorimeters are segmented longitudinally by the use of long fibres, which run over the full depth of the absorber, 165 cm, and short fibres, which start at a depth of 22 cm from the front of the detector. Each set of fibres is read out separately. The different length of the fibres makes it possible to distinguish electromagnetic showers from hadronic ones. The HF tower segmentation in ϕ and in η is 0.175×0.175, except for $|\eta| > 4.7$ where the segmentation is 0.175×0.35.

The energy resolution of a single π with energy 100 GeV is 10%.

3.6 The muon system

The CMS muon system [25, 33] is designed to have the capability of reconstructing the momentum and charge of muons over the the entire kinematic range of the LHC. Three types of gaseous particle detectors for muon identification are used in CMS: Drift Tube chambers (DTs), Cathode Strip Chambers (CSCs) and Resistive Plate Chambers (RPCs). The muon system, hosted in the magnet return yokes of CMS, is divided into the barrel, $|\eta| < 1.2$, and the endcaps $|\eta| < 2.4$. The barrel is made of five rings, "wheels", placed one after the other along the z axis, while each endcap consists of four disks that close both ends of the barrel cylinder.

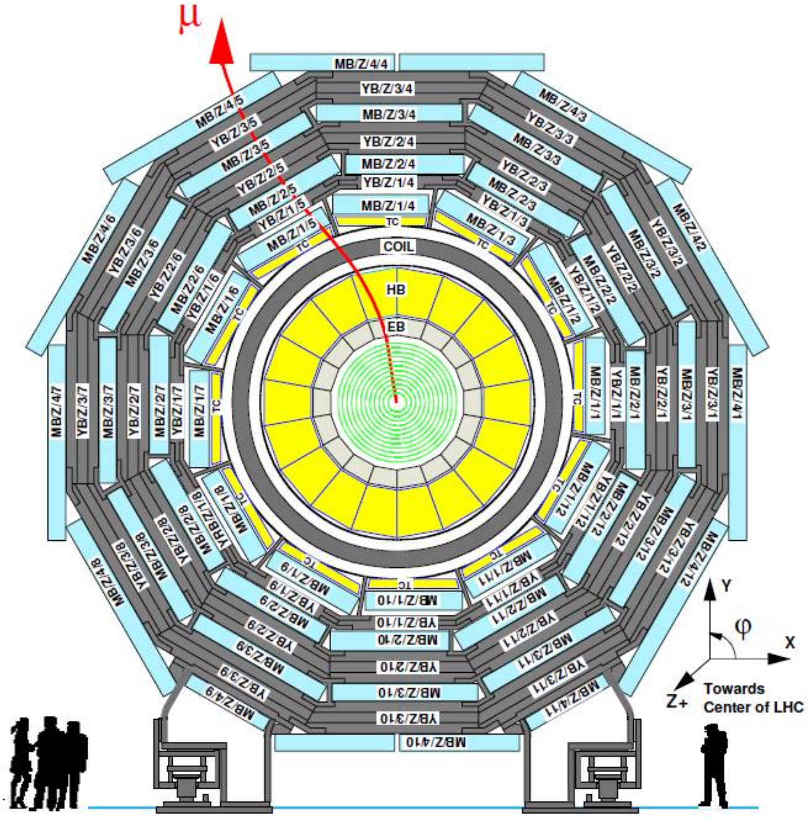

Figure 3.11: A schematic view of the CMS cross section. Details of the muon system are shown, as well as the track of a muon travelling through the detector. Source: [25].

In the barrel, where the muon rate is smaller and the magnetic field weaker and more uniform, Drift Tube chambers (DTs) are employed. They are distributed along the radius of the detector in four "stations" in between the iron yoke layers. The iron yoke contains most of

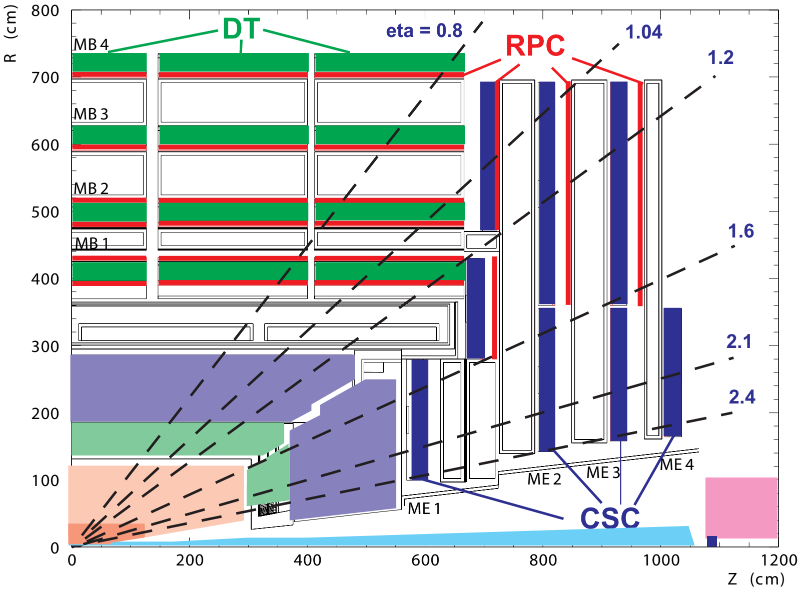

Figure 3.12: Layout of one quarter of the CMS muon system. Source: [26].

the magnetic field and also acts as absorber of particles to reduce the background. The first three innermost stations contain eight chambers each, in two groups of four, which measure the muon coordinate in the $r-\phi$ bending plane, and four chambers which provide a measurement in the z direction, along the beam line. The fourth station does not contain the z-measuring planes. The two sets of four chambers in each station are separated as much as possible to achieve the best angular resolution. The drift cells of each chamber are offset by a half-cell width with respect to their neighbour to eliminate dead spots in the efficiency. This arrangement also provides a convenient way to measure the muon time with excellent resolution, using simple meantimer circuits for efficient, standalone bunch crossing identification. The number of chambers in each station and their orientation were chosen to provide good efficiency for linking together muon hits from different stations into a single muon track and for rejecting background hits.

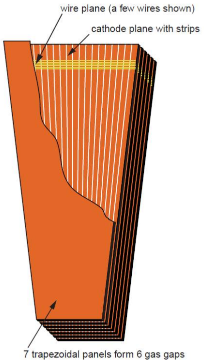

Figure 3.13: A schematic view of a CSC chamber. Source: [25].

In the forward region the magnetic field is strong and inhomogeneous and the muon rate and background levels higher than in the central detector region. Therefore Cathode Strip Chambers (CSCs) are chosen for the Endcaps, for their radiation hardness and fast response. There are four stations of CSCs in each endcap, with chambers positioned perpendicular to the beam line and interspersed between the flux return plates. All CSCs overlap in ϕ to avoid gaps in the muon acceptance. Each CSC is trapezoidal in shape and consists of six gas gaps, each gap having a plane of cathode strips and a plane of anode wires. The cathode strips of each chamber run radially outward and provide a precision measurement in the $r - \phi$ bending plane. The anode wires are running almost perpendicularly to the strips, in order to provide measurements of η and the beam-crossing time of a muon. The gas ionisation and subsequent electron avalanche caused by a charged particle traversing each plane of a chamber produces a charge on the anode wire and an image charge on a group of cathode strips. Thus, each CSC measures the space coordinates (r, ϕ, z) in each of the six layers. Each six-layer CSC provides robust pattern recognition for rejection of non-muon backgrounds and efficient matching of hits to those in other stations and to the CMS inner tracker.

A crucial characteristic of the DT and CSC subsystems is that they can each trigger on the p_{T} of muons with good efficiency and high background rejection, independent of the rest of the detector. Because of the uncertainty in the eventual background rates and in the ability of the muon system to measure the correct beam-crossing time when the LHC reaches full luminosity, a complementary, dedicated trigger system consisting of Resistive Plate Chambers (RPC) was added in both the barrel and endcap regions. The RPCs provide a fast, independent and highly-segmented trigger with a sharp p_{T} threshold over a large rapidity range. The RPCs are double-gap chambers, operated in avalanche mode to ensure good operation at high rates. They produce a fast response, with good time resolution but coarser position resolution than the DTs or CSCs. They also help to resolve ambiguities that occur when attempting to reconstruct tracks from multiple hits in a chamber. In the barrel in front of every DT station there is a layer of RPCs. The two innermost stations consist of "sandwiches" made of a DT chamber placed between two RPCs. The two outermost stations consist of packages of a DT chamber coupled to a layer made of one, two, or four RPCs, depending on the sector and station, placed on the innermost side of the station. At the endcaps there are layers of double-gap RPCs in the outer rings of each station.

The momentum resolution for a muon with energy 1 TeV is 10%.

3.7 Data Acquisition and Triggering

The LHC provides proton-proton and heavy ion collisions at high interaction rates. For protons the beam crossing interval for 2012 was 50 ns, corresponding to a crossing frequency of 20 MHz. Depending on the instantaneous luminosity, many collisions occur at each crossing of the proton bunches. Since it is impossible to store and process the large amount of data associated with the resulting high number of events, a drastic rate reduction in the order of 10^5 has to be achieved. This task is performed by the trigger system [25, 34, 35], which is the start of the physics event selection process. The required rejection is too large to be achieved in a single processing step, if a high efficiency is to be maintained for the physics processes that CMS plans to study. For this reason, the full selection task is split into two steps. The first step, the Level 1 Trigger (L1), is designed to reduce the rate of events accepted for further processing to less than 100 kHz. The second step, the High Level Trigger (HLT), is designed to reduce this maximum Level 1 Accept (L1A) rate of 100 kHz to a final output rate of approximately 100 Hz. The L1 consists of custom designed, largely programmable electronics, whereas the HLT is a software system implemented in a filter farm of about one thousand commercial processors.

The L1 trigger involves the calorimetry and muon systems as well as some correlation of information from these systems. The L1 decision is based on the presence of local objects such as photons, electrons, muons, and jets, using information from a given detector element of η-ϕ space. It also employs global sums of the transverse energy and missing transverse energy. Each of these items is tested against several p_T or E_T thresholds.

It is expected that initial filtering can reduce the event rate by at least one order of magnitude. The data fragments from the same L1 are then collected from the various read out buffers and assembled into a single event by the "event builder". The complete events, the format of which is very similar to the one used in the offline analysis, are sent to the filter farm where the HLT algorithms are executed. The HLT has access to all the information used in L1 since this is stored locally in the L1 trigger crates. Consequently, the HLT can make further combinations and other topological calculations on the digital list of objects transmitted from L1. Much information from detector readouts, such as information from all the calorimeter components and the tracker, is not available on the time scale of the L1 trigger decision but is used by the HLT. Eventually, the HLT uses the full event data for the decision to keep an event or not. The last stage of HLT processing does reconstruction and event filtering with the primary goal of making datasets of different physics signatures.

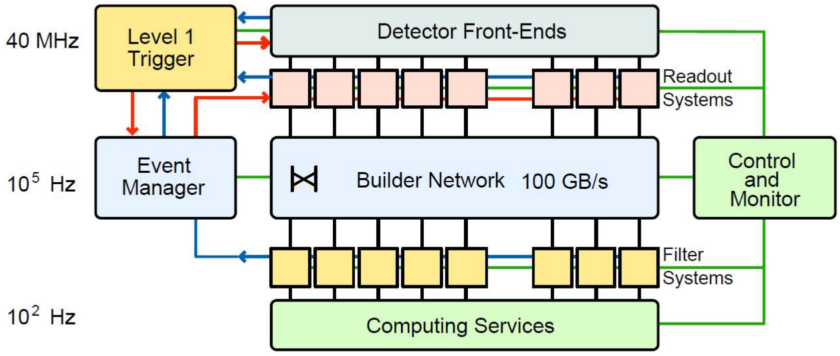

Figure 3.14: Architecture of the CMS Data Acquisition system. Source: [25].

Summarising the functions of the data acquisition system components, it all comes down to fours stages:

- a detector readout stage, which results in storing the event data in a collection of approximately 700 buffers
- an event building stage, in which all the data corresponding to a single event are collected from these buffers via the switch
- a selection stage, in which the event is processed by the HLT in the processor farm
- an analysis or storage stage, in which the events selected by the HLT are forwarded to the computing services for further processing either for storage or for further analysis.

Chapter 4

Trigger selection and datasets

Events are collected through a sophisticated triggering system, described in section 3.7, and are stored according to their particular properties into different datasets. The trigger is the start of the physics event selection process. A trigger path is defined by a sequence of requirements beginning from a seed Level 1 trigger and proceeding through the set of trigger filters imposing various requirements. A decision to retain an event for further consideration is based on the event's suitability for inclusion in one of the various data sets to be used for analysis. The datasets to be taken are determined by CMS physics priorities as a whole. These datasets include dilepton and multi-lepton datasets for top and higgs searches, lepton plus jet datasets for top physics, and inclusive electron datasets for calorimeter calibrations. Particular "primary datasets" are defined typically by the types of objects that are identified in the events. In this document, in both analyses described we are primarily interested in identifying muons. Muons are found by matching a track with consistent track segments reconstructed in the muon chambers outside the CMS magnet. The muon reconstruction is described in section 5.5.

4.1 Muon trigger system

The L1 muon trigger [34] of CMS uses all three kinds of muon detectors, Drift Tubes (DT), Cathode Strip Chambers (CSC) and Resistive Plate Chambers (RPC). Complementary features of muon chambers (DT/CSC) and dedicated trigger detectors (RPC) allows us to build two independent trigger subsystems. Each system reconstructs muon tracks that are then delivered to the "global muon" trigger for comparison. Additionally the global muon trigger checks for calorimetric isolation of the muon candidates and for confirmation of the candidates by checking the energy deposit in the calorimeter, quite bits. The global muon trigger sends the four best muon candidates to the "global" trigger.

The muon track reconstruction algorithm used by the HLT [35] is seeded by the muon candidates found by the L1 global muon trigger. The HLT adds silicon tracker hits to the muon trajectory and thus improving the muon momentum measurement. Isolation criteria can be applied to the muon candidates to provide additional rejection, using the calorimetric energy sum in a cone around the muon and the number of pixel tracks in a region around the projected muon trajectory.

4.2 High Level Triggers

In our analyses the events were selected using the unprescaled HLT muon trigger with the lowest p_{T} threshold. The trigger condition was subject to changes during the operation of the LHC from 2010 till the end of 2012. The data for the $\mathrm{Z} \to \tau\tau \to \mu\mu$ cross section measurement,

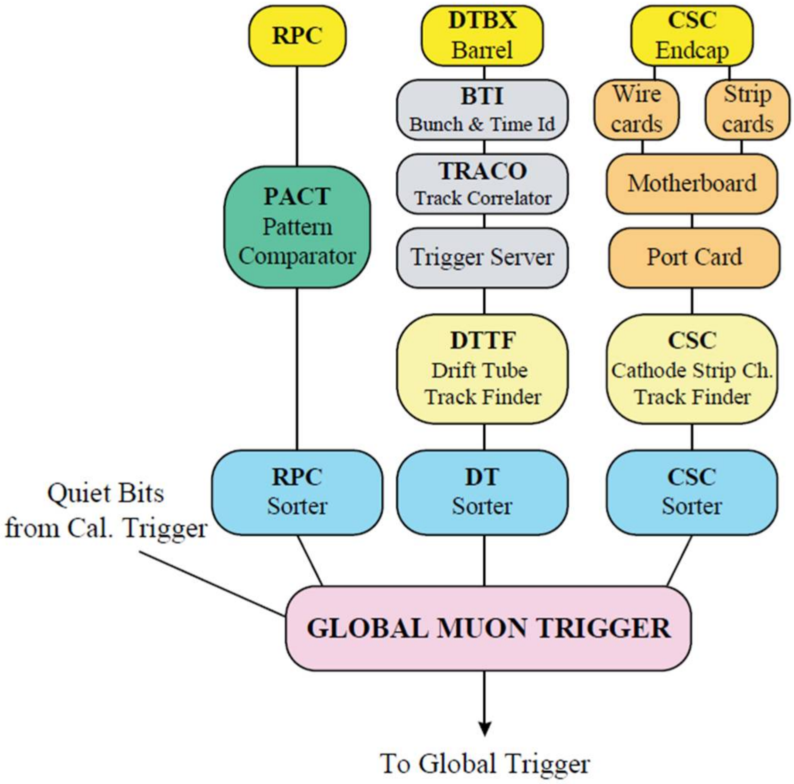

Figure 4.1: The logical structure of the Muon Trigger. Source: [34].

were collected during 2010. The changing running conditions yielded three different trigger periods, HLT with p_{T} threshold 9, 11 and 15 respectively. Only triggers with a p_{T} threshold on a single muon were used in 2010. The Higgs searches were performed with data collected in 2011 and 2012. In the first half of 2011 a single muon trigger with the additional requirement of isolation was used. Later that year, double muon triggers were introduced and were used until the end of 2012. The exact thresholds on p_{T} along with the corresponding run ranges and integrated luminosities are reported in table 4.1 and table 4.2. The luminosity calculation takes into account possible trigger prescales.

Trigger	Run range	Int. Luminosity pb^{-1}
HLT $p_{\mathrm{T}}^{\mu} > 9$	$\leq$147116	7.5
HLT $p_{\mathrm{T}}^{\mu} > 11$	147196-148068	9.5
HLT $p_{\mathrm{T}}^{\mu} > 15$	$\geq$148822	19.1

Table 4.1: Overview of the high level triggers used in the analysis of the 2011 and 2012 data. The second column presents the corresponding run periods and the third column the integrated luminosities.

4.3 Trigger efficiencies

The trigger selection efficiency is estimated using the so called “tag-and-probe” method. applied to muons coming from J/ψ and Z resonances. Using this technique it is possible

Trigger	Run range	Int. Luminosity fb^{-1}
HLT $p_\mathrm{T}^\mu > 17$ isolated	$\leq$170248	1.2
HLT $p_\mathrm{T}^\mu > 8$ and $p_\mathrm{T}^\mu > 13$	170249-190000	3.7
HLT $p_\mathrm{T}^\mu > 8$ and $p_\mathrm{T}^\mu > 17$	>190000	12.1

Table 4.2: Overview of the high level triggers used in the analysis of the 2011 and 2012 data. The runs above 190000 belong to the 2012 data taking period.

to obtain almost unbiased estimates of the efficiencies of the different stages of muon trigger. Events are selected with strict selection requirements on the tag muon, and with a more relaxed selection on the probe muon, such that the selection applied to the probe muon does not bias the efficiency. The fraction of probe muons which passes the selection under study gives an estimate of its efficiency.

The trigger efficiencies measured with the tag-and-probe method from the data are shown in figure 4.2 as a function of the muon transverse momentum. The results of the trigger efficiency measurements from the $\mathrm{Z}/\gamma^* \to \mu\mu$ and $\Upsilon(1S, 2S, 3S) \to \mu\mu$ samples are combined and presented in table 4.3.

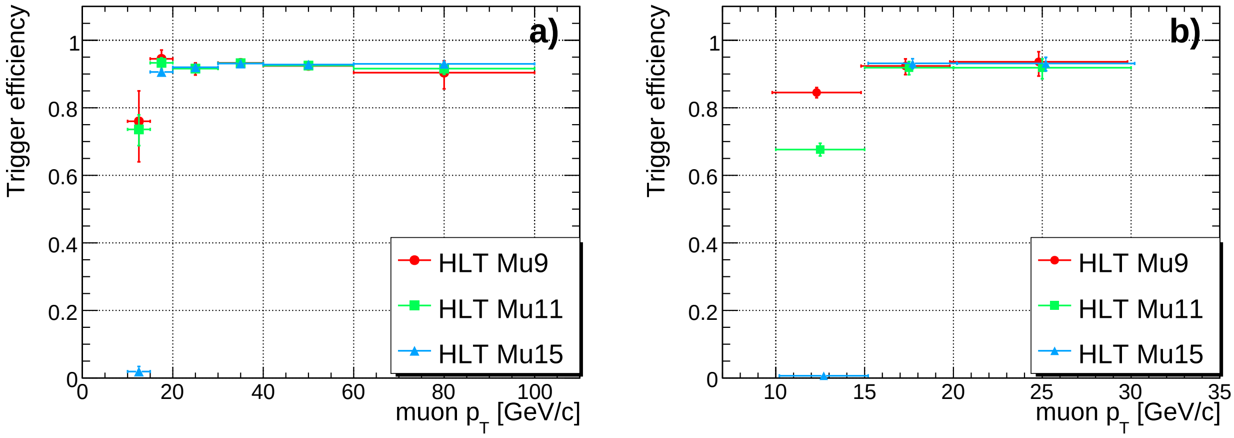

Figure 4.2: Trigger efficiencies measured with the tag-and-probe method in the $\mathrm{Z}/\gamma^* \to \mu\mu$ (left plot) and $\Upsilon(1S, 2S, 3S) \to \mu\mu$ (right plot) samples. The HLT_Mu9, HLT_Mu11 and HLT_Mu15 trigger efficiencies are shown as a function of the muon transverse momentum.

The figures 4.3, 4.4 and 4.5 illustrate the efficiencies of the HLT triggers used in 2011 and 2012 data, measured with the tag-and-probe method. The turn on curves for the HLT trigger with isolated muon $p_\mathrm{T}^\mu > 17\,\mathrm{GeV}$ (HLT_IsoMu17) and the two "legs" of the double muon trigger with $p_\mathrm{T}^\mu > 8\,\mathrm{GeV}$ and $p_\mathrm{T}^\mu > 13\,\mathrm{GeV}$ (HLT_Mu13_Mu8), are presented respectively. Table 4.4 shows the efficiencies of the double muon trigger with $p_\mathrm{T}^\mu > 8\,\mathrm{GeV}$ and $p_\mathrm{T}^\mu > 17\,\mathrm{GeV}$ (HLT_Mu17_Mu8) used in 2012 data.

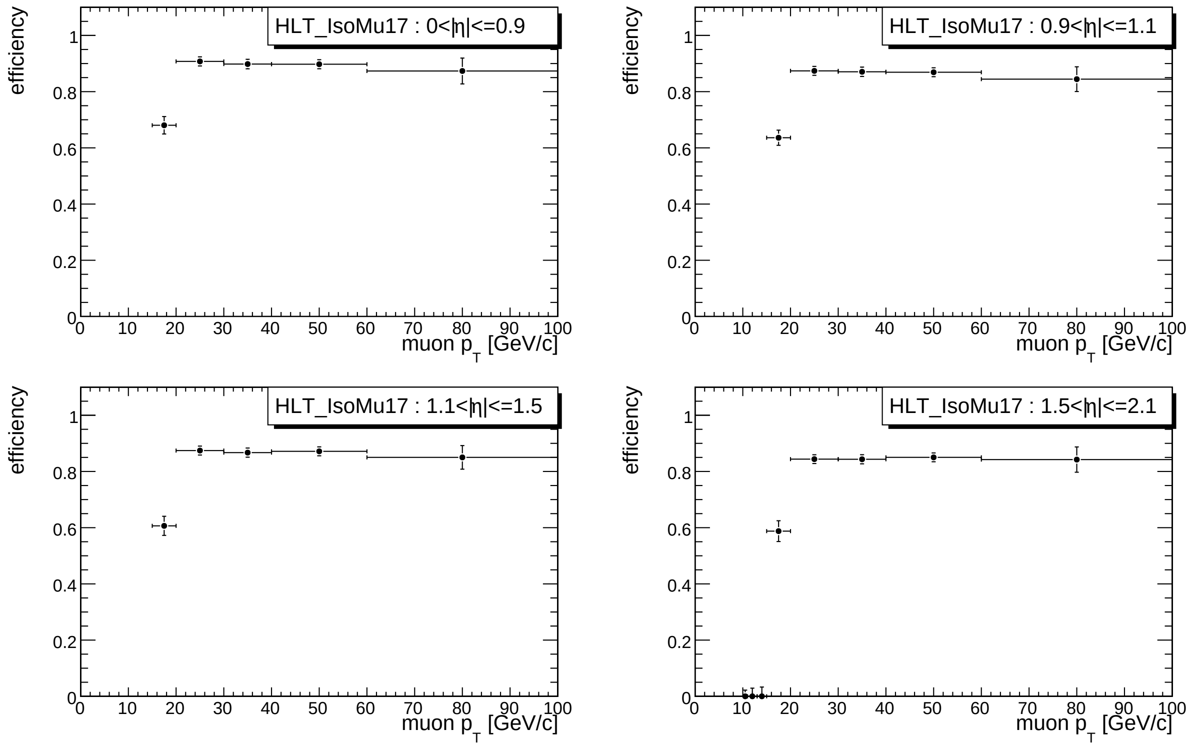

Figure 4.3: Turn-on curves for the HLT_IsoMu17 trigger, measured using the tag-and-probe method with $Z \to \mu\mu$ events.

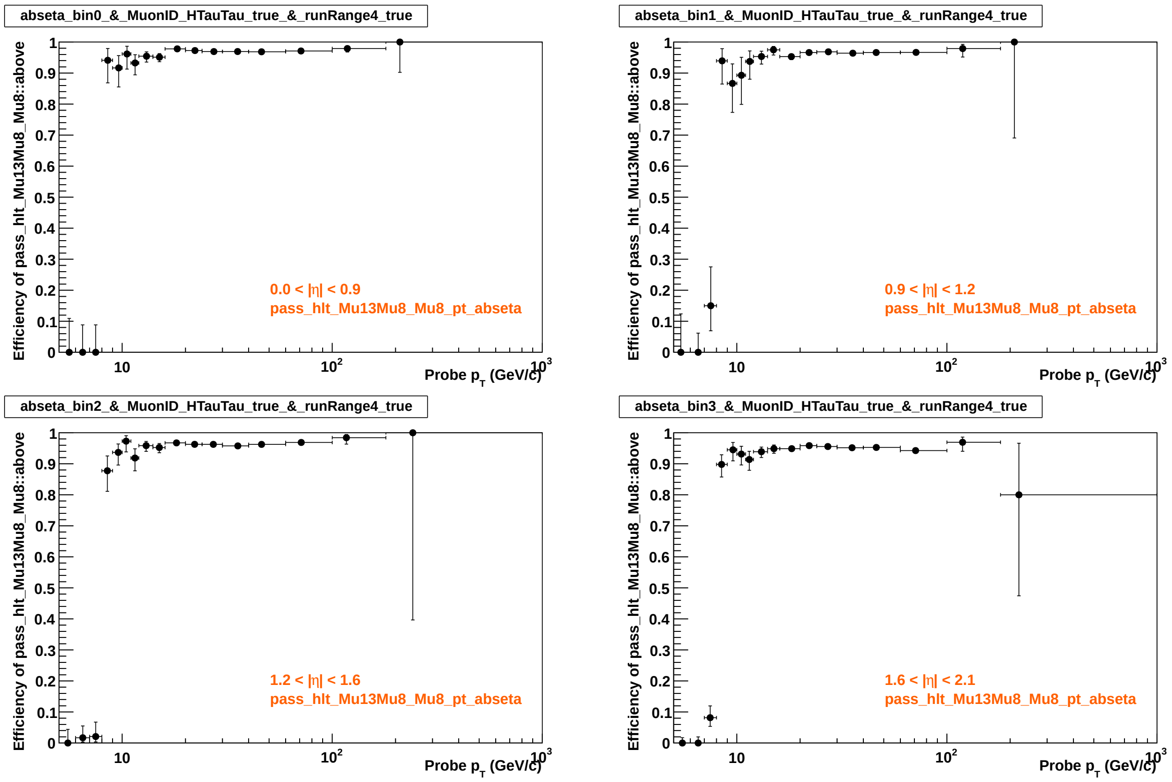

Figure 4.4: Turn-on curves for the Mu8 leg of the HLT_Mu13_Mu8 trigger, measured using the tag-and-probe method with $Z \to \mu\mu$ events.

muon p_{T}	μ trigger ϵ, %		
bin, GeV/c	HLT_Mu9	HLT_Mu11	HLT_Mu15
10−15	$84.3^{+1.5}_{-1.5}$	$68.4^{+1.7}_{-1.8}$	$0.69^{+0.26}_{-0.22}$
15−20	$92.8^{+1.9}_{-2.0}$	$92.5^{+1.3}_{-1.3}$	$92.1^{+0.9}_{-0.9}$
20−30	$91.9^{+1.5}_{-1.7}$	$91.6^{+0.8}_{-0.9}$	$92.3^{+0.5}_{-0.5}$
30−40	$93.3^{+1.0}_{-1.2}$	$93.2^{+0.5}_{-0.5}$	$93.1^{+0.4}_{-0.4}$
40−60	$92.4^{+0.9}_{-1.0}$	$92.5^{+0.4}_{-0.5}$	$92.8^{+0.3}_{-0.3}$
60−100	$90.4^{+3.5}_{-4.8}$	$91.6^{+1.4}_{-1.7}$	$93.0^{+0.9}_{-1.0}$

Table 4.3: Trigger efficiencies in bins of muon p_{T}. Results of the tag-and-probe studies with the $\mathrm{Z} \to \tau\tau$ and $\Upsilon(1S, 2S, 3S) \to \mu\mu$ samples are combined for the first three p_{T} bins. For the remaining bins, the results obtained with only the $\mathrm{Z} \to \mu\mu$ sample are quoted.

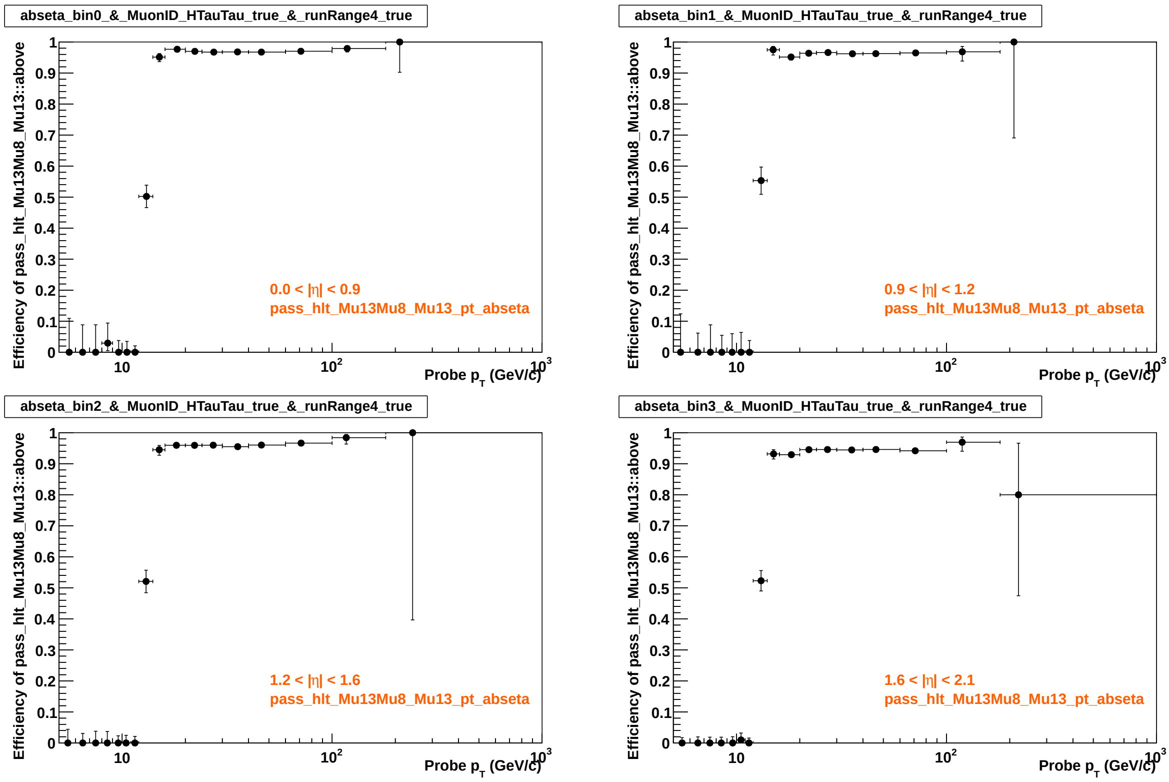

Figure 4.5: Turn-on curves for the Mu13 leg of the HLT_Mu13_Mu8 trigger, measured using the tag-and-probe method with $Z \to \mu\mu$ events.

p_{T} bin	η bin	MC Efficiency	Data Efficiency
$10.0 < p_{\mathrm{T}} \leq 15.0$	$0.0 \leq \mid \eta \mid < 0.8$	0.9873 ± 0.0040	0.9693 ± 0.0045
$10.0 < p_{\mathrm{T}} \leq 15.0$	$0.8 \leq \mid \eta \mid < 1.2$	0.9688 ± 0.0113	0.9411 ± 0.0087
$10.0 < p_{\mathrm{T}} \leq 15.0$	$1.2 \leq \mid \eta \mid < 2.1$	0.9374 ± 0.0108	0.9069 ± 0.0081
$15.0 < p_{\mathrm{T}} \leq 20.0$	$0.0 \leq \mid \eta \mid < 0.8$	0.9876 ± 0.0057	0.9659 ± 0.0046
$15.0 < p_{\mathrm{T}} \leq 20.0$	$0.8 \leq \mid \eta \mid < 1.2$	0.9505 ± 0.0121	0.9298 ± 0.0094
$15.0 < p_{\mathrm{T}} \leq 20.0$	$1.2 \leq \mid \eta \mid < 2.1$	0.9559 ± 0.0109	0.9164 ± 0.0078
$20.0 < p_{\mathrm{T}} \leq 25.0$	$0.0 \leq \mid \eta \mid < 0.8$	0.9883 ± 0.0048	0.9758 ± 0.0039
$20.0 < p_{\mathrm{T}} \leq 25.0$	$0.8 \leq \mid \eta \mid < 1.2$	0.9925 ± 0.0097	0.9460 ± 0.0090
$20.0 < p_{\mathrm{T}} \leq 25.0$	$1.2 \leq \mid \eta \mid < 2.1$	0.9666 ± 0.0083	0.9284 ± 0.0075
$25.0 < p_{\mathrm{T}} \leq 30.0$	$0.0 \leq \mid \eta \mid < 0.8$	0.9892 ± 0.0047	0.9650 ± 0.0048
$25.0 < p_{\mathrm{T}} \leq 30.0$	$0.8 \leq \mid \eta \mid < 1.2$	0.9667 ± 0.0137	0.9492 ± 0.0088
$25.0 < p_{\mathrm{T}} \leq 30.0$	$1.2 \leq \mid \eta \mid < 2.1$	0.9392 ± 0.0156	0.9046 ± 0.0093
$30.0 < p_{\mathrm{T}}$	$0.0 \leq \mid \eta \mid < 0.8$	0.9747 ± 0.0067	0.9704 ± 0.0017
$30.0 < p_{\mathrm{T}}$	$0.8 \leq \mid \eta \mid < 1.2$	0.9671 ± 0.0112	0.9326 ± 0.0039
$30.0 < p_{\mathrm{T}}$	$1.2 \leq \mid \eta \mid < 2.1$	0.9563 ± 0.0101	0.9114 ± 0.0037

Table 4.4: Efficiencies in bins of muon p_{T} and η, for one muon part of the double muon HLT trigger with thresholds 8 and 17 GeV used in 2012 data. The results are obtained with the tag-and-probe method and $\mathrm{Z} \rightarrow \mu\mu$ events.

Chapter 5

Physics objects and analysis tools

5.1 Primary vertex reconstruction

Primary vertices are reconstructed using the so-called Deterministic Annealing (DA) clustering of tracks [36]. Reconstructed vertices are required to have a z position within 24 cm of the nominal detector centre and a radial position within 2 cm from the beamspot.There must be more than four degrees of freedom in the vertex fit. From the set of primary vertices passing these criteria, the vertex with the maximum p_{T} sum of tracks associated with the vertex is chosen as the hard interaction vertex. All rest of the vertices are considered to come from additional soft scattering interactions at collision time. This the so called pile-up.

5.2 Particle Flow algorithm

The aim of the CMS particle flow (PFlow) event-reconstruction algorithm [37, 38] is to identify and reconstruct individually each particle arising from the LHC proton-proton collision, by combining the information from all subdetectors. The resulting global event description leads to an improvement in the performance of the reconstruction of jets and Missing Transverse Energy (MET), and the identification of electrons, muons, and taus. The particle flow algorithm consists in the following steps:

- Fundamental ingredients:
  - calorimeter clustering
  - tracking, and extrapolation to the calorimeters
  - muon identification
  - electron pre-identification
- Linking topologically connected elements
- Particle identification and reconstruction

5.3 Jet reconstruction

The high energy quarks and gluons coming from the colliding protons almost instantly form hadrons that appear in the detector as “jets”. The jet reconstruction is important in all kinds of physics searches. The nature and the properties of the jets provide us information about the physics processes that took place in the event under study. Often the multiplicity and the topology of jets become clear signature for a particular type of event. For example in the Higgs searches the event multiplicity gives us a handle to identify different Higgs production mechanisms, like vector boson fusion, associated production with b-jets and more.

5.3.1 The anti-k_t algorithm

Jet clustering algorithms are among the main tools for analysing data from hadronic collisions. In the search for Higgs decaying to two taus the anti-k_t algorithm is used [39]. In this section gives the definition and describes the behaviour of this algorithm.

The known k_t and Cambridge/Aachen are inclusive jet finding algorithms and belong to a broader class of sequential recombination jet algorithms, parametrised by the power of the energy scale in the distance measure. The general idea of the sequential recombination algorithms is the following. Let d_{ij} be the distance between entities, such as particles and pseudo-jets, i and j, and d_{iB} the distance between entity i and the beam (B). The inclusive clustering proceeds by identifying the smallest of the distances. If it is a d_{ij} the entities i and j are recombined, while if it is d_{iB} i is called a jet and removed from the list of entities. The distances are recalculated and the procedure repeated until no entities are left.

One can generalise the k_t and Cambridge/Aachen algorithms by changing the definition of the distance measures as follows:

$$d_{ij} = min(k_{ti}^{2p}, k_{tj}^{2p})\frac{\Delta_{ij}^2}{R^2} d_{iB} = k_{ti}^{2p} \tag{5.3.1}$$

where $\Delta_{ij}^2 = (y_i - y_j)^2 + (\phi_i - \phi_j)^2$ and k_{ti}, y_i and ϕ_i are respectively the transverse momentum, rapidity and azimuth of particle i. In addition to the radius parameter R, we have added a parameter p to control the relative power of the energy against the geometrical, Δ_{ij}, scales. For $p = 1$ one returns to the inclusive k_t algorithm. It can be shown in general that for $p > 0$ the behaviour of the jet algorithm with respect to soft radiation is rather similar to that observed for the k_t algorithm, because what matters is the ordering between particles and for finite Δ this is maintained for all positive values of p. The case of $p = 0$ is special and it corresponds to the inclusive Cambridge/Aachen algorithm.

The algorithm gives valid results even in the case where p is negative. The behaviour with respect to soft radiation will be similar for all $p < 0$, so here we will concentrate on the case where $p = -1$ which is known as the anti-k_t jet-clustering algorithm. The functionality of the anti-k_t algorithm can be understood by considering an event with a few well separated hard particles with transverse momenta k_{t1}, k_{t2}, . . . and many soft particles. In the anti-k_t algorithm d_{1i} between a hard particle 1 and a soft particle i is:

$$d_{1i} = min\left(\frac{1}{k_{t1}^2}, \frac{1}{k_{ti}^2}\right)\frac{\Delta_{1i}^2}{R} \tag{5.3.2}$$

This quantity is exclusively determined by the transverse momentum of the hard particle and the Δ_{1i} separation. Therefore the d_{ij} between soft particles with similar Δ separation will be much larger. As a result, soft particles will tend to cluster with hard ones long before they cluster among themselves. If a hard particle has no hard neighbours within a distance $2R$, then it will simply accumulate all the soft particles within a circle of radius R, resulting in a perfectly conical jet.

If another hard particle 2 is present such that $R < \Delta_{12} < 2R$ then there will be two hard jets. It is not possible for both to be perfectly conical. If $k_{t1} \ll k_{t2}$ then jet 1 will be conical and jet 2 will be partly conical, since it will miss the part overlapping with jet 1. Instead if $k_{t1} = k_{t2}$ neither jet will be conical and the overlapping part will simply be divided by a straight line equally between the two. For a general situation, $k_{t1} \sim k_{t2}$, both cones will be clipped, with the boundary b between them defined by:

$$\frac{\Delta_{1b}}{k_{t1}} = \frac{\Delta_{2b}}{k_{t2}}. \tag{5.3.3}$$

Similarly, when $\Delta_{12} < R$ the particles 1 and 2 will cluster to form a single jet. If $k_{t1} \ll k_{t2}$ then it will be a conical jet centred on k_1. For $k_{t1} \sim k_{t2}$ the shape will instead be more complex, being the union of cones with radius $< R$ around each hard particle plus a cone of radius R centred on the final jet. The key feature of the anti-k_t algorithm is that the soft particles do not modify the shape of the jet, while hard particles do. The jet boundary in this algorithm is resilient with respect to soft radiation, but flexible with respect to hard radiation. Finally with the anti-k_t algorithm, the hard jets are circular with a radius R, and only the softer jets have more complicated shapes.

5.3.2 Particle Flow jets

The jet used in both analysis present in the current document are reconstructed in the detector using the particle flow algorithm 5.2. Charged hadrons are reconstructed from tracks in the central tracker. Photons and neutral hadrons are reconstructed from energy clusters in the electromagnetic and hadron calorimeters. Clusters separated from the extrapolated position of tracks in the calorimeters constitute a clear signature of these neutral particles. A neutral particle overlapping with charged particles in the calorimeters can be detected as a calorimeter energy excess with respect to the sum of the associated track momenta. PFlow jets are then reconstructed from the resulting list of particles. The jet momentum and spatial resolutions are expected to be improved with respect to other reconstructing methods, as the use of the tracking detectors and of the excellent granularity of the ECAL allows to resolve and precisely measure charged hadrons and photons inside jets, which constitute $\sim 90\%$ of the jet energy.

When analysing data taken in 2011 and 2012 the effect of the pile-up becomes significant. Particles from pile-up vertices can be clustered into a pile-up jet or contaminate jets from the primary vertex. A multivariate boosted decision tree [40] discriminator is used in order to distinguish between jets coming from the hard interaction and those coming from pile-up. This discriminator is based on the following variables: momentum and spacial distribution of the jet particles, charged and neutral particle multiplicities, compatibility of the jet charged hadrons with the primary vertex [41].

5.3.3 b-tagging for jets

Most of the b-hadron properties used for b-tagging can only be exploited using charged particle tracks because only tracking detectors offer the spatial resolution needed to resolve properties of b-hadron decays, such as their significant flight path. Therefore the key ingredient is efficient track reconstruction, and in particular precise spatial reconstruction close to the interaction point. The Combined Secondary Vertex (CSV) b-tagging algorithm [42] is based on the reconstruction of the secondary vertex of the decaying b-hadron. The secondary vertices are reconstructed in an inclusive way inside the jet, using all tracks in the jet and rejecting additional tracks used then to reconstruct more vertices. A dedicated set of selection cut is applied to tracks and secondary vertices separately to reject backgrounds such as c-hadrons, K_s^0, Λ^0 and nuclear interactions in the beam pipe or the first layers on the pixel detector.

Several topological and kinematics variables related to the secondary vertex as well as variables related to the impact parameter significances of charged particle tracks are used. Depending on the multiplicity and the quality of the primary vertices reconstructed the events are divided into categories. In each category a different set of discriminating variables is used.The variables are then combined into a singe discriminating variable using a likelihood ration technique. More recent versions of the algorithm use multivariate analysis techniques.

5.4 Missing transverse energy

Missing energy is used to infer the presence of non-detectable particles such as neutrinos or supersymmetric particles and is expected to be a signature of many new physics events. In hadron colliders, the initial momentum of the colliding partons along the beam axis is not known, however the initial energy in particles travelling transverse to the beam axis is zero, so any net momentum in the transverse direction indicates Missing Transverse Energy (MET). In the case of the Z/H $\rightarrow \tau\tau \rightarrow \mu\mu$ there are four neutrinos involved, therefore our signal events are characterised by high values of MET. The MET is also a key ingredient when reconstructing the ditau invariant mass 5.7.2.Therefore it is important to reconstruct the MET as accurately as possible .

5.4.1 Particle Flow missing transverse energy

An accurate determination of MET, is a major asset for all kinds of physics searches. It is in principle simple to determine MET after the particle flow event reconstruction [37]. It simply comes down to forming the transverse momentum-vector sum over all reconstructed particles in the event and then taking the opposite of this azimuthal, momentum two-vector. The missing transverse energy is the modulus of this vector. The true MET is derived in a similar manner with all visible generated particles or, equivalently, with all invisible generated particles, like neutrinos and neutralinos. Accurate reconstruction of MET is demanding because it entails reconstruction of all visible particles in an event with precision. This requires a hermetic detector which can detect all particles which electromagnetically or strongly interact with matter. With its highly granular electromagnetic calorimeters, hermetic hadronic calorimeters, redundant muon systems, and all silicon trackers in a strong magnetic field, the CMS detector meets this requirement.

The resolution of the PFlow MET degrades rapidly with the number of pile-up interactions. In the Higgs analysis, where 2011 and 2012 data is used a multivariate technique is used to provide a more precise estimation of the MET in the high pile-up environment. Five different MET variables are calculated from particle flow candidates using the information of the pile-up jet identification. These MET variables are derived from:

- charged hadrons from the primary vertex

- charged hadrons from the primary vertex, and neutral particles in jets passing the pile-up identification criteria.

- charged hadrons from pile-up vertices an neutral particles in jets failing the pile-up identification criteria.

- charged hadrons from the primary vertex and all neutral particles in the event, plus the vectorial sum of the transverse momenta of neutral particles within jets failing the pile-up identification criteria.

5.5 Muon reconstruction

In the standard CMS reconstruction for proton-proton collisions, tracks are first reconstructed independently in the silicon tracker and in the muon spectrometer. Based on these, there are two main muon reconstruction approaches [43]:

1. Global muon reconstruction (outside-in): starting from a standalone muon in the muon system, a matching tracker track is found and a global-muon track is fitted combining hits from the tracker track and standalone-muon track. At large transverse momenta($p_{\mathrm{T}} > 200$ GeV/c), the global muon fit can improve the momentum resolution compared to the tracker-only fit.

2. Tracker Muon reconstruction (inside-out): in this approach, all tracker tracks with $p_{\mathrm{T}} > 0.5$ GeV/c and $p > 2.5$ GeV/c are considered as possible muon candidates and are extrapolated to the muon system, taking into account the expected energy loss and the uncertainty due to multiple scattering. If at least one muon segment, which is a short track stub made of either DT or CSC hits, matches the extrapolated track, the corresponding tracker track qualifies as a tracker muon track. The extrapolated track and the segment are considered to be matched if the distance between them in local x is less than 3 cm or if the value of the pull for local x is less than 4. At low momentum, roughly p $<$ 5 GeV/c, this approach is more efficient than the global muon reconstruction, since it requires only a single muon segment in the muon system, whereas global muon reconstruction is designed to have high efficiency for muons penetrating through more than one muon station.

The majority of muons from collisions, with sufficient momentum, are reconstructed either as a global Muon or a tracker Muon, or very often as both. However, if both approaches fail and only a standalone muon track is found, this leads to a third category of muon candidates:

3. Standalone muon track only: this occurs only for about 1% of muons from collisions, thanks to the high tracker-track efficiency. On the other hand, the acceptance of this type of muon track for cosmic-ray muons is a factor 10^2 to 10^3 larger, thus leading to a collision muon to cosmic-ray muon ratio that is a factor 10^4 to 10^5 less favourable than for the previous two muon categories.

5.5.1 Particle Flow muons

The CMS particle flow event reconstruction combines the information from all sub-detectors to identify and reconstruct individually all particles produced in the collision. In order to identify particle flow muons (PFlow muons) [44] a selection is applied to all the muon candidates reconstructed with the standard algorithms. This set of requirements together with the use of the measurement of energy released in the calorimeter define an alternative set of selections which are appropriate for and needed by the particle flow algorithm. This combined selection has been optimised to identify muons in jets with high efficiency, keeping fake rate from misidentified charged hadrons low. This is needed in order to avoid biases in jet and MET measurements coming from non-identified or fake muons. As a consequence, the PFlow muon selection has been designed to retain non-isolated muons, including the muons from hadron decays in flight, usually considered as a background in typical muon analyses. This is achieved by applying selection criteria which differ in strictness depending on whether the muon candidate is isolated or not, and whether its momentum is compatible with the energy deposition in the calorimeters assigned to the candidate by the particle flow event reconstruction.

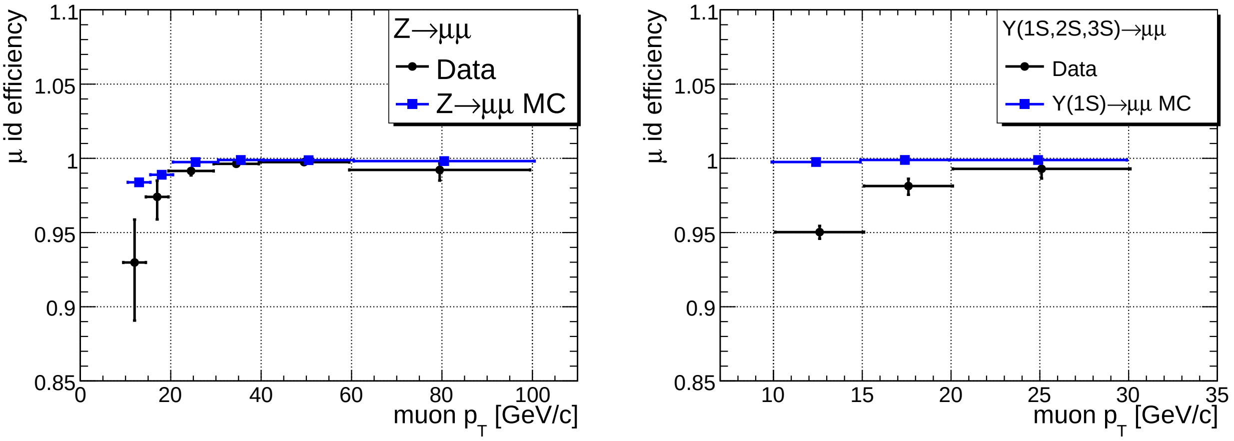

Figure 5.1: Muon identification efficiency determined in data and MC samples with the Z $\rightarrow \mu\mu$ events (left plot) and $\Upsilon(1S, 2S, 3S) \rightarrow \mu\mu$ events (right plot).

Particle Flow isolation

In a similar way the isolation of a muon can be constructed using information from all subdetectors. The particle flow based relative isolation for a muon, is given by the formula:

$$\mathrm{Iso}_{\mu}^{\mathrm{PFlow}} = \frac{\sum (p_{\mathrm{T}}^{\mathrm{charged}} + p_{\mathrm{T}}^{\gamma} + p_{\mathrm{T}}^{\mathrm{neutral}})}{p_{\mathrm{T}}^{\mu}}, \tag{5.5.1}$$

where the sum runs over the transverse momenta of all charged particles, photons and neutral hadrons within a cone $\Delta R < 0.3$ around the muon momentum. p_{T}^{μ} stands for the muon transverse momentum. The relative isolation is important for the event selection in the main analysis. The numerator in equation 5.5.1 is the absolute isolation. The absolute isolation doesn't depend on the p_{T}^{μ}. This feature is used in the analysis for calibrating the MC samples. More details in a later chapter where the analyses procedures are discussed.

Muon Identification efficiency

The muon identification efficiency is measured using the tag-and-probe method. The muons used come from Z and $\Upsilon(1S, 2S, 3S)$decays. The tag muons are global muons passing selection criteria. The reconstructed muon tracks that have a sign opposite to the sign of the tag muon are used as probes. For the study of the Z $\rightarrow \mu\mu$ sample the tracks are required to be isolated, $\mathrm{Iso}_{\mathrm{Trk}}^{\mathrm{PFlow}} < 0.1$. No isolation of the probed tracks is required for the studies with $\Upsilon(1S, 2S, 3S) \rightarrow \mu\mu$ events. The probed track is considered a failure if no global muon, containing the probed track, is found in an event, otherwise the track is considered as having passed the muon identification criteria. Figure 5.1 shows the p_{T} dependence of the muon identification efficiency determined with the tag-and-probe technique in 2010 data and MC samples. The exact numbers and errors are presented in table 5.1. The equivalent studies for the 2011 and 2012 datasets are shown in tables 5.2 and 5.3.

5.6 Tau lepton reconstruction

Because of their higher mass than e and μ, τ leptons play a crucial role in the searches for the SM Higgs boson. The branching fraction of Higgs decaying to a pair of τ leptons is 8%. The lifetime of τ leptons is quite short, so that they decay before reaching the detector

2010		
p_{T} bin	MC Efficiency	Data Efficiency
10−15	$94.98^{+0.43}_{-0.45}$	$99.71^{+0.04}_{-0.04}$
15−20	$97.97^{+0.49}_{-0.52}$	$99.74^{+0.05}_{-0.05}$
20−30	$99.17^{+0.23}_{-0.27}$	$99.76^{+0.02}_{-0.02}$
30−40	$99.63^{+0.10}_{-0.12}$	$99.89^{+0.02}_{-0.03}$
40−60	$99.74^{+0.07}_{-0.08}$	$99.88^{+0.02}_{-0.03}$
60−100	$99.22^{+0.44}_{-0.72}$	$99.81^{+0.04}_{-0.05}$

Table 5.1: Muon identification efficiencies in bins of muon p_{T}. The results of the tag-and-probe studies with the $\mathrm{Z} \rightarrow \tau\tau$ and $\Upsilon(1S, 2S, 3S) \rightarrow \mu\mu$ samples are combined for the first three p_{T} bins. In rest of the bins the results presented are obtained using the $\mathrm{Z} \rightarrow \mu\mu$ sample only.

2011			
p_{T} bin	η bin	MC Efficiency	Data Efficiency
10.0 - 15.0 GeV	$\mid \eta \mid < 1.5$	0.6876 ± 0.0026	0.6804± 0.0093
10.0 - 15.0 GeV	$1.5 \leq\mid \eta \mid < 2.1$	0.6103 ± 0.0031	0.6288± 0.0103
15.0 - 20.0 GeV	$\mid \eta \mid < 1.5$	0.7727± 0.0014	0.7856 ± 0.0048
15.0 - 20.0 GeV	$1.5 \leq\mid \eta \mid < 2.1$	0.6981 ± 0.0020	0.7153 ± 0.0067
>20.0 GeV	$\mid \eta \mid <1.5$	0.9351 ± 0.0001	0.9408± 0.0003
>20.0 GeV	$1.5 \leq\mid \eta \mid < 2.1$	0.8858± 0.0003	0.8986 ± 0.0008

Table 5.2: Muon identification efficiencies in bins of muon p_{T} and η for 2011. These efficiencies were studied by the Muon Physics Object Group (POG) [45].

2012			
p_{T} bin	η bin	MC Efficiency	Data Efficiency
$10.0 < p_{\mathrm{T}} \leq 15.0$	$0.0 \leq\mid \eta \mid< 0.8$	0.6211 ± 0.0052	0.6114 ± 0.0066
$10.0 < p_{\mathrm{T}} \leq 15.0$	$0.8 \leq\mid \eta \mid< 1.2$	0.6808 ± 0.0050	0.6719 ± 0.0059
$10.0 < p_{\mathrm{T}} \leq 15.0$	$1.2 \leq\mid \eta \mid< 2.1$	0.6680 ± 0.0031	0.6631 ± 0.0034
$15.0 < p_{\mathrm{T}} \leq 20.0$	$0.0 \leq\mid \eta \mid< 0.8$	0.7158 ± 0.0026	0.6903 ± 0.0032
$15.0 < p_{\mathrm{T}} \leq 20.0$	$0.8 \leq\mid \eta \mid< 1.2$	0.7645 ± 0.0030	0.7492 ± 0.0035
$15.0 < p_{\mathrm{T}} \leq 20.0$	$1.2 \leq\mid \eta \mid< 2.1$	0.7352 ± 0.0021	0.7323 ± 0.0023
$20.0 < p_{\mathrm{T}}$	$0.0 \leq\mid \eta \mid< 0.8$	0.9260 ± 0.0002	0.9152 ± 0.0002
$20.0 < p_{\mathrm{T}}$	$0.8 \leq\mid \eta \mid< 1.2$	0.9273 ± 0.0003	0.9165 ± 0.0003
$20.0 < p_{\mathrm{T}}$	$1.2 \leq\mid \eta \mid< 2.1$	0.9089 ± 0.0002	0.9035 ± 0.0002

Table 5.3: Muon identification efficiencies in bins of muon p_{T} and η for 2012. These efficiencies were studied by the Muon Physics Object Group (POG) [45].

elements. In two thirds of the cases, τ leptons decay hadronically, typically into one or three charged mesons, often accompanied by neutral pions and a ν_τ.

The Hadron Plus Strips (HPS) algorithm [46] is used as the main algorithm in most CMS τ related analyses.The algorithm uses particle flow particles. The particles are classified into mutually exclusive categories: charged hadrons, photons, neutral hadrons, muons, and electrons. Since charged hadrons and photons are reconstructed with high precision using the PFlow techniques the reconstructed energy is expected to be close to the true energy of its visible decay products. The HPS algorithm is designed to optimise the performance of the τ_{had} identification and reconstruction by considering the different hadronic decay modes of the τ lepton individually. The dominant hadronic decays of τ leptons consist of one or three charged π mesons and up to two π^0 mesons, decaying via $\pi^0 \to \gamma\gamma$. The τ decays taken into account are listed in table 5.4. The algorithm starts the reconstruction of a τ_{had} candidate from a PFlow jet, whose four-momentum is reconstructed using the anti-k_t algorithm. A PFlow jet is used as an initial seed for the π_0 components of the τ_{had}. Then, they are combined with charged hadrons to reconstruct the tau decay mode and calculate the τ lepton four-momentum and isolation quantities.

Decay mode	Resonance	Branching fraction
$\pi^-\nu_\tau$		11.6%
$\pi^-\pi^0\nu_\tau$	ρ^-	26.0%
$\pi^-\pi^0\pi^0\nu_\tau$	α_1^-	9.5%
$\pi^-\pi^+\pi^-\nu_\tau$	α_1^-	9.8%
$\pi^-\pi^+\pi^-\pi^0\nu_\tau$		4.8%

Table 5.4: List of the dominant τ hadronic decays and the corresponding branching fractions. On the second column the intermediate meson resonances are presented.

The HPS algorithm gives special attention to photon conversions in the CMS tracker material. The bending of electron or positron tracks in the magnetic field of the CMS solenoid broadens the calorimeter signatures of neutral pions in the azimuthal direction. This effect is taken into account in the HPS algorithm by reconstructing photons in objects that are built out of electromagnetic particles, PFlow photons and electrons, so called "strips". The strip reconstruction starts by locating the most energetic electromagnetic particle within the PFlow jet and centring the strip round it. The algorithm then searches for other electromagnetic particles within a window of size $\Delta\eta = 0.05$ and $\Delta\phi = 0.20$ around the strip centre. If other electromagnetic particles are found within that window, the most energetic one gets associated with the strip and the strip four-momentum is recalculated. The procedure is repeated until no further particles are found that can be associated with the strip. Strips satisfying a minimum transverse momentum requirement of $p_{\mathrm{T}} > 1$ GeV/c are finally combined with the charged hadrons to reconstruct individual th decay modes.

- Single hadron: corresponds to $\pi^-\nu_\tau$ or $\pi^-\pi^0\nu_\tau$ decays in which the neutral pions have too little energy to be reconstructed as strips.

- One hadron plus one strip: reconstructs the decay mode $\pi^-\pi^0\nu_\tau$ in events in which the photons from π^0 decay are close together on the calorimeter surface.

- One hadron plus two strips: corresponds to the decay mode $\pi^-\pi^0\nu_\tau$ in events in which photons from π^0 decays are well separated.

- Three hadrons: corresponds to the decay mode $\pi^-\pi^+\pi^-\nu_\tau$. The three charged hadrons are required to come from the same secondary vertex.

There are no separate decay topologies for the decay modes $\pi^-\pi^0\pi^0\nu_\tau$ and $\pi^-\pi^+\pi^-\pi^0\nu_\tau$. They are reconstructed via the existing topologies. A number of selection requirements are applied to the τ_{had} candidates. Firstly, all charged hadrons and strips are required to be contained within a cone the size of which depends on the transverse momentum of the τ_{had} as reconstructed by HPS. The reconstructed τ momentum is required to match the direction of the original PFlow jet. In addition the four-momenta of charged hadrons and strips are reconstructed according to the respective τ decay topology hypothesis, assuming all charged hadrons to be pions, and are required to be consistent with the masses of the intermediate meson resonances. Finally, reconstructed candidates are required to be isolated. The τ isolation R^τ_{Iso} is obtained from a multivariate discriminator taking as input a set of transverse momentum sums $S_j = \sum_i p_{\mathrm{T}ij}$ where $p_{\mathrm{T}ij}$ is the transverse momentum of a particle i in a ring j centred on the τ candidate and defined in the (η, ϕ) space. Five equal width rings are used to cover up to $\Delta R = \sqrt{\Delta\eta^2 + \Delta\phi^2} = 0.5$ around the τ candidate.

The overall τ lepton identification efficiency using the tools described here is 60-65%, for a jet fake rate 2-3%.

5.7 Ditau mass reconstruction

5.7.1 Collinear approximation

The collinear approximation is a frequently used technique, and it was the first proposed method to reconstruct the invariant mass in $\tau\tau$ decays of a Higgs boson produced in association with an energetic [47] jet. It is based on two important assumptions. First that the neutrinos from each τ decay are nearly collinear with the corresponding visible τ decay products, $\phi_{nu} \simeq$

ϕ_{vis} and $\theta_\nu \simeq \theta_{\text{vis}}$ and second that the $E_T^{\text{miss}1}$ in the event is due only to neutrinos. In this case, the total invisible momentum carried away by neutrinos in each τ decay can be estimated by solving two equations:

$$E_{Tx}^{\text{miss}} = p_{\text{miss}}^1 \sin\theta_{\text{vis}}^1 \cos\phi_{\text{vis}}^1 + p_{\text{miss}}^2 \sin\theta_{\text{vis}}^2 \cos\phi_{\text{vis}}^2 E_{Ty}^{\text{miss}} = p_{\text{miss}}^1 \sin\theta_{\text{vis}}^1 \sin\phi_{\text{vis}}^1 + p_{\text{miss}}^2 \sin\theta_{\text{vis}}^2 \sin\phi_{\text{vis}}^2 \tag{5.7.1}$$

where E_{Tx} and E_{Ty} are the x and y components of the E_T^{miss} vector, p_{miss}^1 and p_{mis}^2 are the combined invisible momenta of each τ decay, in the case where two neutrinos are produced, and $\theta_{\text{vis}}^{1,2}$ and $\phi_{\text{vis}}^{1,2}$ are the polar and azimuthal angles of the visible products of each τ decay. Then, the invariant mass of the ditau system can be calculated as:

$$M_{\tau\tau} = \frac{m_{\text{vis}}}{\sqrt{x_1 x_2}} \tag{5.7.2}$$

where

$$x_{1,2} = \frac{p_{\text{vis}}^{1,2}}{p_{\text{vis}}^{1,2} + p_{\text{miss}}^{1,2}} \tag{5.7.3}$$

are the momentum fractions carried away by visible τ decay products and m_{vis} is the invariant mass of visible τ decay products. Despite offering the great advantage of a fully reconstructed ditau mass ($M_{\tau\tau}$) instead of a partial visible mass, the collinear approximation still has significant shortcomings. The technique gives a reasonable mass resolution only for the small fraction of events where the ditau system is produced in association with a large E_{T} jet and the visible τ decay products are not back-to-back in the transverse plane. The last requirement is needed, because the system of equations 5.7.2 and 5.7.3becomes degenerate if:

$$\phi_{\text{vis}}^1 = \phi_{\text{vis}}^2 + \pi \tag{5.7.4}$$

and solutions $p_{\text{miss}}^{1,2} \sim \sin^{-1}(\phi_{\text{vis}}^1 - \phi_{\text{vis}}^2)$ diverge as $\mid \phi_{\text{vis}}^1 - \phi_{\text{vis}}^2 \mid \to \pi$. Unfortunately, the majority of H $\to \tau\tau$ events are produced with τ leptons in nearly the back-to-back topology. Therefore, this technique is applicable only to a relatively small fraction of ditau events. The collinear approximation is also very sensitive to the E_T^{miss} resolution and tends to overestimate the τ pair mass, leading to long tails in the reconstructed mass distribution. This effect is especially undesirable for low mass Higgs boson searches, where the tails of the much larger Z $\to \tau\tau$ background completely dominate the expected Higgs signal region.

5.7.2 Secondary vertex fit algorithm

In order to reconstruct the mass of a τ lepton pair the four-momenta of both τ leptons has to be determined.The kinematics of each τ lepton decay is fully described by the four-momenta of the sum of all visible τ decay products and the sum of all invisible particles produced in the τ lepton decays. In the hadronic τ lepton decays there is one neutrino produced while in the leptonic decays there are two. The kinematic properties of the visible decay products can be measured with small uncertainties. The challenge is to reconstruct the four-momenta of the neutrino(s). The system of invisible decay products is massless in case of hadronic τ lepton decays, while the invisible momentum system produced in leptonic τ decays is in general of non-zero mass. The momentum sum of visible and invisible decay products is constrained by the τ lepton mass m_τ.

The Secondary Vertex Fit (SVFit) algorithm [48] is a method of reconstructing the invariant mass of the ditau system using a likelihood maximisation. The fact that the τ lepton decay

---

[1] In this section the symbol E_T^{miss} will be used to denote the missing transverse energy. It is important here to emphasise the distinction between the quantities refering to the visible products and the missing energy and momentum carried by the neutrinos.

kinematics is underconstrained by measured observables is handled via a Dynamical Likelihood Method (DLM). The term DLM refers to applications of likelihood methods to problems of reconstructing kinematic quantities on an event-by-event basis. $M_{\tau\tau}$ values are reconstructed by combining the measured observables E_x^{miss} and E_y^{miss} with a probability model, which in the present version of SVFit includes terms for τ decay kinematics and for the $E_{\text{T}}^{\text{miss}}$ resolution. The model makes a prediction for the probability density $p(\vec{x} \mid \vec{y}, \vec{\alpha})$ to observe the values $\vec{x} = (E_x^{\text{miss}}, E_y^{\text{miss}})$ measured in an event, given that the unknown parameters specifying the kinematics of the τ pair decay are represented with $\vec{\alpha}$ and the four-momenta of the visible decay products are equal to the observed $\vec{y} = (p_1^{\text{miss}}, p_2^{\text{miss}})$. The mass of the ditau system is a well defined function of $\vec{\alpha}$ and $\vec{y}$:

$$M_{\tau\tau} = M_{\tau\tau}(\vec{y}, \vec{\alpha}) \tag{5.7.5}$$

The likelihood model is used to compute the probability

$$P(M^i_{\tau\tau}) = \int p(\vec{x} \mid \vec{y}, \vec{\alpha}) \delta\left(M^i_{\tau\tau} - M_{\tau\tau}(\vec{y}, \vec{\alpha})\right) d\vec{\alpha} \tag{5.7.6}$$

for a series of mass hypotheses $M^i_{\tau\tau}$. The best estimate for the $M_{\tau\tau}$ is the value of $M^i_{\tau\tau}$ maximising $P(M^i_{\tau\tau})$. The probability $p(\vec{x} \mid \vec{y}, \vec{\alpha})$ is the product of three probability functions, two related to the τ decay kinematics and one which quantifies the compatibility of a τ decay hypothesis with the measured missing transverse energy.

τ lepton decay parametrisation

There are a few equivalent parameterisations of the τ lepton decay kinematics. The parameters used in the latest implementation of the SVFit algorithm are:

- The opening angle θ is defined as the angle between the boost direction of the τ lepton and the momentum vector of the visible decay products in the rest frame of the τ.
- the azimuthal angle of the τ lepton momentum with respect to the direction of its visible decay products, $\bar{\phi}$
- the mass of the neutrino pair arising from the fully leptonic decays $m_{\nu\nu}$

Therefore the vector $\vec{\alpha}$ defined earlier can be written as $\vec{\alpha} = (\theta, \bar{\phi}, m_{\nu\nu})$. For each leptonic decay we have three parameters and for each hadronic decay two parameters. Therefore four to six parameters in total. Given $\theta, \bar{\phi}$ and $m_{\nu\nu}$, the energy and direction of the τ lepton can be computed using the following transformations.

Energy and momentum of the visible decay products in the rest frame of the τ lepton are related to the invariant mass of the neutrino system by:

$$E^{\text{vis}} = \frac{m_\tau^2 + m_{\text{vis}}^2 - m_{\nu\nu}^2}{2m_\tau}, \qquad p^{\text{vis}} = \sqrt{(E^{\text{vis}})^2 - m_{\text{vis}}^2} \tag{5.7.7}$$

This equation is valid for both leptonic and hadronic decays. In the latter case $m_{\nu\nu} = 0$. The opening angle θ between the τ lepton direction and the visible momentum vector in the laboratory frame is determined by the rest frame quantities via the Lorentz invariant component of the visible momentum perpendicular to the τ lepton direction:

$$p_\perp^{\text{vis}} = \bar{p}_\perp^{\text{vis}} \Rightarrow \sin\bar{\theta} = \frac{p^{\text{vis}} \sin\theta}{\bar{p}^{\text{vis}}} \tag{5.7.8}$$

The energy of the τ lepton in the laboratory frame, $\bar{E}_\tau$, is obtained using the relation $\bar{E}_\tau = \gamma m_\tau$ by solving for the boost factor γ in the Lorentz transformation which relates the visible momentum component parallel to the τ direction in the τ rest frame and the laboratory frame:

$$\bar{p}^{\text{vis}} \cos\bar{\theta} = \gamma\beta E^{\text{vis}} + \gamma p^{\text{vis}} \cos\theta \Rightarrow \gamma = \frac{E^{\text{vis}}\sqrt{(E^{\text{vis}})^2 + (\bar{p}^{\text{vis}}\cos\bar{\theta})^2 - (p^{\text{vis}}\cos\theta)^2} - p^{\text{vis}}\cos\theta\bar{p}^{\text{vis}}\cos\bar{\theta}}{(E^{\text{vis}})^2 - (p^{\text{vis}}\cos\theta)^2} \tag{5.7.9}$$

The energy of the τ lepton in the laboratory frame, expressed as function of the measured visible momentum $\bar{p}^{\text{vis}}$, depends on two of the three parameters only. The rest frame opening angle θ and the invariant mass $m_{\nu\nu}$ of the neutrino system. The direction of the τ lepton momentum vector lies on the surface of a cone of opening angle $\bar{\theta}$, the axis of which is given by the visible momentum vector. The direction of the τ lepton four-vector p_τ is specified by the addition of $\bar{\phi}$, the third parameter, which gives the azimuthal angle of the τ lepton with respect to the visible momentum vector. The relation between p_τ and p^{vis}, $\bar{\theta}$, $\bar{\phi}$ is illustrated in figure 5.2.

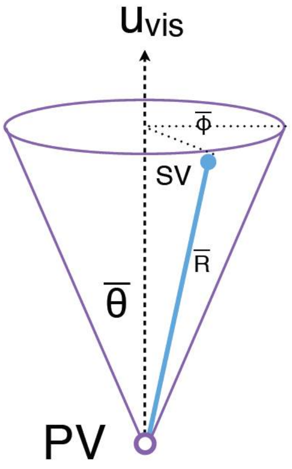

Figure 5.2: The parameters used to describe the decays of τ leptons by the SVFit algorithm.

τ lepton decay widths

Many likelihood models have been tested regarding the τ decay phase kinematics. It turns out that the selection of the likelihood model makes little difference to the distribution of the reconstructed τ pair mass. Therefore, for computational purposes the τ polarisation is not taken into account. In the case of leptonic τ decays the "matrix element model" is selected assuming the unpolarised case (τ helicity $P = 0$):

$$\frac{d\Gamma}{dx_l dm_{\nu\nu}} \sim \frac{m_{\nu\nu}}{4m_\tau^2}\left[\left(m_\tau^2 + 2m_{\nu\nu}\right)\left(m_\tau^2 - m_{\nu\nu}^2\right)\right] \tag{5.7.10}$$

within the physically allowed region $0 \leq x \leq 1$ and $0 \leq m_{\nu\nu} \leq m_\tau\sqrt{1-x}$. For the hadronic decays the simpler "phase space" model is used. The probability density function for the decay width is:

$$\frac{d\Gamma}{dx_h} = \frac{1}{1 - \frac{m_{\text{vis}}^2}{m_\tau^2}} \tag{5.7.11}$$

within the physically allowed region $\frac{m_{\text{vis}}^2}{m_\tau^2} \leq x \leq 1$.

Missing transverse energy

If the neutrinos from the τ decay are the only source of missing energy in the event, then the vectorial sum of their momenta is experimentally constrained by the missing transverse energy $\vec{E}_{\mathrm{T}}^{\mathrm{miss}}$. In a realistic scenario, detector resolution and fluctuations in the undetectable part of the event smear $\vec{E}_{\mathrm{T}}^{\mathrm{miss}}$ around the true value $\sum_i \vec{p}_{\mathrm{T}}^{\nu i}$. The compatibility between the hypothesis $\sum_i \vec{p}_{\mathrm{T}}^{\nu i}$ and the observed value of $\vec{E}_{\mathrm{T}}^{\mathrm{miss}}$ is quantified by the missing transverse energy likelihood $L(\vec{E}_{\mathrm{T}}^{\mathrm{miss}} \mid \sum_i \vec{p}_{\mathrm{T}}^{\nu i})$. In the Gaussian approximation, the likelihood for observing $\vec{E}_{\mathrm{T}}^{\mathrm{miss}}$ given a true missing energy $\sum_i \vec{p}_{\mathrm{T}}^{\nu i}$ is given by

$$L\left(\vec{E}_{\mathrm{T}}^{\mathrm{miss}} \mid \sum_i \vec{p}_{\mathrm{T}}^{\nu i}\right) = \frac{1}{\sqrt{2}\pi \mid V \mid} e^{\left(\vec{E}_{\mathrm{T}}^{\mathrm{miss}} - \sum_i \vec{p}_{\mathrm{T}}^{\nu i}\right)^T V^{-1} \left(\vec{E}_{\mathrm{T}}^{\mathrm{miss}} - \sum_i \vec{p}_{\mathrm{T}}^{\nu i}\right)} \tag{5.7.12}$$

where V is the covariance matrix representing the resolution of transverse energy measurement. The expected resolution is estimated on an event by event basis using the E_T^{miss} algorithm.

Full likelihood

Combining all the above the full likelihood function becomes:

$$\begin{aligned} p(\vec{x} \mid \vec{y}, \vec{\alpha}) \sim & \sum_{i,j} \frac{d\Gamma_i(\vec{x}_- \mid \vec{y}_-)}{d\vec{x}_i} \frac{d\Gamma_j(\vec{x}_+ \mid \vec{y}_+)}{d\vec{x}_j} \times \\ & exp\left\{ -\frac{1}{2} \left(\begin{pmatrix} E_x^{\mathrm{miss}} - \sum p_x^\nu \\ E_y^{\mathrm{miss}} - \sum p_y^\nu \end{pmatrix}^T \cdot V^{-1} \cdot \begin{pmatrix} E_x^{\mathrm{miss}} - \sum p_x^\nu \\ E_y^{\mathrm{miss}} - \sum p_y^\nu \end{pmatrix} \right) \right\} \end{aligned} \tag{5.7.13}$$

Uniform probability density functions have been assumed for the $\bar{\phi}$ angles: $\frac{d\Gamma}{d\bar{\phi}} = \frac{1}{2}\pi$. The functions $d\Gamma(\vec{x} \mid \vec{y}, \vec{\alpha}$ are proportional to the decay widths as given in equations 5.7.10 and 5.7.11.

5.8 Embedding

This section describes a method to model Z → $\tau\tau$ events using Z → $\mu\mu$ events by "embedding" simulated $\tau\tau$ decays in measured Z → $\mu\mu$ events [49]. The original μ pair is replaced by a simulated τ pair with the same kinematic properties while the rest of the original event remains untouched. Therefore in this method systematic errors arising from observables other than the reconstructed τ decay products are much reduced or even absent. The process $Z/\gamma^* \to \mu\mu$ is a clean signature, which can be identified with high efficiency and purity, and the two muons in the final state give access to the properties of the virtual photon or Z boson with very high accuracy. If the muons are removed from the event and τ leptons from simulated Z decays are overlaid instead, one obtains a very realistic description of the full event. The "hybrid event" automatically takes into account time-dependent effects induced by detector performance or running conditions.

The embedding method can be applied to many τ-based studies. In the Z → $\tau\tau$ → $\mu\mu$ analysis the embedded sample is used to estimate the selection efficiency the effect of pile-up and other cross checks. More importantly, in the H → $\tau\tau$ → $\mu\mu$ analysis the embedding sample is used to estimate the number of Z → $\tau\tau$ → $\mu\mu$ background events.

The events are overlaid on the basis of particle flow candidates which together with the collection of tracks, contain all information needed for physics analysis. The disadvantage of this approach is that it does not include a simulation of the trigger system, which operates on

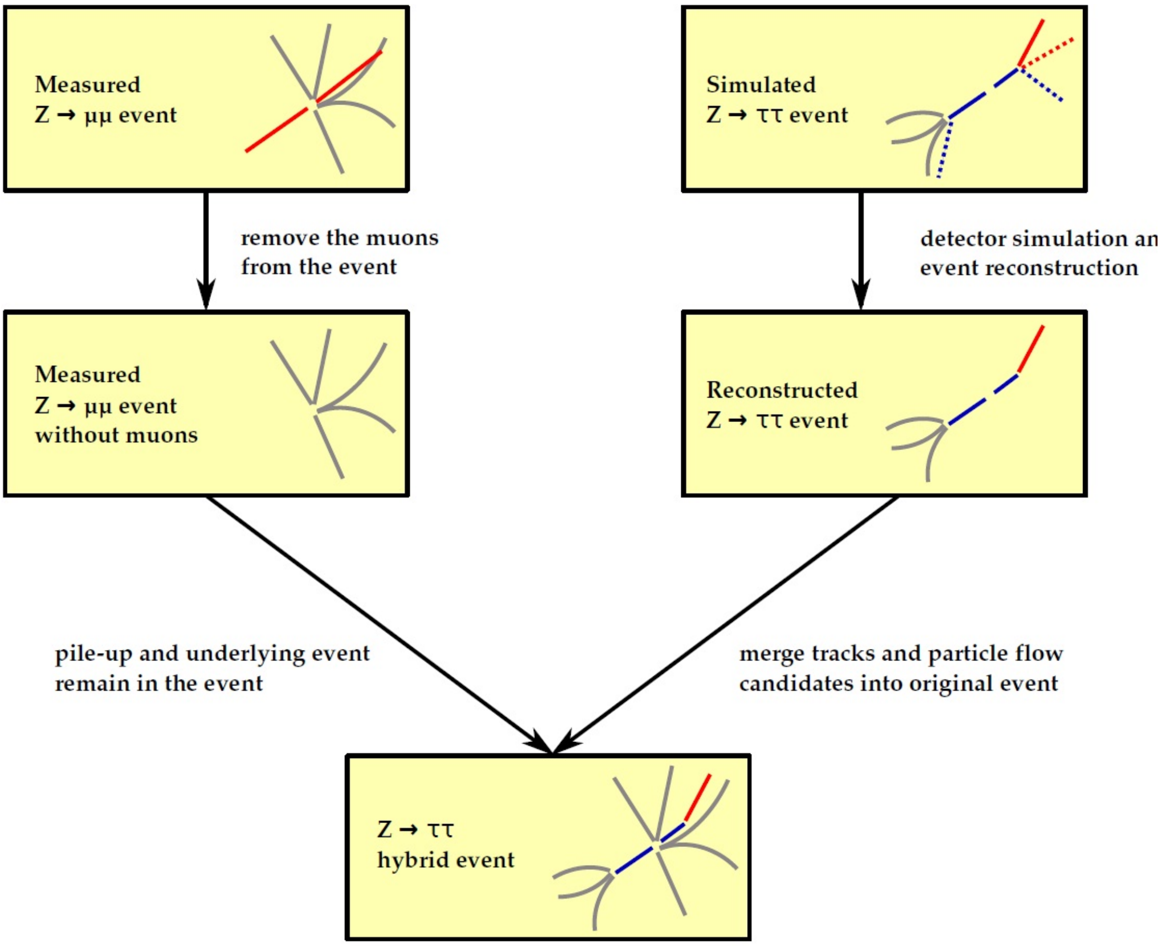

Figure 5.3: Illustration of the embedding procedure. Source: [50]

lower level objects or raw calorimeter information. However, information on energy deposits is included in the various particle flow candidates, so there is only minimal loss of information.

Since the muons are meant to come directly Z decays, only events in which the dimuon invariant mass is in the range $60\,\mathrm{GeV} \leq m_{\mu\mu} \leq 120\,\mathrm{GeV}$ are selected. The four-momentum of the Z boson as mother particle is reconstructed from the four-momenta of the muons. In the next step, the muons are removed from the event and replaced by τ leptons. Meanwhile a decay of the Z boson to a pair of τ leptons is generated in the simulation, such that the direction of decay of the Z boson is preserved in its rest frame. The vertex position of the new event at generator level is the same as the primary vertex of the selected muons. The given mother-daughter relation is exploited by the TAUOLA package to model the polarisation effects in the subsequent τ decay process correctly. This step also allows restrictions on the phase space of the ditau decay to gain statistical precision, in other words it is possible to select a specific decay mode or apply generator preselection based on the sum of the transverse momenta of the visible decay products.

The newly simulated ditau event are inserted to the original event in the place of the muons. The whole process is illustrated in figure 5.3. At the same time, the new track collection is merged in the same way to allow a consistent refit of the vertices in the event. Afterwards the particle flow reconstruction algorithms are run again with the merged collections as input resulting in a final hybrid ditau event.

5.9 TMVA and Boosted Decision Trees

The Toolkit for Multivariate Analysis (TMVA) [40] provides a machine learning environment, integrated in ROOT, for the processing and parallel evaluation of multivariate classification techniques and it is specifically designed to the needs of high energy physics applications. TMVA consists of object-oriented implementations in C++ for a number of multivariate methods and provides training, testing and performance evaluation algorithms and visualisation scripts. The multivariate training and testing is performed with datasets where the true event classification must be known, for example samples created by Monte Carlo simulation. As already mentioned, TMVA has been used to optimise physics objects reconstruction, like MET and jets. In the $H \to \tau\tau \to \mu\mu$ analysis we train boosted decision trees, with TMVA, in order to select Higgs signal.

A decision tree (BDT) is a binary tree structured classifier (figure 5.9). Starting from the root node, successive decision nodes are used to categorise the events as either signal or background. This forms a tree like structure, a decision tree, ending with "leaf nodes". The training, building or growing of a decision tree is the process that defines the splitting criteria for each node. At the root node the initial splitting criterion for the full training sample is determined. The split results in two subsets of training events that each go through the same algorithm of determining the next splitting iteration. This procedure is repeated until a certain node has reached either a minimum number of events, or a minimum or maximum signal purity. The purity of a sample is defined as follows:

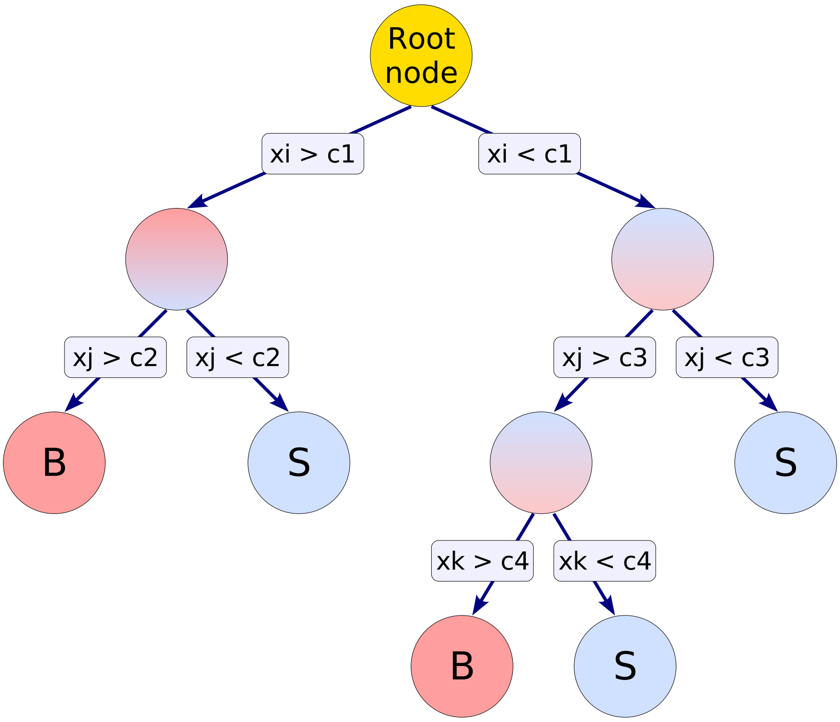

Figure 5.4: Illustration of the structure of a decision tree. Source: [40]

$$P = \frac{\sum_s W_s}{\sum_s W_s + \sum_b W_b} \tag{5.9.1}$$

where W_i is the weight of the i^{th} event, $\sum_s$ is the sum over signal events and $\sum_b$ the sum over background events. A variety of separation criteria can be configured to assess the performance of a variable and a specific cut requirement. The most common one is the Gini Index, defined as:

$$Gini = \left(\sum_{i=1}^{n} W_i \right) P\left(1 - P\right) \tag{5.9.2}$$

Where n is the number of events in the particular node. The value of $P(1 - P)$ is maximum when $P = 0.5$, in the case where signal and background are fully mixed. If the sample is pure signal or pure background $P(1 - P) = 0$. The training procedure selects the variable and cut value that optimises the increase in the Gini Index between the parent node and the sum of the indices of the two daughter nodes, weighted by their relative fraction of events. Or the:

$$Gini(parent) - [Gini(daughter1) + Gini(daughter2)] \tag{5.9.3}$$

has to be maximum. The cut values are optimised by scanning over the variable range.

The weakness of decision trees is their instability with respect to statistical fluctuations in the training sample from which the tree structure is derived. For example, if two input variables exhibit similar separation power, a fluctuation in the training sample may cause the tree growing algorithm to decide to split on one variable, when without that fluctuation the other variable could have been selected. In such a case the whole tree structure is altered below this node, possibly resulting also in a substantially different classifier response. This problem is overcome by constructing a forest of decision trees and classifying an event on a majority vote of the classifications done by each tree in the forest. All trees in the forest are derived from the same training sample, with the events being subsequently subjected to so-called boosting, a procedure which modifies their weights in the sample. Boosting increases the statistical stability of the classifier and typically also improves the separation performance compared to a single decision tree.

The idea behind the boosting is that the events that were misclassified during the training of a decision tree are given a higher event weight in the training of the following tree. Starting with the original event weights when training the first decision tree, the subsequent tree is trained using a modified event sample where the weights of previously misclassified events are multiplied by a common boost weight α. The boosting can be applied several times, typically between 100 and 500. The new type of classifier is called boosted decision tree (BDT).

The most common method of boosting, is the “AdaBoost”. The boost weight is derived from the misclassification rate, err, of the previous tree:

$$\alpha = \ln\left(\frac{1 - err}{err}\right) \tag{5.9.4}$$

If x_i is the tuple of input variables for the i_{th} event, then the result of an individual tree with index m, $\mathrm{H}_m(x_i)$, is $\mathrm{H}_m(x_i) = +1$ when the event is classified as signal and $\mathrm{H}(x) = -1$ if it is classified as background. y_i is 1 or -1, if the event is actually signal or background respectively. Let also $I = 1$ when $\mathrm{H}_m(x_i) \neq y_i$ and the event is misclassified, and $I = 0$ when the event is correctly classified, $\mathrm{H}_m(x_i) = y_i$. Then we define for the m_{th} the err_m as:

$$err_m \frac{\sum_{i=1}^{N} w_i I(h_m(x_i) \neq y_i)}{\sum_{i=1}^{N} w_i} \tag{5.9.5}$$

where the sum runs over the total number of events, N in the sample. The change of weight for the i^{th} event is:

$$w_i \to w_i \times e^{ln(\alpha_m) I(h_m(x_i) \neq y_i)}. \tag{5.9.6}$$

The weights of the entire event sample are then renormalised such that the sum of weights remains constant:

$$w_i \to \frac{w_i}{\sum_{i=1}^{N} w_i} \tag{5.9.7}$$

The boosted classification $\mathrm{H}_{\mathrm{Boost}}(x)$ for a given event is then just the weighted sum of the classification of the individual trees:

$$h_{\mathrm{Boost}}(x) = \sum_{m=1}^{M} \ln(\alpha_m) h_m(x) \tag{5.9.8}$$

where the sum is over all trees. Small values for $\mathrm{H}_{\mathrm{Boost}}(x)$ indicate a background-like event and vice versa.

5.10 Statistical and combination tools

The statistical analysis approach used in a modified-frequentist $\mathrm{CL_S}$ method, as recommended by the LHC HCG group [51, 52]. This approach is different from the ones used before for Higgs searches in LEP and Tevatron. LHC modified-frequentist limits are obtained with a test statistic based on a profile likelihood ratio.

In addition to parameters of interest such as the Higgs production cross section, the signal and background models will contain nuisance parameters whose values are not taken as known a priori but rather must be fitted from the data. Data may refer to observed data from a real experiment or pseudo-data of a simulated “toy” experiment. The values of kinematic variables measured in an experiment are presented as distributions, usually binned. The expected number of events in the i^{th} bin of the distribution can be written as:

$$n_i = \mu s_i + b_i \tag{5.10.1}$$

where μ is a parameter that determines the signal strength with $\mu = 0$ corresponding to the background-only hypothesis and $\mu = 1$ to the signal+background hypothesis. s_i and b_i are the mean contributions for signal and background, given by:

$$s_i = s_{tot} \int_{bin\, i} f_s(x; \boldsymbol{\theta_s}) dx \tag{5.10.2}$$

$$b_i = b_{tot} \int_{bin\, i} f_b(x; \boldsymbol{\theta_b}) dx \tag{5.10.3}$$

The functions $f_s(x; \boldsymbol{\theta_s})$ and $f_b(x; \boldsymbol{\theta_b})$ are the probability density functions (pdfs) of one variable x for signal and background events, and $\boldsymbol{\theta_s}$ and $\boldsymbol{\theta_b}$ represent the nuisance parameters that characterise the shapes of the pdfs. The normalisation of the background, b_{tot}, is also treated as a nuisance parameter. The signal normalisation, s_{tot}, is fixed to the value predicted by the nominal signal model. Hereafter $\boldsymbol{\theta}$ will be used to denote all of the nuisance parameters. Often additional distributions $p(\hat{\boldsymbol{\theta}} \mid \boldsymbol{\theta})$ are taken into account in a background enriched sample in order to further constrain the nuisance parameters.

The systematic uncertainties are treated as nuisance parameters with a pdf $\rho(\boldsymbol{\theta})$ and $\tilde{\boldsymbol{\theta}}$ the best estimate of the nuisance parameters. A common choice is the log-normal pdf:

$$\rho(\boldsymbol{\theta}) = \frac{1}{\sqrt{2\pi} \ln \kappa} exp \left(- \frac{\left(\ln(\boldsymbol{\theta}/\tilde{\boldsymbol{\theta}}) \right)^2}{2(\ln \kappa)^2} \right) \frac{\boldsymbol{\theta}}{\tilde{\boldsymbol{\theta}}} \tag{5.10.4}$$

where κ is a parameter specifying the width of the log-normal distribution.

The likelihood function is the product of Poison probabilities for all the bins in the distribution of the variable x:

$$\mathcal{L}(data \mid \mu, \boldsymbol{\theta}) = \prod_i \frac{(\mu s_i + b_i)^{n_i}}{n_i!} e^{-\mu s_i + b_i} p((\tilde{\boldsymbol{\theta}} \mid \boldsymbol{\theta}) \tag{5.10.5}$$

The formula can be adjusted for the case of continuous distributions. To compare the compatibility of the data with the background-only and signal+background hypothesis we construct the test statistic $\tilde{q}_\mu$ based on the profile likelihood ratio:

$$\tilde{q}_\mu = -2 \ln \frac{\mathcal{L}(data \mid \mu \hat{\boldsymbol{\theta}}_{\boldsymbol{\mu}})}{\mathcal{L}(data \mid \hat{\mu} \hat{\boldsymbol{\theta}})}, \tag{5.10.6}$$

with a constraint

$$0 \leq \hat{\mu} \leq \mu \tag{5.10.7}$$

where $\hat{\boldsymbol{\theta}}_{\boldsymbol{\mu}}$ refers to the conditional maximum likelihood estimators of $\boldsymbol{\theta}$, given the signal strength parameter μ and data. The pair of parameter estimators $\hat{\mu}$ and $\hat{\boldsymbol{\theta}}$ correspond to the global maximum of the likelihood. The lower constraint $0 \leq \hat{\mu}$ has a physical interpretation, it means that the signal rate cannot be negative. The upper constraint is set so that an upward fluctuation in the data such that $\hat{\mu} > \mu$ are not considered evidence against the signal hypothesis. When more channels are combined the test statistic is the product of all the individual test statistics.

The next step in calculating the exclusion limits is to calculate the observed value of the test statistic $\tilde{q}_\mu^{\rm obs}$ for the given signal strength modifier under test. Then the values of the nuisance parameters for both signal-plus-background and background-only hypothesis that describe the observed data the best, are determined. Using Monte Carlo generator toy pseudo-data are created in order to obtain the probability density functions $f(\tilde{q}_\mu \mid \mu, \hat{\boldsymbol{\theta}}_{\boldsymbol{\mu}}^{\mathbf{obs}})$ and $f(\tilde{q}_\mu \mid 0, \hat{\boldsymbol{\theta}}_{\mathbf{0}}^{\mathbf{obs}})$ for the signal-plus-background and background only hypothesis ($\mu = 0$) respectively. From the probability density functions, p-values associated with the actual observation of the signal-plus-background hypothesis and the background-only hypothesis can be defined:

$$p_\mu = P(\tilde{q}_\mu \geq \tilde{q}_\mu^{\rm obs} \mid \text{signal} + \text{background}) = \int_{\tilde{q}_\mu^{\rm obs}}^{\rm inf} f(\tilde{q}_\mu \mid \mu, \hat{\boldsymbol{\theta}}_{\boldsymbol{\mu}}^{\mathbf{obs}}) d\tilde{q}_\mu \tag{5.10.8}$$

$$1 - p_b = P(\tilde{q}_\mu \geq \tilde{q}_\mu^{\rm obs} \mid \text{background} - \text{only}) = \int_{\tilde{q}_0^{\rm obs}}^{\rm inf} f(\tilde{q}_\mu \mid 0, \hat{\boldsymbol{\theta}}_{\mathbf{0}}^{\mathbf{obs}}) d\tilde{q}_\mu \tag{5.10.9}$$

The $\mathrm{CL_s}(\mu)$ ratio can be calculated by:

$$CL_s(\mu) = \frac{p_\mu}{1 - p_b} \tag{5.10.10}$$

If for $\mu = 1$ $\mathrm{CL_s} \leq \alpha$ then the SM Higgs boson is excluded with $(1 - \alpha)$ $\mathrm{CL_s}$ confidence level (CL). In order to obtain the 95% CL upper limit, we try different values of μ until $\mathrm{CL_s}$ =0.05. The p-value when combining more channels is the sum of the p-values of all the channels.

The presence of signal is quantified by the background-only p-value, the probability for the background to fluctuate and give an excess of events as large or larger than the observed one. Usually the p-value is converted into the equivalent significance, Z, defined such that a Gaussian distributed variable found Z standard deviations above its mean has an upper-tail probability equal to the background-only p-value. That is:

$$Z = \Phi^{-1}(1 - p_b) \tag{5.10.11}$$

where Φ^{-1} is the inverse of the cumulative distribution of the standard Gaussian. For a signal process such as the Higgs boson, the particle physics community has tended to regard rejection of the background only hypothesis with a significance $Z = 5$ as an appropriate level to constitute a discovery. For excluding a signal hypothesis, a threshold of p-value=0.05, which corresponds to 95% CL is used. In this case $Z = 1.64$.

Chapter 6

Z boson production cross-section measurement in proton-proton collisions, in the $\mathrm{Z} \to \tau\tau \to \mu\mu$ decay channel.

6.1 Introduction

The process of the Z[1] boson production followed by Z decays into a pair of τ leptons plays an important role in the physics program of the LHC. This channel provides a number of tests to the Standard Model such as the decay properties of the τ lepton, predictions for the Z boson production cross section in proton-proton collisions, and the lepton universality. In addition it provides an experimental sample for the commissioning of τ lepton triggers and identification algorithms. The $\mathrm{Z} \to \tau\tau$ process is a major source of irreducible background to the search for neutral Higgs Bosons. Therefore the study of this Z decay channel is essential.

In the current document, the analysis performed in the channel $\mathrm{Z} \to \tau\tau$ where both τ leptons decay leptonically into muons, is described ($\tau^- \to \mu^- \nu_\tau \bar{\nu}_\mu$ and charge conjugate decay mode). The study is used to measure the process cross section $\sigma(pp \to \mathrm{Z}) \cdot \mathrm{Br}(\mathrm{Z} \to \tau\tau)$ and also serves for the commissioning of the search for neutral Higgs boson decays to τ leptons in the dimuon channel. The topology of the final states is very similar in $\mathrm{Z} \to \tau\tau$ and $\mathrm{H} \to \tau\tau$. In both cases the events are characterised by two muons and missing transverse energy due to the neutrinos. Three more $\mathrm{Z} \to \tau\tau$ final states, defined by the decay modes of τ lepton pairs, have been studied by other groups in the CMS collaboration. These are :

- $\mu + \tau_{\mathrm{jet}}$,
- $e + \tau_{\mathrm{jet}}$,
- $e + \mu$.

The dimuon channel has been combined with the above channels for the final measurement of the Z boson production cross section in CMS.

---

[1] What is actually measured is the Drell Yan (DY) process. Apart from the Z boson there is contribution by a virtual photon γ^*. This contribution is quite small however, therefore it is not taken into account separately. Hereafter, mention to the Z boson is equivalent to the whole DY process.

6.2 CMS and simulation datasets

This analysis is performed on proton-proton collision data collected with the CMS detector in 2010 at a centre-of-mass energy 7 TeV. The analysed data corresponds to an integrated luminosity of 36.1 pb^{-1}.

The full 2010 CMS dataset certified for physics analysis was used taken with single μ trigger as described in chapter 4.

The samples used for the Monte Carlo (MC) simulation studies are listed in table 6.1 along with the corresponding cross section values [53]. The MC samples are produced with PYTHIA [54] event generator. For the Drell-Yan processes, $Z/\gamma^* \to \mu\mu, \tau\tau$, the vector boson production is generated within the POWHEG [55, 56] framework. The polarisation properties of τ lepton decays are modelled with the TAUOLA package [57]. The simulated events are weighted according to the cross section of the process σ, the integrated luminosity $\mathcal{L}$ that corresponds to the data and the number of processed MC events $N_{\text{processed}}$. The weights are given by the following formula:

$$w_{\text{MC}} = \frac{\sigma \cdot \mathcal{L} \cdot \epsilon_{\text{MC}}}{N_{\text{processed}}}, \tag{6.2.1}$$

where ϵ_{MC} is the MC filter efficiency.

MC process	$\sigma \cdot \epsilon_{MC}$, pb
$Z/\gamma^* \to \tau\tau$ mass 10-20 GeV	3892
$Z/\gamma^* \to \tau\tau$ mass$>$ 20 GeV	1666
$Z/\gamma^* \to \mu\mu$ mass 10-20 GeV	3892
$Z/\gamma^* \to \mu\mu$ mass$>$ 20 GeV	1666
QCD $p_{\text{T}} > 20$	84679
W$T \to \mu\nu$	10438
W$T \to \tau\nu$	10438
$\text{t}\bar{\text{t}}$	165

Table 6.1: Monte Carlo samples used in the analysis. The corresponding cross sections multiplied by Monte Carlo filter efficiencies are presented in the second column.

6.3 Analysis procedures

6.3.1 Preselection

The first selection applied to the events is the high level trigger (HLT) selection. In this analysis the unprescaled single muon HLT with the lowest p_{T} threshold is used. Trigger selection details are given in chapter 4. In addition we selected muons reconstructed by the PF algorithm (5.5).

The analysis starts with a preselection of $Z \to \tau\tau \to \mu\mu$ events by imposing the following requirements:

- Each event is required to contain two muons of opposite charge.

- The transverse momenta of the leading and sub-leading muons must be greater than 19 GeV/c and 10 GeV/c respectively
- The pseudorapidity of at least one muon must be within the trigger acceptance: $-2.1 < \eta < 2.1$. No cut is applied on the pseudorapidity of the other muon.
- The PF relative isolation is required to be less than 0.1 for both muons.
- A cut is applied on the missing transverse energy (MET) at MET $<$ 50 GeV. This requirement suppresses $\mathrm{t\bar{t}}$ and W production events with leptons in the final state.
- The azimuthal angle between the muon momenta must be $\Delta\Phi(\mu^+, \mu^-) > 2$ rad. This selection rejects QCD events with opposite sign muon pairs originating from the same quarkonia decays or from the same decay chain of heavy flavor mesons, $B \to \bar{D} + \mu^+\nu_\mu \to \mu^-\bar{\nu}_\mu + X$ and charge conjugate mode.

Figure 6.1 shows the distribution of the muon pair invariant mass after the preselection. In table 6.2 the numbers of events observed in the data and expected by the Monte Carlo simulation are presented. The numbers listed here are obtained after applying corrections to the Monte Carlo samples, which will be discussed later in this chapter.

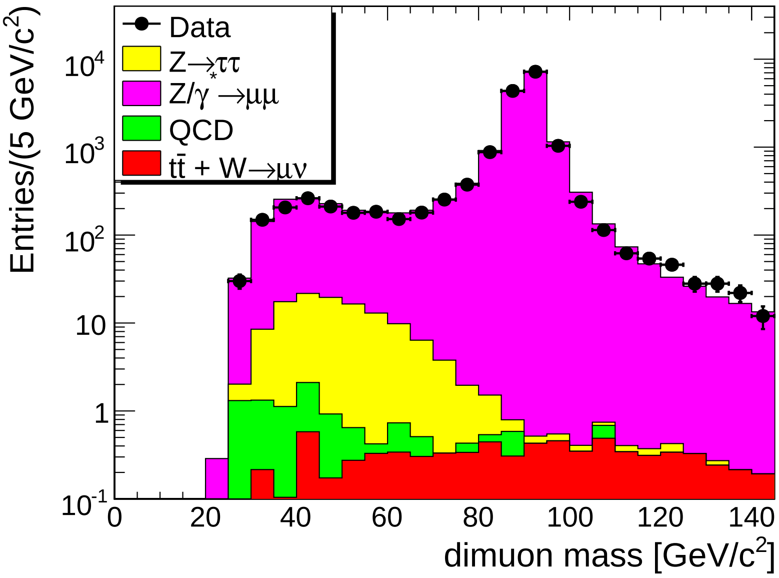

Figure 6.1: Dimuon mass distribution in data and Monte Carlo samples after preselection.

After the preselection the event sample is still dominated by background and the signal-over-background ratio is extremely small, $S/B = 6.9 \cdot 10^{-3}$ for the entire mass range and $S/B = 6.8 \cdot 10^{-2}$ in the signal region of visible dimuon mass $m_{\mu\mu} < 70$ GeV/c^2. The main background contribution is the Drell-Yan process, $\mathrm{Z}/\gamma^* \to \mu\mu$.

6.3.2 Likelihood selection

In order to enhance the signal-over-background ratio, further suppression of the background is necessary. For this purpose we introduce a multivariate analysis technique based on the likelihood ratio method [58]. The likelihood discriminant is constructed to distinguish between two event classes, the $\mathrm{Z} \to \tau\tau \to \mu\mu$ signal and the $\mathrm{Z}/\gamma^* \to \mu\mu$ background. For each event,

Analysed sample	Number of events full mass range	 $m_{\mu\mu} < 70$ GeV/c^2
$\mathrm{Z} \to \tau\tau$	113	106
$\mathrm{Z}/\gamma^* \to \mu\mu$	16447	1547
QCD	7.44	6.78
$\mathrm{W} \to \mu\nu$	1.27	0.77
$\mathrm{W} \to \tau\nu$	0.13	0.13
$\mathrm{t\bar{t}}$	7.71	1.43
Total MC	16577	1662
Data	16316	1553

Table 6.2: Number of events observed in data and expected by Monte Carlo simulations after preselection.

the probability for the event to belong to each of the two event classes is calculated using the probability density functions $f(j, x_i)$ of a number m of discriminating variables x_i:

$$\mathrm{Prob}(j) = \prod_{i=1}^{m} f(j, x_i), \tag{6.3.1}$$

where the index j denotes one of the two event classes, $j = \mathrm{Z} \to \tau\tau$ or $\mathrm{Z}/\gamma^* \to \mu\mu$. The likelihood discriminant then is:

$$L(j) = \frac{\mathrm{Prob}(j)}{\sum_{k=1}^{2} \mathrm{Prob}(k)}, \tag{6.3.2}$$

where in the denominator, the sum runs over the event classes considered, $k = \mathrm{Z} \to \tau\tau$, $\mathrm{Z}/\gamma^* \to \mu\mu$.

The variables used to construct the signal likelihood and discriminate between the $\mathrm{Z} \to \tau\tau \to \mu\mu$ signal and $\mathrm{Z}/\gamma^* \to \mu\mu$ background are the following:

- the ratio of the transverse momentum of the dimuon system over the scalar sum of positive and negative muon momenta, $p_{\mathrm{T}}(2\mu)/\sum p_{\mathrm{T}}(\mu)$
- the muon distance of closest approach (DCA) significance, DCASig(2μ)
- the pseudorapidity of the dimuon system, $\eta(2\mu)$
- the polar angle between the positive muon momentum and the missing transverse energy, $\Delta\Phi(\mu^+, MET)$. Let us note here for completeness that the two variables, $\Delta\Phi(\mu^+, MET)$ and $\Delta\Phi(\mu^-, MET)$, are strongly anti-correlated, but possess identical discriminating power between the $\mathrm{Z} \to \tau\tau \to \mu\mu$ signal and $\mathrm{Z}/\gamma^* \to \mu\mu$ background. Therefore only one of these variables is included in the likelihood discriminant

The variables are chosen such that there is as little dependence on pile-up effects as possible. Three out of the four variables used, $p_{\mathrm{T}}(2\mu)/\sum p_{\mathrm{T}}(\mu)$, DCASig($2\mu$), $\eta(2\mu)$, are based solely on the muon kinematics therefore are quite insensitive to pile-up related systematic effects. The fourth variable, $\Delta\Phi(\mu^+, MET)$, involves missing transverse energy and is therefore expected to be pile-up dependent. Another pile-up dependent variable is the muon isolation variable (equation 5.5.1), used in the event preselection stage. The effect of the pile-up is studied and taken into account by using $Z \to \tau_\mu \tau_\mu$ embedding sample (section 5.8).

All the variables have excellent discriminating power between signal and background events, as it is evident in figure 6.2 where the shapes of chosen variables are compared between $Z \to \tau\tau \to \mu\mu$ and $Z/\gamma^* \to \mu\mu$.

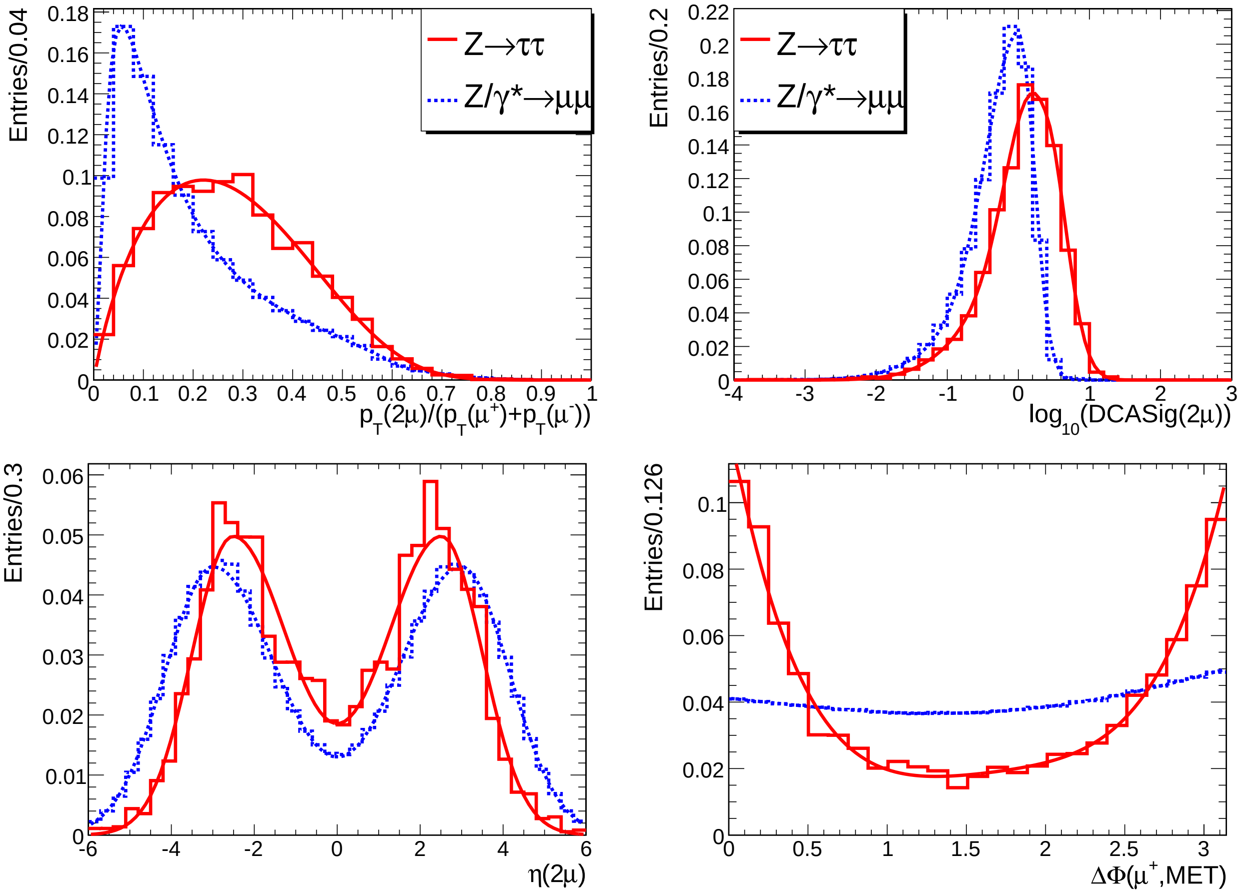

Figure 6.2: Distributions of discriminating variables used to construct the likelihood discriminant. The $Z \to \tau\tau$ signal (solid lines) is compared to the Drell-Yan background $Z/\gamma^* \to \mu\mu$ (dashed lines). The distributions are fitted and the parametric function is the then inserted into the likelihood calculation. Top left: the ratio of the transverse momentum of the dimuon system to the scalar sum of muon transverse momenta. Top right: common logarithm of the muon DCA significance. Bottom left: pseudo-rapidity of the dimuon system. Bottom right: polar angle between the positive muon momentum and the missing transverse energy. The distributions are normalised to unit area.

Figure 6.3 shows the distributions of the discriminating variables for data and Monte Carlo samples. Good agreement in the shapes of the distributions is observed, therefore no bias is introduced in the likelihood discriminant.

The distributions of the signal likelihood in data and Monte Carlo samples are presented in Figure 6.4.

The final event sample is selected by applying a cut on the likelihood discriminant. An event is accepted if $L(\text{sig.}) > 0.874$. This cut is optimised to provide maximum signal over background ratio. Figure 6.5 shows the dimuon invariant mass distributions for the data and

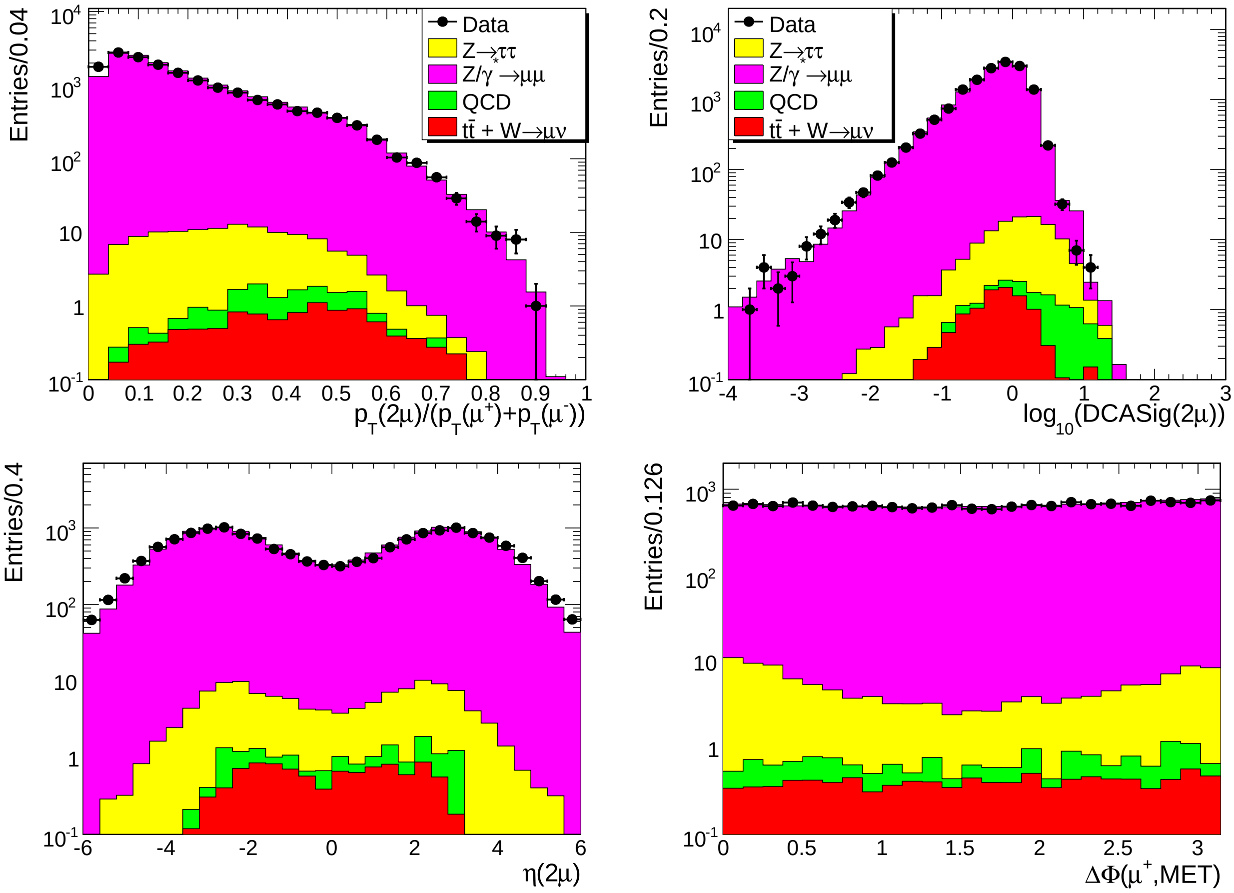

Figure 6.3: Distributions of discriminating variables used to construct the likelihood discriminant. The data (points) is compared to the MC simulations (filled histograms). Top left:the ratio of the transverse momentum of the dimuon system to the scalar sum of muon transverse momenta. Top right: common logarithm of the muon DCA significance. Bottom left: pseudo-rapidity of the dimuon system. Bottom right: polar angle between the positive muon momentum and the missing transverse energy.

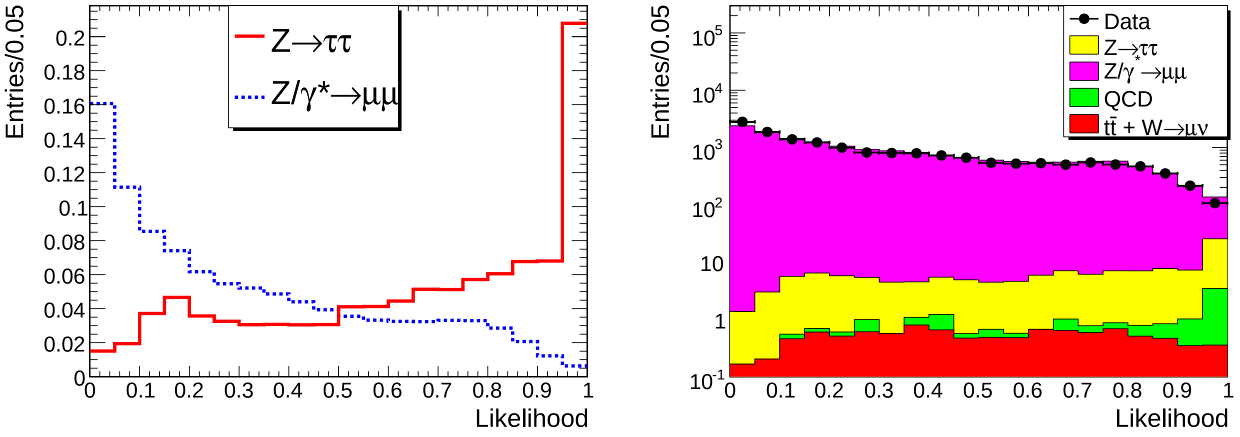

Figure 6.4: Distribution of the likelihood discriminant. Left plot: comparison between the $Z/\gamma^* \to \mu\mu$ (dashed line) and $Z \to \tau\tau$ (solid line) MC samples. The distributions are normalised to unit area. Right plot: comparison between data (dots) and MC samples (filled histograms).

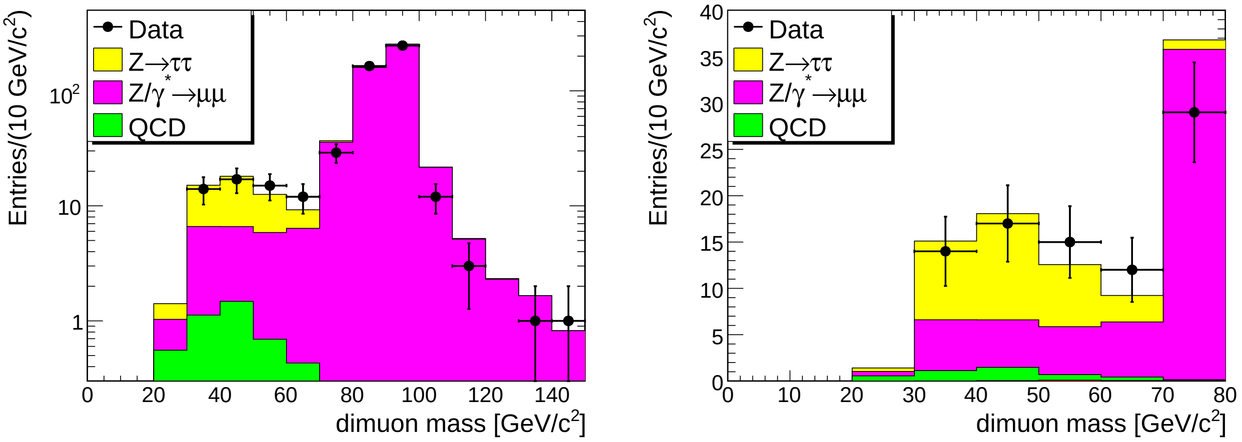

Figure 6.5: Dimuon invariant mass distributions of the data and the Monte Carlo simulation after the likelihood selection. The left plot shows the distributions on logarithmic scale. Right plot: a close up into the signal region ($m_{\mu\mu} < 80$ GeV/c^2) on linear scale.

the Monte Carlo samples after the likelihood selection. The numbers of selected events in data and Monte Carlo samples are presented in table 6.3. These numbers are obtained after applying corrections to the Monte Carlo samples as described later in this chapter. After

Analysed sample	Number of events full mass range	 $m_{\mu\mu} < 70$ GeV/c^2
Z → $\tau\tau$	31.4	29.9
Z/γ^* → $\mu\mu$	504	22.1
QCD	4.35	4.07
W → $\mu\nu, \tau\nu$	0.20	0.063
t$\bar{\text{t}}$	0.59	0.145
Total MC	540	56.3
Data	517	58
$S/\sqrt{B}$	1.39	5.8
$S/\sqrt{S+B}$	1.35	4.0

Table 6.3: Number of events observed in data and predicted by Monte Carlo simulations after the likelihood selection. The last two rows show the values of $S/\sqrt{B}$ and $S/\sqrt{S+B}$, where B denotes the expected number of background events and S the expected number of signal events in the final selected sample.

the final likelihood selection, the Z → $\tau\tau$ → $\mu\mu$ signal is established with signal significance of $S/\sqrt{B}$=6, where $S(B)$ is the expected number of signal (background) events in the final selected sample, respectively.

p_T bin	MC Efficiency	Data Efficiency	Correction Factor
10−15	$94.98^{+0.43}_{-0.45}$	$99.71^{+0.04}_{-0.04}$	0.953 ± 0.004
15−20	$97.97^{+0.49}_{-0.52}$	$99.74^{+0.05}_{-0.05}$	0.982 ± 0.005
20−30	$99.17^{+0.23}_{-0.27}$	$99.76^{+0.02}_{-0.02}$	0.994 ± 0.003
30−40	$99.63^{+0.10}_{-0.12}$	$99.89^{+0.02}_{-0.03}$	0.997 ± 0.002
40−60	$99.74^{+0.07}_{-0.08}$	$99.88^{+0.02}_{-0.03}$	1.000 ± 0.002
60−100	$99.22^{+0.44}_{-0.72}$	$99.81^{+0.04}_{-0.05}$	0.994 ± 0.006

Table 6.4: Muon identification efficiencies in bins of muon p_T. The results of the tag-and-probe studies with the $\mathrm{Z} \to \tau\tau$ and $\Upsilon(1S, 2S, 3S) \to \mu\mu$ samples are combined for the first three p_T bins. For the remaining bins the results obtained with the $\mathrm{Z} \to \mu\mu$ sample are quoted.

6.3.3 Efficiency corrections

A number of correction factors are applied to the Monte Carlo samples in order to compensate for differences in the trigger, the muon identification and the isolation efficiencies found between the data and the Monte Carlo simulations. The efficiencies are measured using the tag-and-probe method (sections 4.3 and 5.5.1) applied to a sample of muon pairs coming from Z boson and $\Upsilon(1S, 2S, 3S)$.

Trigger efficiency corrections

For the analysis of the Monte Carlo samples, the simulation of the trigger response is not used. Instead, in order to account for trigger inefficiencies, each Monte Carlo event is assigned a weight:

$$w_\mathrm{trig} = 1 - \left(1 - \epsilon(p_\mathrm{T}^{+})\right) \cdot \left(1 - \epsilon(p_\mathrm{T}^{-})\right), \tag{6.3.3}$$

where ϵ is the p_T dependent single muon trigger efficiency (section 4.3) and p_T^{+} and p_T^{-} are the transverse momenta of the positive and negative muons, respectively. To take the effect of the run-dependent trigger selection into account, the Monte Carlo samples are divided into three parts, according to the fraction of luminosity in each of the three data taking periods (table 4.1). In every subsample the events are weighted according to the efficiency of the corresponding high level trigger (HLT):

- HLT with single muon p_T threshold 9 GeV/c for the Monte Carlo subsamples with a fraction of 22% (7.5 pb^{-1})
- HLT with single muon p_T threshold 11 GeV/c for the subsamples with a fraction of 27% (9.5 pb^{-1})
- HLT with single muon p_T threshold 15 GeV/c for the subsamples with a fraction of 51% (19.1 pb^{-1})

The p_T dependent efficiencies along with the correction factors applied to the MC samples and the assigned systematic errors are detailed in table 6.4.

Muon isolation efficiency

As illustrated in figure 6.6 on the left, the spectra of the relative muon isolation variable, defined by equation 5.5.1, are different for the $\mathrm{Z} \to \tau\tau \to \mu\mu$ and the $\mathrm{Z} \to \mu\mu$ sample.

The difference is explained by a softer spectrum of muons coming from the τ lepton decays, leading on average to larger values of the relative muon isolation variable in the $Z \to \tau\tau \to \mu\mu$ sample. Therefore, a calibration is performed for the absolute muon isolation variable, which is the numerator of equation 5.5.1. Its distribution is expected to be identical in shape for $Z \to \tau\tau \to \mu\mu$ and $Z \to \mu\mu$ events, as shown in figure 6.6 on the right.

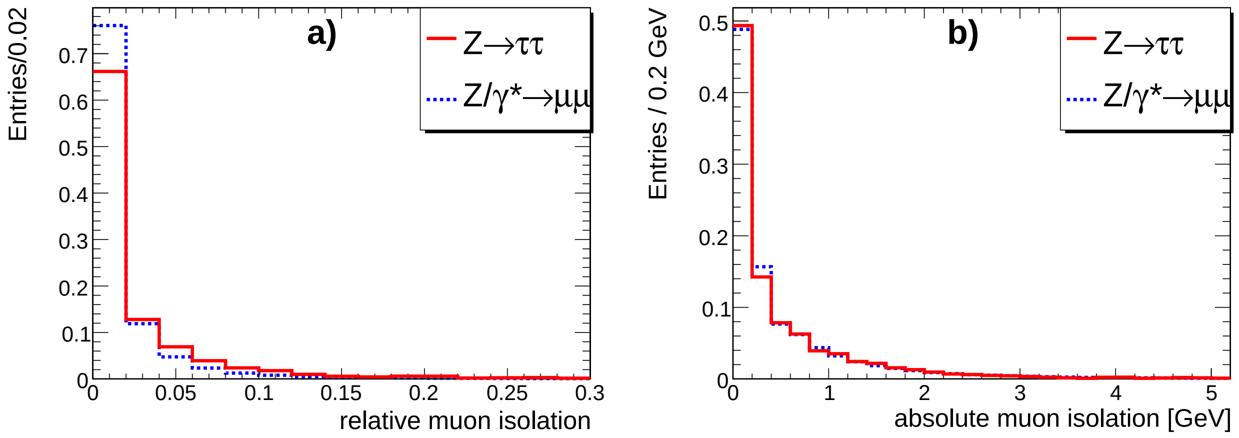

Figure 6.6: Distributions of the relative (left) and absolute (right) muon isolation variables in the Z/ $\to \mu\mu$ (dashed lines) and $Z \to \tau\tau \to \mu\mu$ (solid lines) Monte Carlo samples. The distributions are normalised to unit area.

The spectra of the absolute isolation variable reconstructed using the tag-and-probe technique on the data and the $Z/\gamma^* \to \mu\mu$ MC samples are compared in figure 6.7. To account for the differences between data and Monte Carlo simulations, bin by bin corrections are applied to all Monte Carlo samples, where simulated muons are expected to be isolated[2] in order to bring the simulated distributions of the absolute isolation variable to consistency with the data.

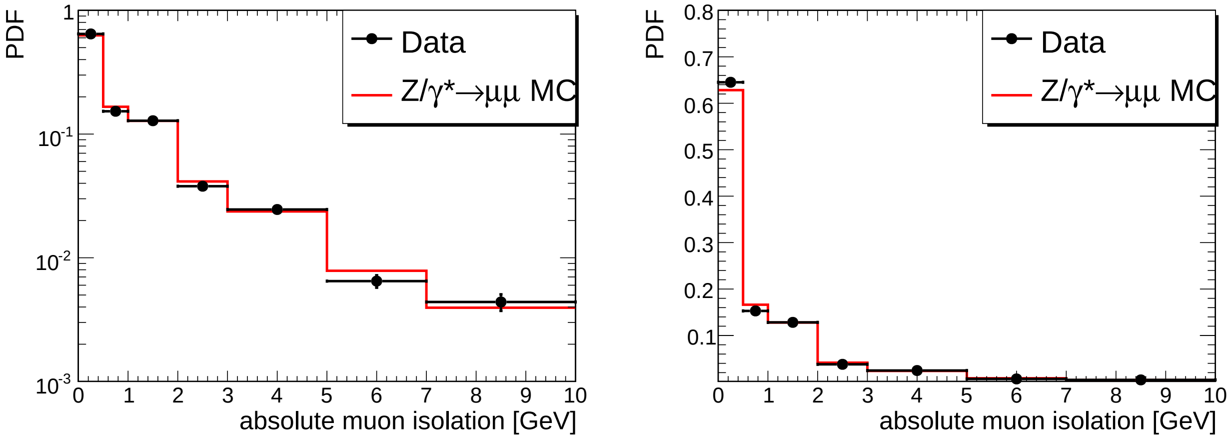

Figure 6.7: Distribution of the absolute muon isolation variable in Monte Carlo (solid lines) and data (dots) shown in logarithmic (left plot) and linear (right plot) scales. The distributions are reconstructed with the tag-and-probe technique applied on the $Z/\gamma^* \to \mu\mu$ sample and normalised to unit area.

---

[2] In all Monte Carlo samples reported in table 7.1 except for the QCD MC muons, are produced in decays of gauge bosons $Z/\gamma*$ and W and therefore expected to be isolated.

6.3.4 Background estimation

Another important part of any analysis is the background estimation. In the $Z \to \tau\tau \to \mu\mu$ analysis four background contributions are taken into account:

- Drell-Yan muon pair production, $Z/\gamma^* \to \mu\mu$
- QCD processes in which muon pairs emerge.
- $t\bar{t}$
- $W \to \mu\nu, \tau\nu$

The Drell-Yan processes are by far the dominant background source. The contribution from QCD events is also significant. The two major background contributions are estimated in data driven ways. The other two background sources are less significant. The $t\bar{t}$ and $W \to \mu\nu, \tau\nu$ are estimated from the Monte Carlo simulation taking into account theory prediction NLO for cross section.

Drell-Yan background

For the DY background estimation, we exploit the definite τ decay length information. The muons coming from τ decays tend to be more displaced with respect to the primary vertex than the muons coming from direct Z decays. A variable that describes this signature is the Distance of Closest Approach (DCA) significance. This variable is used as a discriminating variable in the likelihood method. Figure 6.8 shows the correlation matrix of the discriminating variables, that enter the construction of the likelihood discriminant. The correlations between all the variables are small, therefore we proceed assuming that the DCA is uncorrelated to the other variables.

A new likelihood discriminant is constructed for each event in the same way as in the final selection, described in section 6.3.2 including all the same variables apart from the muon DCA significance. This new likelihood from now on is referred to as "reduced likelihood" (L_{red}). Figure 6.9 shows the reduced likelihood distribution in the signal region, $m_{\mu\mu} < 70\,\mathrm{GeV/c^2}$.

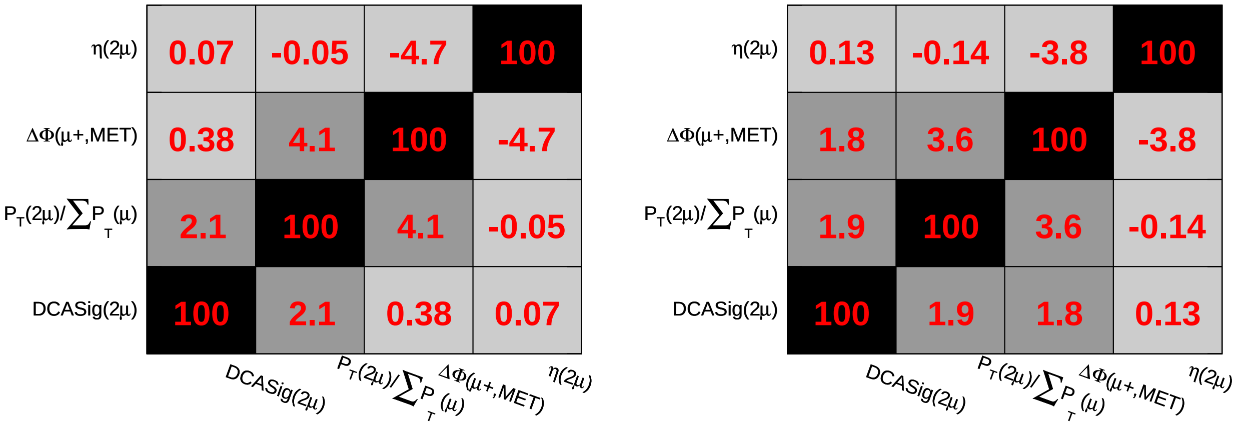

	$DCASig(2\mu)$	$P_T(2\mu)/\sum P_T(\mu)$	$\Delta\Phi(\mu+,MET)$	$\eta(2\mu)$
$\eta(2\mu)$	0.07	-0.05	-4.7	100
$\Delta\Phi(\mu+,MET)$	0.38	4.1	100	-4.7
$P_T(2\mu)/\sum P_T(\mu)$	2.1	100	4.1	-0.05
$DCASig(2\mu)$	100	2.1	0.38	0.07

	$DCASig(2\mu)$	$P_T(2\mu)/\sum P_T(\mu)$	$\Delta\Phi(\mu+,MET)$	$\eta(2\mu)$
$\eta(2\mu)$	0.13	-0.14	-3.8	100
$\Delta\Phi(\mu+,MET)$	1.8	3.6	100	-3.8
$P_T(2\mu)/\sum P_T(\mu)$	1.9	100	3.6	-0.14
$DCASig(2\mu)$	100	1.9	1.8	0.13

Figure 6.8: Correlation matrix in of the discriminating variables used to construct the likelihood discriminant in data (left plot) and Monte Carlo (right plot). The values are shown in percent.

The idea for the background estimation is to parametrise the DCA distribution for signal and background separately and then fit the data as a superposition of these two templates.

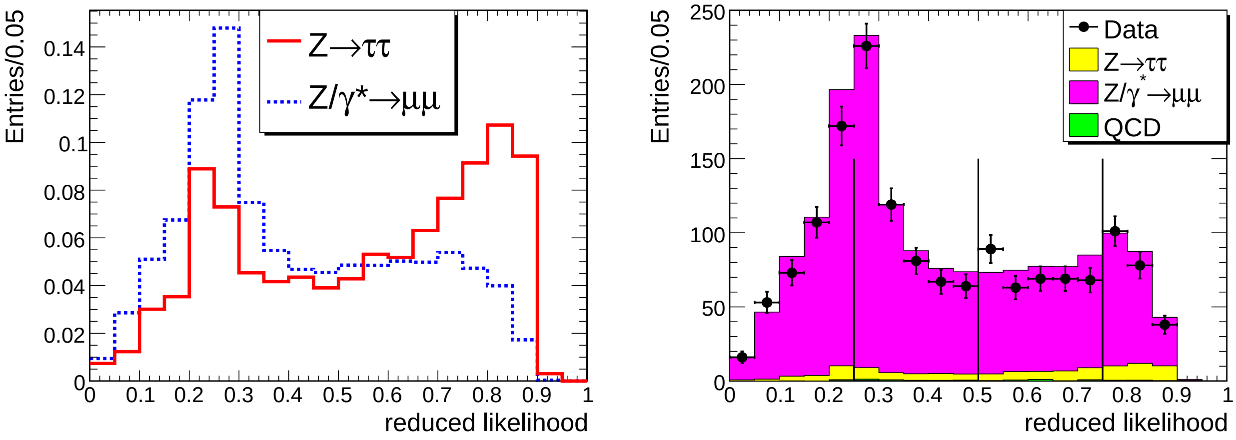

Figure 6.9: Spectra of the reduced likelihood for events in the signal region, $m_{\mu\mu} < 70\,\mathrm{GeV/c^2}$. The left plot shows distributions in the $\mathrm{Z}/\gamma^* \to \mu\mu$ and $\mathrm{Z} \to \tau\tau \to \mu\mu$ Monte Carlo sample. The distributions are normalised to unit area. The distributions of the reduced likelihood in data and Monte Carlo samples are compared in the right plot. The vertical lines show separate L_{red} bins for which correction factors are computed for the $\mathrm{Z}/\gamma^* \to \mu\mu$ Monte Carlo sample.

The contributions from other backgrounds are subtracted in this procedure. In order to obtain a template for the DY background we need to fit the DCA in a background enhanced sample. The distribution of the reduced likelihood in the sample of events with $m_{\mu\mu} < 70\,\mathrm{GeV/c^2}$ is divided into four bins:

1. [0.0-0.25]
2. [0.25-0.5]
3. [0.5-0.75] and
4. [0.75-1.0]

In the first bin of L_{red}, [0.0-0.25], the Drell-Yan background largely prevails over the $\mathrm{Z} \to \tau\tau$ signal, therefore it is used to parameterise the muon DCA significance distribution for the $\mathrm{Z}/\gamma^* \to \mu\mu$ sample. In order to obtain a template for the $\mathrm{Z} \to \tau\tau$ signal, the shape of the DCA significance is taken from the Monte Carlo simulation.

Given that the muon DCA significance is not correlated with the variables used to construct the reduced likelihood, the muon DCA significance distributions are fitted in bins of the reduced likelihood as a superposition of the two templates, the $\mathrm{Z} \to \mu\mu$ template parameterised with the muon DCA significance distribution in the first bin of L_{red} and the $\mathrm{Z} \to \tau\tau$ template provided by MC simulations. With this procedure, the absolute normalisations for Drell-Yan background and $\mathrm{Z} \to \tau\tau \to \mu\mu$ signal are extracted as a function of L_{red}. The results of the fit for each L_{red} bin are presented in figure 6.10.

The extracted absolute normalisations are used to derive the L_{red} dependent correction factors that are then applied to the $\mathrm{Z}/\gamma^* \to \mu\mu$ Monte Carlo sample. The correction factors are shown in figure 6.11. As a cross check, we compare the absolute normalisations derived from the data with the ones derived from the MC. The ratio of the two normalisations for the $\mathrm{Z} \to \tau\tau$ signal is also shown in figure 6.11. Within statistical errors, the ratios are consistent with unity. The number of $\mathrm{Z} \to \mu\mu$ estimated events is:

$$N(Z \to \mu\mu) = 20.1 \pm 1.3. \tag{6.3.4}$$

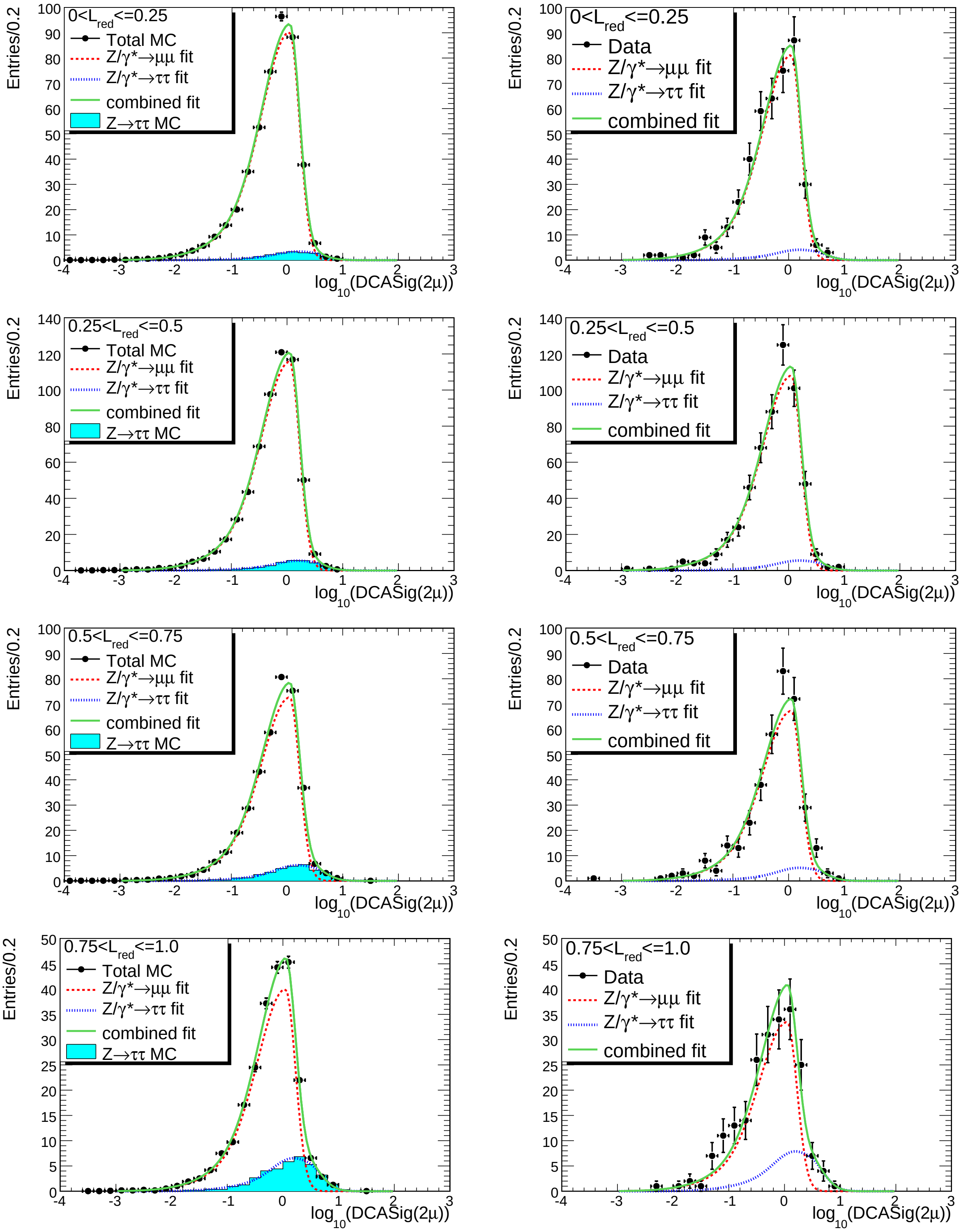

Figure 6.10: Distributions of the muon DCA significance fitted with the Z $\rightarrow \mu\mu$ and Z $\rightarrow \tau\tau$ templates in Monte Carlo (left plots) and data (right plots) for the four L_{red} bins.

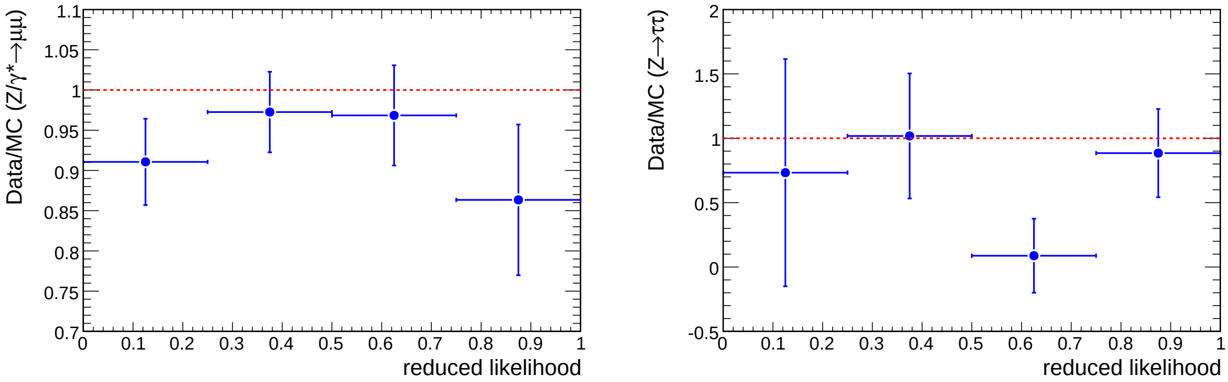

Figure 6.11: The L_{red} dependent ratio of the absolute normalisation obtained from the fit to the muon DCA significance distribution in the data to the one obtained from an analogous fit to the Monte Carlo sample. The left plot shows the ratio for the Z $\rightarrow \mu\mu$ events, the right plot for Z $\rightarrow \tau\tau \rightarrow \mu\mu$ events. The ratios presented in the left plot are used as correction factors for the estimation of the Drell-Yan background.

QCD background

The QCD background contribution is estimated exploiting a sample of the same sign dimuon events and the fact that the isolation variable is independent of the net charge of the muon pair. Figure 6.12 shows the distribution of the relative muon isolation for the simulated opposite sign (OS) and same sign (SS) QCD samples, after the preselection in section 6.3.1. The agreement between the two distribution is very good and there is no evidence for correlation. Indeed, opposite sign muon pairs coming either from the same quarkonia decays or originating from the same decay chain of heavy flavor mesons, $B \rightarrow \bar{D} + \mu^+\nu_\mu \rightarrow \mu^-\bar{\nu}_\mu + X$ and charge conjugate mode, would result to a correlation between the net charge of the muon pair and the isolation, however the cut applied to the the polar angle between positive and negative muon momenta, $\Delta\Phi(\mu^+, \mu^-) > 2.0$ rad rejects such events completely.

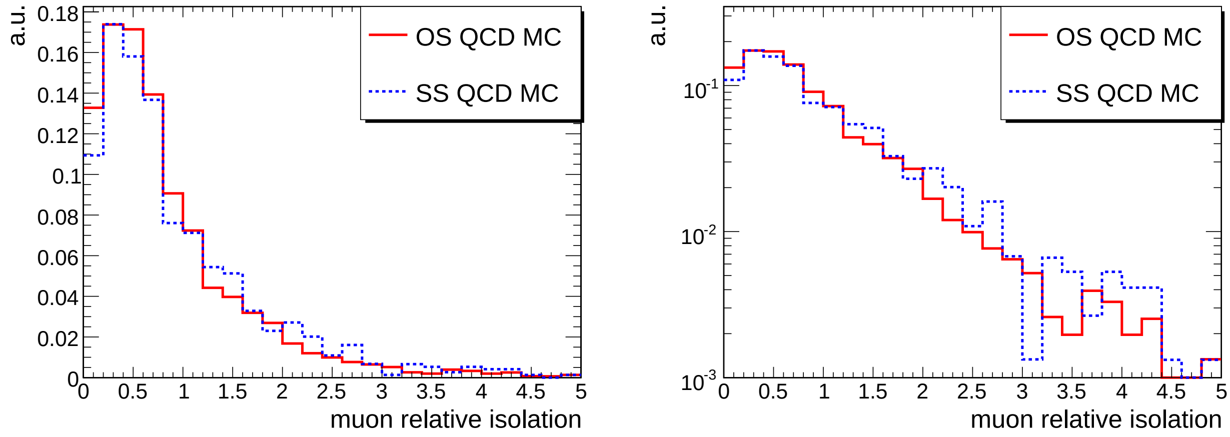

Figure 6.12: Relative muon isolation variable in the QCD OS (solid lines) and SS (dashed lines) Monte Carlo samples, in linear and logarithmic scale.

By inverting the cut on the relative isolation variables of both muons we create pure QCD event samples. Since the isolation is not correlated with the net charge of the muon pair, the ratio OS/SS of QCD events, for the reverse isolation cut sample should be equal to the ratio

OS/SS in the direct isolation cut sample. We want to estimate the QCD events in the OS sample after direct isolation cut, because this is our signal selection. According to the above we can obtain this number by the following formula:

$$N_{QCD}^{\mathrm{OS}} = N_{QCD}^{\mathrm{SS}} \cdot \frac{\mathrm{OS}}{\mathrm{SS}}, \tag{6.3.5}$$

where N_{QCD}^{OS} is the number of QCD events contributing to the final selected sample, N_{QCD}^{SS} is the number of QCD events in the same sign muon sample selected with the same criteria as the opposite sign sample and OS/SS is the ratio of the OS to the SS QCD events evaluated in the pure QCD control samples obtained by inverting the cut on the relative isolation. The inverse isolation cuts used in this analysis are :

- $\mathrm{Iso}_{\mu,1}^{\mathrm{PF}} > 0.5$
- $\mathrm{Iso}_{\mu,2}^{\mathrm{PF}} > 0.5$.

Figure 6.13 shows the distribution of the reconstructed invariant mass of muon pairs in three samples:

- OS muon sample with the inverse isolation cut
- SS muon sample with the inverse isolation cut
- SS muon sample with the direct isolation cut.

Good agreement is observed in the distributions of events between data and Monte Carlo prediction. The numbers of events selected in each of the three samples are presented in table 6.5. No data events are selected in the SS muon sample obtained with the direct isolation cut. Hence an upper limit at 95% C.L. is set on the number of data events in this sample. Table 6.5 also reports the purity of QCD events in the three samples.

Sample	OS, inverse isolation	SS, inverse isolation	SS, direct isolation
QCD Monte Carlo	1671 ± 14	993 ± 11	2.34 ± 0.53
Total Monte Carlo	1673 ± 14	994 ± 11	2.41 ± 0.55
Data	1601 ± 40	976 ± 31	< 3 at 95% C.L
Purity of QCD events	$> 99\%$	$> 99\%$	95.5%

Table 6.5: Number of events in the OS muon sample with the inverse isolation cut (second column), SS muon sample with the direct isolation cut (third column), SS muon sample with the direct isolation (fourth column).

The estimated ratios between opposite sign and same sign QCD events, for data and Monte Carlo samples, are reported in table 6.6. Within statistical errors the OS/SS ratios determined in data and Monte Carlo samples are consistent. An upper 95% C.L. limit on the number of SS QCD events in the selected sample with isolated muons is calculated as using Poisson statistics:

$$N_{\mathrm{QCD}}^{\mathrm{SS}} < N(95\%\ \mathrm{C.L.})_{\mathrm{Data}}^{\mathrm{SS}} - N_{\mathrm{non-QCD\,MC}}^{\mathrm{SS}} = 3 - 0.07 = 2.93, \tag{6.3.6}$$

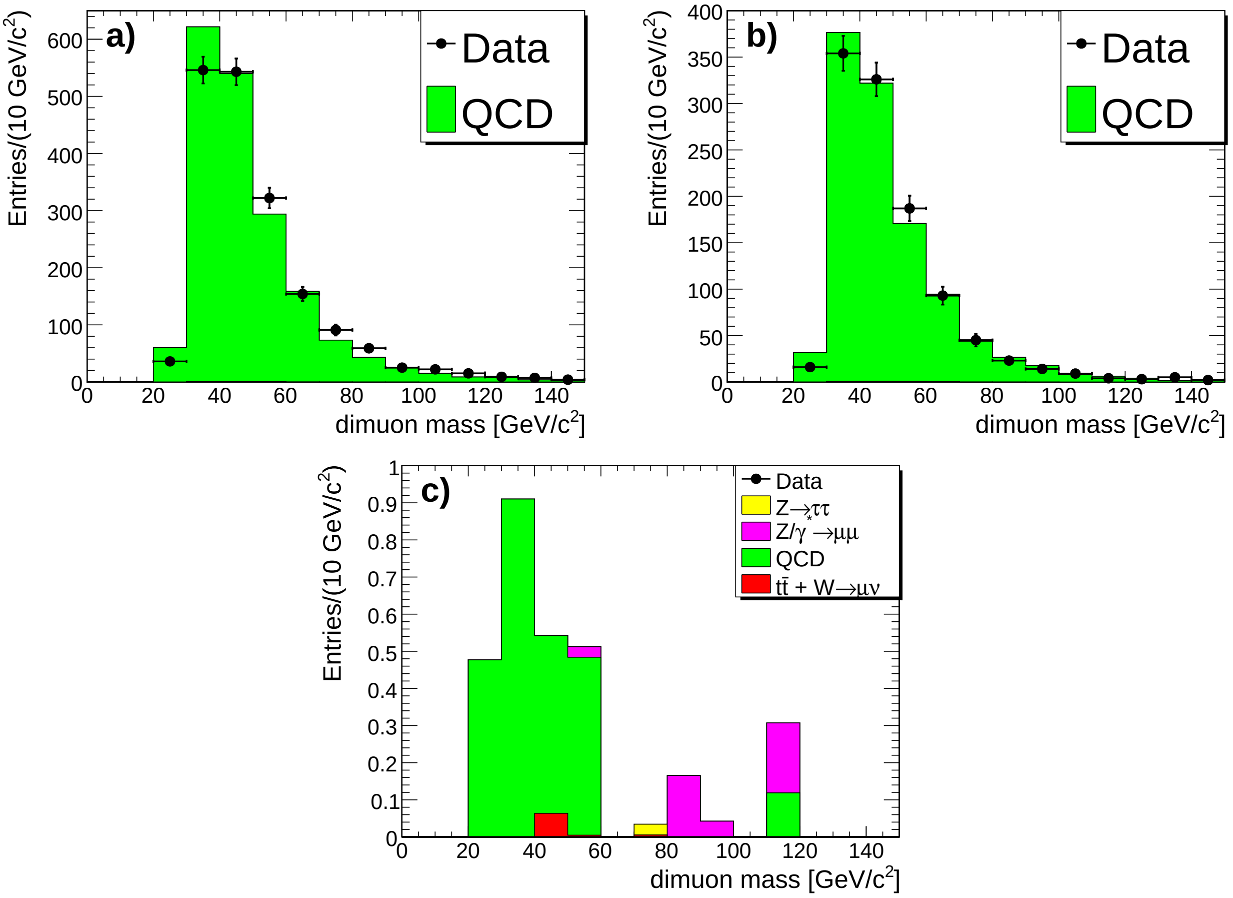

Figure 6.13: Distribution of the dimuon mass in the OS muon sample with the inverse isolation cut (top left), SS muon sample with the inverse isolation cut (top right) and SS muon sample with the direct isolation cut (bottom middle).

Sample	OS/SS
inverse isolation (Monte Carlo)	1.68 ± 0.02 (stat.)
inverse isolation (Data)	1.64 ± 0.07 (stat.)
direct isolation (Monte Carlo)	1.7 ± 0.5 (stat.)

Table 6.6: The OS/SS ratios evaluated in data and Monte Carlo samples.

Source	Method	Value
p_μ scale	Variation of p_μ by 1%	2%
μ trigger efficiency	Tag-and-probe method	0.3%
μ-id and isolation cut efficiency	Tag-and-probe method	1%
Likelihood selection efficiency	$\mathrm{Z} \rightarrow \tau_\mu\tau_\mu$ embedded sample	2%
Parton distribution functions		2%
Luminosity		4%

Table 6.7: Systematic errors on the signal acceptance taken into account in the analysis. The first column shows the source of the uncertainty, the second the method used to estimate it and in the last column its value. The tag-and-probe was performed with the $\mathrm{Z} \rightarrow \mu\mu$ and $\Upsilon(1S, 2S, 3S) \rightarrow \mu\mu$ samples

where $N_{\mathrm{non-QCD\,MC}}$ is the contribution of non-QCD events to the SS sample of isolated muons. This contribution is estimated from MC simulations. The upper limit on the number of OS QCD events in the final sample is

$$N(\mathrm{no\,syst.})^{\mathrm{OS}}_{\mathrm{QCD}} < N(95\%\ \mathrm{C.L.})^{\mathrm{SS}} \cdot \frac{\mathrm{OS}}{\mathrm{SS}}|_{\mathrm{Data}} = 2.93 \cdot 1.64 = 4.8. \qquad (6.3.7)$$

A convolution of this number with the systematic error, defined as the difference between the OS/SS ratio estimated in data (1.64) and the same sign muon Monte Carlo sample selected with the direct isolation cut (1.7), yields:

$$N(\mathrm{syst.})^{\mathrm{OS}}_{\mathrm{QCD}} < 5\ (95\%\ \mathrm{C.L.}). \qquad (6.3.8)$$

6.3.5 Systematic studies

The systematic uncertainties on the signal acceptance taken into account in the Z production cross section measurement are summarised in table 6.7.

Muon momentum scale

The impact of the μ momentum scale uncertainty on the acceptance for dimuon events is evaluated by varying the momentum of the muons by 1%.

Muon trigger efficiency

The systematic effects due to uncertainties on the muon trigger efficiency are studied using the tag-and-probe technique described in section 6.3.3. The measured muon trigger efficiencies are varied within the statistical errors in each bin of muon p_T. The resulting uncertainties, originating from individual p_T bins, are summed up quadratically yielding a systematic uncertainty on the measured cross section of 0.3%.

Muon identification and isolation cut efficiency

The systematic errors associated with the muon identification and isolation selection efficiency are estimated in a way similar to the evaluation of the trigger related systematic

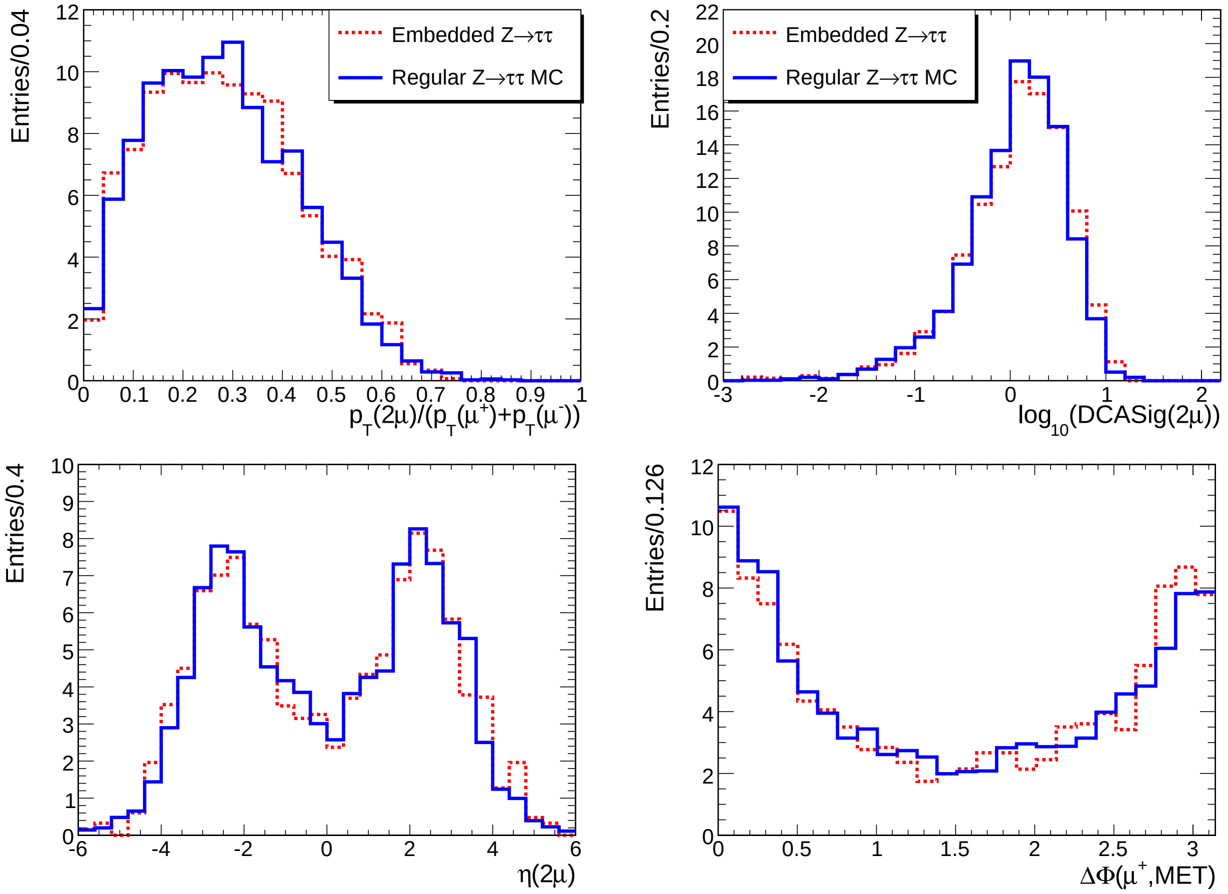

Figure 6.14: Distribution of the variables combined in the likelihood discriminant for the regular Z → $\tau\tau$ MC sample (solid lines) and for the embedded Z → $\tau_\mu\tau_\mu$ sample (points): the ratio of dimuon p_T to the scalar sum of muon p_T (top left), the muon DCA significance (top right), the dimuon pseudorapidity (bottom left), the polar angle between momentum of the positive muon and the missing transverse energy (bottom right).

uncertainty. The efficiency correction factors in each bin of muon p_T and absolute isolation variable, $\mathrm{Iso}^{\mathrm{PF}}_{\mathrm{abs}}$, are varied within the estimated errors and the uncertainties originating from each individual p_T and $\mathrm{Iso}^{\mathrm{PF}}_{\mathrm{abs}}$ bin are added in quadrature. The corresponding global correction factor is 0.963 ± 0.009 and the associated systematic uncertainty is 1%.

Likelihood selection

We have estimated a correction to the likelihood selection efficiency using the Z → $\tau_\mu\tau_\mu$ embedded sample.

Figure 6.14 compares the distributions of the variables combined in the likelihood discriminant for the regular Z → $\tau\tau$ MC and the embedded Z → $\tau_\mu\tau_\mu$ samples. The distributions in the embedded sample are normalised to the number of events in the regular MC sample. Good agreement is found in shapes of the distributions between the two samples.

Figure 6.15 presents the distributions of the likelihood discriminant and the dimuon invariant mass after the likelihood selection. The difference in the likelihood selection efficiency between the regular POWHEG Monte Carlo and the embedded sample is 2%. The correction factor applied to the likelihood selection efficiency of the signal events is 1.019 ± 0.025.

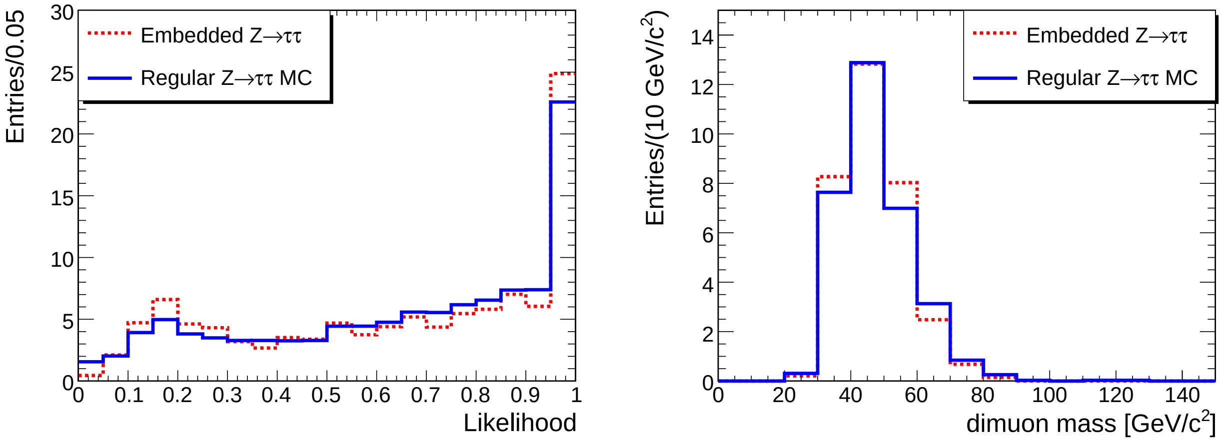

Figure 6.15: Distribution of the likelihood discriminant (left) and dimuon invariant mass in the final selected sample in the regular Z $\to \tau\tau$ MC (solid lines) and embedded Z $\to \tau_\mu\tau_\mu$ (dots) samples.

6.4 Cross section measurement

After the selection procedure the final data sample is determined. The number of events in this sample is N_{Data}. If we subtract from this the number of background events, N_{Bkgd}, estimated with data driven methods and MC, then we obtain the number of Z $\to \tau\tau \to \mu\mu$ candidates. This measurement, allows us to calculate the topological cross section $\sigma(pp \to Z) \cdot \text{Br}(Z \to \tau\tau)$ using the formula:

$$\sigma(pp \to Z) \cdot \text{Br}(Z \to \tau\tau) = \frac{N_{\text{Data}} - N_{\text{Bkgd}}}{\mathcal{A} \cdot \epsilon \cdot [\text{Br}(\tau \to \mu\nu_\mu\nu_\tau)]^2 \cdot \mathcal{L}}, \tag{6.4.1}$$

where $\mathcal{A}$ is the acceptance of signal events, ϵ is the signal selection efficiency, $\text{Br}(\tau \to \mu\nu_\mu\nu_\tau)$ is the branching ratio of the $\tau \to \mu\nu_\mu\nu_\tau$ decay mode, and $\mathcal{L}$ is the integrated luminosity. The detector acceptance of signal events $\mathcal{A}$ is determined with MC samples in the ditau mass range $60\,\text{GeV/c}^2 < m_{\tau\tau} < 120\,\text{GeV/c}^2$. The signal efficiency for the MC in this mass range is 98.5%. The numbers listed in table 6.8, correspond to the signal region, defined as the range $m_{\mu\mu} < 70\,\text{GeV/c}^2$ of the visible dimuon mass spectrum. Using the equation 6.4.1, we find the Z production cross section to be:

$$\sigma(pp \to Z) \cdot \text{Br}(Z \to \tau\tau) = 1.14 \pm 0.27\,(\text{stat.}) \pm 0.04\,(\text{syst.}) \pm 0.05\,(\text{lumi.})\ \text{nb}, \tag{6.4.2}$$

The measured value is compatible with the NNLO prediction, 0.97±0.05 nb [59], as well as previous CMS measurements, $\sigma(pp \to ZX) \cdot \text{Br}(Z \to l^+l^-) = 0.931 \pm 0.026\,(\text{stat.}) \pm 0.023\,(\text{syst.}) \pm 0.102\,(\text{lumi.})$ nb, performed using the Z $\to \mu\mu$ and Z $\to ee$ channels [60].

6.5 Combination with other Z $\to \tau\tau$ final states

The measurement of the inclusive Z cross section in the $\mu\mu$ final state was combined with three more channels: $\mu + \tau_{had}$, $e + \tau_{had}$ and $e + \mu$. In order to estimate the number of signal events, a fit was performed using the visible mass shapes from the simulation, except for the QCD and Z→ l^-l^+ backgrounds, which were obtained from the data. The dimuon visible mass distribution after the fit is performed is shown in figure 6.5. The values of the cross section

Ingredient	Method of determination	Value
$Z/\gamma^* \to \mu\mu$ background	data-driven	20.1±1.3
QCD background	data-driven	2.5±2.5 (<5 95% C.L.)
$t\bar{t}$ background	Monte Carlo	0.15±0.03
$W \to \mu\nu$ background	Monte Carlo	0.06±0.06
Data events		58
Acceptance	Monte Carlo	0.163
Selection efficiency	Monte Carlo, $Z \to \tau_\mu\tau_\mu$ embedding	0.173

Table 6.8: The numbers used in equation 6.4.1 for the cross section measurement: estimated background events, observed data events, signal acceptance and selection efficiency. All numbers in this table correspond to dilepton mass $m_{\mu\mu} < 70\,\mathrm{GeV/c^2}$.

Final State	$\sigma(pp \to ZX) \cdot \mathrm{Br}(Z \to \tau^-\tau^+)$	stat.	syst.	lumi.	τ_{had} ID
$\mu\tau_{had}$	0.83	0.07	0.04	0.03	0.19
$e\tau_{had}$	0.94	0.11	0.03	0.04	0.22
$e\mu$	0.99	0.12	0.06	0.04	
$\mu\mu$	1.14	0.27	0.04	0.05	

Table 6.9: The measured value of the cross section from the four final states considered. The statistical, systematic and luminosity uncertainties are given. The uncertainty to the τ_{had} reconstruction and identification efficiency, τ_{had} ID is shown in the last column were relevant.

measured in the four final states considered, are shown in table 6.9. The uncertainties shown are due to statistical, systematic, integrated luminosity and τ identification uncertainties. The cross section values for all channels, as in the case of the $\mu\mu$ final state alone, are compatible with the theoretical prediction [59], and with the previous CMS measurements [60].

A simultaneous fit is performed to obtain the cross section and a scale factor for the τ_{had} efficiency, defined as the ratio of the efficiency in the data to that in the simulation. The result of the fit is shown in figure 6.17 on the left, where the likelihood contours for the best estimates of the cross section and the τ_{had} efficiency scale factor are shown. In addition to the 1σ deviation contour, the contours for which the likelihood L is reduced by $2\Delta \ln L = 2.30$ and 6.18 compared to the maximum value are also shown, corresponding to a coverage of 68% and 95% in the two parameter space, respectively.

The value of the cross section extracted from the fit is:

$$\sigma(pp \to ZX) \cdot \mathrm{Br}(Z \to \tau^-\tau^+) = 1.00 \pm 0.05\,(\mathrm{stat.}) \pm 0.08\,(\mathrm{system.}) \pm 0.04\,(\mathrm{lumi.})\,\mathrm{nb} \quad (6.5.1)$$

which is compatible with the individual measurements. The comparison is presented in 6.17 on the right. The hadronic decays introduce an extra uncertainty because of the τ_{had} identification, therefore the value of the cross section is dominated by the dilepton final states.

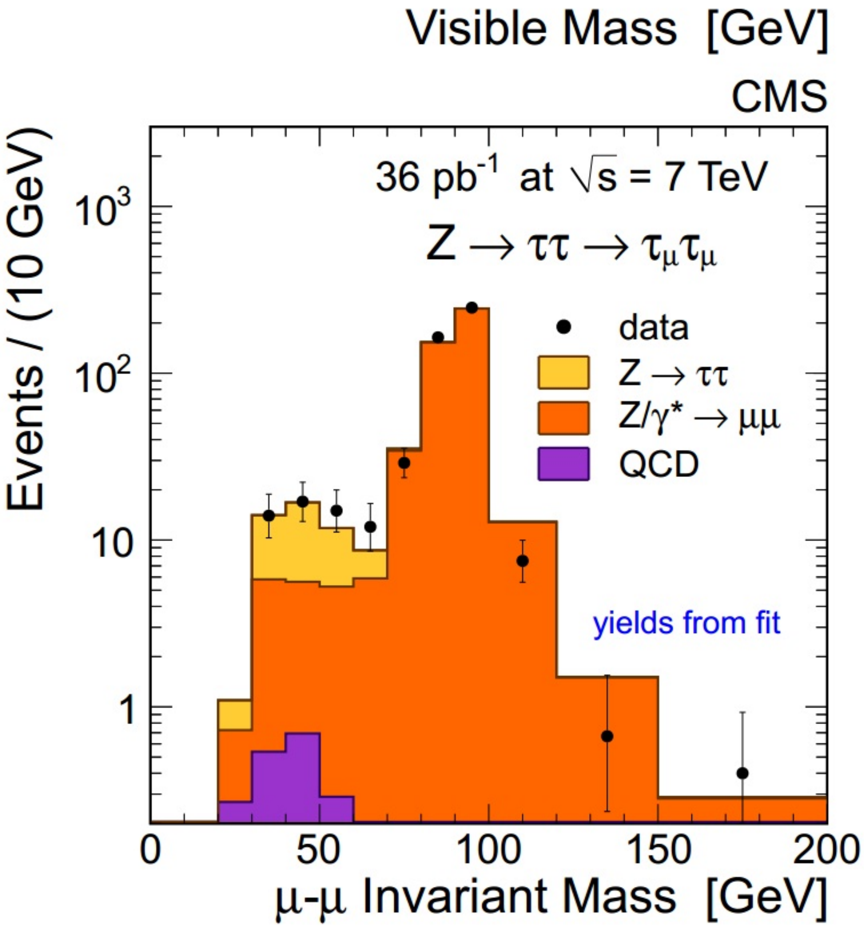

Figure 6.16: Visible mass distribution of the final dimuon sample, after the fit to estimate the number of signal events is performed.

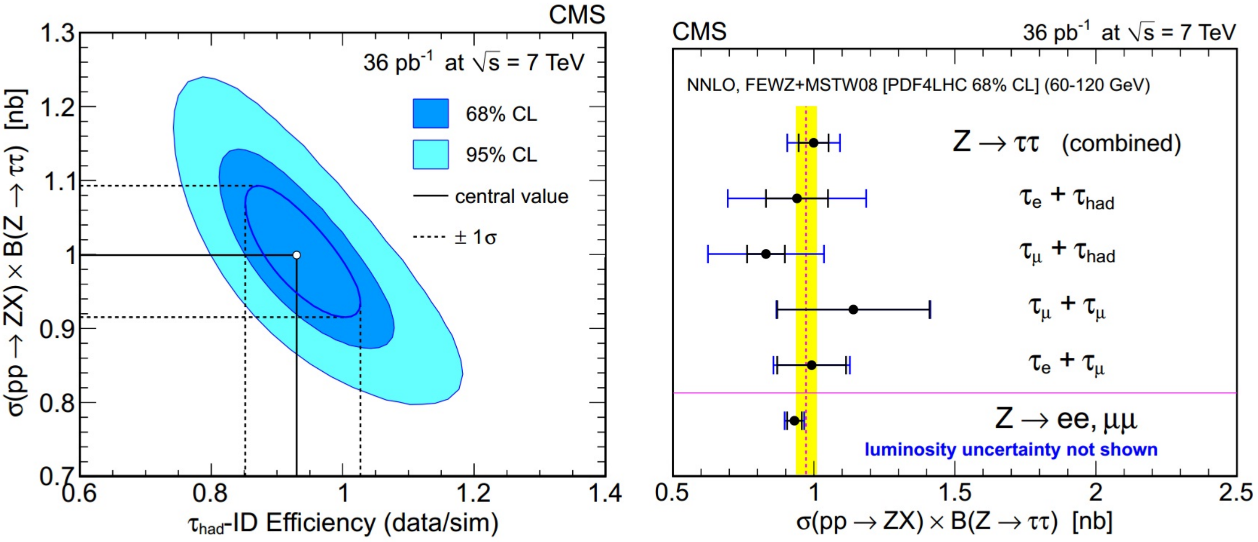

Figure 6.17: The likelihood contours for the joint parameter estimation of the cross section and the τ identification (left). The fitted central values, solid lines, and their estimated 1σ uncertainties, dashed lines, are also shown. The measured Z $\rightarrow \tau\tau$ cross sections in all the different final states and the combined measurement are compared to the theoretical prediction and previous CMS measurements (right). The measurements are performed in the ditau invariant mass range of $60 < M_{\tau\tau} < 120$ GeV

Chapter 7

Neutral Higgs boson searches in the $\mathrm{H} \rightarrow \tau\tau \rightarrow \mu\mu$ decay channel.

7.1 Introduction

As discussed in chapter 2 the Yukawa coupling of the Higgs field to fermions generates the fermion masses. This aspect of the theory is tested directly in the search of the Higgs boson decaying to τ pairs. The $\mathrm{H} \rightarrow \tau\tau$ decay channel has a large branching fraction in the lower Higgs mass region and a relatively clean signature. In addition, the branching fraction of the Higgs decay into τ pairs is enhanced in the MSSM, making this channel sensitive to new physics.

In the current document the analysis searching for neutral Higgs Bosons in the $\mathrm{H} \rightarrow \tau\tau \rightarrow \mu\mu$ channel is presented. The main challenges in the $\mathrm{H} \rightarrow \tau\tau \rightarrow \mu\mu$ decay mode is the large dimuon background $\mathrm{Z}/\gamma^* \rightarrow \mu\mu$, and the small topological branching fraction of the $\tau\tau \rightarrow \mu\mu$ decay, which is BR $\sim$ 2.9%. The analysis described here is performed on 17 fb^{-1} of data recorded in 2011 and 2012 at 7 and 8 TeV respectively by the CMS detector.

During 2011 and 2012, the data-taking conditions have been changing rapidly. With the instantaneous luminosity of the LHC increasing, the number of proton-proton interactions per bunch-crossing, the so called pile-up (PU) (section 5.1), has been increasing as well. The mean number of PU interactions in 2011 was 9.5 and in 2012 was 19. Corresponding distributions are shown in figure 7.1. This effect is very hard to reproduce in the simulation. As a consequence, a difference in the number of reconstructed primary vertices between the data and the Monte Carlo samples is observed. In order to represent in the Monte Carlo simulation the number of PU events as observed in experimental data, the simulated events are reweighted as a function of the simulated PU interactions. The PU affects the particle isolation and therefore in the analysis of 2011 and 2012 data we use "$\Delta\beta$-corrected" isolation as discussed in section 7.3.3. The contribution of PU events also results in distortion of the MET distribution and affects the jet reconstruction. As already mentioned in section 5.4.1, multivariate methods are used for the MET and the jets identification to mitigate the effect of the PU events. It is very important for the analysis that the MET is properly described, since it is used in the SVFit algorithm and the multivariate event selection, discussed later in this chapter. Therefore special corrections have to be applied in order to ensure correct modelling of the MET distribution. In this analysis two different approaches for the recoil correction are used where appropriate (section 7.3.2).

7.2 Simulation datasets

The main Standard Model Higgs production mechanisms have been simulated with the NLO program POWHEG [55, 56] interfaced to the PYTHIA event generator to account for

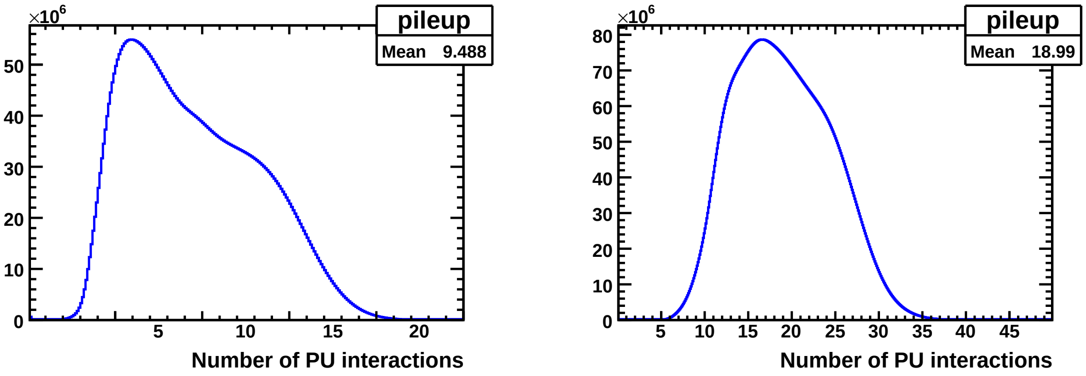

Figure 7.1: The distribution of the number of PU interactions in 2011(left) and 2012(right) events.

QCD initial radiation. The processes of the SM Higgs production in association with W and Z bosons and with top quark pairs are simulated with PYTHIA. The MSSM Higgs production was also simulated with PYTHIA including estimates of the QCD initial and final state radiation.

The background processes W or Z plus jets and the inclusive $t\bar{t}$ were simulated with MADGRAPH [61] event generator implemented into PYTHIA. The QCD background as well as the diboson production processes were simulated with PYTHIA.

For all the signal and background samples including τ leptons, the subsequent decay of the τ is simulated with the TAUOLA software package, taking into account the polarisation properties of the τ [57].

Table 7.1 summarises the Monte Carlo simulation processes taken into account in this analysis and the generator used to create them. In the last column the cross section of each process is given.

7.3 Analysis Procedures

7.3.1 Jets in the Higgs analysis

The analysis searching for neutral Higgs bosons uses jet related variables, in order to classify the events according the Higgs production mechanism. The distribution of the number of all jets and b-tagged jets is shown in figure 7.2. The jets are reconstructed from particle-flow objects using the anti-k_t algorithm with a cone of radius R=0.5. The BDT identification (section 5.3.2) is applied in order to reject the jets coming from PU contribution. Corrections are applied to the jet energy scale as described in [62]. The corrected jets are selected to have a transverse momentum greater than 30 GeV/c within the pseudorapidity range $|\eta| < 4.5$. The jets are also required to be separated by a distance larger than ΔR(jet-muon) > 0.5 from the muons. For b-tagged jets the p_{T} threshold is $p_{\mathrm{T}} > 20$ GeV/c, while the allowed pseudorapidity range is $|\eta| < 2.4$.

7.3.2 Missing transverse energy in the Higgs analysis

In the high PU environment of the LHC in 2011 and 2012, a more sophisticated method of estimating the MET is required. The current analysis, makes use of the missing transverse momentum determined with a boosted decision tree, MVA MET (5.4.1). However, this doesn't correctly simulate the effect of the PU. Inaccurate modelling of the experimental conditions leads to a disagreement between data and simulation in the MET distribution.

Process	Generator	$\sigma \cdot \epsilon_{\mathrm{MC}}$ [pb] 7 TeV	$\sigma \cdot \epsilon_{\mathrm{MC}}$ [pb] 8 TeV
Backgrounds			
Z + Jets, $m_{ll} > 50\mathrm{GeV/c^2}$	MADGRAPH	3048	3504
Z + Jets, $m_{ll} < 50\mathrm{GeV/c^2}$	MADGRAPH	9530	11050
QCD p_T >15 GeV/c^2	PYTHIA	84679	134680
W + Jets	MADGRAPH	31314	36257
$\mathrm{t\bar{t}}$	MADGRAPH	158	225
WW	PYTHIA	44	57
ZZ	PYTHIA	5.9	8.3
WZ	PYTHIA	18.2	32
Signal SM, Higgs mass hypothesis 110-145 GeV/c^2			
$gg \to \mathrm{H}$	POWHEG	–	–
$qq\mathrm{H}$ (VBF)	POWHEG	–	–
WH + ZH + $\mathrm{t\bar{t}H}$	PYTHIA	–	–
Signal MSSM Higgs mass hypothesis 90-1000 GeV/c^2			
bbΦ	PYTHIA	–	–
$gg \to \Phi$	PYTHIA	–	–

Table 7.1: Monte Carlo samples used in the analysis. The corresponding cross sections multiplied by Monte Carlo filter efficiencies are presented in the second column.

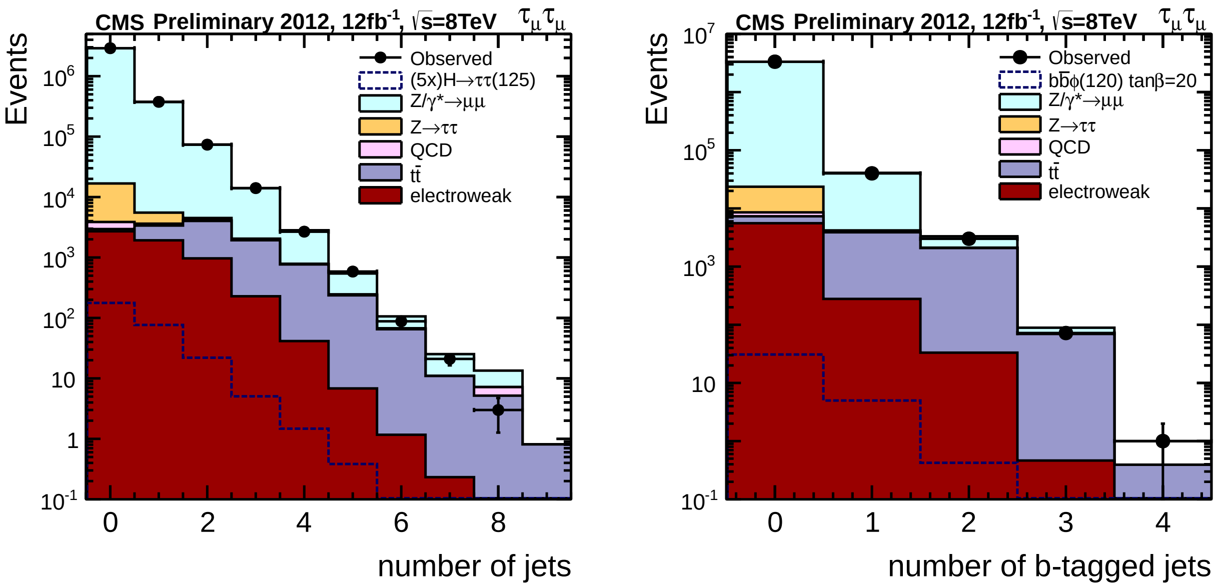

Figure 7.2: The distribution of the number of all jets (left) and b-tagged jets (right) in 2012 data.

The difference observed in the distribution of the missing transverse energy between data and simulation, is eliminated by applying a correction to the resolution of the hadron recoil transverse momentum projected onto the direction parallel and perpendicular to the Z, W or Higgs boson transverse momenta in the corresponding MC samples. This correction is referred to as “recoil correction”. The resolution functions are obtained from Z $\rightarrow \mu\mu$ events and are parametrised as a function of the transverse momentum p_{T} of the Z boson and jet multiplicity. This parameterisation is then used to correct the Monte-Carlo simulation in order to match the experimental data.

Two different approaches have been tested. The first is a parametric data-to-simulation correction, via rescaling the resolution of the recoil momenta using scaling factors derived from data. The second correction, involves an isomorphic mapping of the recoil momentum distributions from the Z $\rightarrow \mu\mu$ Monte Carlo sample onto those from experimental data. The latter approach has the advantage that it reproduces more accurately the shapes of the projected recoil momentum distributions in the Z + jets events and it also preserves the correlations in the Z + jets events.

The isomorphic mapping technique, as already mentioned, is performed using Z $\rightarrow \mu\mu$ events, selected in the mass region $60\,\mathrm{GeV/c^2} < m_{\mu\mu} < 120\ \mathrm{GeV/c^2}$. U_1 and U_2 are the recoil momentum components projected on the axis parallel and perpendicular to the transverse momentum of the Z boson respectively. Figure 7.3 illustrates the method. The vectors are related by:

$$\vec{p_{\mathrm{T}}^{Z}} = \vec{p_{\mathrm{T}}^{\mu}} + \vec{p_{\mathrm{T}}^{\mu}}$$

$$\vec{U_T} \equiv \vec{p_{\mathrm{T}}^{\mu}} + \vec{p_{\mathrm{T}}^{\mu}} + \vec{p_{\mathrm{T}}^{MET}} \tag{7.3.1}$$

$$\vec{U_T} \equiv \vec{U_1} + \vec{U_2} \tag{7.3.2}$$

The distributions of U_1 and U_2 are fitted in the data and Z $\rightarrow \mu\mu$ MC simulation sample, in bins of Z p_{T} and jet multiplicity, N_{jets}. The U_1 distributions are fitted with a double asymmetric Gaussian, while the U_2 distributions are fitted with a double symmetric Gaussian. Cumulative functions $F_{\mathrm{DATA}}(U_{1,2})$ and $F_{\mathrm{MC}}^{Z\rightarrow\mu\mu}(U_{1,2})$ are extracted for a given ranges of Z p_{T} and N_{jets}. The recoil corrections are performed via monotonic isomorphic mapping:

$$U_{1,2}^{\mathrm{corr}} = F_{\mathrm{DATA}}^{-1}(F_{\mathrm{MC}}^{Z\rightarrow\mu\mu}(U_{1,2}^{\mathrm{uncorr}})). \tag{7.3.3}$$

After applying the recoil correction via isomorphic mapping, the projected momenta of the simulated recoil are in excellent agreement with the ones from experimental data. Relevant plots can be found in the appendix A. The effect of the correction on the MET distribution is illustrated in figure 7.4. With the isomorphic mapping technique applied, agreement between the data and the MC is significantly improved.

However, the isomorphic mapping technique is not applicable to the simulated samples of the W + jets and diboson backgrounds and the Higgs Boson signal. Therefore, for these MC samples the recoil correction is done via rescaling of the recoil resolution.

7.3.3 Muon isolation

To reduce the contamination from muons originating from hadron decays within jets or decays in flight, the selected muons are required to be isolated. The isolation is based on particle flow candidates as discussed previously in section 5.5.1. However in the case of the 2011 and 2012 data analysis there is contribution by PU events. To account for the energy of additional neutral particles coming from PU special corrections are applied. The transverse momentum of all charged hadron candidates within the isolation cone, which do not fulfil

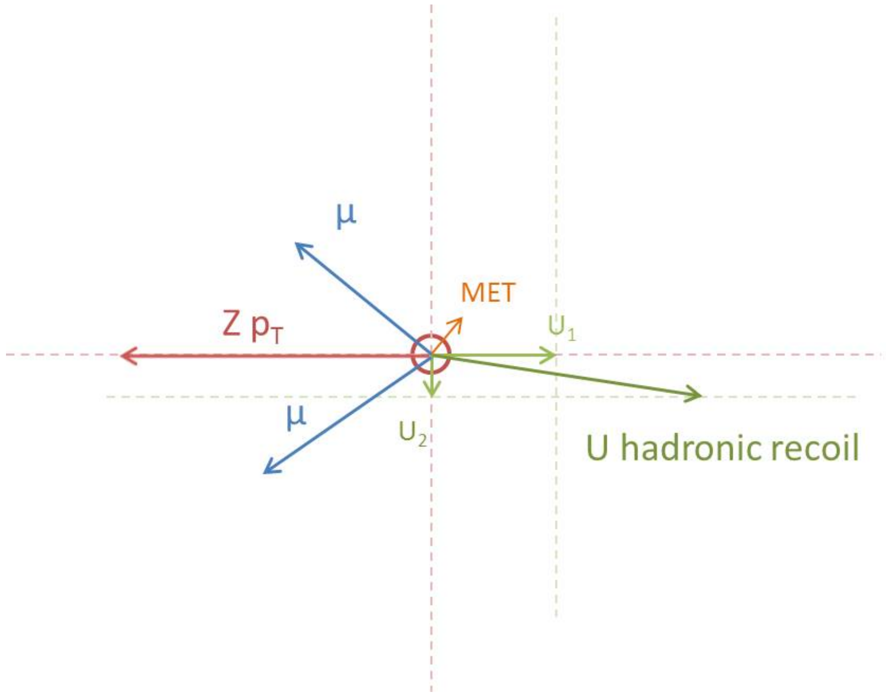

Figure 7.3: Illustration of the hadronic recoil.

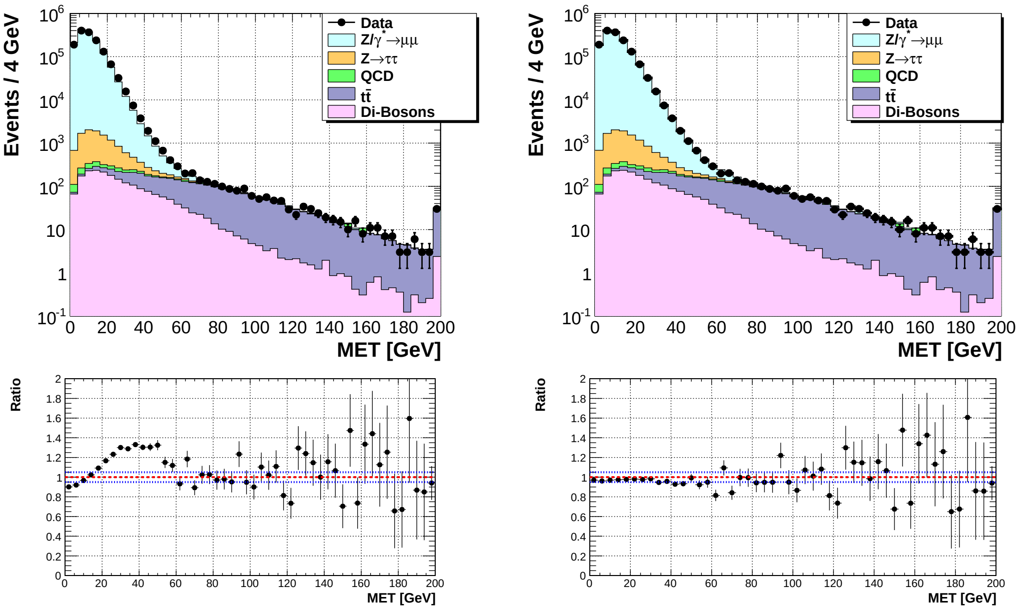

Figure 7.4: Distributions of the MVA MET after preselection of dimuon events before (left) and after (right) applying the recoil corrections via isomorphic mapping. In the small panel below, the data/MC ratio is displayed.

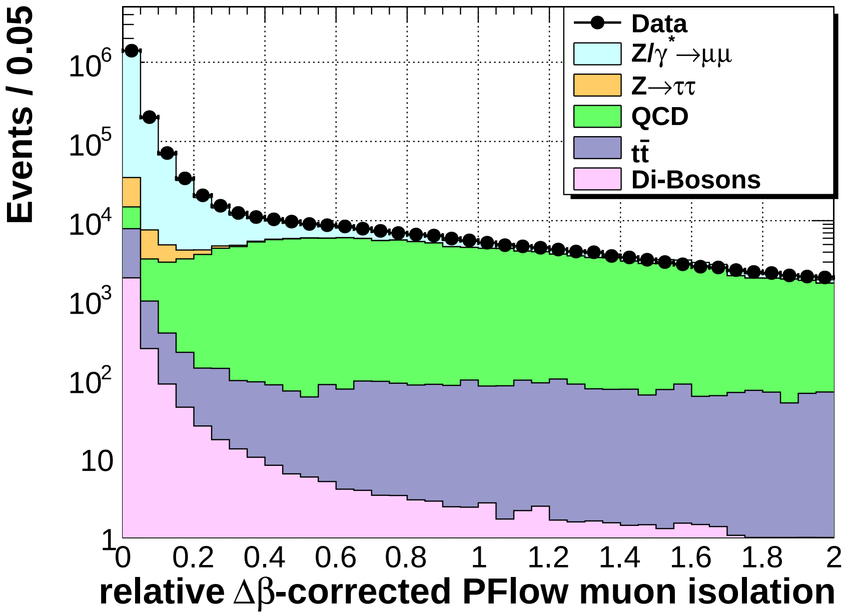

Figure 7.5: Distribution of the $\Delta\beta$-corrected muon isolation variable. The simulation (filled histograms) is compared with data (points).

the primary vertex requirements (section 5.1) is summed. This transverse momentum sum is corrected by a factor of 2:1 to roughly account for the amount of neutral energy with respect to the amount of charged energy in the isolation cone. A relative isolation variable is then defined as:

$$\mathrm{Iso}_{\mu}^{\mathrm{PF}} = \frac{\sum \left(p_{\mathrm{T}}^{\mathrm{charged}} + p_{\mathrm{T}}^{\gamma} + p_{\mathrm{T}}^{\mathrm{neutral}} \right) - \Delta\beta}{p_{\mathrm{T}}^{\mu}} \tag{7.3.4}$$

where $p_{\mathrm{T}}^{\mathrm{charged}}$ corresponds of the p_{T} of all charged particle candidates, p_{T}^{γ} and $p_{\mathrm{T}}^{\mathrm{neutral}}$ correspond to the transverse energy of the photon and neutral hadron candidates and $\Delta\beta$ corresponds to the energy estimate of neutral particles due to event PU as described above. The isolation given by the equation 7.3.4 is referred to as $\Delta\beta$-corrected relative isolation and the corresponding distribution is shown in figure 7.5.

7.3.4 Efficiency corrections

Differences in the efficiencies between data and MC are taken into account, and the MC are corrected by applying scaling factors. The efficiencies are measured using the tag-and-probe method as described in sections 4.3 and 5.5.1. The tables 7.2, 7.3 and 7.4 summarise the scaling factors applied.

7.3.5 Preselection

The first selection of events applied is the trigger selection as described in chapter 4. Subsequently muons are selected if they are of opposite charge, reconstructed within the inner tracker and the muon stations, and are identified as muons by particle-flow algorithm as described in section 5.5. The selected reconstructed muons must fulfil the following criteria:

- the global muon must have at least one good hit in muon stations

p_T bin	η bin	MC Efficiency	Data Efficiency	Correction Factor
$10.0 < p_T \leq 15.0$	$0.0 \leq \mid \eta \mid < 0.8$	0.9873 ± 0.0040	0.9693 ± 0.0045	0.9818 ± 0.0060
$10.0 < p_T \leq 15.0$	$0.8 \leq \mid \eta \mid < 1.2$	0.9688 ± 0.0113	0.9411 ± 0.0087	0.9713 ± 0.0145
$10.0 < p_T \leq 15.0$	$1.2 \leq \mid \eta \mid < 2.1$	0.9374 ± 0.0108	0.9069 ± 0.0081	0.9675 ± 0.0142
$15.0 < p_T \leq 20.0$	$0.0 \leq \mid \eta \mid < 0.8$	0.9876 ± 0.0057	0.9659 ± 0.0046	0.9781 ± 0.0073
$15.0 < p_T \leq 20.0$	$0.8 \leq \mid \eta \mid < 1.2$	0.9505 ± 0.0121	0.9298 ± 0.0094	0.9782 ± 0.0158
$15.0 < p_T \leq 20.0$	$1.2 \leq \mid \eta \mid < 2.1$	0.9559 ± 0.0109	0.9164 ± 0.0078	0.9587 ± 0.0137
$20.0 < p_T \leq 25.0$	$0.0 \leq \mid \eta \mid < 0.8$	0.9883 ± 0.0048	0.9758 ± 0.0039	0.9873 ± 0.0062
$20.0 < p_T \leq 25.0$	$0.8 \leq \mid \eta \mid < 1.2$	0.9925 ± 0.0097	0.9460 ± 0.0090	0.9532 ± 0.0130
$20.0 < p_T \leq 25.0$	$1.2 \leq \mid \eta \mid < 2.1$	0.9666 ± 0.0083	0.9284 ± 0.0075	0.9605 ± 0.0114
$25.0 < p_T \leq 30.0$	$0.0 \leq \mid \eta \mid < 0.8$	0.9892 ± 0.0047	0.9650 ± 0.0048	0.9755 ± 0.0067
$25.0 < p_T \leq 30.0$	$0.8 \leq \mid \eta \mid < 1.2$	0.9667 ± 0.0137	0.9492 ± 0.0088	0.9818 ± 0.0167
$25.0 < p_T \leq 30.0$	$1.2 \leq \mid \eta \mid < 2.1$	0.9392 ± 0.0156	0.9046 ± 0.0093	0.9632 ± 0.0188
$30.0 < p_T$	$0.0 \leq \mid \eta \mid < 0.8$	0.9747 ± 0.0067	0.9704 ± 0.0017	0.9956 ± 0.0070
$30.0 < p_T$	$0.8 \leq \mid \eta \mid < 1.2$	0.9671 ± 0.0112	0.9326 ± 0.0039	0.9644 ± 0.0119
$30.0 < p_T$	$1.2 \leq \mid \eta \mid < 2.1$	0.9563 ± 0.0101	0.9114 ± 0.0037	0.9530 ± 0.0108

Table 7.2: Efficiencies in bins of muon p_T and η, for one muon part of the double muon HLT trigger with thresholds 8 and 18 GeV used in 2012 data. The last column shows the scaling factors applied to the MC samples.

- the muon track must have more than 5 hits in the inner tracker and at least one pixel hit
- $\chi^2/\text{ndof} < 10$ of the global muon track fit
- impact parameter in transverse plane $|d_0| < 0.04$ cm w.r.t. primary vertex
- longitudinal impact parameter w.r.t. primary vertex $|d_z| < 0.1$ cm

After imposing the above requirements, a sample of good quality muons is obtained. Then a kinematic preselection is applied, similar to the one used in the measurement of the Z production cross section, in section 6.3.1.

- The pseudorapidity of the leading (sub-leading) muon should be smaller than 2.1 (2.4) in case of dataset taken with the single, isolated muon trigger, and smaller than 2.1 for both leading and sub-leading muon when double muon triggers are used.
- The p_T of the leading (sub-leading) muon should be greater than 20 (10) GeV/c.
- The relative p_T resolution should be better than 10%
- The $\Delta\beta$-corrected relative isolation variable $\text{Iso}_\mu^{\text{PF}}$ (7.3.4) is required to be less than 0.1 (0.15) for muons with p_T greater (smaller) than 20 GeV/c.
- The azimuthal angle between the muon momenta must be greater than 2 rad. This requirement rejects QCD events where two muons originate from the same quarkonia decay

		2011		
p_{T}	η bin	MC Efficiency	Data Efficiency	Correction Factor
10.0 - 15.0 GeV	$\mid \eta \mid < 1.5$	0.6876 ± 0.0026	0.6804 ± 0.0093	0.9895 ± 0.0141
10.0 - 15.0 GeV	$1.5 \leq \mid \eta \mid < 2.1$	0.6103 ± 0.0031	0.6288 ± 0.0103	1.0303 ± 0.0177
15.0 - 20.0 GeV	$\mid \eta \mid < 1.5$	0.7727 ± 0.0014	0.7856 ± 0.0048	1.0168 ± 0.0065
15.0 - 20.0 GeV	$1.5 \leq \mid \eta \mid < 2.1$	0.6981 ± 0.0020	0.7153 ± 0.0067	1.0247 ± 0.0100
>20.0 GeV	$\mid \eta \mid < 1.5$	0.9351 ± 0.0001	0.9408 ± 0.0003	1.0061 ± 0.0004
>20.0 GeV	$1.5 \leq \mid \eta \mid < 2.1$	0.8858 ± 0.0003	0.8986 ± 0.0008	1.0144 ± 0.0010

Table 7.3: Muon identification efficiencies in bins of muon p_{T} and η for 2011. The last column shows the scaling factors applied to correct the Monte Carlo samples.

		2012		
p_{T} bin	η bin	MC Efficiency	Data Efficiency	ScaleFactor
$10.0 < p_{\mathrm{T}} \leq 15.0$	$0.0 \leq \mid \eta \mid < 0.8$	0.6211 ± 0.0052	0.6114 ± 0.0066	0.9845 ± 0.0134
$10.0 < p_{\mathrm{T}} \leq 15.0$	$0.8 \leq \mid \eta \mid < 1.2$	0.6808 ± 0.0050	0.6719 ± 0.0059	0.9869 ± 0.0113
$10.0 < p_{\mathrm{T}} \leq 15.0$	$1.2 \leq \mid \eta \mid < 2.1$	0.6680 ± 0.0031	0.6631 ± 0.0034	0.9927 ± 0.0069
$15.0 < p_{\mathrm{T}} \leq 20.0$	$0.0 \leq \mid \eta \mid < 0.8$	0.7158 ± 0.0026	0.6903 ± 0.0032	0.9644 ± 0.0057
$15.0 < p_{\mathrm{T}} \leq 20.0$	$0.8 \leq \mid \eta \mid < 1.2$	0.7645 ± 0.0030	0.7492 ± 0.0035	0.9800 ± 0.0060
$15.0 < p_{\mathrm{T}} \leq 20.0$	$1.2 \leq \mid \eta \mid < 2.1$	0.7352 ± 0.0021	0.7323 ± 0.0023	0.9961 ± 0.0042
$20.0 < p_{\mathrm{T}}$	$0.0 \leq \mid \eta \mid < 0.8$	0.9260 ± 0.0002	0.9152 ± 0.0002	0.9884 ± 0.0003
$20.0 < p_{\mathrm{T}}$	$0.8 \leq \mid \eta \mid < 1.2$	0.9273 ± 0.0003	0.9165 ± 0.0003	0.9884 ± 0.0004
$20.0 < p_{\mathrm{T}}$	$1.2 \leq \mid \eta \mid < 2.1$	0.9089 ± 0.0002	0.9035 ± 0.0002	0.9941 ± 0.0004

Table 7.4: Muon identification efficiencies in bins of muon p_{T} and η for 2012. The last column shows the scaling factors applied to correct the Monte Carlo samples.

or the same decay chain of heavy flavor hadrons. However, the events are categorised according to the production mechanism (section 7.3.6). In the cases where the Higgs boson is produced via vector boson fusion or boosted mechanisms, it can have a large transverse momentum, leading on average to smaller azimuthal angles between muons. Therefore cut on the azimuthal angle between the transverse momenta of two muons is omitted is these categories.
Instead:

- a cut on the invariant mass of the two muons is introduced, $m_{\mu\mu} > 35\,\mathrm{GeV/c^2}$.

7.3.6 Event classification

To exploit the distinct signatures of the main Higgs production mechanisms and to further suppress SM background processes, the preselected events are classified into four event categories, according to the jet type and multiplicity:

- **Vector Boson Fusion (VBF):** This event category exploits the production of Higgs bosons in VBF. The event selection for this category is the subject of section 7.3.7.
- **1 Jet:** Events in this category are required to have at least one jet with $p_\mathrm{T} > 30\,\mathrm{GeV}$, to not be part of the VBF category. Production processed with one jet in the final state are gluon fusion with an extra gluon radiation, associated production of the Higgs with vector bosons decaying hadronically and more.
- **b Jets:** This category is intended to select events where the Higgs is produced in association with b quarks, which may be enhanced in the MSSM. In this category at least one b-tagged jet with $p_\mathrm{T} > 20$ GeV/c is required and not more than one jet with $p_\mathrm{T} > 30$ GeV/c.
- **0 Jet:** All selected events that are not part of any other event category described above are collected in this event category. It contains no jet with $p_\mathrm{T} > 30$ GeV and no b-tagged jet with $p_\mathrm{T} > 20$ GeV/c.

The event categories are defined such that are mutually exclusive. There is no overlap of events among the categories. In the SM search, the 1 jet and 0 jets categories are further divided into subcategories according to the p_T of the leading muon. If for the leading muon $p_\mathrm{T} > 30$ GeV/c the event is classified into the high-p_T lepton category. Otherwise, the event falls into the low-p_T lepton category. Using this subcategorisation, in the high p_T lepton class the irreducible background from Drell-Yan production of τ pairs is suppressed and the ditau mass resolution is increased. The 0 jets category is background dominated, therefore not used in the statistical analysis. The events in this category are used for background evaluation and normalisation. In the MSSM search only two categories are used b-tag and no b-tag, in order to reduce theory related systematic uncertainties.

7.3.7 Multi-variate selection

The distribution of the invariant mass of muon pairs after the preselection is shown in figure 7.6. At this stage of the analysis, the sample is still largely dominated by $\mathrm{Z}/\gamma^* \to \mu\mu$ background. The second largest contribution comes from $\mathrm{Z} \to \tau\tau \to \mu\mu$ events. Further suppression of the background is achieved by applying multivariate analysis using a boosted decision tree (BDT) [40]. The BDT is trained to distinguish between three event classes, $\mathrm{Z} \to \tau\tau \to \mu\mu$ and $\mathrm{Z}/\gamma* \to \mu\mu$ backgrounds and the $\mathrm{H} \to \tau\tau \to \mu\mu$ signal. The following variables are included in the BDT:

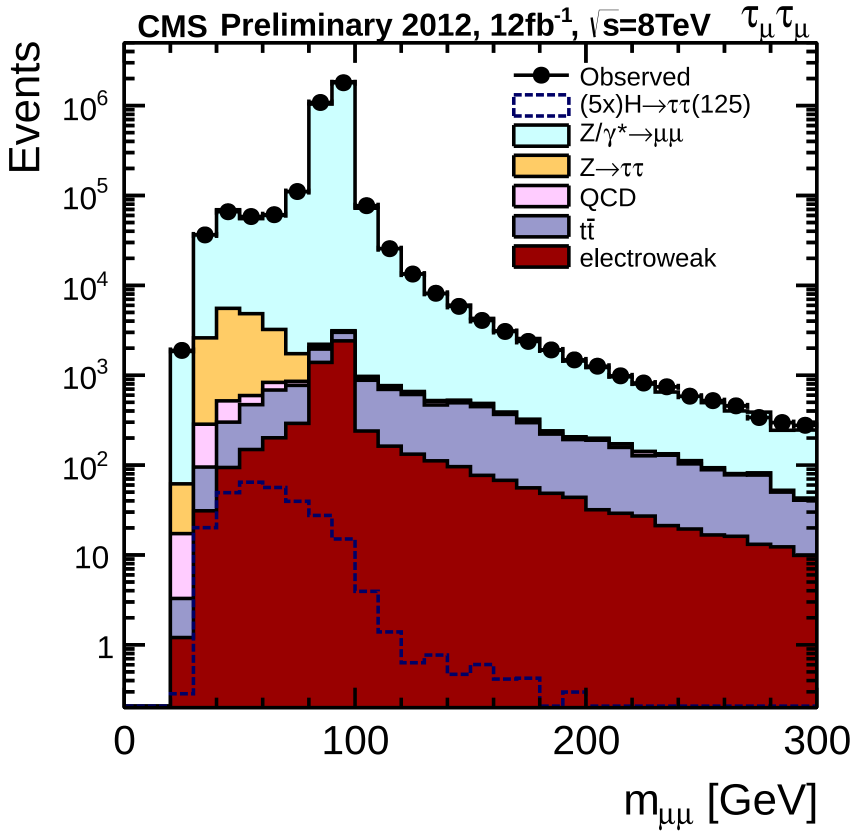

Figure 7.6: The dimuon invariant mass distribution after preselection. Data are shown as points, while the simulated background contributions are displayed as filled histograms, as indicated in the legend. The simulated SM Higgs signal, as expected for a mass of 120 GeV/c^2 and scaled to the SM cross section multiplied by a factor of 5, is shown as a dashed line.

- The ratio of the transverse momentum of the dimuon system to the scalar sum of positive and negative muon momenta, $p_{\mathrm{T}}(2\mu)/\sum p_{\mathrm{T}}(\mu)$.
- The muon distance of closest approach (DCA) significance, DCASig(2μ).
- The pseudorapidity of the dimuon system, $\eta(2\mu)$.
- The azimuthal angle between direction of the positively charged muon three-momentum and the missing transverse energy, $\Delta\Phi(\mu^+, MET)$ [1].
- The decay angle θ^* of the positively charged muon in the rest frame of the dimuon system, assuming that two muons originate directly from the Z boson decay.
- The angle ω^* between three-momentum of the positively charged muon and production plane of the dimuon system, assuming that the two muons originate directly from the Z boson decay. The Z boson production plane is defined as the plane spanned by the three-momentum vector of the dimuon system and the beam axis.
- The last variable, "CA solution", is discrete. It is set to 1 if the collinear approximation for the reconstruction of τ lepton pair kinematics (section 5.7.1) yields a physical solution for the neutrino energies, otherwise is set to 0.

Figures 7.7 and 7.8 show the distributions of the discriminating variables and figure 7.9 the BDT discriminant for data and Monte Carlo samples, for Higgs boson mass hypothesis $m_H = 125\,\mathrm{GeV/c^2}$. Good agreement in the shapes of the distributions is observed, indicating that no bias is introduced in the computation of the BDT discriminant. This BDT selection is employed in all event categories except for the VBF category, where a dedicated BDT is trained, as discussed in the following section.

An event is accepted in the final samples if it passes a lower cut on the signal BDT discriminant. The cut is optimised separately for each event category by minimising the expected exclusion limits. The exact values for each category included in the SM Higgs search, 1 and 0 jets categories, are listed in table 7.5. When studying the MSSM scenario, taken into account are the b-tag and no b-tag categories. The lower accepted values of the BDT discriminant for the MSSM categories are listed in table 7.6.

	1 Jet	0 Jets
hight p_{T}	-0.5	-0.5
low p_{T}	-0.5	-0.4

Table 7.5: List of the different cuts on the BDT discriminant for the 1 and 0 jets SM categories. The cuts are optimised to give the best exclusion limits.

Vector Boson Fusion Analysis

The topological signature of SM Higgs boson production via the vector boson fusion (VBF) is characterised by two energetic jets, with a large gap in rapidity and minimal hadronic activity

---

[1] It was found that the two variables, $\Delta\Phi(\mu^+, MET)$ and $\Delta\Phi(\mu^-, MET)$, are strongly anti-correlated, but possess identical discriminating power between the $Z \to \tau\tau \to \mu\mu$ signal and the $Z/\gamma* \to \mu\mu$ background. Hence only one of these variables is included in the BDT discriminant.

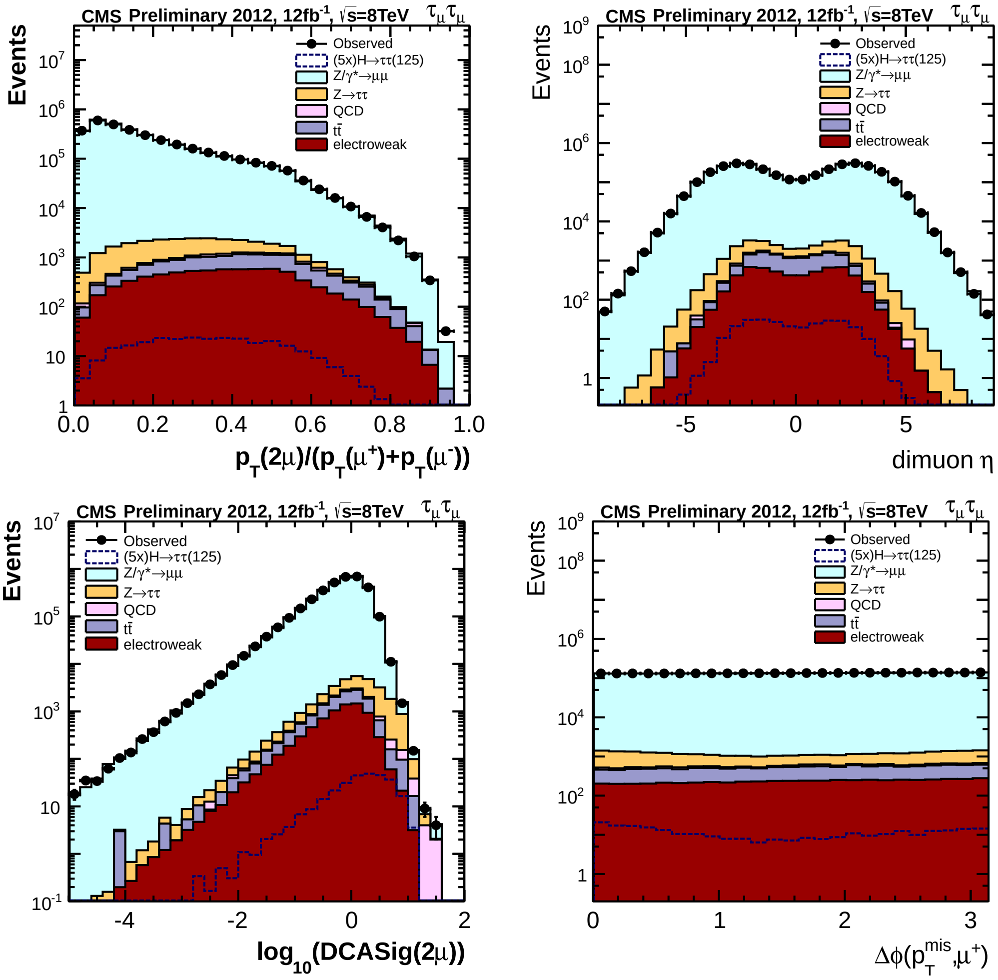

Figure 7.7: Distribution of the variables included in the BDT discriminator. In this figure starting from top left: the ratio of the dimuon transverse momentum and the scalar sum of muon transverse momenta, pseudorapidity of the dimuon system, common logarithm of the muon DCA significance and azimuthal angle between the positive muon momentum and the missing transverse momentum

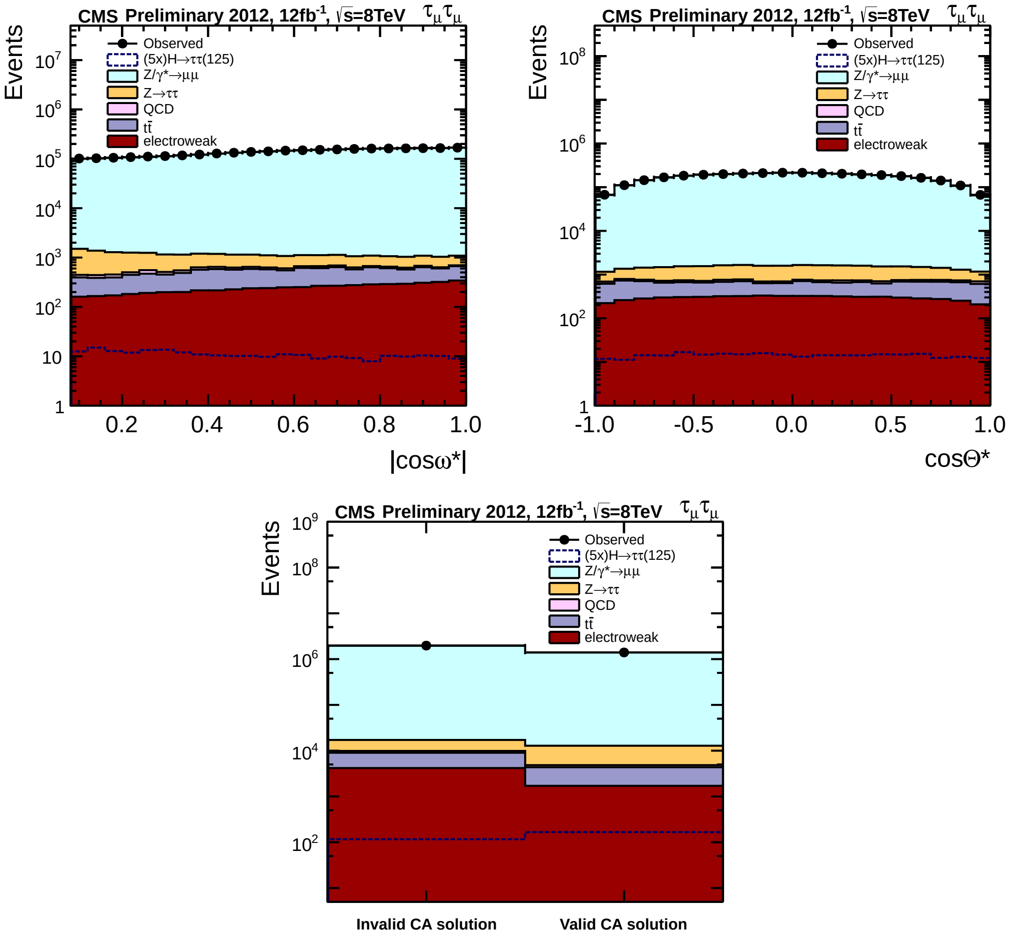

Figure 7.8: Distribution of the variables included in the BDT discriminator. In this figure starting from top left: angle between positive muon momentum and Z boson production plane in the rest frame of the Z boson, decay angle of the positive muon in the rest frame of the Z boson and the validity of the collinear approximation (CA) solution for the reconstruction of the τ pair kinematics

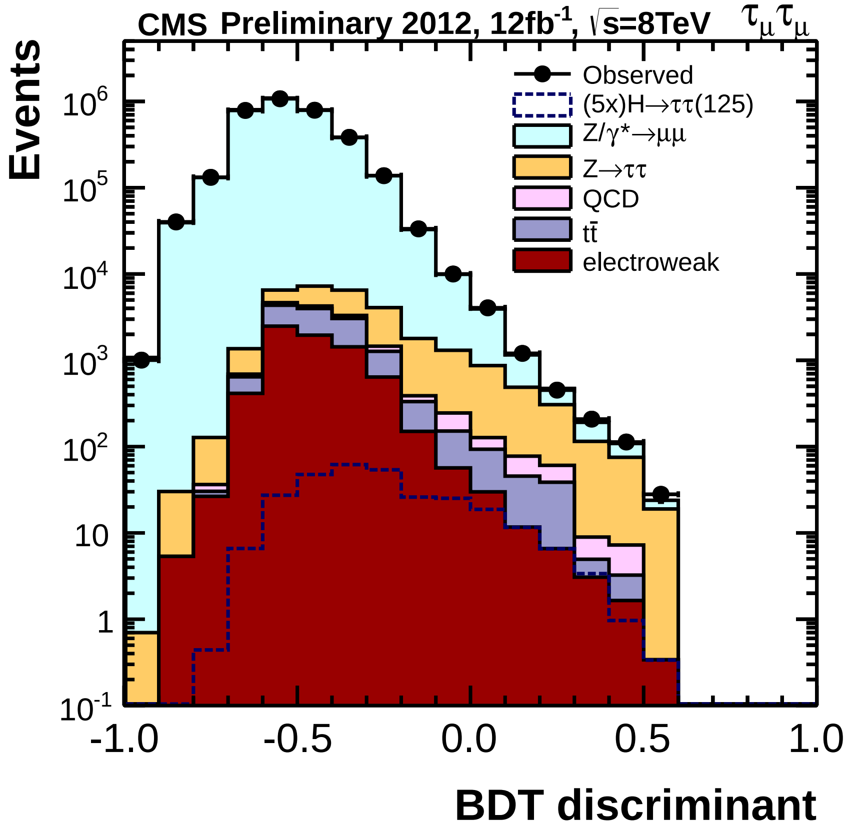

Figure 7.9: The BDT discriminant used in the inclusive analysis.

b-tag jet	no b-tag jet
-0.3	-0.1

Table 7.6: List of the different cuts on the BDT discriminant the MSSM categories. The cuts are optimised to give the best exclusion limits.

between them. The selection of Higgs candidates produced via VBF, starts with the preselection of dimuon events, as described in section 7.3.5. Then a set of criteria are applied to select events compatible with the signatures of SM Higgs boson production via the VBF mechanism:

- There should be at least two jets with $p_{\mathrm{T}} > 30$ GeV/c and $|\eta| < 4.5$. The two leading jets are chosen for further analysis.
- No additional jets with $p_{\mathrm{T}} > 30$ GeV/c are allowed in the rapidity gap between the two leading jets.

After this preselection of events, a BDT based selection is employed to discriminate $\tau\tau \to \mu\mu$ events from muons coming from $\mathrm{Z} \to \mu\mu$ decays. The BDT discriminant, $\mathrm{BDT_{VBF}}$ combines the following variables:

- Invariant mass of the two tagged jets
- Pseudorapidity difference between the two tagged jets
- DCA significance

- MET
- Validity of CA solution
- Azimuthal angle between direction of the positively charged muon three-momentum and MET
- The decay angle θ^* of the positively charged muon in the rest frame of the dimuon system, assuming that two muons originate directly from the Z boson decay.
- The angle ω^* between three-momentum of the positively charged muon and production plane of the dimuon system, assuming that the two muons originate directly from the Z boson decay.

Figures 7.10 and 7.11 show the distributions of the discriminating variables listed above. The distribution of the BDT discriminant is compared between data and simulation in figure 7.12.

An event is accepted for further analysis if the BDT discriminant $\mathrm{BDT_{VBF}} > 0.25$.

7.4 Evaluation of backgrounds

7.4.1 Dimuon Drell-Yan background

In order to evaluate the dimuon Drell-Yan background the τ decay length information is exploited. In $\mathrm{Z} \to \tau\tau \to \mu\mu$ and $\mathrm{H} \to \tau\tau \to \mu\mu$ events the muons originate from τ lepton decays and generate displaced tracks while in $\mathrm{Z}/\gamma^* \to \mu\mu$ events prompt muons are expected. Therefore the distributions of the DCA significance is different for the two types of decays. The method is very similar to the one used in the $\mathrm{Z} \to \tau\tau$ analysis (section 6.3.4). The $\mathrm{Z}/\gamma^* \to \mu\mu$ contribution to the final sample is estimated in three dimensional bins of visible dimuon mass, reconstructed ditau mass and DCA significance. The dimuon mass spectrum is divided in bins:

- low dimuon mass region, $m_{\mu\mu} < 70\,\mathrm{GeV/c^2}$, with significant contribution from $\mathrm{Z} \to \tau\tau \to \mu\mu$ events
- radiative tail of the Z peak, $70\ \mathrm{GeV/c^2} < m_{\mu\mu} < 91\,\mathrm{GeV/c^2}$
- right side of the Z peak, $91\ \mathrm{GeV/c^2} < m_{\mu\mu} < 110\ \mathrm{GeV/c^2}$
- high dimuon mass region, $110\ \mathrm{GeV/c^2} < m_{\mu\mu}$

The ditau mass bins are:

- $m_{\tau\tau} < 110\ \mathrm{GeV/c^2}$
- $110\ \mathrm{GeV/c^2} < m_{\tau\tau} < 140\ \mathrm{GeV/c^2}$
- $m_{\tau\tau} > 140\ GeV/c^2$

For each event, a new BDT is trained in the same way as described in section 7.3.7, including all the previously used variables with the exception of the inter-muon DCA significance. This BDT is referred to hereafter as “reduced BDT” ($\mathrm{BDT_{red}}$). Three bins of $\mathrm{BDT_{red}}$ are considered:

- [-1.0,-0.5]
- [-0.5,-0.3]

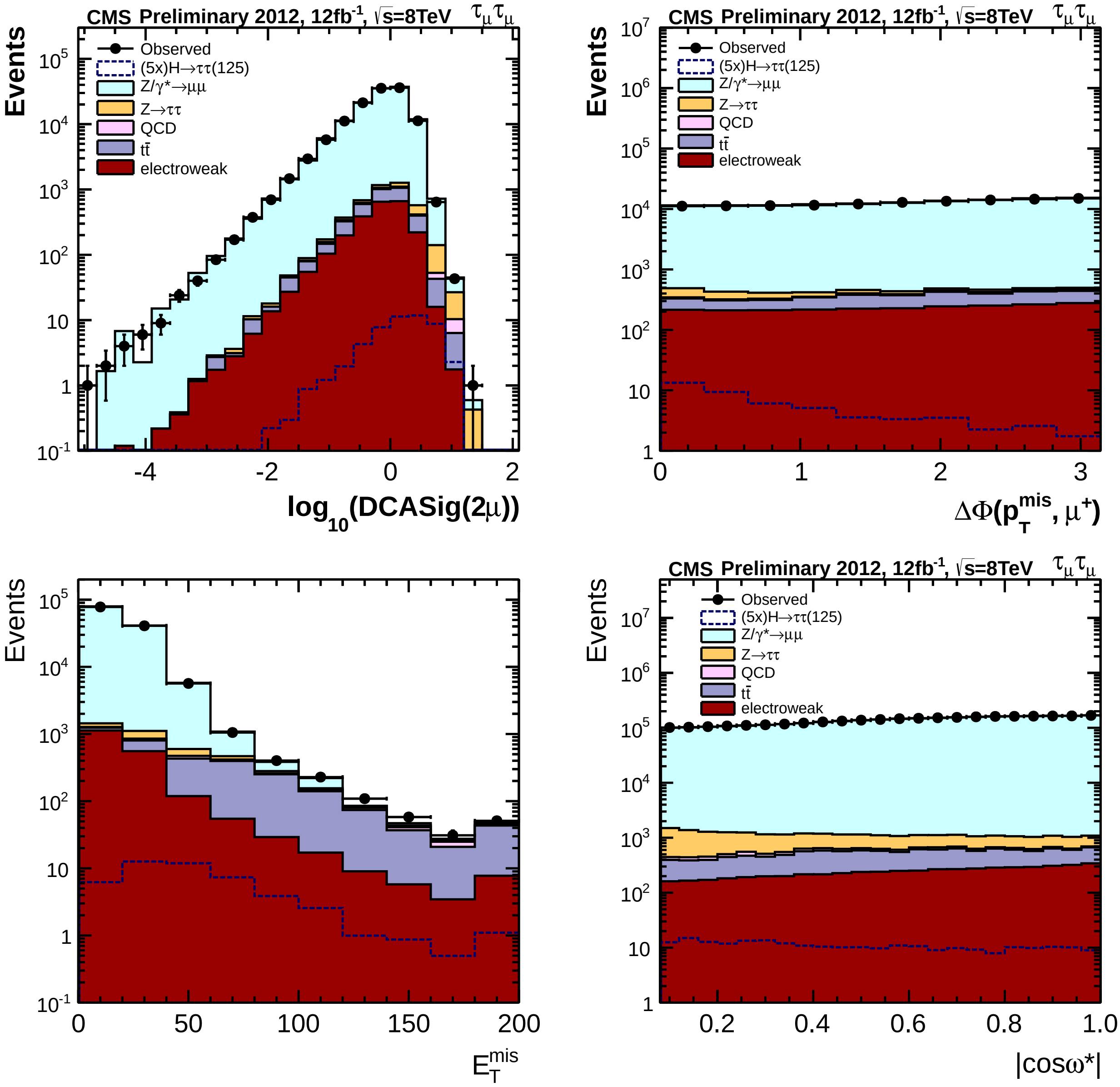

Figure 7.10: Distributions of the variables used in the training of the BDT discriminator in the VBF event category. In this figure starting from top left: the common logarithm of the muon DCA significance, azimuthal angle between the positive muon momentum and the missing transverse momentum, the missing transverse energy and the angle between positive muon momentum and Z boson production plane in the rest frame of the Z boson.

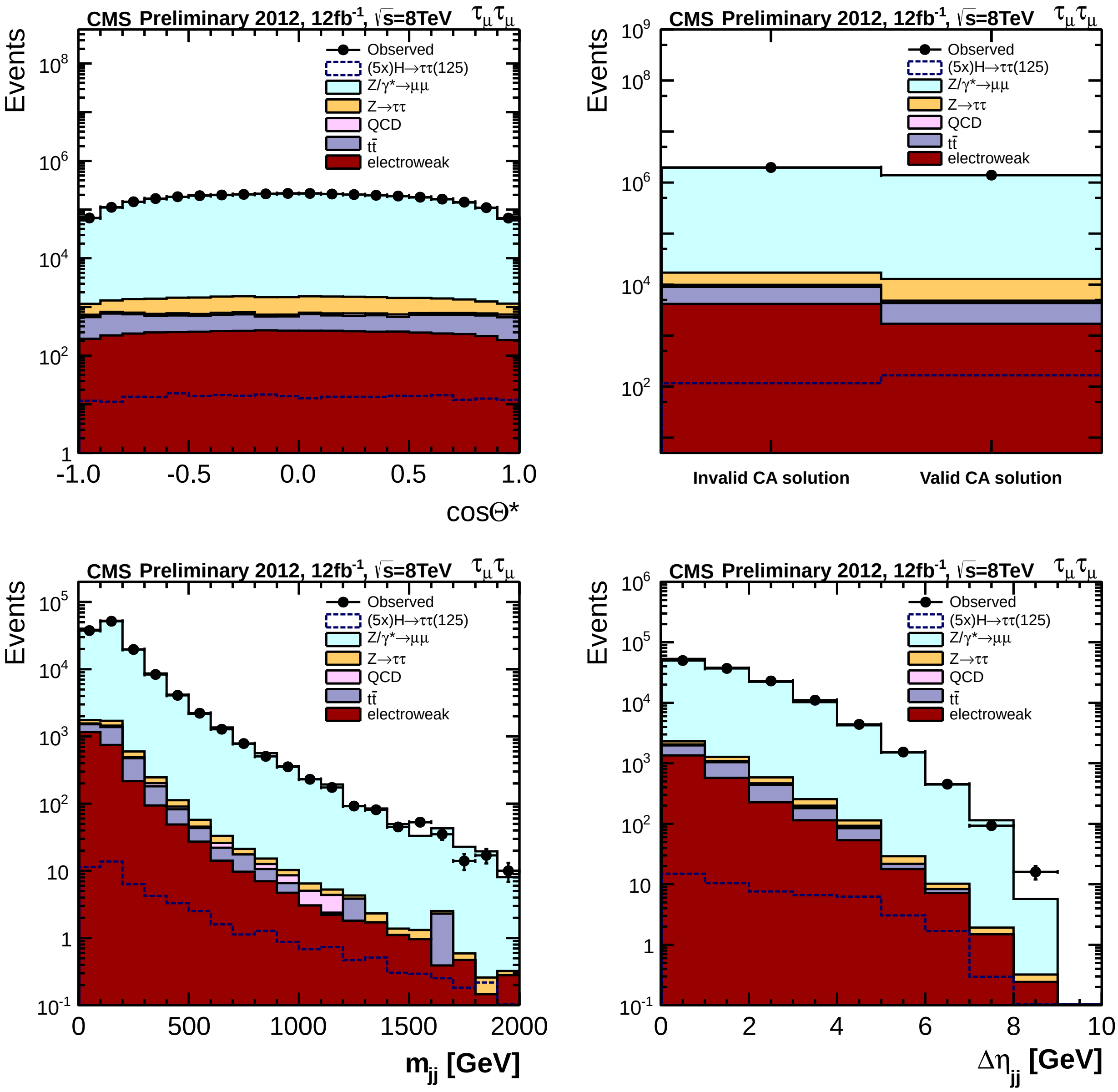

Figure 7.11: Distributions of the variables used in the training of the BDT discriminator in the VBF event category. In this figure starting from top left: decay angle of the positive muon in the rest frame of the Z boson, the validity of the collinear approximation (CA) solution for the reconstruction of the τ pair kinematics, the mass of the dijet system and the pseudorapidity gap between the two jets.

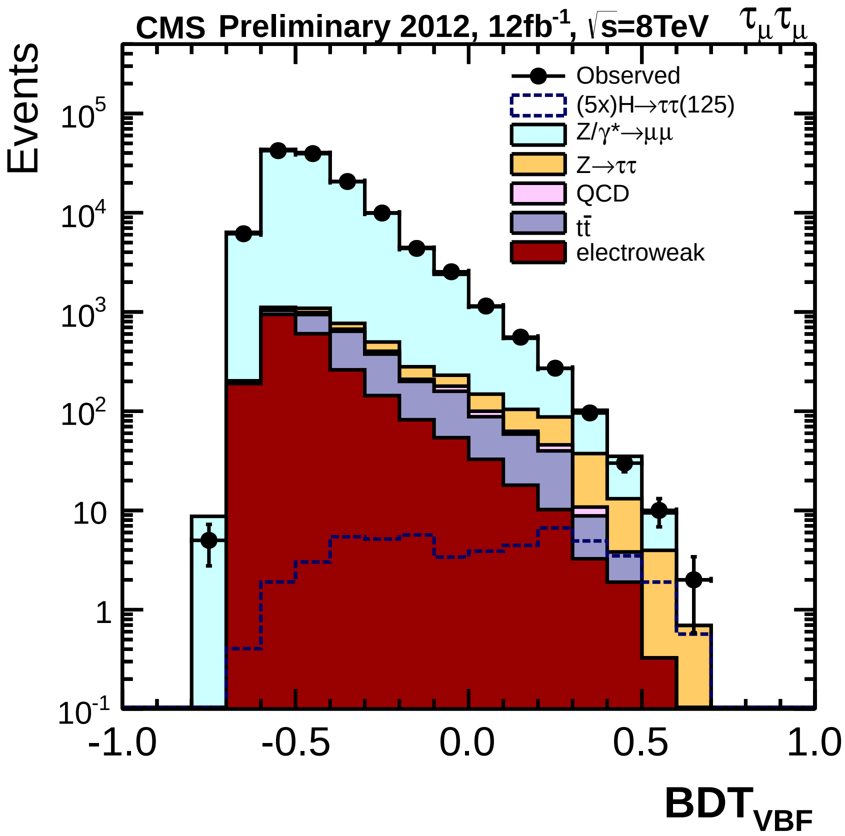

Figure 7.12: Distribution of the BDT discriminator in the VBF event category.

- [-0.3,1.0]

and in the VBF case :

- [-1.0,-0.4]
- [-0.4,-0.25]
- [-0.25,1.0]

The DCA significance in the Monte Carlo samples is fitted for every bin of BDT$_{\text{red}}$, dimuon mass and ditau mass. This procedure is performed for both Z/$\gamma^* \to \mu\mu$ and Z/$H \to \tau\tau$ samples. Template functions that describe the shape of the DCA significance distributions are extracted from the fits. Then the data are fitted as a superposition of the two templates, one describing the muon DCA significance shape in the Z/$\gamma^* \to \mu\mu$ events and the other the one in the Z/$H \to \tau\tau$ samples. The normalisations for the Z/$\gamma^* \to \mu\mu$ templates, derived from the fitting procedure in data and Monte Carlo, are compared with each other and used to determine ($m_{\mu\mu}$,$m_{\tau\tau}$,BDT$_{\text{red}}$) dependent correction factors applied to the Z/$\gamma^* \to \mu\mu$ Monte Carlo sample. The fits to the data are performed after subtracting the contributions from t$\bar{\text{t}}$, W + Jets, QCD and diboson backgrounds. The whole procedure is performed for the inclusive and the VBF category.

The statistical uncertainty on the normalisation of the Z/$\gamma^* \to \mu\mu$ background is estimated to vary between 1-4% for the three dimensional bins where the fitting is performed. The impact of the shape uncertainties in the template distributions on the predicted number of Z/$\gamma^* \to \mu\mu$ events in different ($m_{\mu\mu}$,$m_{\tau\tau}$,BDT$_{\text{red}}$) bins is estimated by releasing the parameters describing the shapes of the Z/$\gamma^* \to \mu\mu$ template distributions in the template fits and then varying these

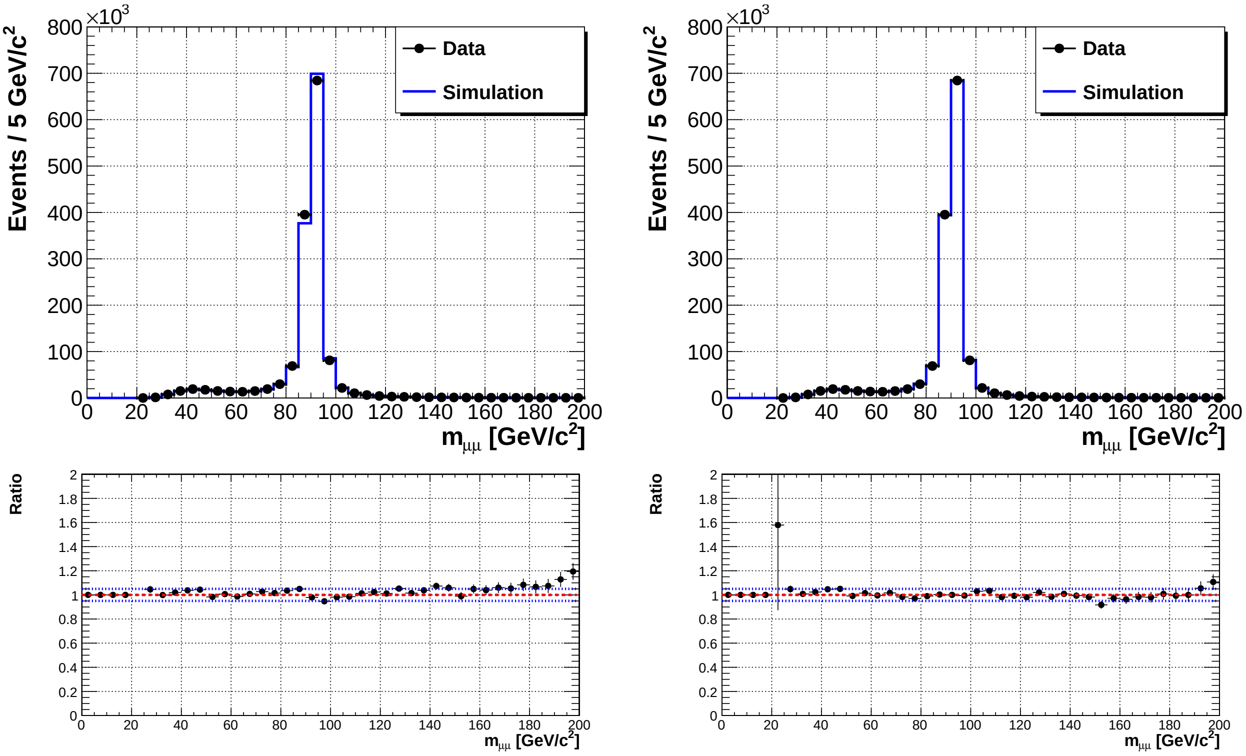

Figure 7.13: dimuon mass distributions before (left) and after (right) applying corrections to the $Z/\gamma^* \to \mu\mu$ Monte Carlo sample as described in text.

parameters within the uncertainties returned by the fit. The resulting systematic uncertainty on the $Z/\gamma^* \to \mu\mu$ background normalisation due to the uncertainties on the template shapes is estimated to vary between 2% and 6% depending on the dimuon or ditau mass region and BDT bin. These uncertainties are added in quadrature to the statistical uncertainty. The distributions of the dimuon invariant mass before and after the correction procedure is shown in figure 7.13.

The correction procedure described above improves the agreement between data and simulation of the $Z/\gamma* \to \mu\mu$ background.

7.4.2 $t\bar{t}$ background

A systematic uncertainty of 8% is assigned on the $t\bar{t}$ background normalisation, which is taken from the CMS measurements of the top pair production cross section [63]. These measurements are consistent with the approximate NNLO calculations [64, 65], which have an uncertainty of 10%. The shape and normalisation of this background are estimated from the Monte Carlo simulation scaled to the NNLO production cross section.

The top pair background is controlled in the side-band region, MET > 80 GeV (figure 7.14), before applying the BDT selection.

To account for possible contaminations of the control region by any signal of a heavy resonance decaying to τ leptons, the muon DCA significance distribution is fitted with templates for top pair events and for possible events with heavy resonance decays. Both templates are derived from Monte Carlo samples: $t\bar{t}$ production followed by $t\bar{t} \to b\bar{b}W^+W^- \to b\bar{b}\mu\nu\mu\nu$ and MSSM Higgs signal, $\Phi \to \tau\tau \to \mu\mu$. The normalisation extracted from the fit of the top contribution to the control region,

$$N^{t\bar{t},\,\mathrm{Data}}_{\mathrm{MET}>80} = 772 \pm 30, \tag{7.4.1}$$

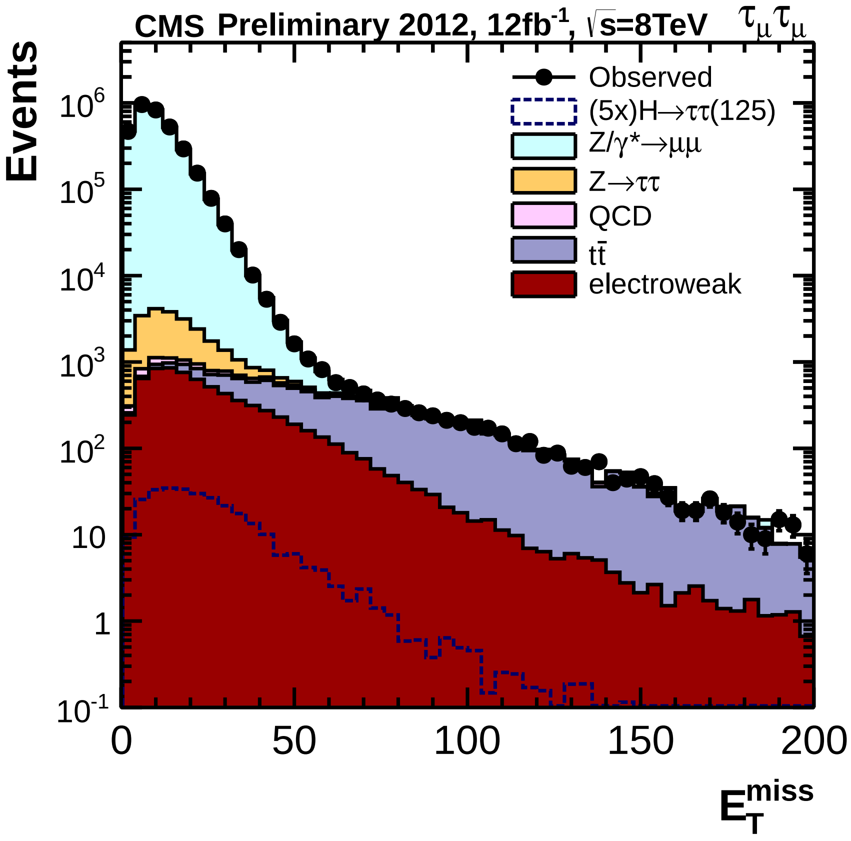

Figure 7.14: Distribution of the missing transverse energy, MET, before applying the likelihood selection. The $t\bar{t}$ background normalisation is controlled in the side-band region, MET $>$ 80 GeV, where top pair events dominate the sample.

is found to be in good agreement with Monte Carlo predictions scaled to NNLO cross section:

$$N_{\mathrm{MET}>80}^{\mathrm{t\bar{t}},\,\mathrm{MC}} = 769 \pm 64. \tag{7.4.2}$$

7.4.3 Z $\rightarrow \tau\tau$ background

The normalisation of the Z $\rightarrow \tau\tau$ background after preselection of dimuon events is estimated from the simulation, taking into account the trigger efficiency, as well as the reconstruction and selection efficiencies. According to earlier studies by CMS [66], the inclusive Z boson production cross section is known to a precision of 2.5%. Additionally, there is an uncertainty associated with the non-linearity of the luminosity measurement of 2%, which is added in quadrature.

A sample of embedded Z $\rightarrow \tau\tau \rightarrow \mu\mu$ events is used to model the shapes of the mass distributions and the distributions of the variables used in the in the BDT selection. This technique is described in detail in section 5.8. The trigger and the kinematic selection criteria for the muons that are replaced by τ leptons is identical to the requirements in this analysis. The invariant mass of the selected dimuon pair has to be $m_{\mu\mu} > 50$ GeV/c^2 to provide a clean sample.

The embedding process comprises a minimum transverse momentum for the visible decay products of the generated τ leptons with a transverse momentum of 18 GeV/c and 8 GeV/c, respectively. Events with smaller transverse momenta for the τ decay products are not generated as such events would not pass the basic kinematic selection criteria of this analysis in the first place.

The event selection in the different event categories in this analysis are affected by the recoil of the system against the Z boson. The proper modelling of the recoiling properties is inherent to the embedded sample.

Example distributions of important for the analysis variables are presented in figure 7.15. The shapes of the dimuon mass, the SVFit ditau mass and the MET distributions for regular Z $\rightarrow \tau\tau$ Monte Carlo events and an embedded sample after preselection are compared to each other.

The uncertainty on the Z $\rightarrow \tau\tau$ background due to the multivariate selection is evaluated by comparing a regular MC Z $\rightarrow \tau\tau$ sample with a sample of embedded events. Figure 7.16 shows a comparison of both samples for the BDT discriminant and some of discriminating variables used in the training for the VBF category. The good agreement for these quantities also verifies that the corrections applied to the simulated events as discussed in section 7.3.2 are valid.

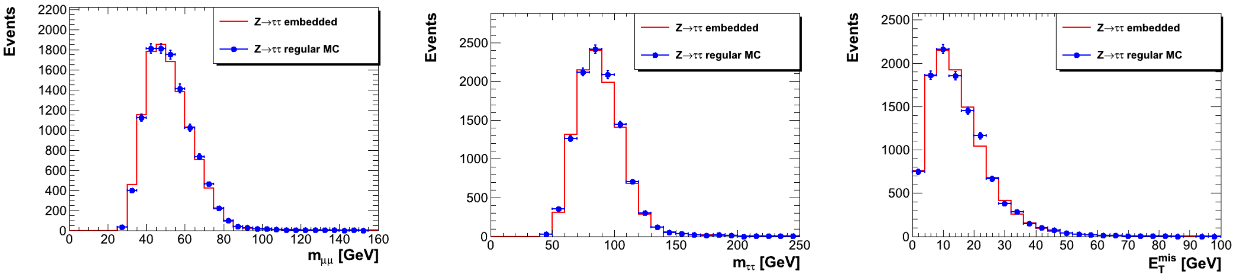

Figure 7.15: Distributions of the dimuon mass (left), SVFit ditau mass (center) and missing transverse energy (right) in the regular Z $\rightarrow \tau\tau$ Monte Carlo sample and in the embedded sample.

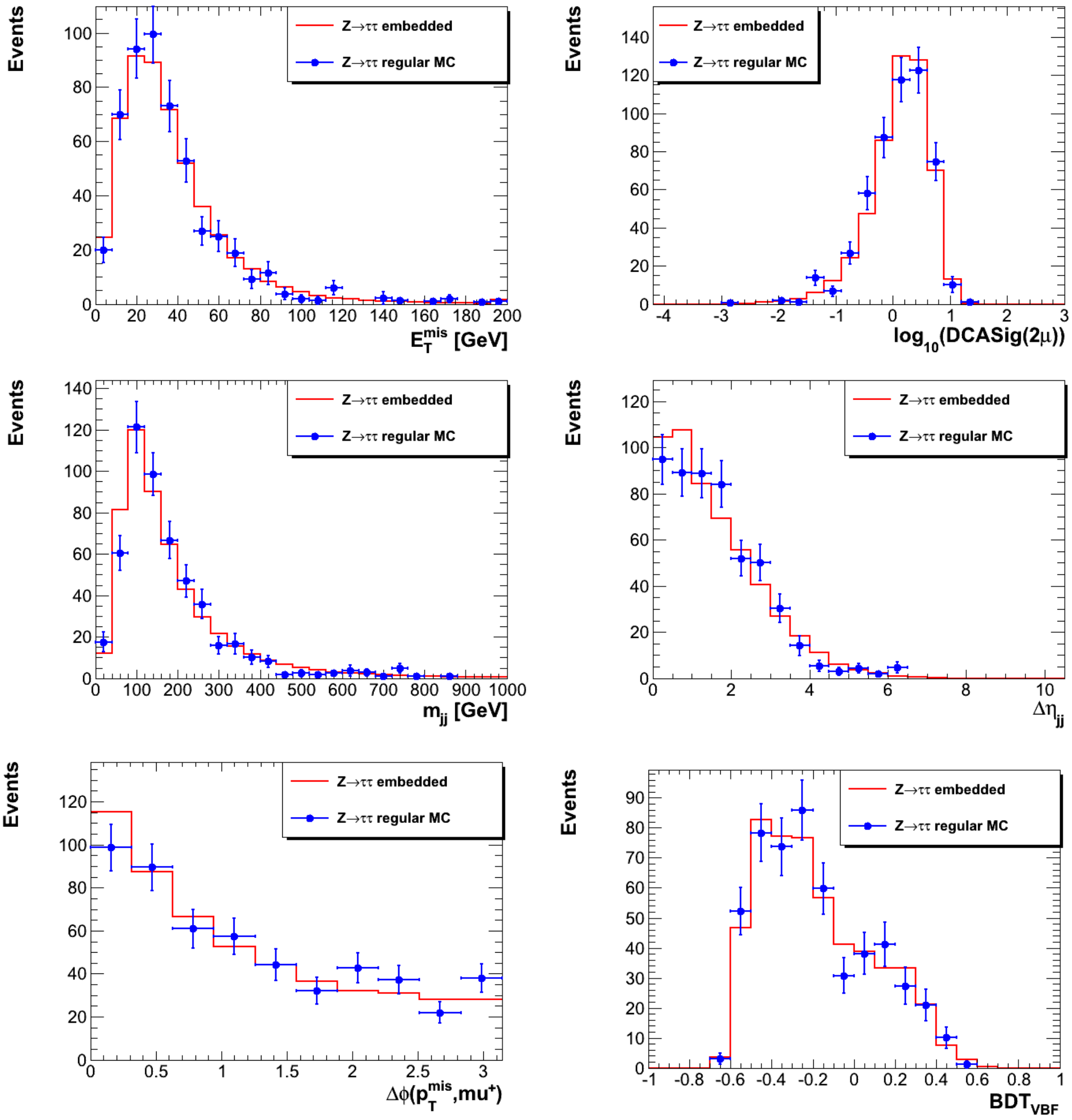

Figure 7.16: Distributions of the variables used for the construction of the multivariate discriminant for the VBF category and the BDT output (bottom right) in the regular $Z \to \tau\tau$ Monte Carlo sample and a sample of embedded events.

The difference in the BDT selection efficiency between a regular Z $\rightarrow \tau\tau$ Monte Carlo sample and the embedded sample is found to be 2-3%, depending on the BDT discriminant cut, therefore covered within the statistical uncertainties. A closure test, comparing embedded samples obtained from $Z/\gamma^* \rightarrow \mu\mu$ events from Monte Carlo with regular Monte Carlo, reveals no significant differences. The systematic uncertainty on the Z $\rightarrow \tau\tau$ background due to the BDT-based MVA selection is conservatively taken to be 3%. In addition, an uncertainty between 0.5% and 8% is assigned to the estimated yields of Z $\rightarrow \tau\tau$ events selected in different SM and MSSM event categories due to the limited statistics of the embedded sample.

7.4.4 QCD background

The QCD background contribution is estimated by exploiting a sample of same sign dimuon events. The method is the same as in the Z $\rightarrow \tau\tau$ analysis (section 6.3.4). For events preselected using the criteria outlined in section 7.3.5, no indication of strong correlations between the muon isolation variables and the net charge of the muon pair is found in the QCD Monte Carlo sample. The preselection cut on the azimuthal angle between the momentum vectors of the positively and the negatively charged muon, $\Delta\Phi(\mu^+, \mu^-) > 2.0$ rad, or cut on the dimuon invariant mass, $m_{\mu\mu} > 35$ GeV/c^2 used in the analysis in the 1 jet and VBF event categories, entirely eliminates opposite sign muon pairs originating either from the same quarkonia decays or from the same decay chain of heavy flavor mesons, $B \rightarrow \bar{D} + \mu^+\nu_\mu \rightarrow \mu^-\bar{\nu}_\mu + X$ and charge conjugated mode. These processes would be only possible source of correlation between the net charge of muons and their isolation variables.

The number of QCD events contributing to selected samples is estimated using the relation:

$$N^{\mathrm{OS}}_{QCD} = N^{\mathrm{SS}}_{QCD} \cdot \frac{\mathrm{OS}}{\mathrm{SS}}\,, \tag{7.4.3}$$

where N^{OS}_{QCD} is the number of opposite sign (OS) QCD events contributing to the selected sample, N^{SS}_{QCD} is the number of QCD events in the same sign (SS) muon sample selected with the same criteria as the OS sample and OS/SS is the ratio of the OS to the SS QCD events evaluated in control samples dominated by QCD events, obtained using a selection criterion orthogonal to the net charge of the muon pair. As no indication of a correlation between the muon isolation variables and the net charge of the muon pairs is found, the pure SS and OS QCD samples for the evaluation of the OS/SS ratio are selected by inverting the cut on the relative isolation variables of both muons:

- $\mathrm{Iso}^{\mathrm{PF}}_{\mu,1} > 0.5$;
- $\mathrm{Iso}^{\mathrm{PF}}_{\mu,2} > 0.5$.

In order to take into account variations of the running and trigger conditions, the 2011 and 2012 data are divided in different periods. The results are consistent for all of the subsamples. Figure 7.17 compares the distributions of the dimuon mass and SVFit ditau mass between QCD-enriched SS and OS samples. Good agreement in the shapes is observed between SS and OS samples.

The estimated ratio between OS and SS QCD events is found to be independent from cut on the BDT discriminant used to select events in all event categories, except for VBF. The OS/SS ratios for data and Monte Carlo samples are reported in table 7.7.

The OS/SS ratios determined in data and Monte Carlo samples are consistent within the statistical uncertainties. The number of QCD events is then calculated as

$$N^{\mathrm{OS}}_{\mathrm{QCD}} = (N^{\mathrm{SS}}_{\mathrm{Data}} - N^{\mathrm{SS}}_{\mathrm{non-QCD\,MC}}) \cdot \frac{\mathrm{OS}}{\mathrm{SS}}, \tag{7.4.4}$$

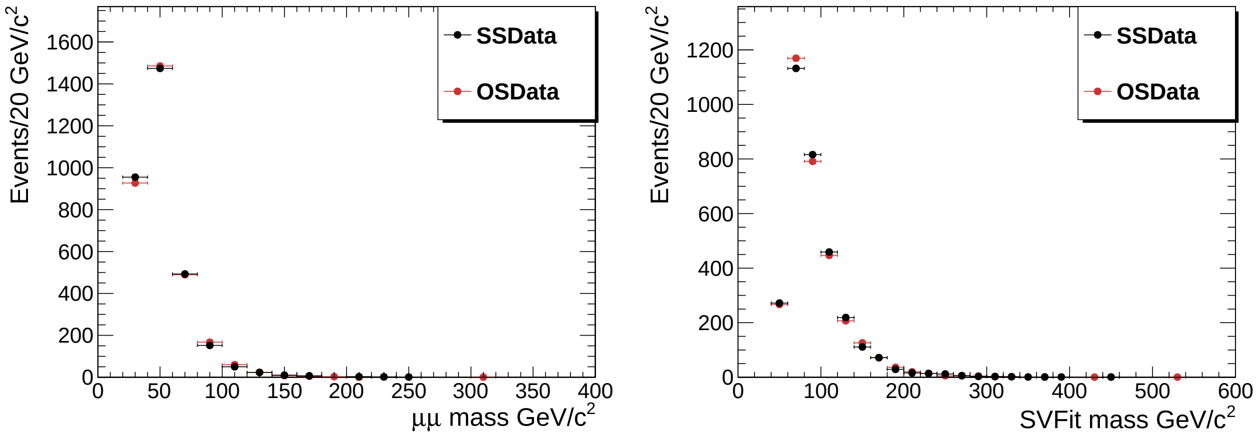

Figure 7.17: Distributions of the dimuon mass (left) and SVFit ditau mass in the OS and SS dimuon samples. Distribution in the OS dimuon sample is normalised to the number of events in the SS dimuon sample

Sample	OS/SS	
	$BDT_{\tau\tau}$ > -0.2	no cut on $BDT_{\tau\tau}$
inverse isolation (Monte Carlo)	2.03 ± 0.13	2.10 ± 0.09
inverse isolation (Data)	2.06 ± 0.04	2.08 ± 0.04
direct isolation (Monte Carlo)	1.50 ± 0.97	2.57 ± 1.15

Table 7.7: The OS/SS ratios evaluated in data and Monte Carlo samples with and without applying the cut on the BDT discriminant used in the inclusive selection.

where $N_{\mathrm{non-QCD\,MC}}$ denotes the contribution of background events, other than QCD, to the SS sample of isolated muons. This contribution is estimated from Monte Carlo simulations.

7.4.5 Diboson and W+jets backgrounds

Contributions from diboson production and W+jets backgrounds are estimated from Monte Carlo. The uncertainty of the W+jets background is driven by limited Monte Carlo statistics of the selected W+jets events and amounts to 25-50% but has no visible effect on the analysis performance. An uncertainty of 30% is assigned on the normalisation of the diboson backgrounds.

7.5 Systematic uncertainties

The theoretical uncertainties taken into account for the statistical analysis of the data, are associated with the Higgs production cross section, the parton distribution functions (PDFs), the strong coupling constant α_s and the the simulation of the underlying event and parton showering. For the SM gluon fusion the uncertainty on the Higgs production cross section is 12-25% while it is 4% for the VBF. In the MSSM case, the uncertainty assigned to the gluon fusion is 10-15% and the associated production with b quarks is 15-25% [67]. The uncertainties associated with PDFs and α_s translate into an uncertainty of 8% on the signal event yields. Lastly, uncertainties related to the simulation of the underlying event and parton showering result in an uncertainty of 4% on the signal event yields.

In addition to the uncertainties on the background normalisations discussed earlier, the following experimental uncertainties are considered:

- Luminosity uncertainty:

  The uncertainty of 2.2% is assigned to the luminosity estimate for 7 TeV and 4.5% for 8 TeV.

- Trigger, muon identification and selection efficiencies:

  The uncertainty on the muon identification, trigger and isolation efficiency is estimated with a tag-and-probe method and found to be 2% for every muon. Since in the analysis presented here final states with two muons are selected, the systematic uncertainty on the normalisation of the signal and background Monte Carlo samples is 4%.

- Identification of b jets:

  The uncertainty on the b jet identification directly translates into an uncertainty on the event yields in the event categories of the MSSM Higgs search. The assigned systematic uncertainty to the b-tagging efficiency is 10% and to the mis-tag rate 30% [68]. Both uncertainties are anti-correlated between the two MSSM event categories.

- Jet Energy Scale:

  The uncertainty on the jet energy scale is between 2 and 5%, depending on the jet transverse momentum and pseudorapidity and directly translates into an uncertainty on event yields in each event category of the SM and MSSM Higgs boson searches.

- MET scale:

The MET scale is extracted by template fitting of the MET spectrum for preselected dimuon events shown in figure 7.14. The templates of the MET distribution are produced for the nominal value and MET scale shifts up to ±10% with 1% step. As an example, figure 7.18 illustrates the effect of a ±5 (10)% shift in the MET scale on the MET distribution in the sample of preselected events and for events selected in the VBF event category, respectively. The template interpolation is performed bin-by-bin, and the method guarantees that all bins have positive entries and that the bin values are continuously differentiable with respect to the MET shift parameter.

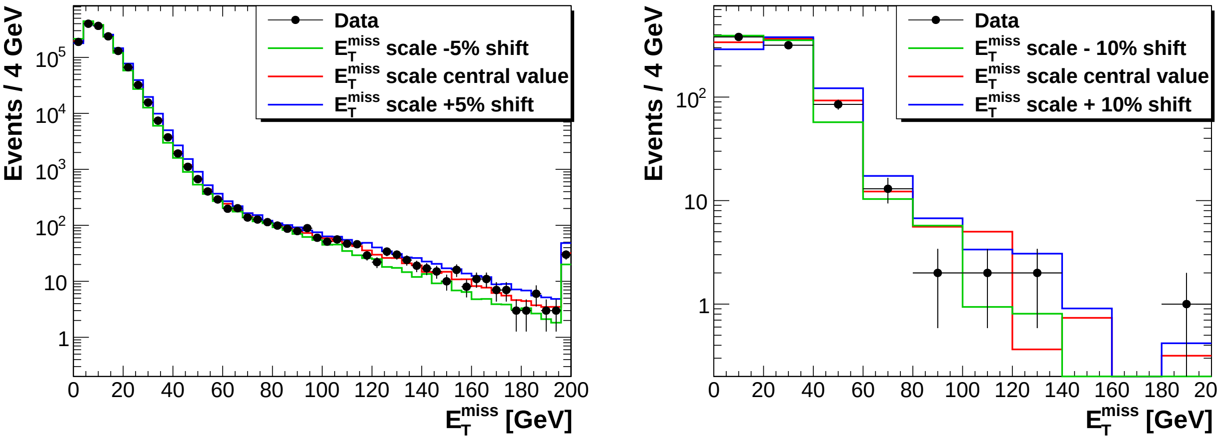

Figure 7.18: The MET distribution in data and in simulated sample for preselected dimuon events events (left) and for events selected in the VBF category (right). The coloured lines indicate the effect of a ±5(10)% shift in the MET scale on the MET distributions.

The MET scale is estimated independently for two classes of events $Z/\gamma^* \to \mu\mu$ and $t\bar{t}$ events. The first class already includes recoil corrections (section 7.3.2), while the $t\bar{t}$ sample in the second class does not contain any recoil correction.

Firstly, the MET is fitted in the region MET > 80 GeV, which is dominated by $t\bar{t}$ events. The fit is performed with the absolute normalisation and the MET scale shift for top pair events as free parameters. At this stage, the MET scale for the $Z/\gamma^* \to \mu\mu$ sample is set to zero. The fit yields the following values for the $t\bar{t}$ normalisation relative to the value predicted by MC simulation:

$$\text{Norm.}(t\bar{t}) = 0.95 \pm 0.07.$$

and the relative shift in the MET scale is estimated to be

$$\Delta(\alpha_{\text{MET}})(t\bar{t}) = (1.2 \pm 4.0)\%$$

The correlation matrix for the two fit parameters is

$$\begin{pmatrix} 1 & -0.05 \\ -0.05 & 1 \end{pmatrix}.$$

The second fit is performed in the region MET > 80 GeV, which is dominated by $Z/\gamma^* \to \mu\mu$ events. The absolute normalisation and MET scale of the $t\bar{t}$ sample are fixed to the optimised values from the first fit. The shift in the MET scale for the inclusive $Z/\gamma^* \to \mu\mu$ sample is found to be consistent with zero within the uncertainty of 0.5%.

The MET scale is determined separately for the VBF event category, where the MET variable is directly used in the event selection. This category suffers from low statistics so the determination of the absolute normalisation and the MET scale for the $t\bar{t}$ sample is not possible. The corresponding parameters are therefore fixed to the nominal values and a fit is performed to extract the MET scale in the sample of $Z/\gamma^* \to \mu\mu$ events, selected in the VBF category. The parameter optimisation yields:

$$\Delta(\alpha_{\mathrm{MET}}^{\mathrm{VBF}})(\mathrm{Z} \to \mu\mu) = (-3 \pm 3)\%$$

Since the missing transverse energy is one of the variables used to construct the MVA discriminant that is used to select events in the VBF event category, for this category the uncertainty on the MET scale affects the normalisation of backgrounds estimated from MC simulation. Furthermore the MET is used for the reconstruction of the ditau mass with the SVFit method and therefore affects the shape of the SVFit ditau mass distribution. Therefore the MET scale uncertainty considered in the limit calculations by allowing the shapes and normalisations of the ditau invariant mass distributions to vary within the corresponding uncertainties while performing the fits to the observed data.

For the Higgs boson signal and $\mathrm{W} + \mathrm{Jets}$ and diboson background MC samples, parametric recoil corrections are applied and an uncertainty of 5% on the MET scale evaluated by other studies is considered for these samples.

MC statistical uncertainty

The limited statistics of the MC samples results in a statistical uncertainty of about 20% in the low statistics event categories, such as VBF and 1 jet categories, for the dominant $\mathrm{t\bar{t}}$ and $\mathrm{Z} \to \mu\mu$ backgrounds and of 10-100% for the signal MC samples.

The uncertainties considered in the analysis are summarised in table 7.8.

Experimental Uncertainties		Propagated to Limit Calculation			
Uncertainty	Estimate	0 jets	1 jet	VBF	b-tag
Muon ID and trigger	±2%	±4%	±4%	±4%	±4%
Jet energy scale	±2 − 5%	∓1%	±5%	±10%	±3 − 5%
b-tag efficiency	±10%	∓1%	∓2%	∓2%	±5 − 7%
Mis-tagging	±30%	±1%	±1%	±1%	∓2%
Norm. $\mathrm{Z} \rightarrow \tau\tau$	±3%	±3%	±5%	±13%	±3%
Statistics of the $\mathrm{Z} \rightarrow \tau\tau$ embedded sample		$< 1\%$	±3.5%	±8%	±3.5%
Norm. $\mathrm{Z} \rightarrow \mu\mu$ scaling factor	±2 − 10%	±2 − 10%	±2 − 10%	±2 − 10%	±2 − 10%
Rel. stat. uncert. $\mathrm{Z} \rightarrow \mu\mu$		–	±3%	±5%	±3%
Norm. $\mathrm{t\bar{t}}$	±8%	±8%	±8%	±8%	±8%
Norm. dibosons	±30%	±30%	±15 − 30%	±30 − 100%	±30%
Lumi for dibosons, W+jets and signal	±2.2%	±2.2%	±2.2%	±2.2%	±2.2%
MC statistics					
VBF signal		±8 − 10%	±20 − 23%	±8 − 10%	–
$gg \rightarrow \mathrm{H}$ signal		±6 − 8%	±20 − 30%	±50 − 100%	–
$\mathrm{b\bar{b}}\Phi$ signal		–	–	–	±7 − 18%
$gg \rightarrow \Phi$ signal		–	–	–	±22 − 100%
$\mathrm{Z} \rightarrow \mu\mu$		$< 1\%$	±20%	±22%	±1 − 2.5%
$\mathrm{t\bar{t}}$		±4%	±17%	±19%	±4 − 7%
MET scale	±1 − 5%	shape-altering uncertainty			

Theory Uncertainties (SM)		Propagated to Limit Calculation			
Uncertainty	Estimate	0 jets	1 jet	VBF	b-tag
PDF+α_s ($gg \rightarrow \mathrm{H}$)	-	±8%	±8%	±8%	-
PDF+α_s ($qq \rightarrow \mathrm{H}$)	-	±8%	±8%	±8%	-
PDF+α_s ($VH + t\bar{t}\mathrm{H}$)	-	±2%	±2%	±2%	-
$\mu_r/\mu_f(gg \rightarrow \mathrm{H})$	-	±12%	±17%	±25%	-
$\mu_r/\mu_f(qq \rightarrow \mathrm{H})$	-	±4%	±4%	±7%	-
$\mu_r/\mu_f(\mathrm{VH} + \mathrm{t\bar{t}H})$	-	±4%	±4%	±7%	-
Underlying event and PS	-	∓4%	±5%	±5%	-

Table 7.8: Uncertainties used for the statistical analysis.

7.6 Results

7.6.1 Composition of final selected samples

The numbers of expected background events and signal yields for the various event categories in the analysis are reported in table 7.9.

Process	0-Jets	1-Jet	VBF
Z→ $\tau\tau$	15202 ± 519	4047 ± 169	87 ± 8
Z→ $\mu\mu$	1425917 ± 87710	530352 ± 39352	256 ± 54
QCD	1026 ± 50	520 ± 34	7 ± 4
$t\bar{t}$	3996 ± 361	1942 ± 184	16 ± 3
W+jets	42 ± 2	688 ± 69	3.3 ± 0.4
Dibosons	2479 ± 581	4587 ± 1118	11 ± 4
Total Background	1448705 ± 87710	541484 ± 39368	377 ± 56
H→ $\tau\tau$	-	36 ± 3	3 ± 0.6
Data	1420083	533257	360
Signal Eff.			
gg→ H	-	$1.39{\cdot}10^{-3}$	$6.99{\cdot}10^{-5}$
qq→ qqH	-	$2.93{\cdot}10^{-3}$	$1.17{\cdot}10^{-3}$
qq→ H$t\bar{t}$ or VH	-	$3.64{\cdot}10^{-3}$	$1.65{\cdot}10^{-4}$

Table 7.9: Numbers of expected and observed events in the event categories for the data taken in 2011 and 2012, corresponding to 17 fb^{-1}, as described in section 7.3. The categories of high and low p_T are summed. Listed are the expected signal yields for SM Higgs boson with $m_H = 125$ GeV as well as the reconstruction and selection signal efficiency for the various production mechanisms considered. Combined statistical and systematic uncertainties on each estimate are reported.

7.6.2 Mass information used for statistical inference

The final discriminating object used for the statistical interpretation of the observed data is a two dimensional distribution of the the visible invariant mass of the muon pair and the invariant mass reconstructed using the SVFit algorithm (section 5.7.2). This way the optimal separation between signal and background is achieved. The two-dimensional distributions are shown in figure 7.19 for the dominant background processes $Z/\gamma^* \to \mu\mu$ and $Z \to \tau\tau$ and for the signal expected for different Higgs boson mass hypotheses. It is clear that the signal and the most significant background processes lay on different areas of the two dimensional plane.

7.6.3 Statistical method

The results are interpreted as 95% confidence level (CL) exclusion limits on the Higgs cross section in the SM case and the $\tan\beta$ as a function of m_A in the MSSM case. For the statistical analysis, combination and limit calculation the ROOSTATS package was used [69].

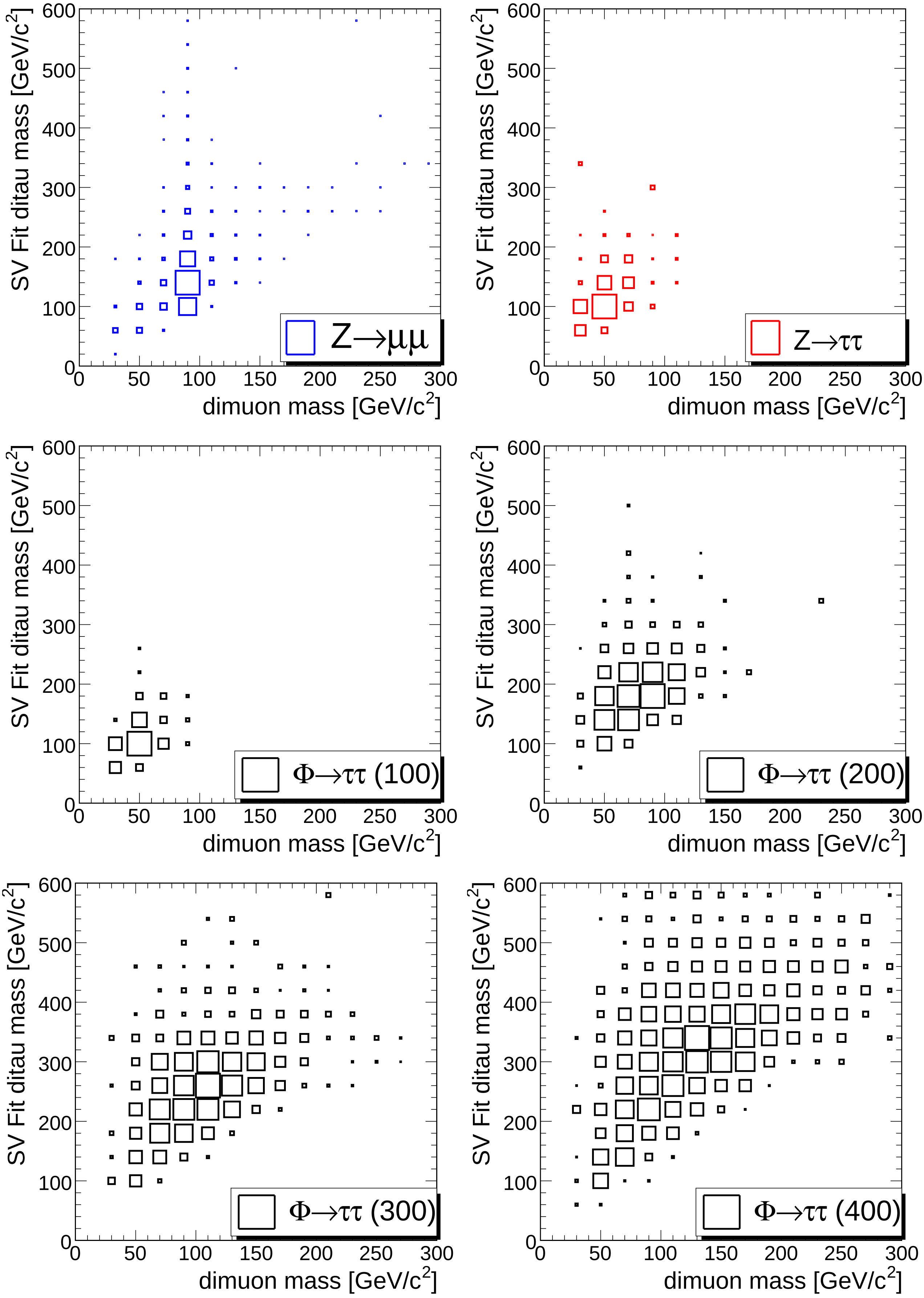

Figure 7.19: Two-dimensional distributions of the ditau mass reconstructed with SVFit algorithm against the visible dimuon mass, illustrating their discriminating power. The two main background processes and signal are presented, as indicated.

The statistical analysis approach used in a modified-frequentist $\mathrm{CL_S}$ method, as recommended by the LHC HCG group [51]. Modified-frequentist limits are obtained with a test statistic based on a profile likelihood ratio. The nuisance parameters are determined so that they best describe the experimental data and therefore maximise the likelihood function. More details on this method can be found in section 5.10.

The prior probability on the nuisance parameters is assumed to have a log-normal form for each of the sources assumed. When needed, they are correlated among categories of events, signal or background sources.

The two-dimensional distribution of the ditau mass against the dimuon mass is binned with a non-equidistant binning that allows to keep sufficient statistics in large mass tails of the distributions. The probability for the observation in each bin is described as a Poisson probability with a mean corresponding to the sum of yields expected from each of the sources of events assumed. The processes considered are the qqH, $gg \to \mathrm{H}$, WH, ZH and $\mathrm{t\bar{t}H}$ SM signal, $\mathrm{b\bar{b}}\Phi$ and $gg \to \Phi$ MSSM signal, as well as six background processes $\mathrm{Z} \to \tau\tau$, $\mathrm{Z}/\gamma* \to \mu\mu$, QCD, $\mathrm{t\bar{t}}$ plus jets, dibosons, W jets.

The exclusion limits on $\sigma(pp \to \mathrm{H})/\sigma_{SM}$, in the SM analysis, are set for m_{H} masses assumed in the range 110-145 GeV/c^2.

Following the blinding policy, the analysis was optimised without looking at the data in the signal region of the ditau mass distribution. Figure 7.20 shows expected and observed limits on the cross section of the SM Higgs production relative to the value predicted by the SM.

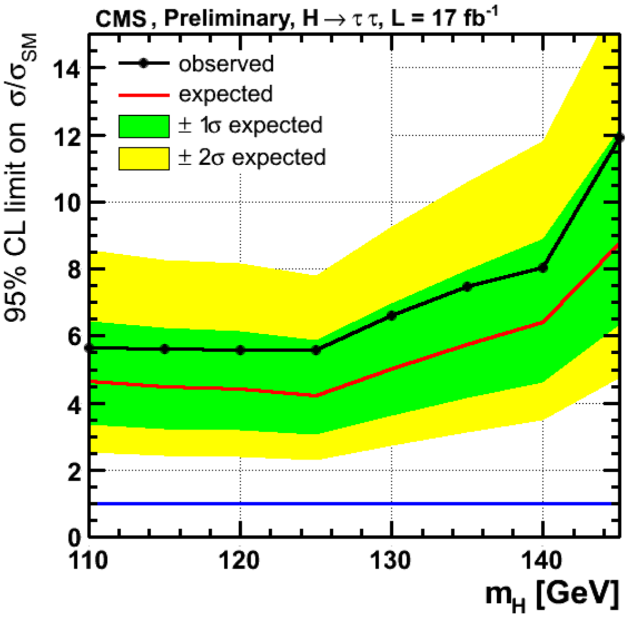

Figure 7.20: The expected 95% C.L. upper limits on the ratio r of the cross section of the SM Higgs boson, $\sigma(pp \to H)$, relative to the value predicted by the SM as a function of the SM Higgs boson mass m_{H}. The observed limit (black line with points) is shown together with $\pm 1\,\sigma$ and $\pm 2\,\sigma$ bands with respect to the expected median limits (red line).

7.7 Combination of all $\mathrm{H} \to \tau\tau$ final states

7.7.1 Search for the Standard Model Higgs boson

The search for the SM Higgs boson decaying to τ leptons, in CMS is performed in five final states [48]:

- $e\mu$
- $\mu\mu$
- $\mu\tau_{had}$
- $e\tau_{had}$
- $\tau_{had}\tau_{had}$

where τ_{had} denotes the hadronic tau decay.

In all final states datasets of 4.9 pb^{-1} and 12.1 fb^{-1} at 7 and 8 TeV were used respectively. Exception is the $\tau_{had}\tau_{had}$ channel where a special trigger was introduced in 2012 and made this search possible. The events in all final states are categorised according to jet multiplicity and the p_{T} of the leading τ_{had} or μ in the fully leptonic final states, as described in section 7.3.6. Different selection techniques are applied in each channel, but the final signal yield is taken from the ditau invariant mass reconstructed with the SVFit algorithm. Exception is the $\mu\mu$ final state where a two dimensional distribution was used as described in the previous section. Figure 7.22 shows the distribution of the ditau reconstructed mass for the $\mu\mu$ channel after the global fit is performed. The signal sensitivity that can be expected from each final state alone and their combination, is illustrated in figure 7.21, on the left, in terms of exclusion limits. Figure 7.21, on the right shows the expected limits for each category and their combination.

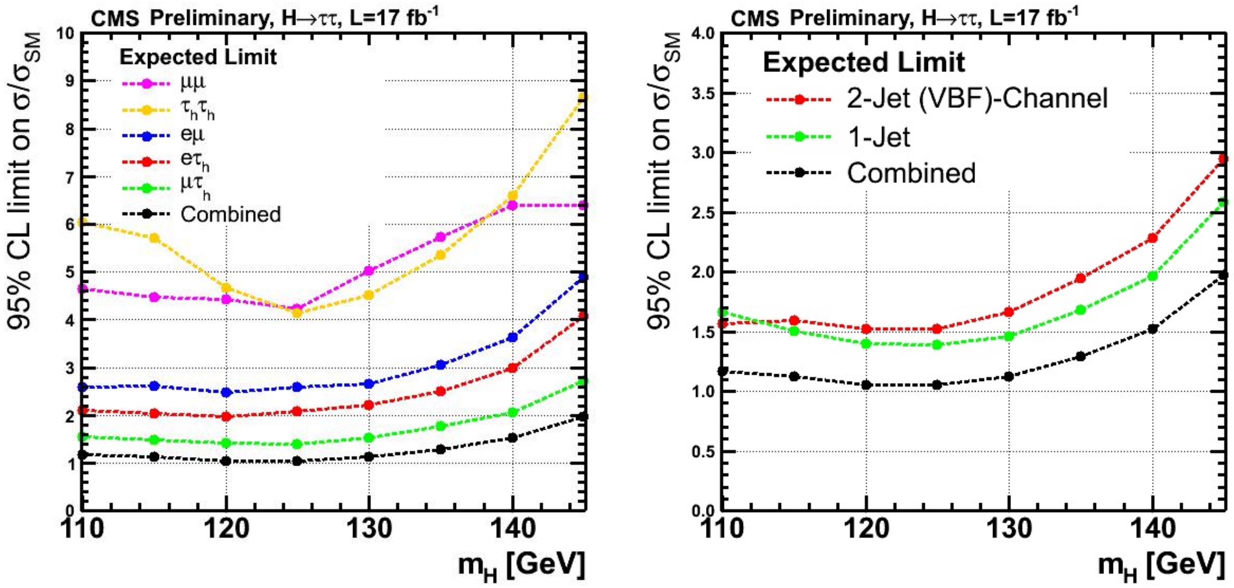

Figure 7.21: The SM analysis sensitivity is compared channel by channel on the left and by category on the right, in terms of expected limits. Source: [48]

In addition, there are two more independent searches, looking for Higgs produced in association with a vector boson Z or $W^{\pm}$ [70]. These searches suffer less from background than

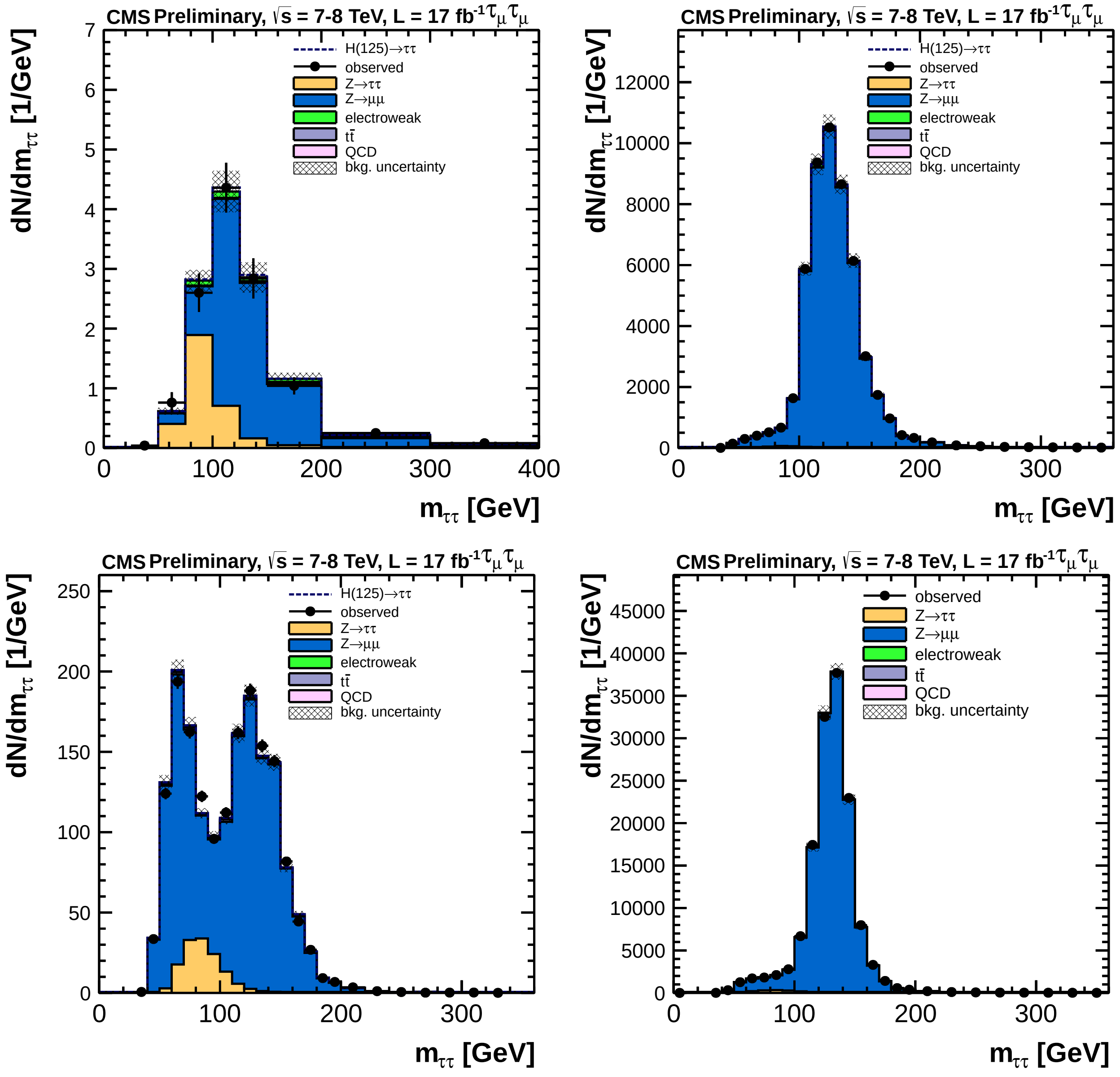

Figure 7.22: Distributions of the ditau reconstructed mass of the event categories combined in the $\mu\mu$ channel, after the global fit is performed. From the top left: VBF, 1 jet high-p_T, 1 jet low-p_T and 0 jets categories. Source: [48]

the inclusive search. The final signal yield is extracted from the visible mass of the final decay products.

The CMS result is a combination of all the above final states. No evidence of Higgs signal was observed therefore the results are interpreted as upper 95% CL limits to the SM Higgs production cross section times the branching fraction of the Higgs decaying into a tau pair. The limits are calculated using the modified CL_s method, as in the $\mu\mu$ analysis (section 7.6). In the limit setting only the 1 jet and VBF categories contribute. Figure 7.23 shows the combined limits. On the left the background only hypothesis is presented and on the right our observation is compared to the expectation by a SM Higgs with mass 125 GeV. The best fit signal strength is shown in figure 7.24. The data seem to be compatible with both hypothesis. More results are needed at this point for a conclusive result. An update of this analysis with the full 2012 dataset is presented in the next chapter, section 7.9.

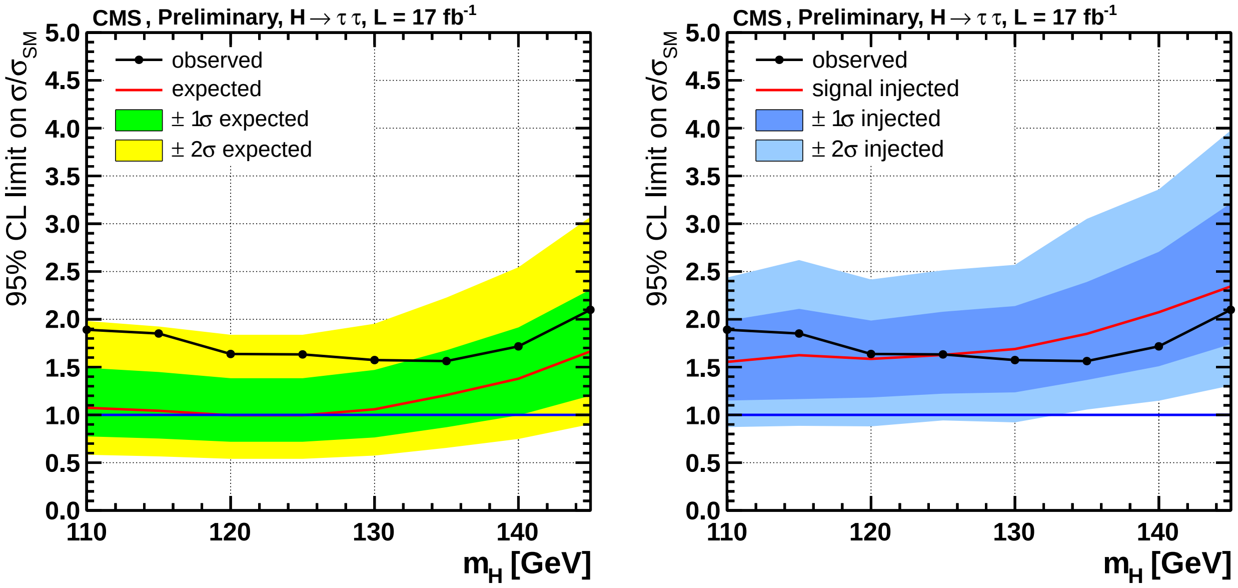

Figure 7.23: The observed 95% CL upper limit, together with the expected one and two standard deviation ranges on the cross section normalised to the SM expectation for Higgs boson production as a function of m_{H}. On the left the observed limit compared to the expectation for the background only hypothesis. On the right our observation is compared against the expectation for a SM Higgs with $m_{\mathrm{H}} = 125$ GeV. The experimental results seem compatible with both hypothesis. Source: [48]

7.7.2 Search for an MSSM Higgs boson

The $\mathrm{H} \to \tau\tau$ is the only channel exploited for MSSM Higgs searches in CMS [71]. The $\tau\tau$ final states included in this study are those where at least one of the τ decays leptonically:

- $e\mu$
- $\mu\mu$
- $\mu\tau_{had}$
- $e\tau_{had}$

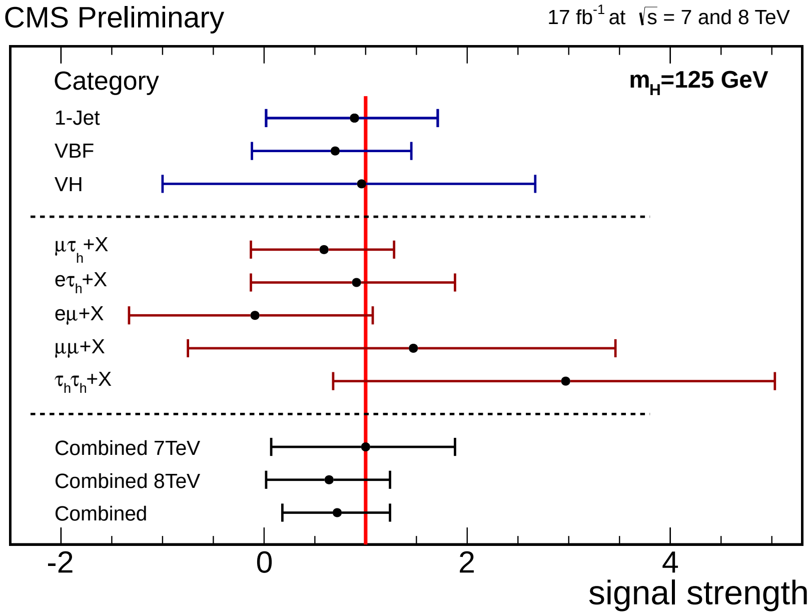

Figure 7.24: Best fit signal strength $\sigma/\sigma_{\mathrm{SM}}$, by category with all decay channels combined, by final state and the combination of all decay modes. The red line at one indicated the SM Higgs expectation. Source: [48]

All the channels used the same event categorisation as in the $\mu\mu$ final state. To enhance the sensitivity to neutral MSSM Higgs bosons, the search exploited the case where the Higgs boson is produced in association with a b quark jet, therefore the categories combined are the b-tag and the no b-tag category. The analysis sensitivity in the form of expected exclusion limits, is compared in every channel and every category in figure 7.25. The reconstructed ditau mass distributions for the $\mu\mu$ channel are shown in figure 7.26. No excess is observed in the tau pair invariant mass spectra in any of the channels, thus exclusion limits are calculated for the m_{maxh} scenario in the MSSM parameter space. The result is presented in figure 7.27.

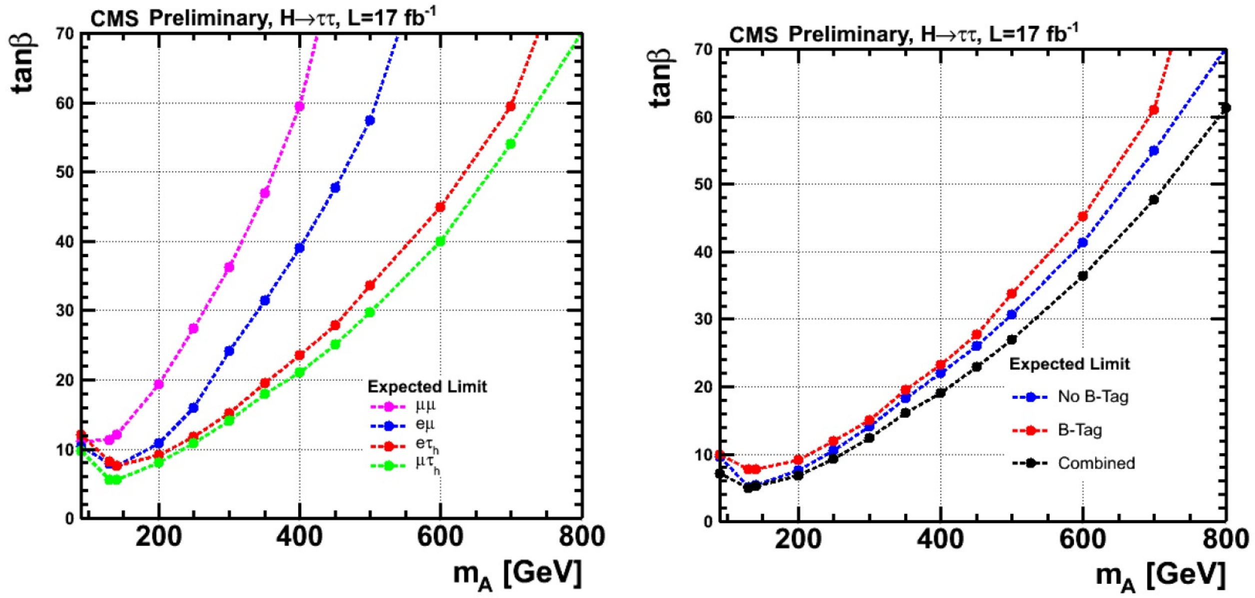

Figure 7.25: The MSSM analysis sensitivity is compared channel by channel on the left and by category on the right, in terms of expected limits. Source: [71]

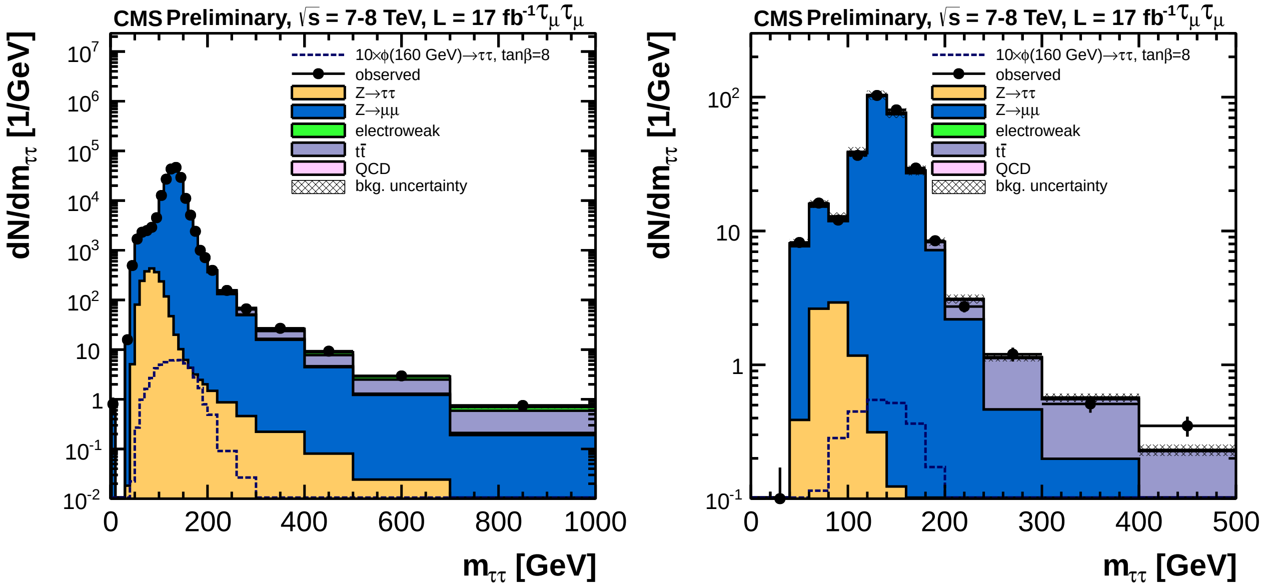

Figure 7.26: The reconstructed ditau invariant mass for the $\mu\mu$ channel. Left is the no b-tag category and right the b-tag category. Source: [71]

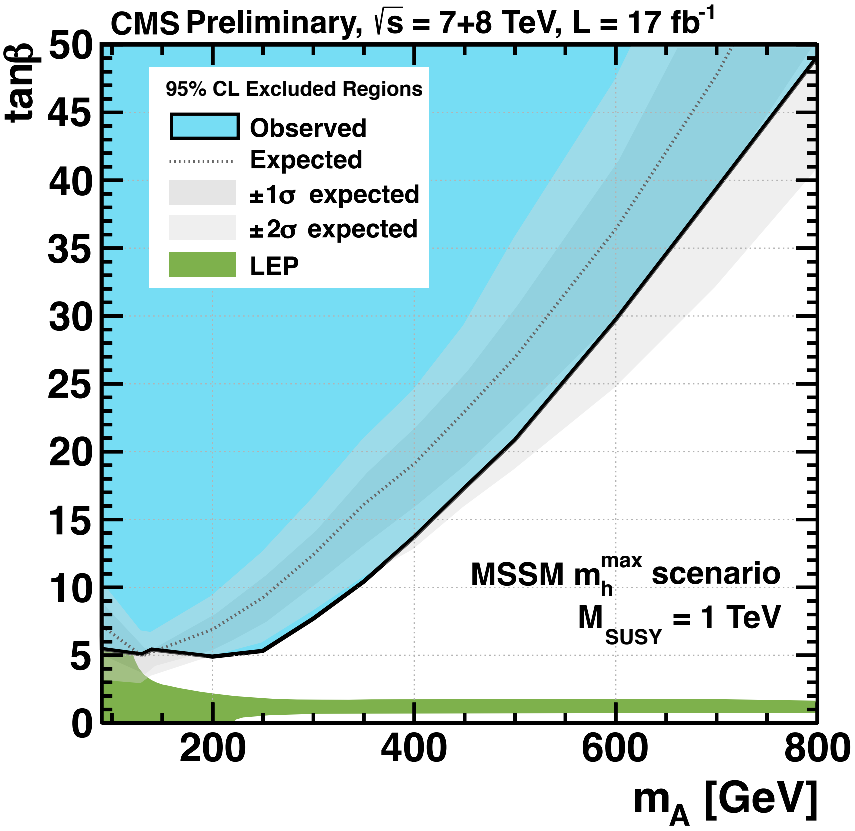

Figure 7.27: Exclusion at 95% CL in the ($\tan\beta$, m_A) parameter space for the MSSM m_{maxh} scenario. The exclusion limits from the LEP experiments are also shown. Source: [71]

7.8 The Higgs boson discovery

On the 4^{th} of July 2012, the discovery of a new scalar boson was announced by both CMS and ATLAS collaborations [72, 73]. The news caused a lot of excitement in the physics community. It was a historical day for particle physics and the discovery of the new boson is considered a triumph for the SM theory. The CERN general director Rolph Heuer said at the time: "As a layman I would say 'We have it', but as a scientist I would have to say 'What do we have?'".

"We have it" In CMS five decay modes of the Higgs are studied: $\gamma\gamma$, ZZ, WW, $\tau\tau$ and $b\bar{b}$. At the time of the Higgs discovery, the data analysed corresponded to integrated luminosities of 5.1 fb^{-1} at 7 TeV centre of mass energy and 5.3 at 8 TeV. An excess of events above the expected SM background was observed with a local significance of 4.9 σ around 125 GeV (figure 7.28), attributed to a new particle. A five-sigma level of certainty is the definition of discovery within the field of particle physics. Equivalent results were published at the same time by the ATLAS collaboration.

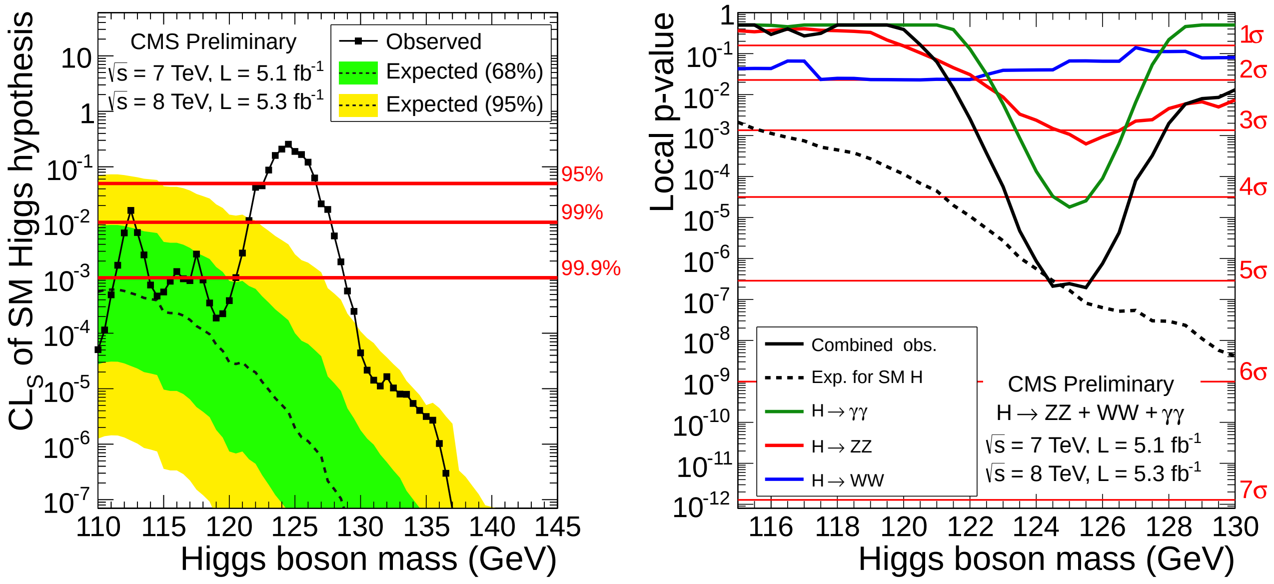

Figure 7.28: Left: The CLs values for the SM Higgs boson hypothesis as a function of the Higgs boson mass in the range 110-145 GeV. Right: The observed local p-value for the bosonic decay modes, $\gamma\gamma$, ZZ→ $4l$, and WW $\rightarrow l\nu$, as a function of the Higgs boson mass. The dashed lines show the expected local p-values $p_0(\mathrm{m_H})$, should a SM Higgs boson with a mass $\mathrm{m_H}$ exist. Source: [72]

"What do we have?" Physicists expect this new particle to be a Higgs boson. A Higgs with mass 125 GeV is favoured by the SM. However there are SUSY scenarios which predict a Higgs boson at this mass, as well as other beyond SM theories to be examined.

The latest CMS results are obtained with data corresponding to integrated luminosities of 5.1 fb^{-1} at 7 TeV and 19.6 fb^{-1} at 8 TeV [74]. The mass of the new boson is measured to be 125.7±0.3(stat.)±0.3(syst.) GeV/c^2. Further studies were made to test the consistency with a SM Higgs. The best fit value for signal strength modifier $\hat{\mu} = \hat{\sigma}/\sigma_{SM}$, for all channels combined, was compared to the the SM expectation. The observed value, 0.80±0.14 σ_{SM} at the measured mass, is compatible with $\mu_{SM} = 1$. In addition measurements of the Higgs couplings and spin were in agreement with the SM expectation.

So far there is no evidence for new physics, however the current statistics is not sufficient for concluding results. More data are needed in order to determine the properties of the new boson.

Until otherwise proven, this new particle will be referred to as “the Higgs boson”.

7.9 Evidence for Higgs coupling to τ leptons

The CMS searches the $\mathrm{H} \rightarrow \tau\tau$ channel in five final states:

- $e\mu$
- $\mu\mu$
- $\mu\tau_{had}$
- $e\tau_{had}$
- $\tau_{had}\tau_{had}$

plus two more, for the case where the Higgs is produced in association with a vector boson Z or W:

- $\mathrm{WH} \rightarrow l\tau\tau$
- $\mathrm{ZH} \rightarrow ll\tau\tau$

The final result is a combination of all the above final states. The analysis of the $\mu\mu$ final state included in the latest CMS combination is the same as the one described in the previous chapters, with a few minor changes. The combination of these searches using all the data collected in 2011 (4.9 fb^{-1}) and 2012 (19.4 fb^{-1}) in the LHC [75], shows an excess of events with with a maximum local significance 2.93 σ at $m_{\mathrm{H}} = 120$ GeV. This excess is compatible with the presence of a standard model Higgs boson of mass $m_{\mathrm{H}} = 125$ GeV, for which the local significance is 2.85 σ. Figure 7.29 shows the exclusion limits for the background only and the signal plus background expectation, as well as the observe and expected p-value curves.

The best fit value for the common signal strength modifier $\hat{\mu} = \sigma/\sigma_{SM}$, obtained in the combination of all search channels, shown in figure 7.30, provides the another compatibility test. It is found to be $\hat{\mu} = 1.1 \pm 0.4$ at $\mathrm{m_H} = 125$ GeV which is consistent with the SM ($\hat{\mu} = 1$). These are the first indications that the new boson discovered last year couples to τ leptons, with a strength compatible to the one predicted by the standard model.

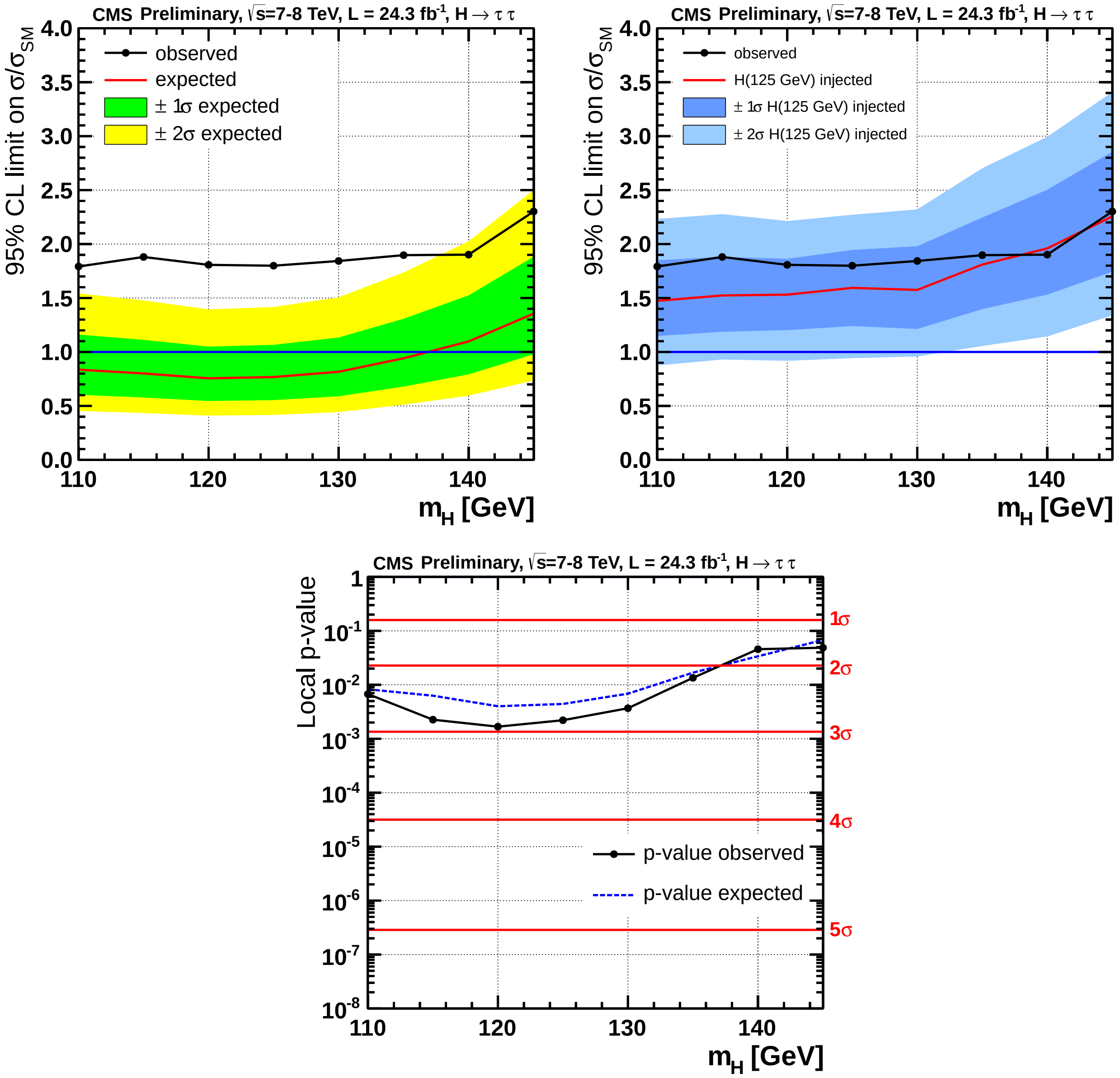

Figure 7.29: Combined observed 95% CL upper limit on the signal strength parameter $\mu = \sigma/\sigma_{SM}$, together with the expected limit obtained in the background hypothesis (top), the signal plus background hypothesis for a SM Higgs boson with $m_H = 125$ GeV (bottom left). The bands show the expected 1 and 2 σ probability intervals around the expected limit. These results include the search for a SM Higgs boson decaying into a τ pair and produced in association with a W or a Z boson decaying leptonically. Source: [75]

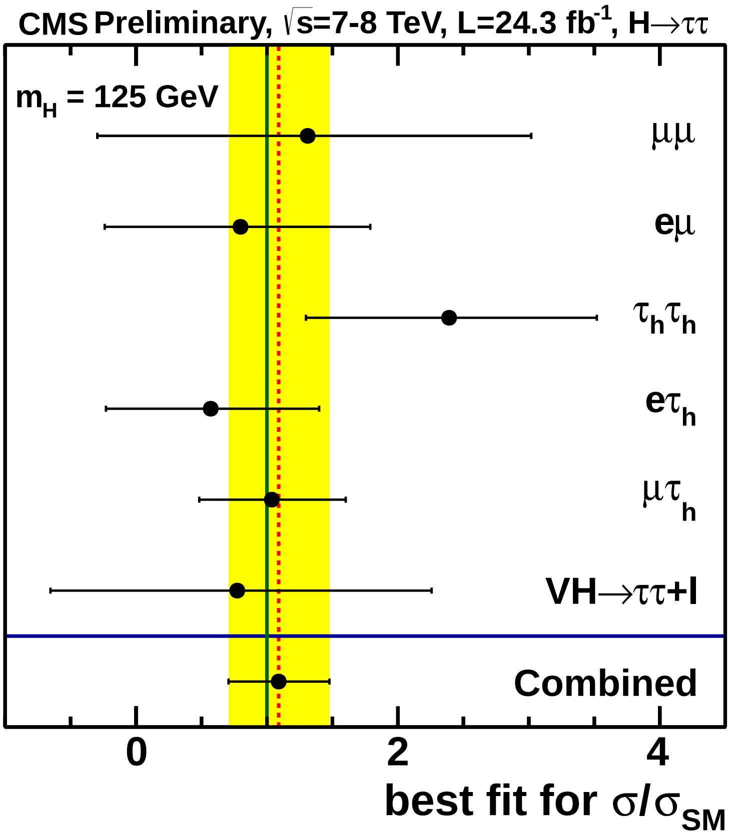

Figure 7.30: The best fit value for the common signal strength modifier $\hat{\mu} = \sigma/\sigma_{SM}$, obtained in the combination of all search channels, versus the hypothesised Higgs boson mass m_{H}. The band corresponds to the $\pm 1\,\sigma$ uncertainty. The combined result of the analysis with the search for a SM Higgs boson decaying into a τ pair and produced in association with a W or Z boson decaying leptonically, is shown as the red dotted line. Source: [75]

Chapter 8

Summary

This doctoral thesis describes the efforts to observe and analyse $\tau\tau$ events when both τ leptons decay into muons. This final state is particularly challenging because of the high DY background and the small branching fraction of the $\tau\tau \rightarrow \mu\mu$, which is 2.9%.

Starting in 2010 we studied the Z $\rightarrow$ $\tau\tau$ $\rightarrow$ $\mu\mu$ decay and we measured the Z boson production cross section in proton-proton collisions to be:

$$\sigma(pp \rightarrow Z) \cdot \mathrm{Br}(Z \rightarrow \tau\tau) = 1.14 \pm 0.27\,(\mathrm{stat.}) \pm 0.04\,(\mathrm{syst.}) \pm 0.05\,(\mathrm{lumi.})\ \mathrm{nb}.$$

The data analysed correspond to 36 pb^{-1}. The events were selected using a multivariate likelihood technique. The main background contributions were estimated in data driven ways. The analysis methods developed for the study of the Z boson decay, were used for commissioning the neutral Higgs boson searches that followed. The results, combined with other $\tau\tau$ final states, $\mu\tau_{had}$, $e\tau_{had}$ and $e\mu$, lead to the final CMS measurement of the Z production cross section. The measurements are consistent with each other, but also in agreement with theoretical NNLO prediction and previous CMS measurements.

The search for neutral Higgs bosons in the H $\rightarrow$ $\tau\tau$ $\rightarrow$ $\mu\mu$ channel, was performed in CMS data, 5 fb^{-1} collected at 7 TeV in 2011 and 12 fb^{-1} at 8 TeV in 2012. In this data-taking period the running conditions of the LHC changed and the instantaneous luminosity increased, increasing at the same time the number of pile-up events. A number of corrections were applied to the MC samples in order to model the pile-up and new definitions for physics objects, like MET and jets, were introduced taking into account the pile-up effect. The analysis was optimised by using sophisticated methods. The events were classified according to the Higgs production mechanism and the final samples were selected by a boosted decision tree. The irreducible background of Z $\rightarrow$ $\tau\tau$ was evaluated using the embedding technique, were muons in real Z $\rightarrow$ $\mu\mu$ events are replaced by simulated τ leptons. Both the SM and the MSSM scenario were examined, using different event categorisation in each of them.

In the meantime on the 4th of July last year (2012), a new neutral boson, with mass around 125 GeV was discovered by the final states with high mass resolution $\gamma\gamma$ and ZZ $\rightarrow 4l$. Measurements of the spin show that the boson is scalar which makes it compatible with the Higgs boson as expected by the SM. According to the latest CMS measurement, the Higgs boson mass is 125.7±0.3(stat.)±0.3(syst.) $\mathrm{GeV/c^2}$.

An update of the H $\rightarrow$ $\tau\tau$ $\rightarrow$ $\mu\mu$ analysis, based entirely on the analysis presented in this thesis, was performed with the full 2011 and 2012 datasets. The data analysed correspond to integrated luminosity of 19 fb^{-1} at 8 TeV plus 7 fb^{-1} at 5 TeV from 2011. The results were combined with the four more $\tau\tau$ final states, $\mu\tau_{had}$, $e\tau_{had}$, $e\mu$ and $\tau_{had}\tau_{had}$ as well as two more final states where the Higgs is produced in association with a vector boson Z or W, $ll\tau$ and $l\tau$ respectively. This combination lead to the first evidence of the Higgs boson coupling to τ leptons.

Declaration

The work presented in this thesis was carried out between January 2010 and November 2012.

The first year was spent studying the Z $\rightarrow \tau\tau \rightarrow \mu\mu$ decay that lead to the measurement of the Z production cross section. This is the result of my own studies, with the support of the DESY and the KIT CMS groups.

In 2011 and 2012 the study was focused on Higgs searches in the H $\rightarrow \tau\tau \rightarrow \mu\mu$ channel. I personally worked on every stage of the analysis during this time, with my major contribution being the multivariate signal selection and the data driven background estimations. The final result was collaborative work between the members of the joint DESY/KIT Higgs analysis group and constrained by the guidelines of the CMS H $\rightarrow \tau\tau$ group. The main methods developed in this analysis were applied in the search for Higgs bosons in the H $\rightarrow \tau\tau \rightarrow ee$ final state.

Some results of other CMS groups are mentioned in this thesis in order to set the H $\rightarrow \tau\tau \rightarrow \mu\mu$ analysis into the context of Higgs searches at CMS. This is explicitly referenced in the corresponding sections.

References

[1] S. Glashow. *Partial symmetries of weak interactions.* Nucl.Phys., 22:579–588, 1961. doi:10.1016/0029-5582(61)90469-2.

[2] S. Weinberg. *A model of leptons.* Phys. Rev. Lett., 19:1264–1266, 1967. doi:10.1103/PhysRevLett.19.1264.
URL `http://link.aps.org/doi/10.1103/PhysRevLett.19.1264`

[3] A. Salam. *Weak and electromagnetic interactions.* In *Elementary particle theory*, 367–377. Almquist & Wiksell, 1968.

[4] M. Gellmann. *A schematic model of baryons and mesons.* Physics Letters, 8:214–215, 1964. doi:10.1016/S0031-9163(64)92001-3.

[5] G. Zweig. *An SU_3 model for strong interaction symmetry and its breaking.* CERN-TH-412, 22–101, 1964.

[6] M. E. Peskin and D. V. Schroeder. *An introduction to quantum field theory.* Westview Press, 1995.

[7] C. Burgess and G. Moore. *The Standard Model: A Primer.* Cambridge University Press, 2006.
URL `http://dx.doi.org/10.1017/CBO9780511819698`

[8] F. Englert and R. Brout. *Broken symmetry and the mass of gauge vector mesons.* Phys. Rev. Lett., 13:321–323, 1964. doi:10.1103/PhysRevLett.13.321.
URL `http://link.aps.org/doi/10.1103/PhysRevLett.13.321`

[9] P. W. Higgs. *Broken symmetries and the masses of gauge bosons.* Phys. Rev. Lett., 13:508–509, 1964. doi:10.1103/PhysRevLett.13.508.
URL `http://link.aps.org/doi/10.1103/PhysRevLett.13.508`

[10] P. W. Higgs. *Spontaneous symmetry breakdown without massless bosons.* Phys.Rev., 145:1156–1163, 1966. doi:10.1103/PhysRev.145.1156.

[11] G. S. Guralnik, C. R. Hagen and T. W. B. Kibble. *Global conservation laws and massless particles.* Phys. Rev. Lett., 13:585–587, 1964. doi:10.1103/PhysRevLett.13.585.
URL `http://link.aps.org/doi/10.1103/PhysRevLett.13.585`

[12] B. W. Lee, C. Quigg and H. B. Thacker. *Weak interactions at very high energies: The role of the Higgs boson mass.* Phys. Rev. D, 16:1519–1531, 1977. doi:10.1103/PhysRevD.16.1519.
URL `http://link.aps.org/doi/10.1103/PhysRevD.16.1519`

[13] J. Casas, J. Espinosa and M. Quiros. *Standard Model stability bounds for new physics within LHC reach.* Phys.Lett., B382:374–382, 1996. doi:10.1016/0370-2693(96)00682-X. `hep-ph/9603227`.

[14] T. Hambye and K. Riesselmann. *Matching conditions and Higgs mass upper bounds revisited.* Phys.Rev., D55:7255–7262, 1997. doi:10.1103/PhysRevD.55.7255. `hep-ph/9610272`.

[15] G. Isidori, G. Ridolfi and A. Strumia. *On the metastability of the Standard Model vacuum.* Nucl.Phys., B609:387–409, 2001. doi:10.1016/S0550-3213(01)00302-9. `hep-ph/0104016`.

[16] S. P. Martin. *A Supersymmetry primer.* Perspectives on supersymmetry II, 1–153, 1997. `hep-ph/9709356`.

[17] S. Dimopoulos and H. Georgi. *Softly broken Supersymmetry and SU(5)* . Nuclear Physics B, 193(1):150 – 162, 1981. ISSN 0550-3213. doi:10.1016/0550-3213(81)90522-8.
URL `http://www.sciencedirect.com/science/article/pii/0550321381905228`

[18] J. Wess and B. Zumino. *Supergauge transformations in four dimensions.* Nuclear Physics B, 70(1):39 – 50, 1974. ISSN 0550-3213. doi:10.1016/0550-3213(74)90355-1.
URL `http://www.sciencedirect.com/science/article/pii/0550321374903551`

[19] LHC Higgs Cross Section Working Group. 2010-2013.
URL `https://twiki.cern.ch/twiki/bin/view/LHCPhysics/CrossSections`

[20] L. Evans and P. Bryant. *LHC Machine.* Journal of Instrumentation, 3(08):S08001, 2008.
URL `http://stacks.iop.org/1748-0221/3/i=08/a=S08001`

[21] J.-L. Caron. *CERN accelerator complex (operating and approved projets).*, 1991. AC Collection. Legacy of AC. Pictures from 1992 to 2002.

[22] V. Duvivier. *Cross section of LHC dipole.*, 2001. AC Collection. Legacy of AC. Pictures from 1992 to 2002.

[23] J.-L. Caron. *LHC layout.*, 1997. AC Collection. Legacy of AC. Pictures from 1992 to 2002.

[24] The CMS Collaboration. *Public CMS luminosity information.* 2010-2013.
URL `https://twiki.cern.ch/twiki/bin/view/CMSPublic/LumiPublicResults`

[25] The CMS Collaboration. *The CMS experiment at the CERN LHC.* Journal of Instrumentation, 3(08):S08004, 2008. doi:10.1088/1748-0221/3/08/S08004.
URL `http://stacks.iop.org/1748-0221/3/i=08/a=S08004`

[26] The CMS Collaboration. *CMS Physics: Technical Design Report Volume 1: Detector Performance and Software.* Technical Design Report CMS. CERN, Geneva, 2006.

[27] The CMS Collaboration. *CMS Physics: Technical Design Report Volume 2: Physics Performance.* Technical Design Report CMS. CERN, Geneva, 2006.

[28] The CMS Collaboration. *The CMS magnet project: Technical Design Report.* Technical Design Report CMS. CERN, Geneva, 1997.

[29] The CMS Collaboration. *The CMS tracker system project: Technical Design Report.* Technical Design Report CMS. CERN, Geneva, 1997.

[30] The CMS Collaboration. *The CMS electromagnetic calorimeter project: Technical Design Report.* Technical Design Report CMS. CERN, Geneva, 1997.

[31] The CMS Collaboration. *The CMS hadron calorimeter project: Technical Design Report.* Technical Design Report CMS. CERN, Geneva, 1997.

[32] T. Virdee, M. Brice and L. Veillet. *Images of cms hcal endcap (he)*, 2008. CMS Collection.

[33] The CMS Collaboration. *The CMS muon project: Technical Design Report*. Technical Design Report CMS. CERN, Geneva, 1997.

[34] The CMS Collaboration. *CMS TriDAS project: Technical Design Report, Volume 1: The Trigger Systems*. Technical Design Report CMS. CERN, Geneva, 2000.

[35] The CMS Collaboration. *CMS The TriDAS Project: Technical Design Report, Volume 2: Data Acquisition and High-Level Trigger. CMS trigger and data-acquisition project*. Technical Design Report CMS. CERN, Geneva, 2002.

[36] E. Chabanat and N. Estre. *Deterministic annealing for vertex finding at CMS*. Computing in High Energy Physics and Nuclear Physics, 2004.

[37] The CMS Collaboration. *Particle-flow event reconstruction in CMS and performance for jets, taus, and MET*. Technical Report CMS-PAS-PFT-09-001, CERN, 2009. Geneva, 2009.

[38] The CMS Collaboration. *Commissioning of the particle-flow reconstruction in minimum bias and jet events from pp collisions at 7 TeV*. Technical Report CMS-PAS-PFT-10-002, CERN, Geneva, 2010.

[39] M. Cacciari, G. P. Salam and G. Soyez. *The anti-k_t jet clustering algorithm*. Journal of High Energy Physics, 2008(04):063, 2008.
URL `http://stacks.iop.org/1126-6708/2008/i=04/a=063`

[40] A. Hoecker et al. *TMVA - Toolkit for Multivariate data Analysis*. PoS ACAT, 2009. `physics/0703039`.
URL `http://arxiv.org/abs/physics/0703039`

[41] The CMS Collaboration. *Determination of jet energy calibration and transverse momentum resolution in CMS*. Journal of Instrumentation, 6(11):P11002, 2011.
URL `http://stacks.iop.org/1748-0221/6/i=11/a=P11002`

[42] The CMS Collaboration. *Performance of the b-jet identification in CMS*. Technical Report CMS-PAS-BTV-11-001, CERN, Geneva, 2011.

[43] The CMS Collaboration. *Performance of CMS muon reconstruction in pp collision events at $\sqrt{s}$= 7 TeV*. Journal of Instrumentation, 7(10):P10002, 2012.
URL `http://stacks.iop.org/1748-0221/7/i=10/a=P10002`

[44] The CMS Collaboration. *Particle-flow commissioning with muons and electrons from J/Psi and W events at 7 TeV*. Technical Report CMS-PAS-PFT-10-003, CERN, 2010. Geneva, 2010.

[45] Muon POG. *Reference efficiencies*. 2011,2012.
URL `https://twiki.cern.ch/twiki/bin/view/CMS/MuonReferenceEffs`

[46] The CMS Collaboration. *Performance of τ-lepton reconstruction and identification in CMS*. Journal of Instrumentation, 7(01):P01001, 2012.
URL `http://stacks.iop.org/1748-0221/7/i=01/a=P01001`

[47] R. Ellis, I. Hinchliffe, M. Soldate and J. V. D. Bij. *Higgs decay to $\pi^+\pi^-$: A possible signature of intermediate mass Higgs bosons at high energy hadron colliders.* Nuclear Physics B, 297(2):221 – 243, 1988. ISSN 0550-3213. doi:10.1016/0550-3213(88)90019-3.
URL `http://www.sciencedirect.com/science/article/pii/0550321388900193`

[48] The CMS Collaboration. *Search for the Standard Model Higgs boson decaying to tau pairs.* Technical Report CMS-PAS-HIG-12-043, CERN, Geneva, 2012.

[49] M. Bluj, A. Burgmeier, T. Früboes, G. Quast and M. Zeise. *Modelling of $\tau\tau$ final states by embedding τ pairs in $z \to \mu\mu$ events.* CMS Note, AN-2011-020, 2011.

[50] A. Burgmeier. *Data-driven estimation of Z^0 background contributions to the Higgs search in the $h \to \tau^+\tau^-$ channel with the CMS experiment at the LHC.* Master's thesis, Karlsruhe Institute of Technology, 2011.

[51] ATLAS and CMS Collaborations, LHC Higgs Combination Group. *Procedure for the LHC higgs boson search combination in Summer 2011.* ATL-PHYS-PUB/CMS NOTE 2011-11, 2011/005, CERN, 2011.
URL `http://cdsweb.cern.ch/record/1379837`

[52] G. Cowan, K. Cranmer, E. Gross and O. Vitells. *Asymptotic formulae for likelihood-based tests of new physics.* The European Physical Journal C, 71(2):1–19, 2011. ISSN 1434-6044. doi:10.1140/epjc/s10052-011-1554-0.
URL `http://dx.doi.org/10.1140/epjc/s10052-011-1554-0`

[53] R. Chierici et al. *Standard Model cross sections for CMS at 7 TeV.* https://twiki.cern.ch/twiki/bin/viewauth/CMS/StandardModelCrossSections, 2010.

[54] T. Sjöstrand, S. Mrenna and P. Skands. *Pythia 6.4 physics and manual.* JHEP, 0605:026, 2006.

[55] S. Alioli, P. Nason, C. Oleari and E. Re. *NLO vector-boson production matched with shower in POWHEG.* JHEP, 0807:060, 2008.

[56] S. Frixione, P. Nason and C. Oleari. *Matching NLO QCD computations with parton shower simulations: the POWHEG method.* JHEP, 0711:070, 2007.

[57] S. Jadach, Z. Was, R. Decker and J. Kuhn. *The tau decay library TAUOLA: Version 2.4.* Comput. Phys. Commun., 76:361–380, 1993.

[58] A. Ackerstaff et al. *Search for the Standard Model Higgs boson in e^+e^- collisions at $\sqrt{s}$ = 161 GeV - 172 GeV.* Eur. Phys. J., C1:425–438, 1998.

[59] K. Melnikov and F. Petriello. *Electroweak gauge boson production at hadron colliders through $\mathcal{O}(\alpha_s^2)$.* Phys. Rev. D, 74:114017, 2006. doi:10.1103/PhysRevD.74.114017.
URL `http://link.aps.org/doi/10.1103/PhysRevD.74.114017`

[60] The CMS Collaboration. *Measurement of the inclusive Z cross section via decays to tau pairs in pp collisions at $\sqrt{s} = 7$ TeV.* JHEP, 1108:117, 2011. doi:10.1007/JHEP08(2011)117. `1104.1617`.

[61] F. Maltoni and T. Stelzer. *Madevent: Automatic event generation with MADGRAPH.* JHEP, 0302:027, 2003.

[62] The CMS collaboration. *Determination of jet energy calibration and transverse momentum resolution in CMS.* Journal of Instrumentation, 6(11):P11002, 2011.
URL `http://stacks.iop.org/1748-0221/6/i=11/a=P11002`

[63] The CMS Collaboration. *Combination of top pair production cross sections measurements.* Technical Report CMS-PAS-TOP-11-024, CERN, Geneva, 2011.

[64] R. Kleiss and S. W.J. *Top quark production at hadron colliders: Some useful formulae.* Z. Phys., C40:419–423, 1988.

[65] U. Langenfeld, S. Moch and P. Uwer. *Measuring the running top-quark mass.* Phys. Rev., D80:054009, 2009.

[66] The CMS Collaboration. *Measurement of the W and Z inclusive production cross sections at* $\sqrt{s} = 7$ TeV *with the CMS experiment at the LHC.* Technical Report CMS-PAS-EWK-10-005, CERN, Geneva, 2010.

[67] S. Dittmaier et al. *Handbook of LHC Higgs cross sections: 1. inclusive observables.* CERN-2011-002, 2011. `1101.0593`.

[68] The CMS Collaboration. *B-tagging performance (efficiency and mistag rate) measurements from cms.* Technical Report CMS-PAS-BTV-11-001, CERN, Geneva, 2011.

[69] L. Moneta, K. Belasco, K. Cranmer, A. Lazzaro, D. Piparo, G. Schott, W. Verkerke and M. Wolf. *The RooStats Project.* In *13th International Workshop on Advanced Computing and Analysis Techniques in Physics Research (ACAT2010).* SISSA, 2010. PoS(ACAT2010)057, `1009.1003`.
URL `http://pos.sissa.it/archive/conferences/093/057/ACAT2010_057.pdf`

[70] The CMS Collaboration. *Search for the Standard Model Higgs boson decaying to tau pairs produced in association with a W or Z boson.* Technical Report CMS-PAS-HIG-12-051, CERN, Geneva, 2012.

[71] The CMS Collaboration. *Search for MSSM neutral Higgs bosons decaying to tau pairs in pp collisions.* Technical Report CMS-PAS-HIG-12-050, CERN, Geneva, 2012.

[72] The CMS Collaboration. *Observation of a new boson at a mass of 125 GeV with the CMS experiment at the LHC.* Phys.Lett., B716:30–61, 2012. doi:10.1016/j.physletb.2012.08.021. `1207.7235`.

[73] The ATLAS Collaboration. *Observation of a new particle in the search for the Standard Model Higgs boson with the ATLAS detector at the LHC.* Phys.Lett., B716:1–29, 2012. doi:10.1016/j.physletb.2012.08.020. `1207.7214`.

[74] The CMS Collaboration. *Combination of Standard Sodel Higgs boson searches and measurements of the properties of the new boson with a mass near 125 GeV.* Technical Report CMS-PAS-HIG-13-005, CERN, Geneva, 2013.

[75] The CMS Collaboration. *Search for the Standard Model Higgs boson decaying to tau pairs in proton-proton collisions at* $\sqrt{s} = 7$ *and 8 TeV.* Technical Report CMS-PAS-HIG-13-004, CERN, Geneva, 2013.

Appendix A

Recoil Corrections

In this appendix control plots showing the effect of the recoil corrections applied in order to bring simulation of the missing transverse energy in agreement with data. In order to reproduce the shapes of recoil momentum distributions, an isomorphic mapping technique is applied.

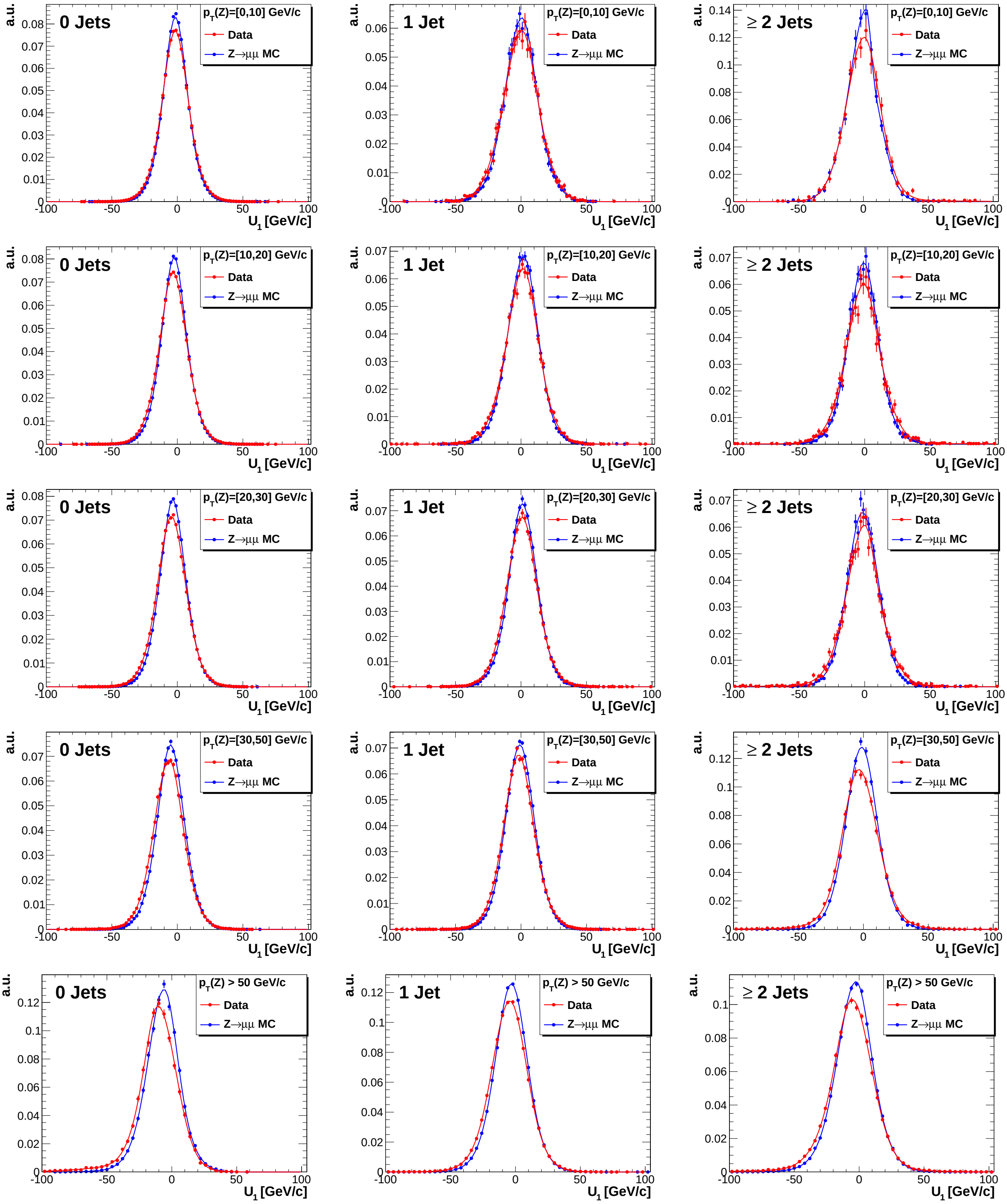

Figure A.1: Projected recoil momenta U_1 before the isomorphic mapping technique in 5x3 bins of Z-p_T (rows) and N_{jets} (columns)

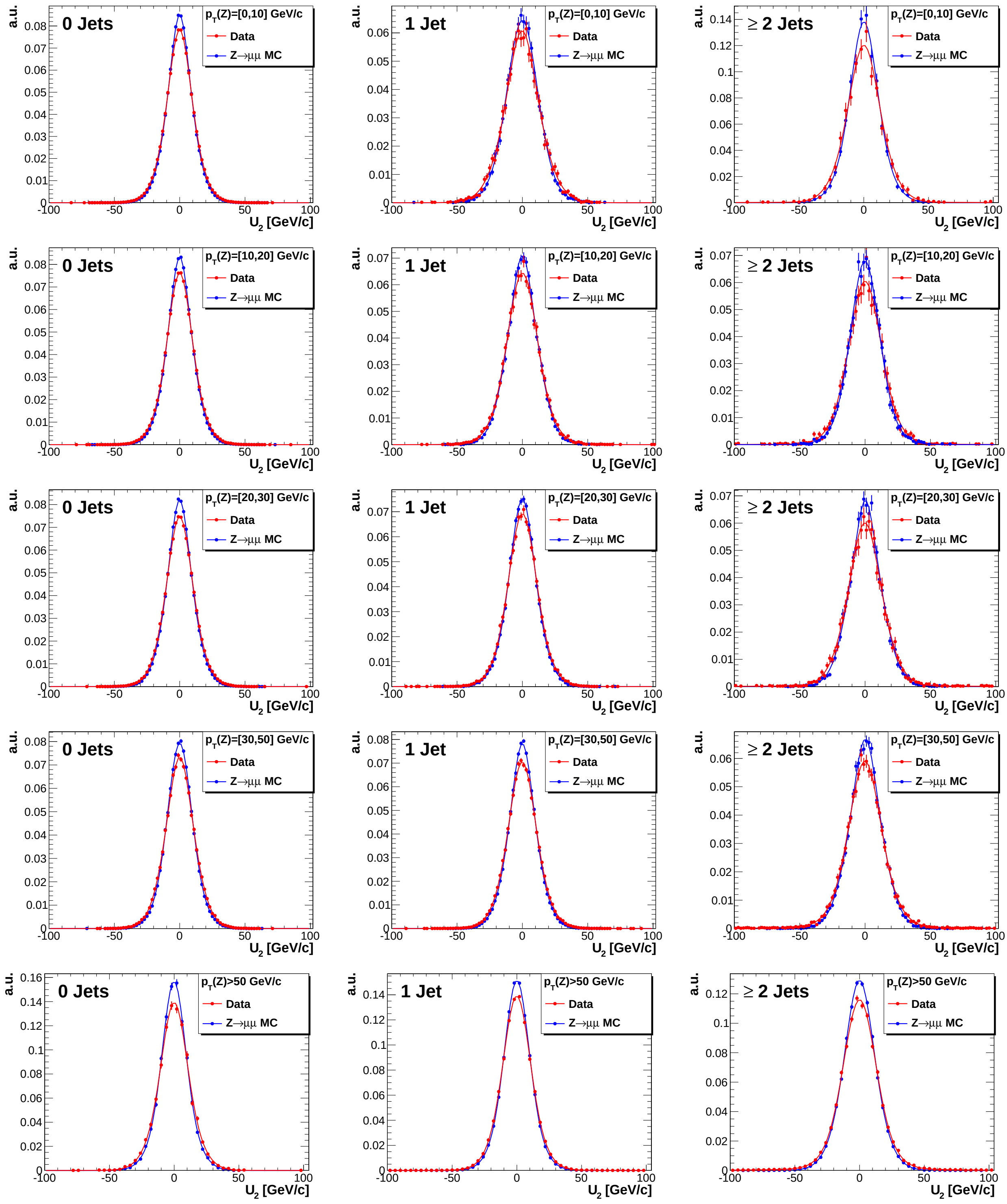

Figure A.2: Projected recoil momenta U_2 before the isomorphic mapping technique in 5x3 bins of Z-p_T (rows) and N_jets (columns)

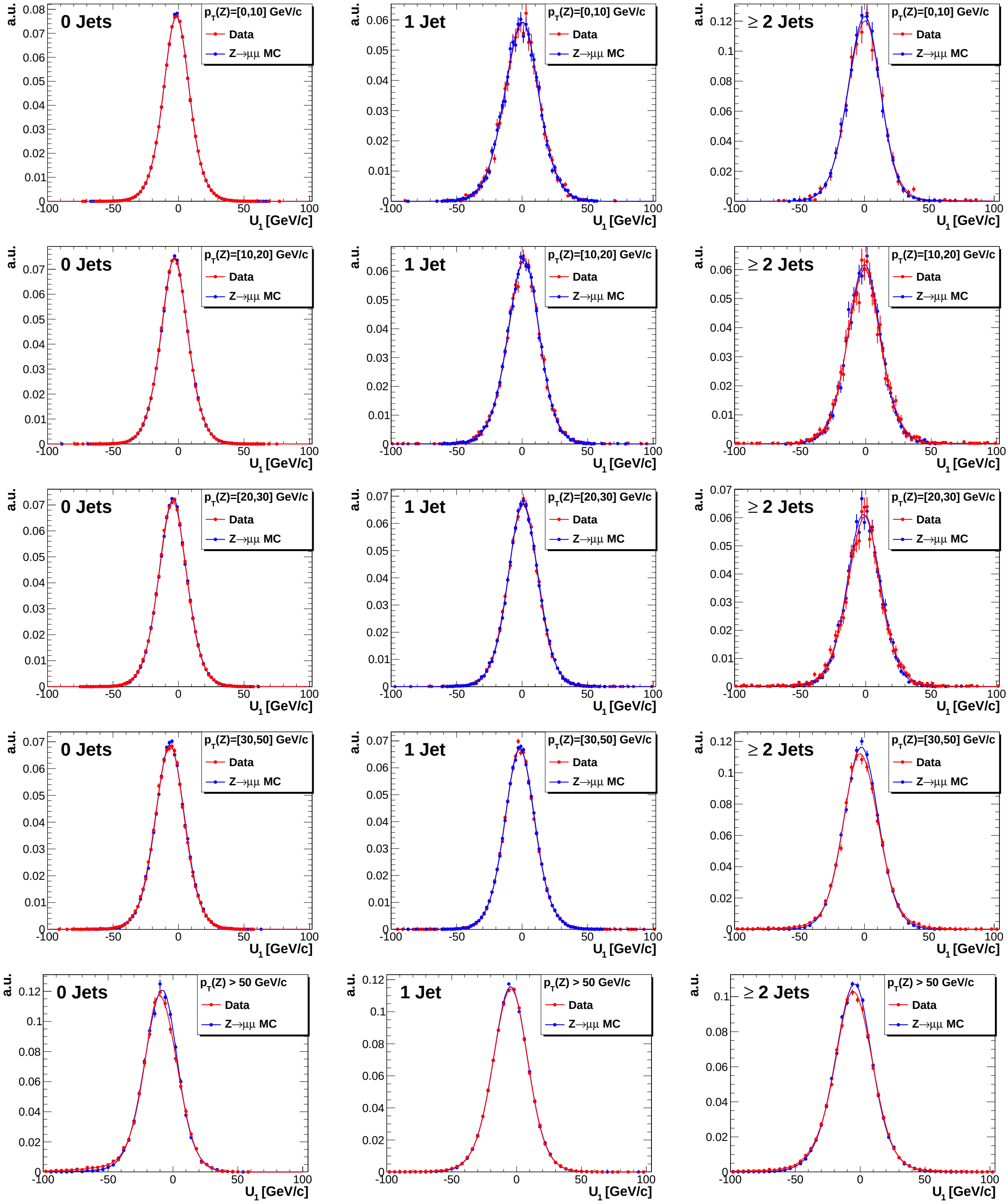

Figure A.3: Projected recoil momenta U_1 after the isomorphic mapping technique in 5x3 bins of Z-p_{T} (rows) and N_{jets} (columns)

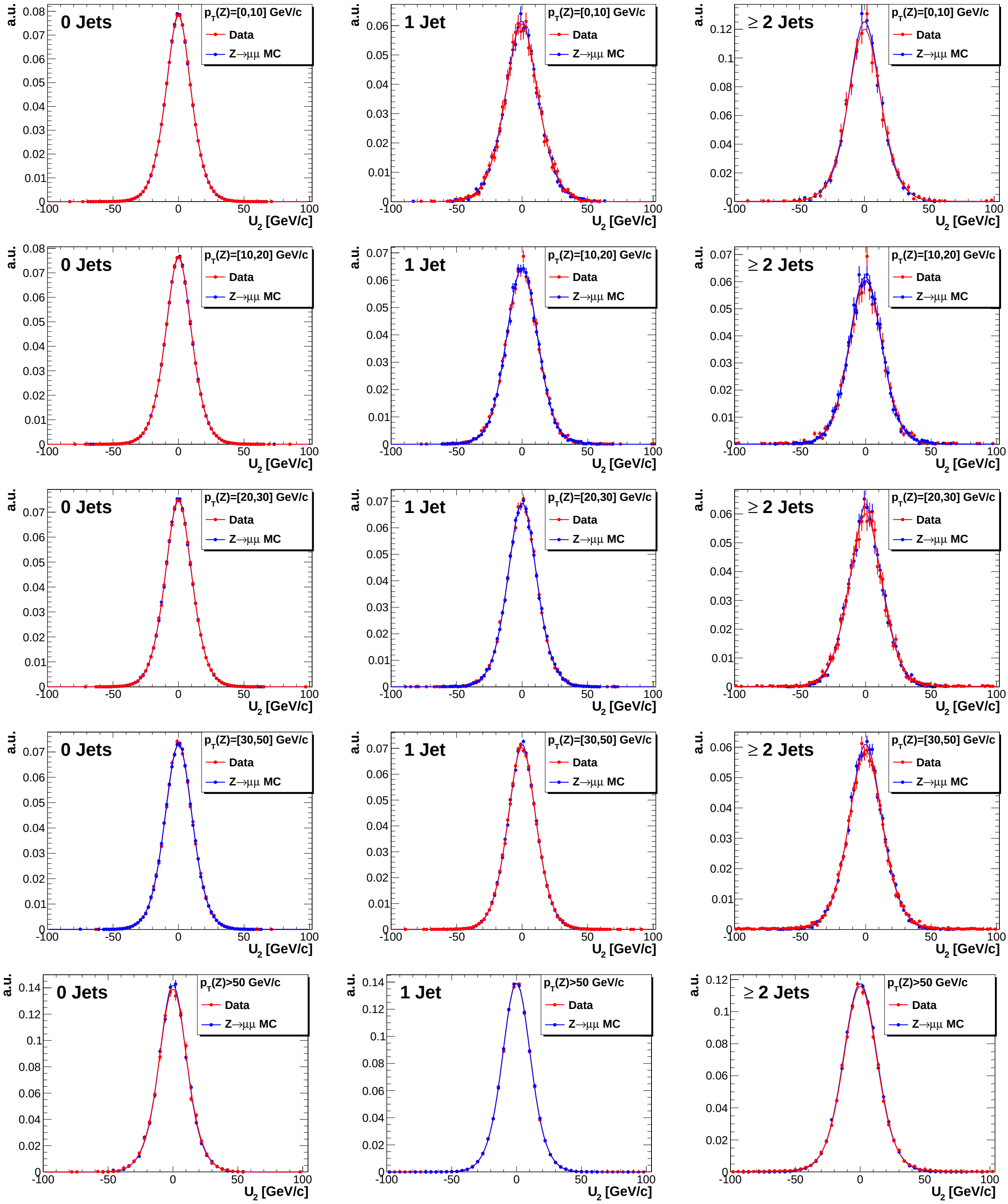

Figure A.4: Projected recoil momenta U_2 after the isomorphic mapping technique in 5x3 bins of Z-p_{T} (rows) and N_{jets} (columns)

Appendix B

DCA template fits

This appendix compiles the DCA template fits needed for the evaluation of the Drell-Yan background. Figures B.1-B.8 show dimuon DCA significance distributions, and fits to these distributions, for different bins of the invariant mass of the dimuon system, at the same time binned in the reduced BDT.

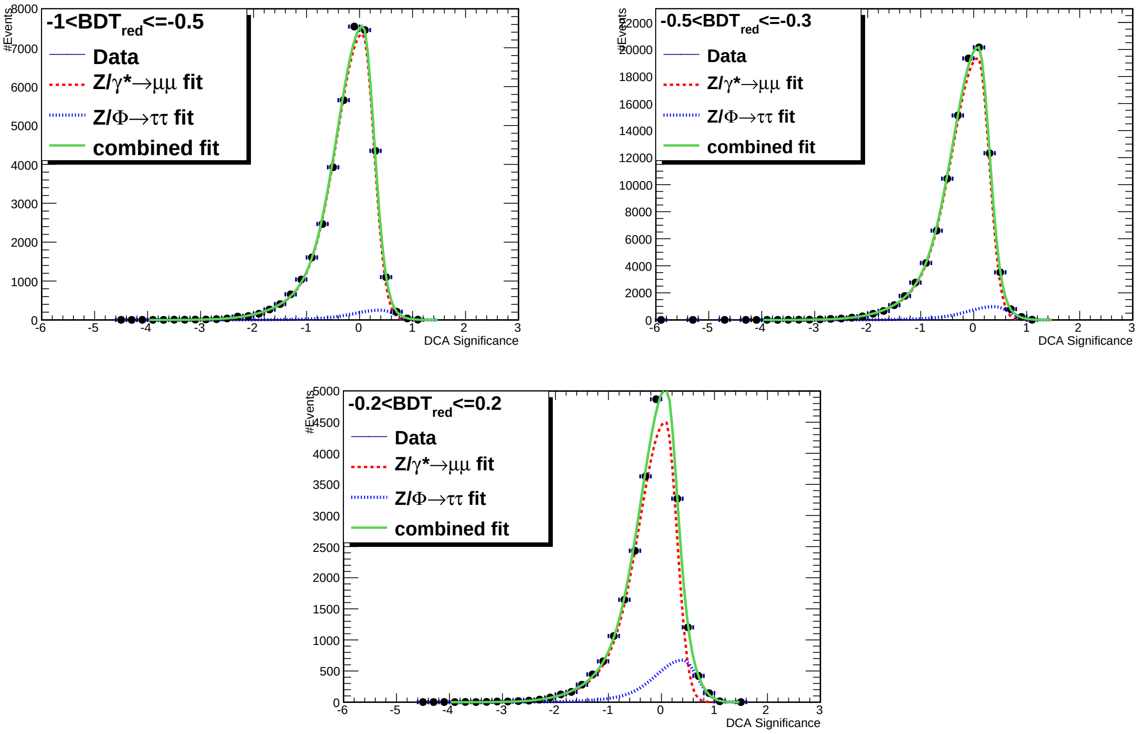

Figure B.1: Template fits of the dimuon DCA significance distributions in different bins of the reduced BDT for events in the dimuon mass range $m_{\mu\mu} < 70\,\mathrm{GeV/c^2}$.

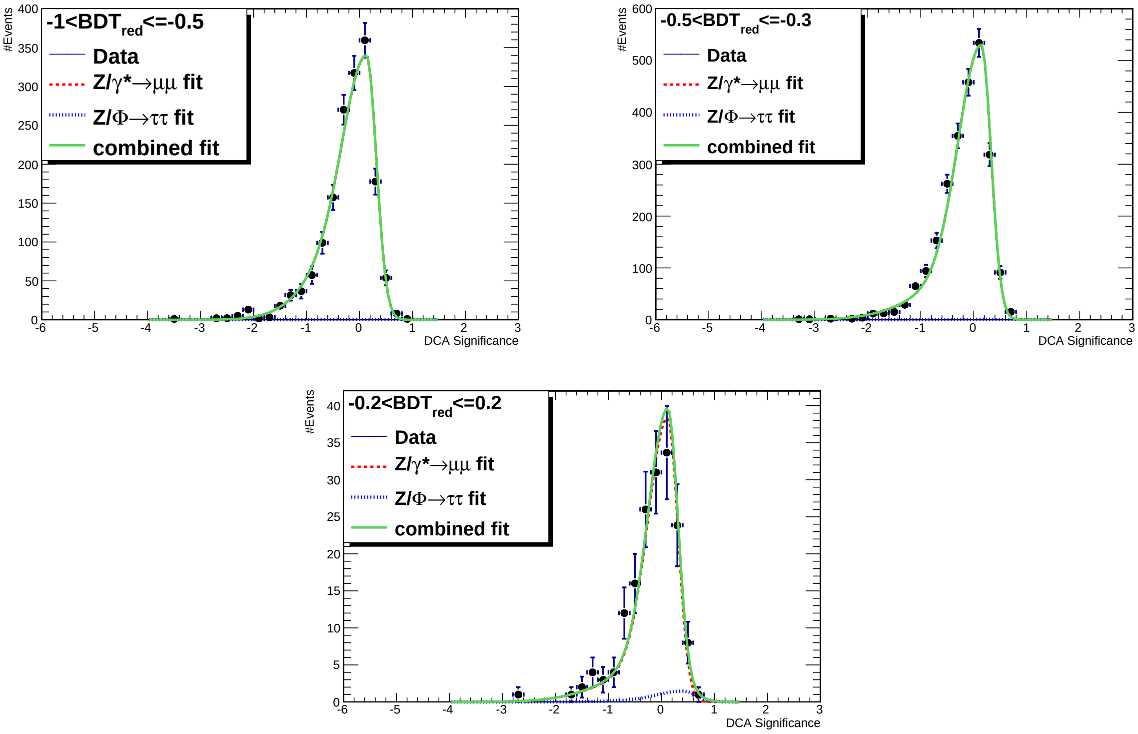

Figure B.2: Template fits of the dimuon DCA significance distributions in different bins of the reduced BDT for events in the dimuon mass range $70\,\mathrm{GeV/c^2} < m_{\mu\mu} < 91\,\mathrm{GeV/c^2}$.

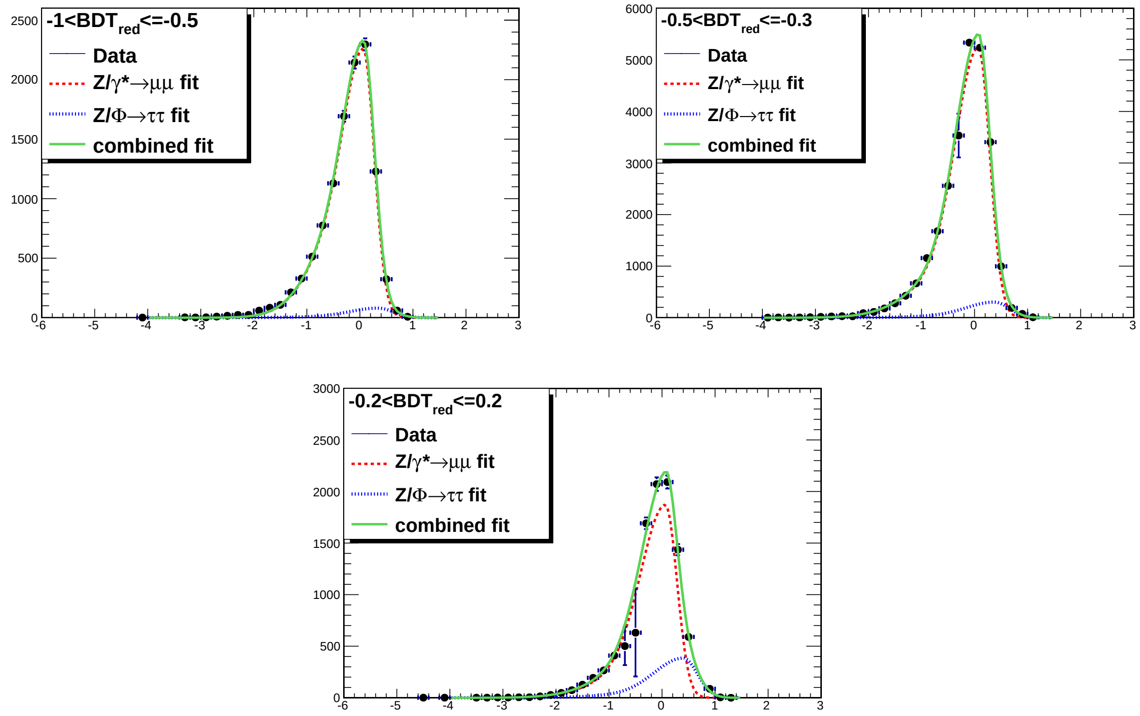

Figure B.3: Template fits of the dimuon DCA significance distributions in different bins of the reduced BDT for events in the dimuon mass range $m_{\mu\mu} < 70\,\mathrm{GeV/c^2}$.

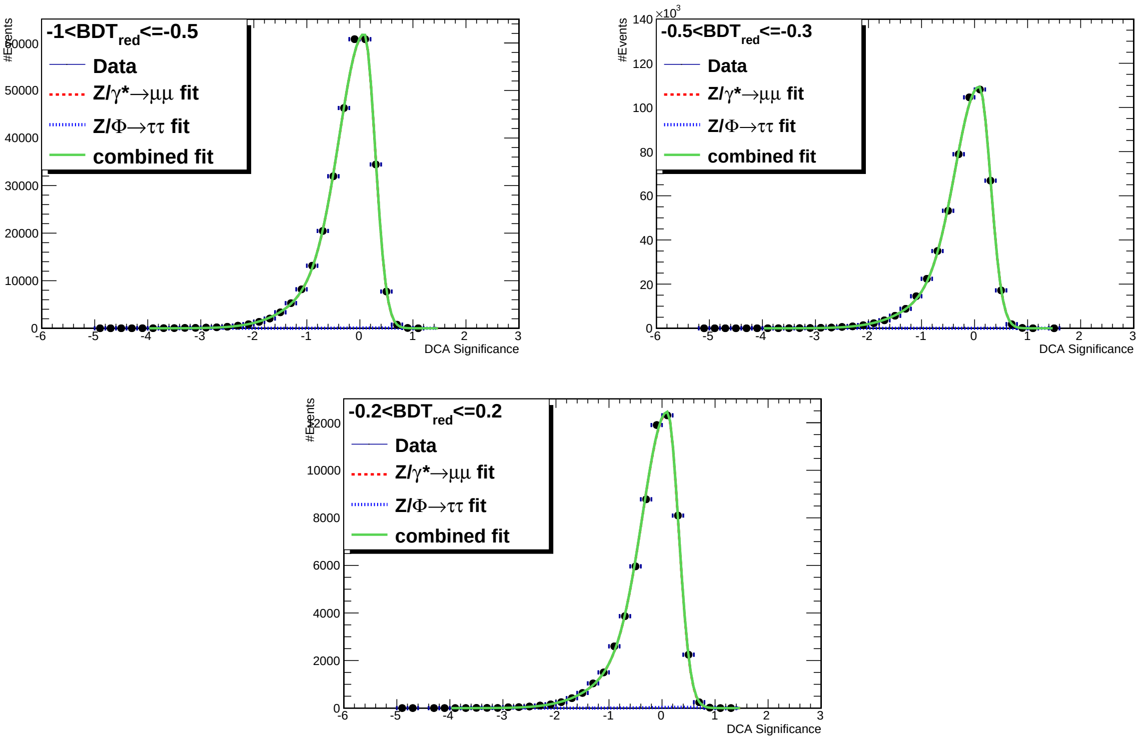

Figure B.4: Template fits of the dimuon DCA significance distributions in different bins of the reduced BDT for events in the dimuon mass range $70\,\mathrm{GeV/c^2} < m_{\mu\mu} < 91\,\mathrm{GeV/c^2}$.

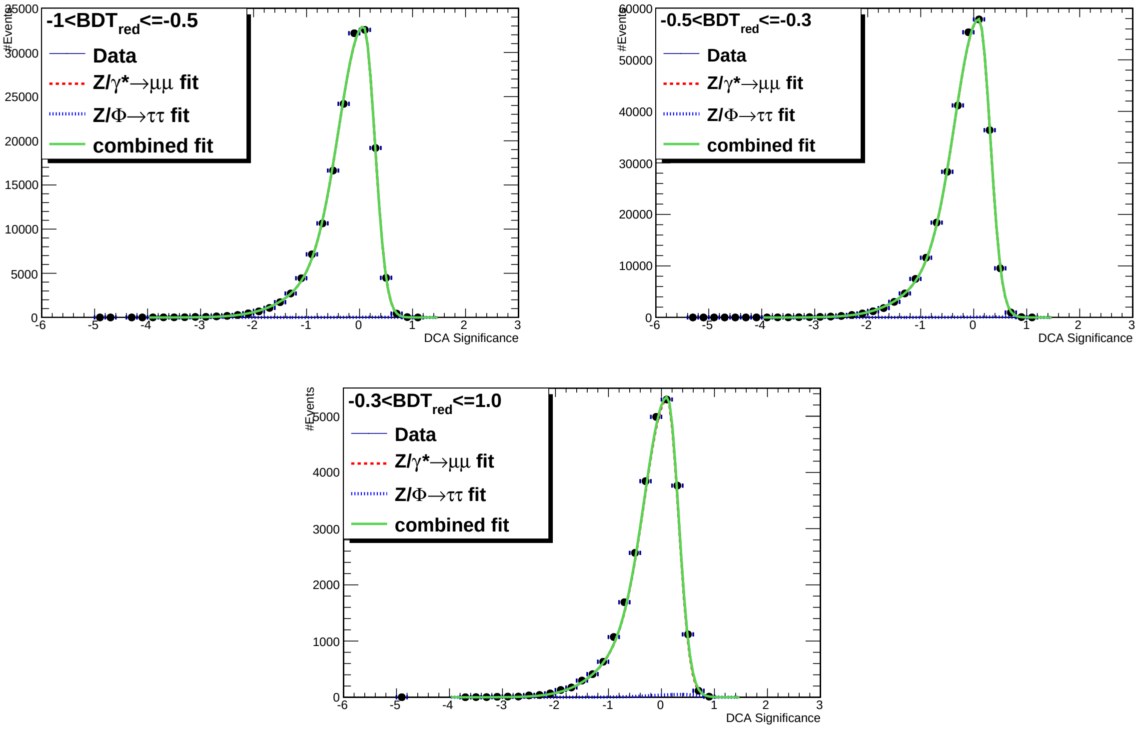

Figure B.5: Template fits of the dimuon DCA significance distributions in different bins of the reduced BDT for events in the dimuon mass range $91\,\mathrm{GeV/c^2} < m_{\mu\mu} < 110\,\mathrm{GeV/c^2}$.

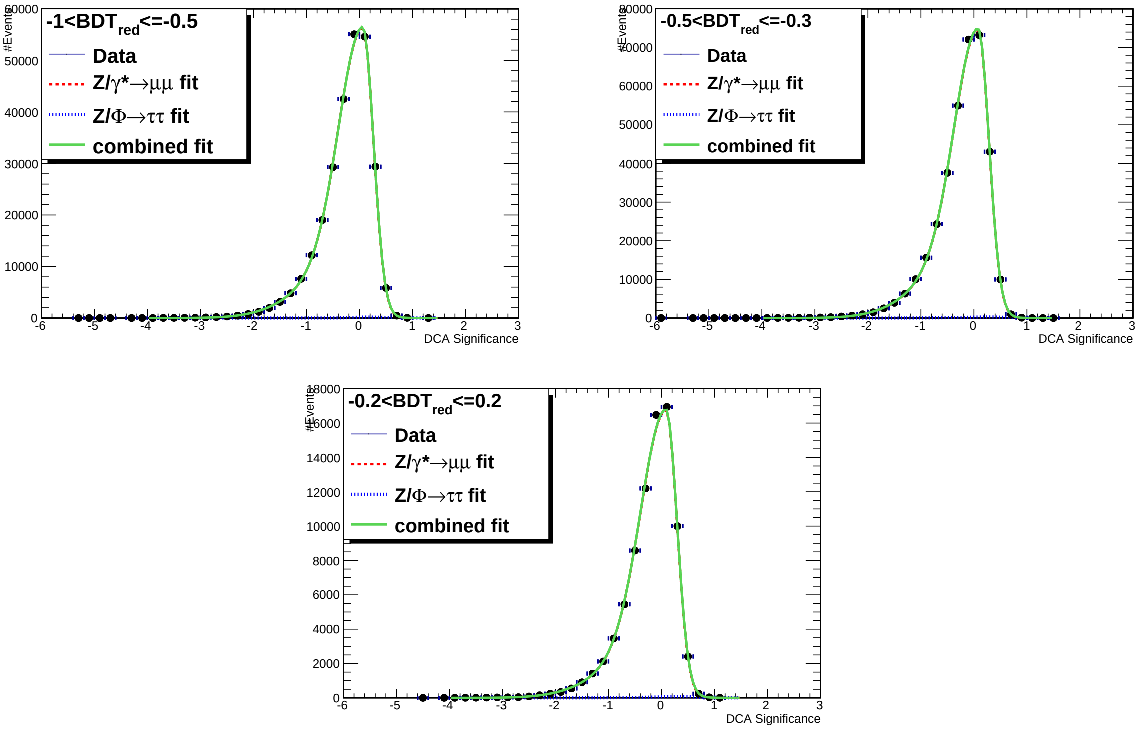

Figure B.6: Template fits of the dimuon DCA significance distributions in different bins of the reduced BDT for events in the dimuon mass range $70\,\mathrm{GeV/c^2} < m_{\mu\mu} < 91\,\mathrm{GeV/c^2}$.

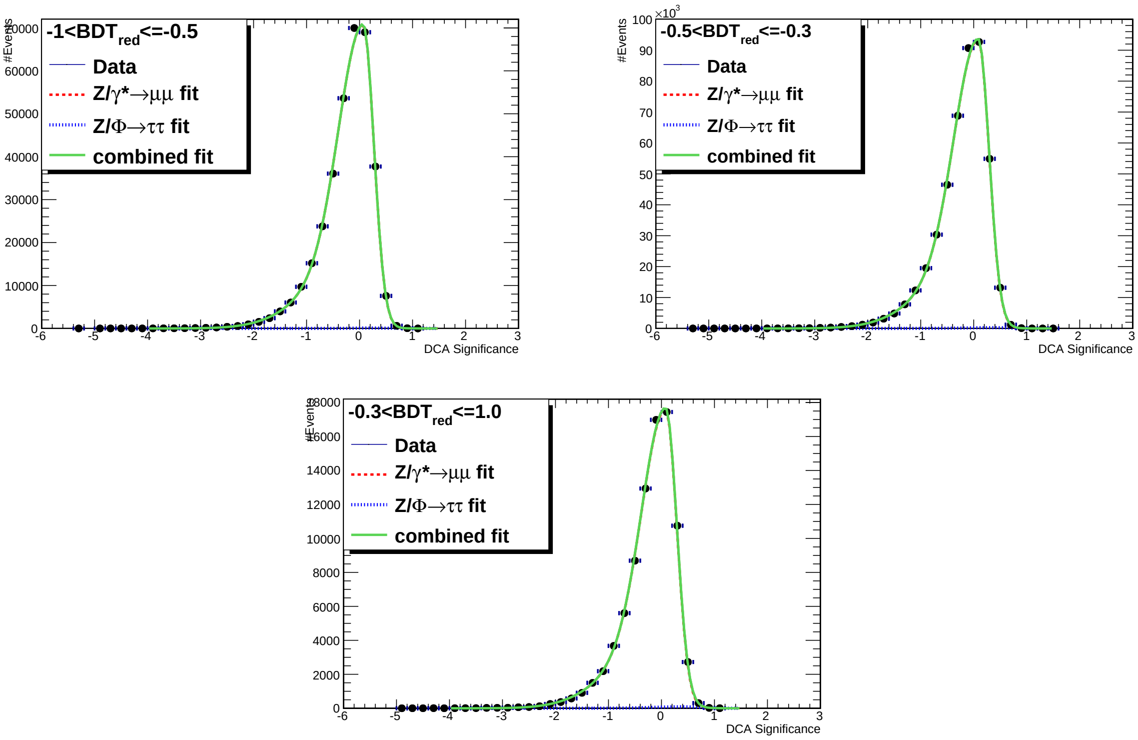

Figure B.7: Template fits of the dimuon DCA significance distributions in different bins of the reduced BDT for events in the dimuon mass range $91\,\mathrm{GeV/c^2} < m_{\mu\mu} < 110\,\mathrm{GeV/c^2}$.

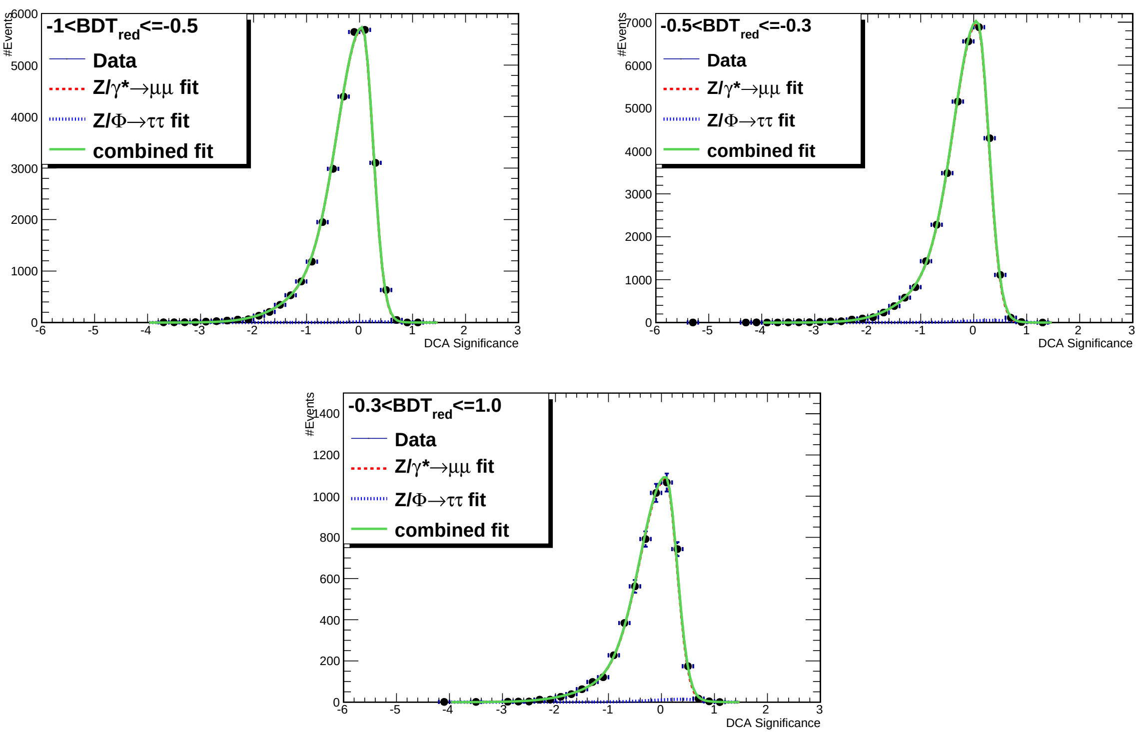

Figure B.8: Template fits of the dimuon DCA significance distributions in different bins of the reduced BDT for events in the dimuon mass range $110\,\mathrm{GeV/c^2} < m_{\mu\mu} < 140\,\mathrm{GeV/c^2}$.